

THREE-DIMENSIONAL ANALYSIS OF DIGITAL  
SUBTRACTION ANGIOGRAMS FOR STEREOTACTIC  
NEUROSURGERY PLANNING

G.M.Mawko

Dept. of Radiology / Medical Physics Unit  
McGill University, Montreal

May 1989

A thesis submitted to the Faculty of Graduate Studies and Research in  
partial fulfillment of the requirements for the degree of Doctor of  
Philosophy.

© George Mawko, 1989

### **3-D ANALYSIS OF DSA IMAGES FOR STEREOTACTIC NEUROSURGERY PLANNING**

## ABSTRACT

Geometric and tomographic methods of reconstructing three-dimensional cerebral blood vessels from two-dimensional digital subtraction angiograms are studied experimentally.

Three-dimensional vessel geometry is reconstructed from center-line coordinates of corresponding vessel branches in both stereo and biplane angiogram pairs. The problem associated with finding corresponding vessel branches in biplane images was shown to be reduced by re-projection of stereoscopically reconstructed vessels. Results indicate that the limiting factor in reconstruction accuracy is the degree of vessel foreshortening in biplane image pairs.

An iterative algorithm ('Clean') is adapted to tomographic reconstruction of vessel cross-sections from a small number of views. Star-pattern artifacts in images initially formed by back-projection are removed by iterative deconvolution guided by 'a priori' object knowledge. This procedure is repeated for a set of two-dimensional sections that describe the three-dimensional vascular structure. Results show that there is sufficient detail in reconstructed sections to determine the location of vascular structures.

## RÉSUMÉ

Des méthodes géométriques et tomographiques ont été étudiées expérimentalement pour reconstruire les vaisseaux sanguins cérébraux en trois dimensions à partir d'angiographies soustraites numérisées.

La géométrie tri-dimensionnelle des vaisseaux est reconstruite à partir des coordonnées sur la ligne centrale des branches correspondantes dans les angiographies biplane et stéréo. On montre que la difficulté associée à trouver les branches correspondantes dans les paires d'images biplanes est réduite par reprojexion des vaisseaux reconstruits en stéréo. Les résultats démontrent que le facteur qui limite la précision de la reconstruction est le degré de raccourci des vaisseaux dans les paires d'images biplanes.

Un algorithme itératif ('Clean') a été adapté à la reconstruction tomographique d'un petit nombre d'images de coupe transversale des vaisseaux. Les erreurs d'images formées par la surimpression en forme d'étoile sont enlevées par une déconvolution itératif guidée par des connaissances 'a priori' de l'objet. La procédure est répétée pour un groupe de sections bi-dimensionnelles qui décrit la structure vasculaire tri-dimensionnelle. Les résultats démontrent qu'il existe des détails suffisantes dans les sections reconstruites pour déterminer la position des structures vasculaires.



## ACKNOWLEDGMENTS

I am especially grateful to Prof. T.M. Peters and Prof. M. Cohen for their support, patience, and encouragement throughout my studies. My special thanks to Prof. T.M. Peters for his constructive and very helpful review of this thesis.

I also extend my gratitude to Dr. J.H.T. Bates for his helpful discussions on the concept of subtractive image restoration, particularly the Clean algorithm.

I would like to thank all my colleagues at the Montreal Neurological Institute for their discussions, in particular John Clark, Edmund Madevu, and Bruce Pike. Thanks are due to Louis Collins for translating the abstract into French. I would also like to thank the following for their support and interest in this work: Dr. R. Ethier and Dr. A. Olivier. I am also grateful to my current employer, the Saskatchewan Cancer Foundation, for providing me with access to their computing facilities through which this document was prepared.

During the course of my Ph.D. research I was financially supported by Postgraduate Fellowships from the McConnell Foundation and the Medical Research Council of Canada, for which I am very grateful.

Finally, I would like to thank my family for their uncommon support, understanding, and encouragement.

## PREFACE

This thesis arose out of the need for a three-dimensional (3-d) image of the cerebral blood vessels to assist the neurosurgeon in the planning of safe stereotactic surgery. The major concern in planning passage of probes or biopsy needles in the brain is blood vessel hemorrhage. In order to minimize trauma it is necessary to determine the 3-d position of blood vessels in relation to the target volume. The work presented in this thesis is a step in meeting this long term goal.

Chapter 1 is an overview of the broad subject of 3-d vessel reconstruction. This chapter begins with a brief description of modalities used to image vessels and makes the case for the use of angiography. Of the three physical characteristics of blood vessels, flow, morphology, and position, the latter is the most important in surgical planning. Methods that reconstruct the 3-d position of vessels from angiograms are reviewed. Reconstruction methods are subdivided into related groups: 1) stereoscopic display, 2) geometric reconstruction from stereo and biplane images, and 3) tomographic image reconstruction. This chapter reviews the different methodologies being followed and outlines our present understanding of the problems in 3-d vascular reconstruction from angiograms. The most likely approaches are stereo and biplane analyses and tomography. Both these approaches are considered further in this thesis. The scope of this thesis is restricted to the evaluation of reconstruction algorithms of these methods.

Digital subtraction angiography (DSA) imaging systems have several physical problems associated with the measurement process. In chapter 2 these problems are described in the context of image formation, detection, and processing. The consequences of measurement error in DSA image acquisition are discussed from the point of view of subsequent 3-d analysis of the angiograms.

The third chapter describes an interactive reconstruction method that uses stereo and biplane angiograms. A 'lateral' stereo DSA image pair and a single image in a direction orthogonal to the lateral pair (i.e. 'anterior-

posterior') are acquired. The biplane pair is made up of the anterior-posterior image and one of the lateral stereo images. This new method uses the results of stereo reconstruction to assist the observer in selecting corresponding vessel branches in the anterior-posterior angiogram. The idea is to use the computer to provide an orthogonal view of the stereo reconstructed vessels, rather than have the observer mentally interpret such a view from a stereoscopically perceived 3-d image of the vessels. The graphical overlay of re-projected vessels in the anterior-posterior angiogram simplifies the task of resolving the ambiguities of vessel superposition. Having found corresponding vessel branches in the biplane images, a final reconstruction is performed. In order to evaluate reconstruction accuracy, both numerical and phantom experiments were carried out. This is reported in chapter 4.

Chapter 5 investigates the problem of tomographic image reconstruction from a small number of projections. The reconstruction problem is simplified to a form that can be solved using a subtractive deconvolution technique. The proposed method uses 'a priori' information about the blood vessels to guide the deconvolution process. This method, known as modified-Clean (McClean), attempts to maximally retrieve the reconstructed object consistent with its projections and reduce artifacts to an acceptable level. In this manner the best possible use of the available projections is made. Chapter 5 concludes with a discussion of the uniqueness and limitations of the proposed reconstruction algorithm.

Chapter 6 concludes this thesis with a summary and presents suggestions for further research in the 3-d analysis of cerebral angiograms.

The following are believed to be original contributions made by this thesis:

- 1) The extension of practical applications of the known principles of stereo and biplane analyses.
- 2) The demonstration of the utility of re-projecting stereo reconstructed cerebral blood vessels as a tool for finding the corresponding vessels in the anterior-posterior projection.

- 3) The demonstration of the limitations of stereo-biplane stereotactic reconstruction technique as a function of measurement noise and correspondence errors.
- 4) Thorough analysis of the propagation of errors in quantitative analysis of digital stereoscopic and biplane angiograms made under stereotactic conditions.
- 5) Experimental and observational extensions of knowledge in tomographic image reconstruction of vessel-like objects from a small number of projections.
- 6) The experimental extension of the Clean algorithm to include removal of star-pattern artifacts in vascular images reconstructed from a few projections.

# TABLE OF CONTENTS

	<u>Page</u>
Abstract	ii
Résumé	iii
Acknowledgments	iv
Preface	v
Table of Contents	viii
<b>Chapter 1 Introduction</b>	
1.1 Overview . . . . .	1
1.2 Rationale . . . . .	1
1.3 Vascular imaging techniques . . . . .	2
1.3.1 X-ray subtraction angiography . . . . .	2
1.3.2 Computed tomography . . . . .	3
1.3.3 Magnetic resonance imaging . . . . .	4
1.4 Overview of 3-d vascular reconstruction from angiograms . . . . .	4
1.4.1 Stereoscopic angiography . . . . .	5
1.4.2 3-d measurements from stereo and biplane angiograms . . . . .	8
1.4.2.1 Reconstruction from stereo images . . . . .	9
1.4.2.2 Reconstruction from biplane images . . . . .	12
1.4.3 Few view tomography . . . . .	15
1.5 Conclusion . . . . .	19
<b>Chapter 2 Physical Aspects of Digital Subtraction Angiography</b>	
2.1 Introduction . . . . .	21
2.2 Imaging principle . . . . .	21
2.3 Measurement system . . . . .	22
2.3.1 X-ray source . . . . .	24
2.3.2 X-ray detector . . . . .	24
2.3.3 Processor . . . . .	25
2.4 System non-linearities. . . . .	26
2.4.1 Beam energy . . . . .	27
2.4.2 Beam shape . . . . .	27
2.4.3 Noise . . . . .	32
2.4.4 X-ray scatter and veiling glare . . . . .	32
2.4.5 Sampling . . . . .	33
2.4.6 Pin-cushion distortion . . . . .	35
2.4.7 Patient motion . . . . .	36
2.5 Conclusion . . . . .	36
<b>Chapter 3 Geometric Reconstruction from DSA Image Pairs: Method</b>	
3.1 Introduction . . . . .	39
3.2 Problems in 3-d vessel reconstruction from cerebral DSA images . . . . .	39
3.3 Vessel trace correspondence principle. . . . .	44
3.3.1 Background . . . . .	44
3.3.1.1 Vessel correspondence problem. . . . .	44

		<u>Page</u>
3.3.1.2	Correlation-based algorithms . . . . .	47
3.3.1.3	Ray-based algorithms. . . . .	51
3.3.2	Proposed algorithm . . . . .	55
3.4	Stereo-biplane reconstruction method . . . . .	56
3.4.1	Overview of proposed method . . . . .	57
3.4.2	Stereo and biplane acquisition of DSA images . . . . .	59
3.4.3	Calibration . . . . .	61
3.4.3.1	Description of the MNI stereotactic frame . . . . .	61
3.4.3.2	X-ray beam geometry calibration . . . . .	61
3.4.3.3	Image pin-cushion distortion correction . . . . .	64
3.4.4.	3-d display of stereo DSA images . . . . .	67
3.4.4.1	Implementation of colour anaglyph method . . . . .	71
3.4.5	Tracking of vessels in DSA images . . . . .	73
3.4.6	Reconstruction and re-projection algorithms . . . . .	75
Chapter 4	<b>Geometric Reconstruction from DSA Image Pairs: Implementation &amp; Evaluation</b>	
4.1	Introduction . . . . .	78
4.2	Reconstruction sensitivity to measurement error . . . . .	78
4.2.1	Reconstruction coordinate system . . . . .	79
4.2.2	Definition of error measures . . . . .	79
4.2.3	Sources of measurement error . . . . .	81
4.2.4	Measurement error in image pair coordinates . . . . .	82
4.2.4.1	Theory . . . . .	82
4.2.4.2	Simulation experiments . . . . .	84
4.2.5	Measurement error in fiducial image coordinates . . . . .	92
4.2.5.1	Simulation experiments . . . . .	94
4.2.6	Physical determination of accuracy: phantom test. . . . .	104
4.2.6.1	Description of experiment . . . . .	104
4.2.6.2	Results . . . . .	106
4.2.7	Summary . . . . .	111
4.3	Reconstruction sensitivity to correspondence error . . . . .	112
4.3.1	Correspondence measure sensitivity to measurement error . . . . .	113
4.3.1.1	Simulation experiments . . . . .	113
4.3.2	Error sensitivity of correspondence algorithm . . . . .	117
4.3.2.1	Method . . . . .	120
4.3.2.2	Example 1 . . . . .	121
4.3.2.3	Example 2 . . . . .	126
4.3.3	Application to cerebral DSA . . . . .	126
4.3.3.1	Method . . . . .	126
4.3.3.2	Example 1 . . . . .	131
4.3.3.3	Example 2 . . . . .	134
4.3.4	Summary . . . . .	137
4.4	Conclusions . . . . .	138
Chapter 5	<b>Iterative 3-d Reconstruction of Vascular Images from a Few Views</b>	
5.1	Introduction . . . . .	140
5.2	Reconstruction theory overview . . . . .	140
5.2.1	Preliminaries . . . . .	140

	<u>Page</u>
5.2.2	Transform reconstruction methods . . . . . 141
5.2.2.1	Reconstruction by direct inversion . . . . . 143
5.2.2.2	Simple back-projection . . . . . 145
5.2.2.3	Filtered back-projection . . . . . 145
5.2.3	Sampling requirements . . . . . 147
5.2.3.1	$\xi$ sampling . . . . . 147
5.2.3.2	$\phi$ sampling . . . . . 148
5.2.4	Algebraic reconstruction methods . . . . . 148
5.2.4.1	Fundamentals . . . . . 148
5.2.4.2	Matrix inversion . . . . . 149
5.2.4.3	Iterative reconstruction methods . . . . . 150
5.2.5	Comparison between transform and algebraic methods 151
5.3	Reconstruction from a few views . . . . . 151
5.3.1	Previous work . . . . . 152
5.3.1.1	Interpolation of missing projections . . . . . 155
5.3.1.2	Application of global image constraints . . . . . 156
5.3.1.3	Application of 'a priori' image information . . . . . 156
5.3.2	'A priori' image information . . . . . 157
5.4	Problem statement . . . . . 160
5.5	Reconstruction method . . . . . 161
5.5.1	Clean algorithm . . . . . 161
5.5.2	Modified-Clean (Mclean) algorithm . . . . . 163
5.5.3	Implementation . . . . . 165
5.5.3.1	Back-projection algorithm . . . . . 165
5.5.3.2	Re-projection algorithm . . . . . 166
5.5.3.3	Estimation of image extent . . . . . 167
5.6	Computational experiments . . . . . 167
5.6.1	Simulation of projection data . . . . . 168
5.6.2	Comparison criteria . . . . . 171
5.6.3	Basic experiment . . . . . 173
5.6.3.1	Method I: Convolution back-projection . . . . . 174
5.6.3.2	Method II: Masked convolution back-projection . . . . . 180
5.6.3.3	Method III: Mclean . . . . . 186
5.7	Phantom experiments . . . . . 196
5.7.1	Results . . . . . 198
5.8	Conclusions . . . . . 202
 Chapter 6	 <b>Conclusions and Suggestions for Future Research</b>
6.1	Geometric reconstruction from DSA image pairs . . . . . 205
6.2	Iterative 3-d reconstruction of vascular images from a few views . . . . . 207
6.3	Summary . . . . . 208
 Appendix A	 <b>Display of 3-d Reconstruction Results</b>
A.1	Display of 3-d data . . . . . 209
A.2	Re-projection algorithm . . . . . 211
 Appendix B	 <b>Interaction With Stereoscopic Images . . . . . 214</b>
 References	 . . . . . 218
 Glossary	 . . . . . 235

## CHAPTER ONE

### INTRODUCTION

#### 1.1 Overview

In this chapter the motivation for a three-dimensional (3-d) image of the cerebral blood vessels and a historical review of techniques to construct such an image are presented. §1.2 describes the need for a 3-d image of the cerebral blood vessels in neurosurgical planning, and §1.3 discusses the current techniques that are used to image the cerebral blood vessels.

To date the technique of choice is x-ray subtraction angiography, and the various methods that have been used to visualize and reconstruct blood vessels from angiograms are reviewed in §1.4. This chapter concludes with a summary of the limitations of the existing reconstruction methods.

#### 1.2 Rationale

A 3-d image of the cerebral blood vessels is important to the safe planning of stereotactic neurosurgery (Szikla et al. 1975). The term 'stereotaxy' means 'arrangement in space' and refers to any neurosurgical procedure which places a probe in the region of the brain or spinal cord without directly visualizing that region (Bosh 1986). Stereotactic operations are used to safely approach small regions located in critical areas of the brain. This is achieved by referencing structures to a rigid frame (i.e. stereotactic frame) which is fixed to the patient's skull during imaging and surgical procedures. Through small burr holes in the skull recording-stimulating electrodes or biopsy needles can reach almost any brain region without having to make a large incision in the brain or use general anesthesia. Irradiation can also be focused stereotactically on small regions in the brain (Hartmann et al. 1985; Colombo et al. 1985; Heifetz et al. 1984; Pike et al. 1987).



Since the primary risk to the patient during such interventions is hemorrhage, then by plotting probe trajectories or isodose distributions in the 3-d image of the cerebral blood vessels, trauma can be minimized. In order to accomplish this the stereotactic system requires three components: an image generating device, historically film x-ray system (Leksell 1951), but more recently computed tomography (CT) scanners, digital subtraction angiography (DSA) and magnetic resonance (MR) imaging systems (Peters et al. 1983,1986; Alker et al. 1984; Suetens et al. 1982; Kelly et al. 1984), a mechanical frame (Leksell 1949; Brown 1979; Peters et al. 1983; Olivier et al. 1985), and a procedure to transform image-system coordinates to frame positions (Lirov et al. 1986; Peters et al. 1986; Saw et al. 1987).

Another advantage of having a 3-d image of the cerebral blood vessels is the possibility to construct any arbitrary perspective view of the vessels. Tomographic sections can also be selected and used to augment a corresponding MR or CT section image. Integrated images would provide precise information about the correlation between anatomical and radiographic data.

Such clinical tasks as neurosurgical planning and correlative studies require a 3-d image of the cerebral vasculature in which the positions of the blood vessels are accurately known.

### **1.3 Vascular imaging techniques**

The cerebral blood vessels can be visualized by a number of two-dimensional (2-d) imaging techniques. These include x-ray subtraction angiography, computed tomography, and magnetic resonance imaging. Although Doppler ultrasonography is often used to image vessels, it is ineffective in the cranium (Wedeen et al. 1985).

#### **1.3.1 X-ray subtraction angiography**

In x-ray subtraction angiography the cerebral blood vessels can be made visible by injecting them with a radio-opaque or contrast material, typically containing iodine. Subtraction techniques are then employed to

eliminate the intervening tissue so that the contrast visualization is limited solely by noise. The subtraction technique involves obtaining data both before and after the administration of contrast agent and subtracting the result. Pre- and post-opacified images can be recorded on either film or digitally. The subtraction concept is not new (Ziedses des Plantes 1934;1962), but not until the development of digital subtraction angiography (DSA) has subtraction accuracy been sufficient to isolate less than 1% image contrast (Kruger and Riederer 1984).

Since the angiogram is just a 2-d projection image, the loss of depth information limits analysis of the 3-d structure of the vessels. Furthermore, interpretation is complicated by vessel foreshortening (i.e. vessels parallel to the line of the x-ray source to the image detector) and by the overlapping or superposition of vessels in the angiogram.

#### 1.3.2 Computed tomography

Similarly, computed tomography (CT) scanning immediately after the intravenous injection of a bolus of contrast material enables visualization of the cerebral blood vessels. This method of combined computed tomography-angiography is often referred to as 'arterial bolus dynamic computed tomography scanning' (Nauta et al. 1984). The resultant images show vessels associated with lesions and tumours in the CT plane (Nauta et al. 1984).

Although relatively large vascular structures can sometimes be visualized on CT scans, many vessels are beneath the resolution of CT scanners (Bergström et al. 1976; Weinstein et al. 1977). The limit of the size of a blood vessel that can be defined with CT is 1.5mm when the blood iodine level is about 4mg/ml (Bergström et al. 1976). There are also some regions in the head, particularly near the base of the brain, where vessels cannot be demonstrated in a scan because of vascular blushes and bone artifacts (Naidich et al. 1977).

For those cases in which the stereotactic biopsy trajectory must pass through several CT planes, it becomes more difficult to show all the vessels

along the entire trajectory. Even if vessels can be reconstructed over all regions of the brain, multiple overlapping sections would have to be collected almost simultaneously which is beyond the capabilities of present equipment (Scanlon et al. 1980; Block et al. 1984).

### 1.3.3 Magnetic resonance imaging

Several methods have been developed for magnetic resonance (MR) flow imaging (Nishimura et al. 1986; Wedeen et al. 1985; Hale et al. 1985; Valk et al. 1985; Feinberg et al. 1984; Singer and Crooks 1983; Macovski 1982). In these methods an image based on flowing material is acquired by discriminating between static and flowing material during the excitation portion of the imaging process. Static material signals are either subtracted out (temporal subtraction) or not generated while flowing material becomes an active source of signal (canceling excitation). Moreover, these excitation procedures can be applied to both cross sectional and 'projective' imaging. MR vascular imaging combines the advantages of 3-d imaging and soft tissue subtraction techniques. The 3-d reconstruction of vessels can be shown in any projection, and overlapping vessel segments can be readily differentiated on the depth encoded image. MR flow imaging is clinically practical in only large vessels such as the carotids. Limitations of existing methods are most often attributed to the inherent difficulty of flow imaging 'in vivo' including the small size and complicated anatomy of important vessels and the high velocity they sustain (Wedeen et al. 1986).

Of the three vascular imaging techniques, angiography is preferred on the basis of better resolution and good image contrast due to the subtraction of background (e.g. tissue and bone) from the image. Although the blood vessels are conspicuous in the angiogram, the interpretation of vessel depth position usually requires both observer training and additional angiograms taken at different views. The methods available to recover depth information from the angiogram are presented in the next section.

### 1.4 Overview of 3-d vascular reconstruction from angiograms

Angiograms all have the fundamental disadvantage that they provide no

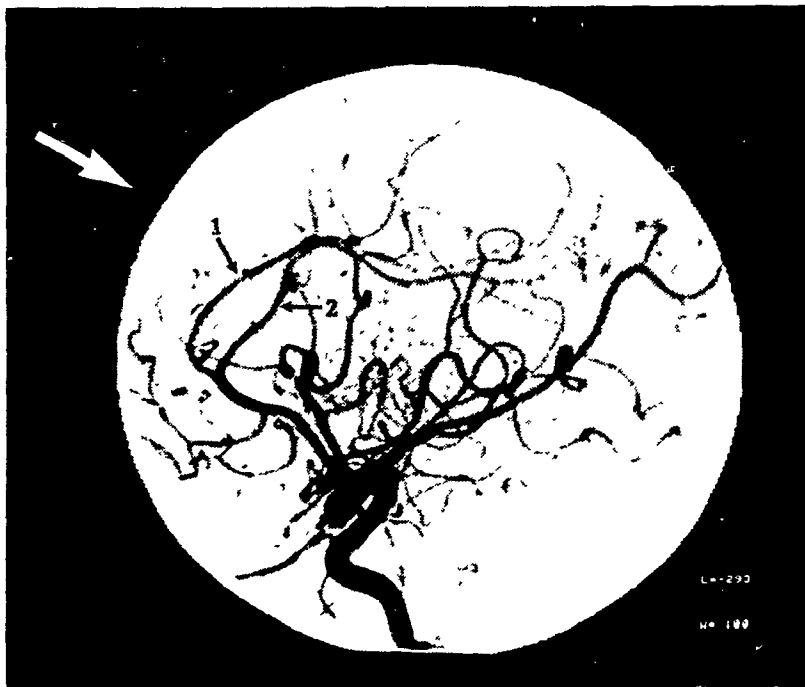
information as to the position in depth and the shape or lumen geometry of the vessels (Fig. 1.1). Two important and distinct features in the angiograms shown in Fig. 1.1 are the highly curved paths of the blood vessels and the large number of blood vessels in the image. The primary result of this combination is the high degree of vessel overlap in angiograms from whatever view they are taken. There will always be a certain number of blood vessels that are obscured, and they will be different from view to view. This result makes finding efficient and rigorous solution(s) to the reconstruction problem difficult.

In this section a number of approaches to the problem of recovering vessel depth position from angiograms are reviewed. They include visual stereoscopic analysis, 3-d measurement or geometric reconstruction from stereo and biplane angiograms, and tomographic reconstruction from a few views. Methods of reconstructing vascular morphology and flow from angiograms are discussed elsewhere (Reiber et al. 1984; Parker et al. 1987).

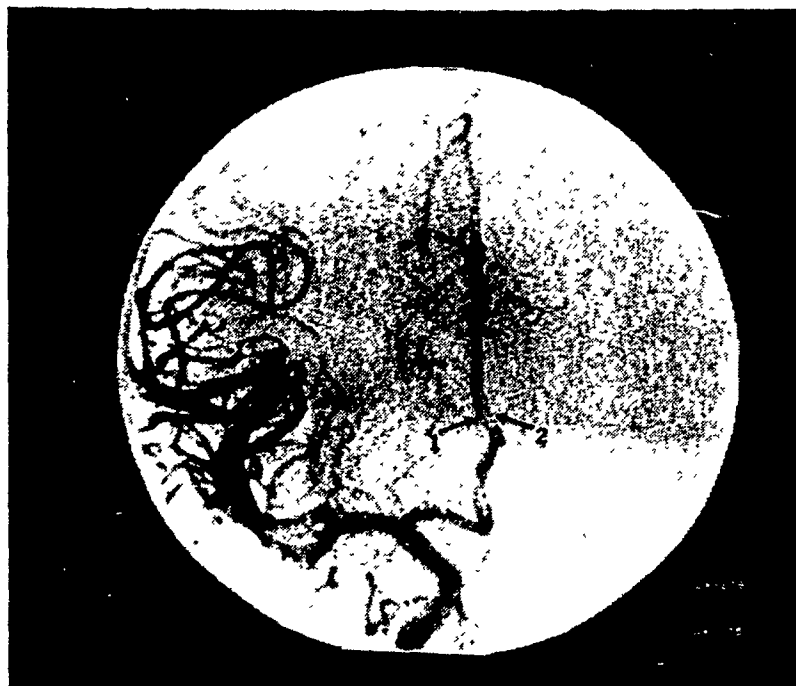
#### 1.4.1 Stereoscopic angiography

The most commonly used clinical procedure to study the 3-d structure of the cerebral vasculature is stereoscopic angiography (Doi et al. 1981). Stereoscopic imaging techniques are simple and usually require no special equipment. One image is recorded for each eye. Between the recording of each image the x-ray tube is shifted from the left eye to the right eye position while keeping the image detector fixed. The shift in the tube focus is usually about 10% of the focus-detector distance (Christensen et al. 1972). In some radiographic units the x-ray tube and image detector are connected rigidly together to form a c-arm structure. With these units it is easier to shift the c-arm a certain number of degrees rather than a specific distance. In stereo radiography the c-arm is usually rotated 6 to 10 degrees between images (Christensen et al. 1972). Figs. 1.2 a) and b) give examples of typical stereoscopic cerebral angiograms using a c-arm rotation technique.

The basis of stereoscopic depth perception is binocular disparity or the horizontal parallax between corresponding points from images that are projected on the left and right retinae (Davson 1963; Julesz 1971). A 3-d



a) Lateral view

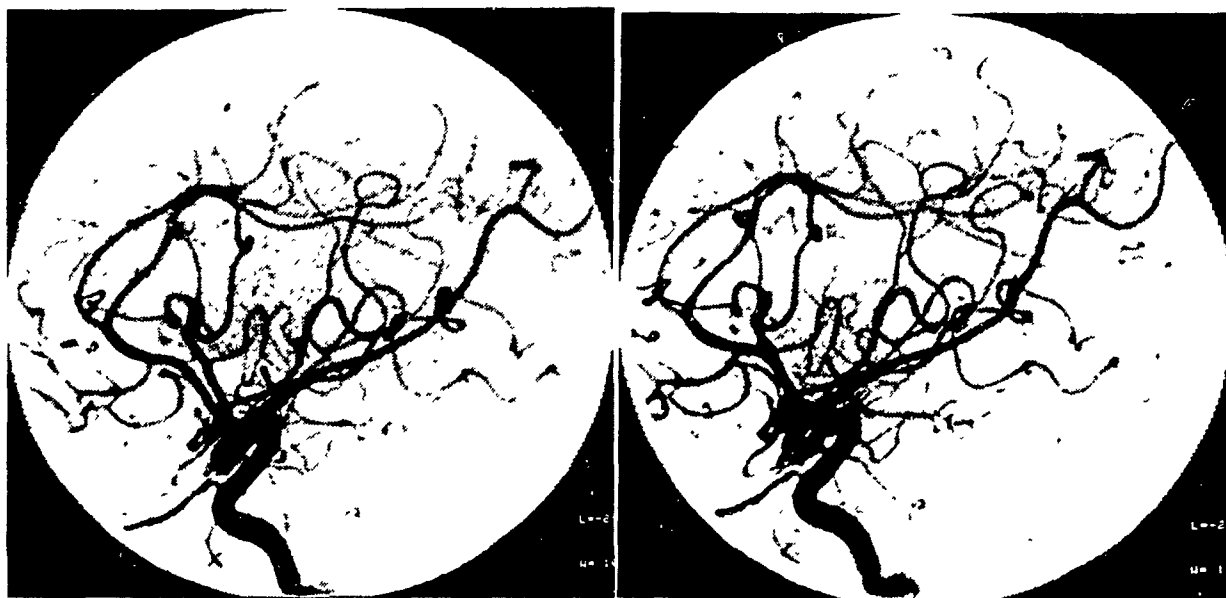


b) Anterior-posterior view

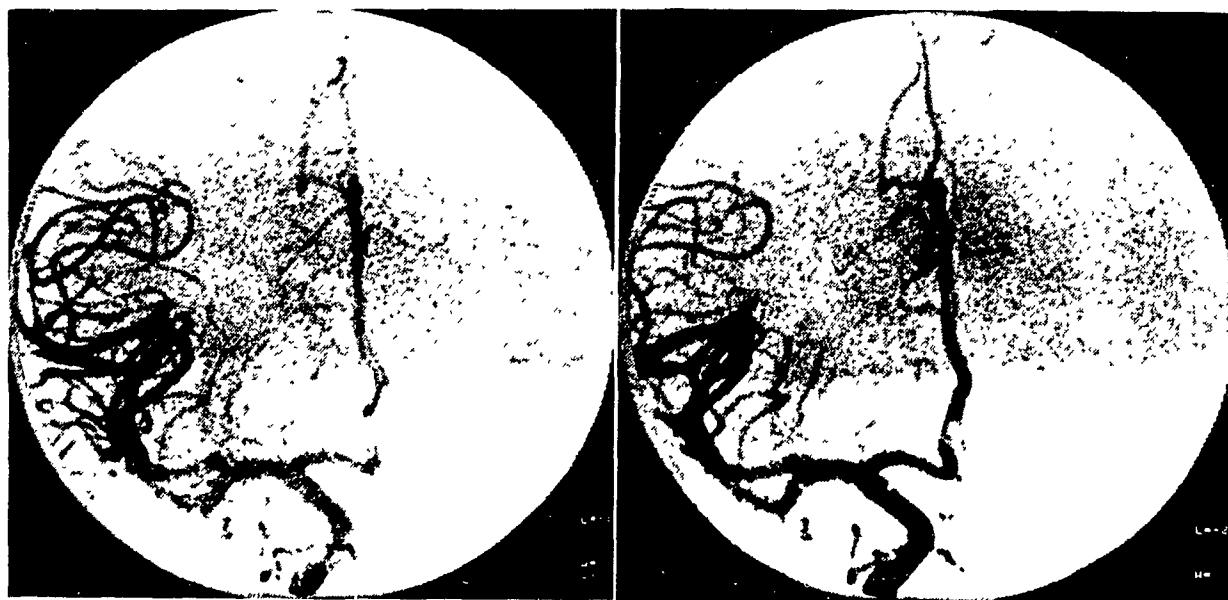
Figure 1.1 Orthogonal DSA images of the right internal carotid system of arteries with the 1) callosomarginal and 2) pericallosal branches indicated. The direction of the x-ray beam for the anterior-posterior projection is indicated by the large arrow in a).

Figure 1.2 Stereoscopic DSA images of the right internal carotid system of arteries taken from a) lateral and b) anterior-posterior directions. The angular separation between left and right stereo images is 7 degrees.

a) Lateral stereo pair



b) Anterior-posterior stereo pair



impression of the blood vessels is easily obtained from a stereo pair of angiograms by direct viewing or by means of a stereoscope, an optical instrument used to superimpose the stereo images. In this manner, stereoscopy is very useful in aiding the observer to differentiate superimposed vessels. Although depth information can be recovered easily, there are three important limitations to such procedures.

Firstly, stereoscopic depth perception is only relative, it ranks objects in their order of closeness, but does not disclose the distance between them. Secondly, the stereoscopic procedure is dependent on both the stereo recording and viewing geometries. Ideally the stereoscopic image pair should render an equal or isotropic perception of 3-d space (Jarre and Teschendorf 1933; Saunders 1968). This is possible by ensuring that the stereo shift is the same as the distance between the pupils of the viewer of the stereograms and that the distance from which the stereograms are viewed is the same as the focus to image detector distance (Kimura et al. 1983). Practically these geometrical requirements are not always possible to achieve. Departures from the ideal geometry results in distorted or unevenly perceived spatial relationships. Variability in pupil to pupil distances of different observers, vertical parallax due to differences in geometric magnification of the object, and restrictions on the possible x-ray tube or c-arm shifts can all affect the geometry required for isotropic stereoscopic viewing.

The final limitation of this procedure is that depth perception of the vasculature is restricted in one direction. Although biplane stereo pairs can be used, it is often difficult to fuse the resulting perceived depth images together into one mental image (Fig. 1.2). For these reasons visual inspection of stereo images alone is not always sufficient to meet the requirements of stereotactic neurosurgery planning.

#### 1.4.2 3-d measurements from stereo and biplane angiograms

Stereo and biplane analyses are based on the principle that the 3-d position of a point can be computed from measurements of that point's position in two or more 2-d images (Sutherland 1974). The reconstruction

procedure consists of two basic steps: calibration and matching. In the calibration step the positions of the x-ray source and image detector for each view in the reconstruction are computed to give the transformation function that describes the mapping of 3-d space onto the image. In the next step, points in one view are matched with the corresponding points in the other views. From the measured 2-d coordinates of the point in each view its 3-d position is computed. The process of matching corresponding points is often referred to as the 'correspondence problem' (Duda and Hart 1973).

In angiograms, points are selected along the vessel mid- or center-line, and if enough points are used vessels can be traced accurately in 3-d space. Given either stereo or biplane angiograms the correspondence problem is non-trivial because of vessel superposition. A number of different methods for reconstructing blood vessels from stereo or biplane angiograms have been reported.

#### 1.4.2.1 Reconstruction from stereo images

The most common approach to reconstructing the cerebral blood vessels has been to stereoscopically trace vessel center-line points in 3-d from a stereo pair of angiograms. Lateral angiograms are most often used because small vessels are best visualized in these projections (Fig. 1.2a). Small vessels are incompletely observed on other projections because of increased superposition.

Early examples of this approach require an observer to stereoscopically trace vessel center-lines (Vignaud and Korach 1973; Rabischong et al. 1975; Vignaud et al. 1979). This approach is often known as 'stereogrammetry' or 'stereoradiogrammetry.' With the aid of a stereoscope and operator controlled stereo cursor, known collectively as a stereocomparator, the center-line of vessels can be traced in 3-d from a stereo pair of film angiograms. The observer usually enters as few points as is necessary to trace a vessel accurately. The reconstructed vessels are approximated as a series of 3-d points connected by straight line segments. Accurate reconstruction of vessel depth position (i.e. 0.5-1.0mm) has been demonstrated with film angiograms recorded at x-ray source to film distances



of approximately two meters (Vignaud and Korach 1973). Long focal lengths in addition to an adequate stereo shift (see §1.4.1) and sub-millimeter accuracy in disparity measurements are necessary for such reconstruction accuracy (Suetens et al. 1983).

This procedure of recording the data, at about 150 points per hour, may be too time consuming to be used clinically if many vessels are to be reconstructed (Vignaud et al. 1979; Rabischong et al. 1975). In spite of this limitation, stereoradiogrammetry is still the method of choice (Garibotto et al. 1985; Legout et al. 1985). Only a skilled observer is able to detect and outline all the blood vessels unambiguously.

Recently efforts are being made to automate reconstruction from stereo images (Suetens et al. 1983; Hoffmann et al. 1987). Two essential steps in automating reconstruction are blood vessel delineation or segmentation on angiograms and establishing correspondence of vessels between stereo angiograms. Suetens' method uses a thinning technique to delineate blood vessels from a digitized film angiogram as a string of line segments characterized by an orientation, width, and intensity. Vessel line segments are then matched on how well line features in both images conform to each other. This is approached in an iterative way and is based on the 'consistency' property of disparity (Barnard and Thompson 1980). At vessel crossovers observer intervention is required. It is unlikely that one of these features alone will be invariant from one projection image to another because of the physics of the imaging process and superposition of vessels in projection. Suetens et al. (1983) recognize this important aspect of the correspondence problem and require conformity of several vessel features. Matching is successful when all or most of the line features are invariant in both images. The weak aspect of this method is its sensitivity to errors in vessel delineation (Suetens et al. 1983). Reconstruction errors arise when the blood vessels are delineated incorrectly and inconsistencies are introduced into the characterization of vessel-center line features.

Hoffmann et al. (1987) attempt to correlate vessel trace intensity profiles in order to establish vessel correspondence in digitized film angiograms. Their method uses a 'double-square-box' region of search

technique to track vessels in stereo angiograms and obtain vessel intensity profiles along a line perpendicular to the tracking direction. As a vessel is tracked in one image its intensity profile is correlated with candidate profiles along the stereoscopic image shift line in the other image. The center-point of the candidate profile that compares best is taken as the corresponding point. Vessel profile matching should work well when a high spatial correlation between the stereoscopic images exists. A geometric magnification of two is used to achieve reconstruction accuracy of approximately 1mm. This method shares the same potential limitations as Suetens', a sensitivity to both tracing errors and inconsistencies in the vessel features that arise from inadequate spatial correlation between stereo images. Even with recording conditions such as long focal lengths or large geometric magnifications, some projected vessels may be foreshortened or superimposed in only one image and spatial correlation for that vessel is lost.

Rather than determining a probe's trajectory through the reconstructed vascular structure, its path may be plotted in a stereoscopic pair of angiograms (Suetens et al. 1984; Ghosh and Boulianne 1984; Cloutier et al. 1985). Viewing a stereo pair of angiograms an observer with the aid of a stereo image of a straight line or 'floating-line' representing a probe can simulate implantation by localizing visually this line in the 3-d space of the angiogram (Ghosh and Boulianne 1984). Once a safe path has been found the image coordinates of the stereo probe end points are read and the 3-d spatial trajectory computed. Since this method relies on stereo depth perception, requirements for isotropic perception of 3-d space should be met (Saunders 1968). Visual path determination has the advantage that its practical implementation is relatively simple and economically feasible (Cloutier et al. 1985). A shortcoming of this method is that the observer cannot look around the object. Blood vessels and probes can only be viewed from one direction.

Most common c-arm digital subtraction angiography units are not capable of meeting the requirements of stereo reconstruction for high spatial correlated images and accurate measurement. Realization of stereo reconstruction needs special DSA units in order to meet these requirements.

Another approach to the reconstruction problem is to use biplane rather than stereo angiograms.

#### 1.4.2.2 Reconstruction from biplane images

Vessel reconstruction from biplane angiograms generally incorporate a 'ray-projection' technique to find vessel point correspondences. Ray-projection methods are based on the relationship that a point in one 2-d view or image can be back-projected as a line for any other view (Sayre et al. 1974). The display of a back-projected position from one view onto another view limits the search space for a corresponding point to a line. Rather than being required to recognize the position of the same point as seen in the conjugate view, the observer is required only to recognize the intersection of the back-projected line and the vessel being traced. As a result, analysis is no longer limited to stereo views, any arbitrary set of views can be used providing they have been calibrated.

This method has been used to reconstruct blood vessels from biplane film cerebral angiograms (Sayre et al. 1979; Potel et al. 1979) and coronary arteries from biplane cinefluoroscopic films (MacKay et al. 1982; Potel et al. 1983). In spite of the reduced requirements on the observer, this method is still time consuming and is better suited to studies which restrict attention to a few vessels or even to a few points. Although intersection of the back-projected line with the trace in the other view is necessary for correspondence, it is not sufficient. Problems occur when a back-projected line does not intersect a vessel, or intersects several vessels, or one vessel several times, and when some candidate points are obscured by vessel superposition. In practice the observer uses gross morphology such as arterial tree connectivity or additional views to resolve the correspondence problem (Rubin et al. 1978; 1980).

There have been several attempts at completely automating vessel reconstruction from biplane angiograms. Kim et al. (1982) used a contrast-edge tracking algorithm to resolve the problem of finding vessel correspondence in biplane digital subtraction angiograms. Starting with completely opacified vessels in biplane images, the center-lines are traced

along vessels to provide the necessary pixel position data. Next, in each image frame of both studies the moving edge of contrast density along the center-line is detected and evaluated using a matching method of cross-correlation for the two sequential frames' contrast-density. In synchronized biplane studies the contrast-edge points of two images are considered as the corresponding points at each frame. The advantage of this method is that if the arrival times of the contrast media are different for neighboring or superimposed vessels, ambiguous correspondences can be avoided. Also, finding a match in a foreshortened vessel can easily be located by the stationary contrast-edge points. To date the use of the 'time history' of vessel center-line pixels has been the only known technique to directly address the problems of vessel superposition and foreshortening.

For small sized vessels ( $<2.0\text{mm}$ ) the accuracy of this method is low, and back-projection lines are used to determine corresponding points on vessels. Errors in the 3-d reconstruction are related to the cross-correlation matching method of tracking contrast-edge densities and are sensitive to noise effects existing in the DSA system. Reconstruction errors would also occur if the vessel center-line is incorrectly traced.

Fujii et al. (1983) describe a method of matching graph representations of the vessel center-line in biplane cerebral angiograms. This method is used to find corresponding vessel branches in biplane images from where the method proceeds to match individual branch points. The method consists of two steps. In the first step the center-line points of the vessels from biplane digital angiograms are extracted separately and their structure represented as graphs by computer. A graph is formed by characterizing as nodes, pixels such as end points, crosses, and bifurcations. All other pixels are characterized as constituents of arcs. The list of nodes and arcs include various attributes describing both the structure of the graph and the features of the vascular image. In the second step, using the back-projection lines of node points and taking into account node attributes and the knowledge that node ordering is preserved from one view to another, corresponding node point locations are matched. This is followed by matching the center-line points of corresponding vessel branches using the back-projection lines of each point.

By matching vessel branches first, ambiguities that arise when the back-projected line crosses several branches can be resolved. The potential problem of multiple crossings along the same branch still remains. Blume (1984) suggests 'a priori' information about the vessels be used to determine correspondences in these cases. 'A priori' knowledge can take the form of previously determined correspondences (Barba et al. 1987) or vessel connectivity (Parker et al. 1985;1987). Another difficulty occurs when vessels are superimposed and cannot be completely detected by the computer. In the event of missing vessel center-line points the procedure requires the observer to complete the matching. Other examples of graph matching used in biplane reconstruction methods can be found in Smith and Starmer (1976), Gerbrands et al. (1982), and Blume (1984).

Parker et al. (1985;1987) address the problem of reconstructing coronary vessels from biplane digital subtraction angiograms. In their method, forks in the arteries or bifurcation points are manually identified and matched with the assistance of back-projection lines in each view. Thereafter the blood vessels between the bifurcations or nodes in the angiograms are isolated and given a center-line description by computer. Center-line points of the vessel between matched nodes are then automatically matched to reconstruct the vessel in 3-d space. Their method of finding correspondences between nodes is different from Fujii's, it is based on how 'close' 3-d lines from a possible match of point pairs intersect. For each vessel center-line point in one image a set of measures of possible candidate points in the other image is constructed. Corresponding points are selected which minimize the intersection distance at all points along the vessel branch under a constraint of vessel connectivity. Given a pair of corresponding branches where the order of vessel points along both branches is known, it is reasonable to assume that the order of individual points in corresponding pairs should also be preserved. When one of the vessels of a matched pair of branches is foreshortened, the longer branch (containing more points) is matched onto the shorter branch.

The use of a 'distance minimizing point matching' technique also takes into account that the back-projection line only provides an approximation of

corresponding locations due to the probable propagation of measurement errors in the reconstruction calculations. Parker's results indicate the usefulness of the intersection distance as a measure of correspondence.

When accurate reconstruction is required, biplane analysis is desirable. The chief factor in determining the applicability of biplane reconstruction methods is the degree of difficulty in determining both branch and point correspondences. This largely depends on the geometry of the vascular tree being imaged. In the case of coronary vessels, biplane analysis is possible because there are few vessels and their paths follow a relatively straight course. The usefulness of the described biplane reconstruction methods is limited for cerebral angiograms. The cerebral blood vessels are more numerous, and finding correspondences in biplane images is difficult because of the large degree of vessel projection superposition. Referring to the angiograms in Fig. 1.1, vessels indicated in the lateral projection angiogram are shown as superimposed and foreshortened in the anterior-posterior projection. The lack of sufficient bifurcation points makes it difficult to represent vessels in angiograms as graphs. Matching longer vessel branches to shorter branches in cerebral angiograms is not always possible because of the varying degrees of foreshortening in corresponding vessel branches. The projection of long lengths and folding paths of the cerebral branches is unlikely to produce images where all or most of the vessel foreshortening is restricted to one of the branch pairs.

#### 1.4.3 Few view tomography

The last approach considered in the construction of a 3-d angiogram is to reconstruct a stack of 2-d parallel plane sections through the cerebral vasculature tomographically from a set of its angiograms. The reconstructed sections are then reassembled into a 3-d stack. Image reconstruction from a set of projections would be suitable given the availability of DSA. However in DSA it is undesirable under constraints of patient exposure, data collection time, and computational expense to collect a set of projection measurements that is complete in the sense of CT. Reconstruction from incomplete projection sets almost always leads to unacceptable artifacts in the image (Heffernan and Bates 1982). The reconstruction image will show

streaks radiating away from dense objects. Even for a small number of objects in a section, the overlap of streaks results in spurious detail that may be hard to recognize and discount. Current methods deal with the absence of measured projections by either estimating the missing projections or by minimizing the artifacts in the reconstructed image.

A number of interpolation methods for reconstructing images in which small numbers of widely spaced projections of order of 10 have been studied (Heffernan and Bates 1982; Suetens et al. 1982). Heffernan and Bates (1982) described methods which estimated missing projections using Fourier series and Gerchberg-type interpolation (Gerchberg 1974). After comparing the result of reconstruction on a numerical phantom they found that interpolation schemes were improved by incorporation of prior knowledge about the object. They concluded that the general structure of how 'a priori' knowledge is incorporated, rather than the detailed form of the recursive scheme used, determines its usefulness as an interpolation method. Suetens et al. (1982) using an interpolation scheme based on Lent and Tuy's (1981) algorithm, with prior constraints on the density values of the pixels in the image, confirmed that incorporation of 'a priori' information into interpolation schemes gives considerable improvement of the reconstructed images. The strategy of interpolating the missing projections on the basis of 'a priori' knowledge has not been entirely successful with actual measured projection data. Such methods are quite sensitive to noise in the data (Garden and Bates 1984).

Another approach taken to this problem of few projections is to minimize the artifacts in the reconstructed image using 'a priori' information about the object. By minimizing artifacts the most probable image of the object is reconstructed from the available projections. Heffernan and Bates (1982) showed that the incorporation of such constraints as image positivity and size into the reconstruction process rendered images which are superior to those which did not utilize such information. Garden and Bates (1984) demonstrated how object size or extent can be estimated and incorporated in reconstruction using an interactive method. Their method is based on the observation that in most images reconstructed from an incomplete set of projections, the boundaries of piece-wise constant regions are reconstructed

well enough to be recognizable by a human observer. After the observer traces the outline of object boundaries in the reconstructed image, the object is reconstructed again with this information. They found that this method gave quite faithful reconstructions. The application of 'a priori' object knowledge in image reconstruction from a set of incomplete projections has also appeared in the context of radio astronomy (Högbom 1974) and 'non-destructive testing' (Heffernan and Robb 1985).

Rougee et al. (1988) describe the use of ART (algebraic reconstruction techniques) to reconstruct blood vessels from 15 projections. From the given projections, object regions thought to contain vessels are defined and used to eliminate reconstruction from where no object is present. The detection of object regions is based on the extreme value reconstruction method which was initially developed for tomosynthesis. This is discussed later in this section. The use of ART with region of support detected reduces the level of streak artifact in reconstructed images. The final level of streak artifact in these images depends on how well the object regions are detected. Both the complexity of the vasculature and the number of available projections will determine the 'faithfulness' of estimated object regions.

Spears et al. (1988) reconstructed coronary vessels from 6 to 18 angiographic views by incorporating a global image constraint into the reconstruction scheme. Specifically, entropy was maximized in an attempt to reduce artifacts caused by the limited number of views. This led to a smoothed reconstruction image where streak artifacts were reduced. Results of reconstruction depended on the number of available projections and the complexity of the anatomic vascular structure.

Instead of trying to reconstruct the images tomographically in the sense of CT, tomosynthetic reconstruction has been proposed for DSA (Kruger et al. 1983; 1984; Maravilla et al. 1984). Tomosynthesis or back-projection techniques use a limited number of x-ray projection images over a limited range of angles. Based on the principles of classical circular tomography (Ziedses des Plantes 1932), tomosynthesis involves the analysis of a series of discrete x-ray images produced by multiple exposure of an x-ray source occupying known positions in a circular path in a plane located above the



object to be reconstructed. Below the object the image detector moves synchronously with the x-ray source in an opposite direction about a fulcrum residing in the plane of interest (Grant 1972). Alternatively, a 2-d planar array of sources of a known geometric relationship to each other (Nadjmi et al. 1980; Haaker et al. 1985) or a rotating focal spot x-ray tube (Smith and Kruger 1987; Kruger and Smith 1988) can be used instead of moving the x-ray source through a circular path. Since the focal plane is parallel to the recorded projection images, the back-projection step is accomplished by simple addition of images. Tomosynthetic reconstructions result in a sharp image of structures lying in the tomosynthetic plane on which blurred images of the object detail lying outside the plane of interest are superimposed.

The major advantage of tomosynthesis is that any tomographic plane parallel to the original plane of focus can be produced by summation of the same set of projections provided each image is shifted an appropriate amount in an appropriate direction within the the image plane. Tomosynthesis is also more suitable in cases of limited angular sampling in which conventional techniques cannot be directly applied. Implementation of tomosynthesis to DSA systems that scan rotationally is not as straightforward. Such systems have no naturally focused plane and the back-projection step is more complicated than simple translations and summations (Kampp 1986; Liu et al. 1987; Ning et al. 1988).

Tomosynthetic reconstruction methods suffer mainly from the disadvantage that isolation of a tomosynthetic slice is incomplete because structures in outlying planes are only blurred rather than removed. This makes constructing a 3-d image of the vessels difficult because blurred arteries need to be removed. Haaker et al. (1985) showed that the degree of blurring can be reduced by non-linear reconstruction. Referred to as 'extreme value reconstruction,' this method selects the minimum of the back-projection values assigned to a reconstruction pixel rather than the sum of these values. Hence, the value of each pixel location and consequently blurring is reduced by the lack of support existing for that location in the given projection set. Extreme value reconstruction requires that each pixel has a free projection in at least one view. This condition is more likely to be met as the number of views available is increased. Improvements to the

extreme value reconstruction algorithm are described by Kruger et al. (1987) (see also Ning et al. 1988). Although such techniques may remove blur in one region, not every region of the image will be affected in the same way. Object visualization may be degraded with excessive noise in a region originally free from overlapping blur (Kruger et al. 1987).

Other methods of removing blurring involve deconvolution techniques (Ruttimann et al. 1984; Kawata and Sklansky 1985; Ghosh-Roy et al. 1985). Restoration does not result in a faithful reconstruction, rather a spatially filtered (high-pass) version of the tomosynthetic slice results. Success in removing blurring is limited because in absence of additional information no amount of image manipulation can restore the missing projections (Hanson 1982a). Furthermore the solution will not be unique as the information provided is incomplete.

Preferred methods to the image reconstruction problem of few projections are of an 'ad hoc' nature; they all incorporate to some extent 'a priori' knowledge about the object. The accuracy of the reconstructed image appears to depend on the discriminating nature or the uniqueness of the 'a priori' information available.

## 1.5 Conclusion

With the aim of developing new methods to reconstruct the 3-d geometry of the cerebral vasculature for purposes of neurosurgery planning, existing imaging modalities and reconstruction methods were reviewed. Of the available imaging modalities DSA seems best suited for the reconstruction task. Since it must be accepted that only a small number of angiographic projections are practically available, two approaches are applicable.

The first approach is characterized by methods that attempt to recognize object information or features in the projections needed for matching the same object in multiple images. If all object points are uniquely determined in all views, the reconstruction problem is solved. Stereo reconstruction from DSA images recorded using common c-arm units is not expected to be sufficiently accurate for surgical planning. For reasons of limited digital

spatial resolution, vessel superposition and foreshortening in projection, and system noise, resulting tracing and correspondence errors would limit accuracy. Reconstruction accuracy can be improved by more exact methods of vessel tracing, or by reducing its sensitivity to errors by changing image recording parameters, or instead using an orthogonal pair of images. Increasing the focal length or geometric magnification is not always possible or practical with most c-arm DSA units, and in these circumstances biplane analyses would be preferred. The problem faced with using biplane cerebral angiograms is that vessel superposition and foreshortening make finding corresponding vessel branches in anterior-posterior angiograms difficult.

In light of these limitations, a new geometric reconstruction method which uses both stereo and biplane images is presented in chapter 3. This method has two distinguishing features. The first is the use of lateral stereo reconstruction results to match corresponding vessel branches between image pairs which are not spatially correlated as in the extreme case of biplane images. The other feature is the vessel correspondence algorithm which uses existing techniques modified and applied in a novel manner. This algorithm assigns an initial point-pair matching between vessel branches on the basis of 'intersection distance' (Parker et al. 1985;1987). Unlike Parker's method, matching errors are reduced iteratively by a relaxation labeling process (Barnard and Thompson 1980; Suetens et al. 1983) which is better suited to this task because of the ease with which 'a priori' object information can be incorporated. In addition to 'continuity of disparity' (Barnard and Thompson 1980), the relaxation labeling process incorporates a vessel connectivity constraint; the order of individual vessel points in corresponding pairs should be preserved. Chapter 4 assesses the accuracy level achievable in the planning of neurosurgical procedures based on angiograms using the method described in chapter 3.

Tomographic image reconstruction from a few given angiographic views is the other possible approach considered. Problems arise due to the limited number of projections available for reconstruction which lead to unacceptable image artifacts. However, previous work indicates that this lack of information may be made up in part by adequate 'a priori' knowledge

about the image. Such knowledge may be used to improve constraints on the solution of the reconstruction procedure in an attempt to maximally retrieve the reconstructed object consistent with its projections.

A new method of reconstructing images of the cerebral blood vessels from a few projections is proposed. The method reduces reconstruction artifacts by a process of iterative deconvolution guided by 'a priori' knowledge about the vessels. This method is based on the 'Clean' technique introduced by Högbom (1974) to restore radio-source maps reconstructed from an incomplete set of observations or measurements. Chapter 5 describes the modification of Clean and its novel application to the problem of vascular image reconstruction from a few projections.

The next chapter is concerned with image acquisition and display in DSA. Common techniques and problems are discussed together with typical properties of the image which help to define the problem of 3-d analysis of angiograms.

## CHAPTER TWO

### PHYSICAL ASPECTS OF DIGITAL SUBTRACTION ANGIOGRAPHY

#### 2.1 Introduction

A common goal of all digital subtraction angiography (DSA) systems is to isolate object contrast which results from the passage of an iodine dye through some blood vessels of interest (Kruger and Riederer 1984). Object contrast is isolated by the subtraction of angiograms taken before and after patient injection or administration of iodine dye. This technique is known as 'mask-mode' subtraction. Once the subtracted image is in digitized form, image processing techniques (e.g. filtering, averaging, windowing, etc.) can be employed to further enhance image contrast (Kruger and Riederer 1984).

The ease of subtraction and digital processing afforded by DSA has made angiographic examinations safer, allowing examinations on patients where conventional film angiography would not have been considered previously. Other advantages of DSA over film angiography include decreased dye requirement, reduced need for selective catheterization, diminished film costs, lessened examination time, and increased contrast recognition (Crummy et al. 1982).

This chapter examines how attenuation thickness of iodine in opacified vessels is measured in a typical DSA system. §2.2 describes the imaging principle of mask-mode subtraction in DSA. An overview of the DSA measurement system and the causes of measurement error are described in §2.3 and §2.4 respectively. §2.5 concludes the chapter with a discussion of the relative importance of measurement errors on quantitative analysis of DSA images.

#### 2.2 Imaging principle

In digital subtraction angiography the quantity imaged is the attenuation coefficient distribution of the administered contrast agent. For

photon energies in the diagnostic range, 40 to 100 keV, attenuation occurs primarily by photo-electric and Compton scatter interactions. The basics of the attenuation process can be found described in Johns and Cunningham (1984).

Fig. 2.1 illustrates the principle of mask-mode subtraction. Referring to Fig. 2.1, let  $\mu_t$  be the linear attenuation coefficient of the tissue and  $\mu_i$  be the linear attenuation coefficient of the administered iodine dye in the anatomical region under study. For an incident photon fluence at energy  $E_0$ , the background transmitted fluence or 'mask' signal at the detector is

$$\Phi_1 = \Phi_0(E_0) \exp [ -\mu_t(E_0)d_t ] \quad (2.1)$$

where  $d_t$  is the tissue thickness. After the administration of iodine dye, a certain amount of blood is replaced by iodine and the new or 'live' signal becomes

$$\Phi_2 = \Phi_0(E_0) \exp [ -\mu_t(E_0)(d_t-d_i) - \mu_i(E_0)d_i ] \quad (2.2)$$

where  $d_i$  is the iodine thickness. It is reasonable to assume that  $d_i \ll d_t$  such that  $(d_t-d_i) \sim d_t$ , hence,

$$\Phi_2 = \Phi_0(E_0) \exp [ -\mu_t(E_0)d_t - \mu_i(E_0)d_i ] \quad (2.3)$$

Linearizing (2.1) and (2.3) by taking logarithms of both sides and then subtracting them gives rise to the line integral of the attenuation coefficient of the iodine dye,

$$C = \log (\Phi_2/\Phi_1) = -\mu_i(E_0)d_i \quad (2.4)$$

The logarithmic subtraction estimates the desired attenuation thickness of iodine. This quantity,  $C$ , represents the radiographic or object contrast of iodine.

### 2.3 Measurement system

The measurement system used in DSA generally consists of three physical components: an x-ray source, an x-ray detector, and digital processor. These components are depicted in Fig. 2.2 for a typical measurement system and are described in the following subsections.

Figure 2.1 Formation of the subtraction signal. (Adapted from Shaw et al. 1981)

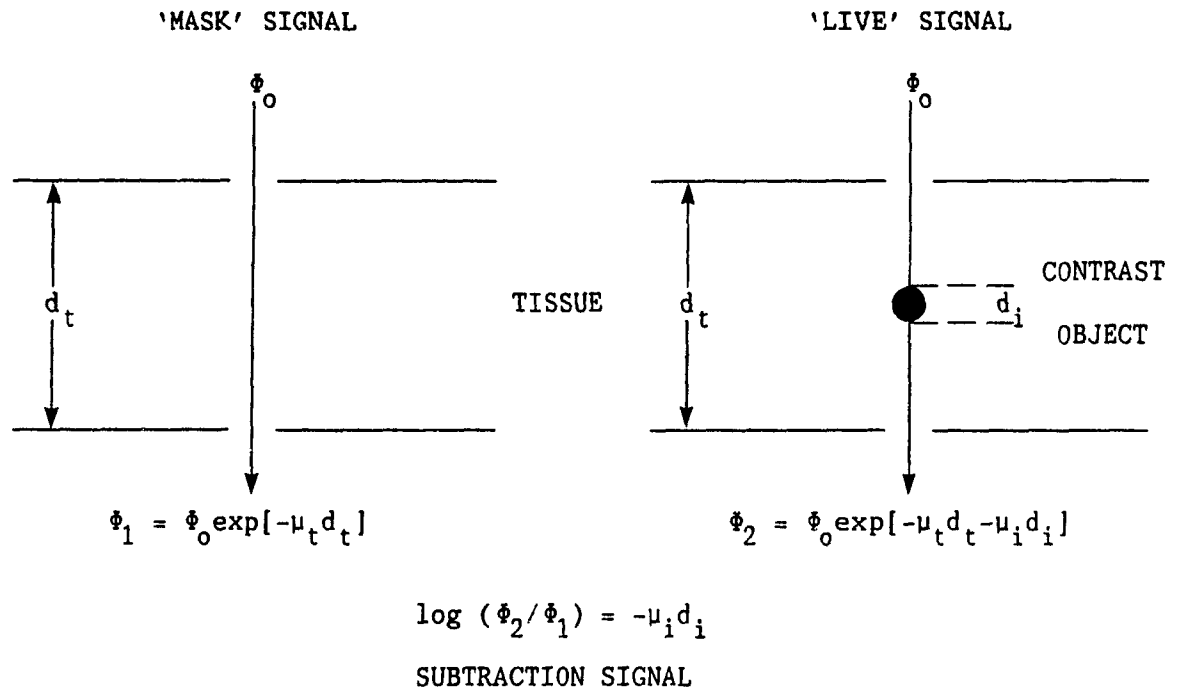
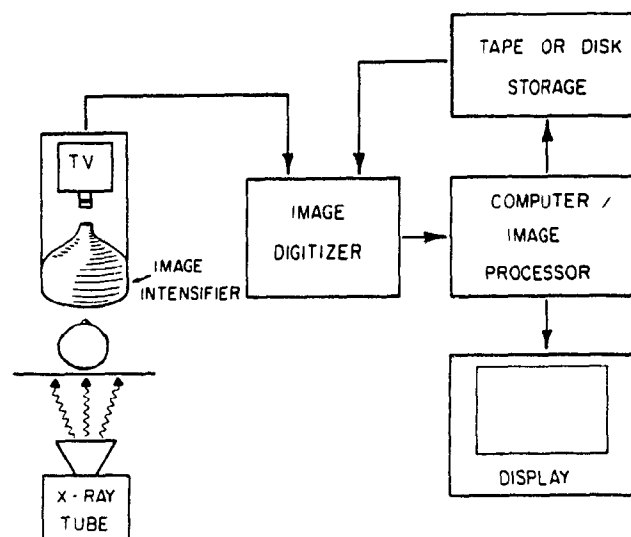


Figure 2.2 Basic block diagram of a DSA imaging system. (Adapted from Kruger and Riederer 1984)



### 2.3.1 X-ray source

X rays are generated when electrons emitted from a heated filament are accelerated by the voltage (kV) applied across the tube to the focal spot of the anode or target. The target consisting of a heavy metal, usually tungsten, acts to slow down the electrons to produce a continuous distribution of radiation (Johns and Cunningham 1984). This continuous distribution of radiation is often called 'Bremsstrahlung' radiation.

There are two physical problems associated with real x-ray sources: polyenergetic x rays and the shape of the x-ray beam. Because subtraction techniques are based on a model for monoenergetic x rays, a polyenergetic x ray beam gives rise to error in the determination of iodine thickness. This error is due to the phenomenon known as 'beam hardening' and depends on both the beam energy spectrum and the object (§2.4.1). The physical problems related to the shape of the x-ray beam are characterized by the finite size of the x-ray tube focal spot and the divergent shape of the generated beam. These two factors have a major influence on spatial resolution (§2.4.2).

### 2.3.2 X-ray detector

Most systems employ an image intensifier (II) as the x-ray detector (Fig. 2.2). In addition to the primary x rays, scattered x rays are also detected. Often image intensifiers include a grid in order to preferentially attenuate scattered x rays. Such grids consist of thin lead strips aligned parallel to the primary radiation direction. However, the use of scatter reduction grids can attenuate as much as 50-60% of the primary radiation (Kruger and Riederer 1984), and as a result wider air gaps between patient and detector are used where possible. The effect of detected scattered x rays is to reduce object contrast and contribute effectively random noise in the measured intensity. The deterministic component of scatter is considered in §2.4.4.

At the image intensifier x-rays strike a CsI (cesium iodide) phosphor layer which converts their energy into light. The emitted light is then



converted into electrons from an underlying photocathode, and under the influence of a potential drop of 20 to 30 kV these electrons are accelerated and focused onto a minified output phosphor. This process results in a brightness gain of 5,000 to 10,000 times at the output phosphor (Kruger and Riederer 1984). The resulting pattern of light intensity at the output of the image intensifier is read-out by a television video camera via a set of lenses or fibre-optic coupling.

The output image of some image intensifiers is geometrically distorted by the curvature of the input screen and the electron optics. The output image has a 'pin-cushion' appearance and results in the non-uniform representation of area by picture elements (§2.4.6). Images also suffer from veiling glare, the scatter of electrons and light photons within the image intensifier and light photons within the optical coupling. The result of veiling glare leads to a decreased measurement of iodine contrast thickness.

The resolution limit of current CsI image intensifiers range from 4 to 5 line pairs per mm ( $\text{lp mm}^{-1}$ ) (Kruger and Riederer 1984). This generally exceeds the spatial resolution limits of present DSA systems (§2.4.5). Therefore the image intensifier is usually not a limiting factor on spatial resolution.

The ideal detector has an output signal whose statistical properties and behavior are exactly those of the transmitted photons. In actual practice statistical noise from the image-intensifier-camera chain makes preservation of the input signal difficult. The effect of noise on the measurement of information from the transmitted signal is considered in §2.4.3.

### 2.3.3 Processor

The major functions of the digital processor are analog-to-digital conversion (ADC) of the video signal, storing digital images for latter recall, and manipulating digital images (e.g. subtraction, averaging, windowing, etc.).

The video signals are spatially sampled and stored in one of two image

memories in the processor as a two-dimensional matrix of grey scale values. Each element of the image matrix is referred to as a 'pixel.' Typically the video signal is spatially sampled to form a 512x512 or 1024x1024 image matrix, and the intensity of each pixel is sampled to either 8 or 10 bits.

The mask image is usually acquired first and stored in one memory. During contrast administration, a sequence of live images is acquired and stored in the other memory. These live images are then recalled and subtracted from the stored mask to give a series of difference images. Once subtracted, the image is then windowed and changed back to an analog signal by the digital-to-analog converter (DAC) to be displayed on a TV monitor. Windowing refers to the linear stretching of the mapping between grey levels in an image,

$$b_{out} = \begin{cases} 0 & , b_{in} \leq b_1 \\ B(b_{in}-b_1)/(b_2-b_1) & , b_1 < b_{in} \leq b_2 \\ B & , b_{in} \geq b_2 \end{cases} \quad (2.5)$$

where  $b_{out}$  is the grey level after windowing,  $b_{in}$  is the initial grey level, and  $(b_1, b_2)$  is the band of levels expanded to cover the entire brightness range  $(0-B)$ . Depending on the application, various image processing techniques can be performed in addition to mask-mode subtraction or windowing (Mistretta 1974).

Generally logarithmic processing of the video signal is used to insure density uniformity of the vessels in the subtracted image (§2.2). The video signal may be processed using a logarithmic amplifier on the incoming analog signal or by using a look-up table on the digitized signal.

## 2.4 System non-linearities

From the previous description of the physical components of a DSA system it is evident that errors in the measurement of position and amplitude of the subtraction signal are possible in practice. The basic limits to the linearity between the subtraction signal and the contrast thickness at image formation are: the physical properties of the incident x-ray beam (§2.4.1 and §2.4.2), noise (§2.4.3), x-ray scatter (§2.4.4), the effects of spatial

sampling (§2.4.5), pin-cushion distortion (§2.4.6), and patient motion (§2.4.7). This section briefly discusses these sources of measurement error and where possible suggests how they can be overcome.

#### 2.4.1 Beam energy

A consequence of polyenergetic x-ray beams is that lower energy x rays are attenuated more strongly by matter than those of higher energy. As the beam propagates through the object its energy distribution or spectrum 'hardens' as the low energy or 'softer' x rays are preferentially removed from the beam. This phenomenon is called 'beam hardening' (Nalcioğlu and Lou 1979) and results in a reduction of measured object contrast (Shaw et al. 1981).

Although for simple objects these non-linearities can be predicted and identified, they are object dependent. Beam hardening is important in circumstances when measurements from regions of widely varying tissue and bone thicknesses in an angiogram or measurements from different views are to be compared.

The most common approach to correct for beam hardening in DSA is to fix plates of attenuating materials between the x-ray source and object. In this way the beam hardening property can be employed advantageously to constrain or filter the x-ray spectrum. Copper and aluminum filters can be used to narrow the spectrum and shift it towards the higher energies over which the variations in attenuation coefficients are negligible (Bursch et al. 1971; Heintzen et al. 1971). This is achieved at the expense of object contrast. Another approach is to apply a non-linear correction factor determined experimentally for an homogeneous object (Nalcioğlu et al. 1983). This technique is only adequate when the anatomical location under study can be simulated using a calibration object.

#### 2.4.2 Beam shape

The angular divergence of the x-ray beam and finite focal spot size may under certain circumstances render a spatially distorted subtraction image.

The effects of angular divergence and finite focal spot are described.

X rays form a beam which diverges from a point source. The effect associated with divergent or cone beam projections is geometric or object depth-dependent magnification. An object's apparent size will depend on its depth position within the diverging beam (Fig. 2.3). The projection of an object point at  $(x_o, y_o, z_o)$ , with respect to the focal spot, onto the image or detector plane at  $(x, y)$  is given by

$$(x, y) = (x_o, y_o) M(f_1) \quad (2.6)$$

where  $M(f_1)$  is the geometric magnification of the size of the object seen by the detector. The geometric magnification is

$$M(f_1) = f/f_1 \quad (2.7)$$

where  $f$  is the focus to detector distance and  $f_1$  is the horizontal distance between the object and focus (i.e.  $f_1 = z_o$ ). If the object is tilted (Fig. 2.4), it will not be uniformly magnified. As a consequence, incorrect interpretations about an object's size may be made from its projection image unless its orientation and shape are known 'a priori.' The limiting spatial resolution of the primary x-ray image at the detector also depends on geometric magnification.

The effective resolution of the imaging system increases by the same magnification factor at the expense of a decreased field of view and increased patient exposure. After a certain point, increasing the magnification will decrease the effective spatial resolution due to increased geometric unsharpness resulting from the finite focal spot. The effect of a finite source is now considered.

In practice the source distribution is a three-dimensional surface, square in shape and planar. Fig. 2.5 represents a cross section of the focal spot and the effect of focal spot size on a point object being imaged. The size of the focal spot causes a broadening of the signal due to spatial averaging or convolution over the area of the magnified focal spot size at the detector. The consequence of finite source size is to 'blur' the available information or limit the resolution. The width of blurring  $s_x$  due

Figure 2.3 Magnification of an object by oblique rays. (Adapted from Macovski 1983)

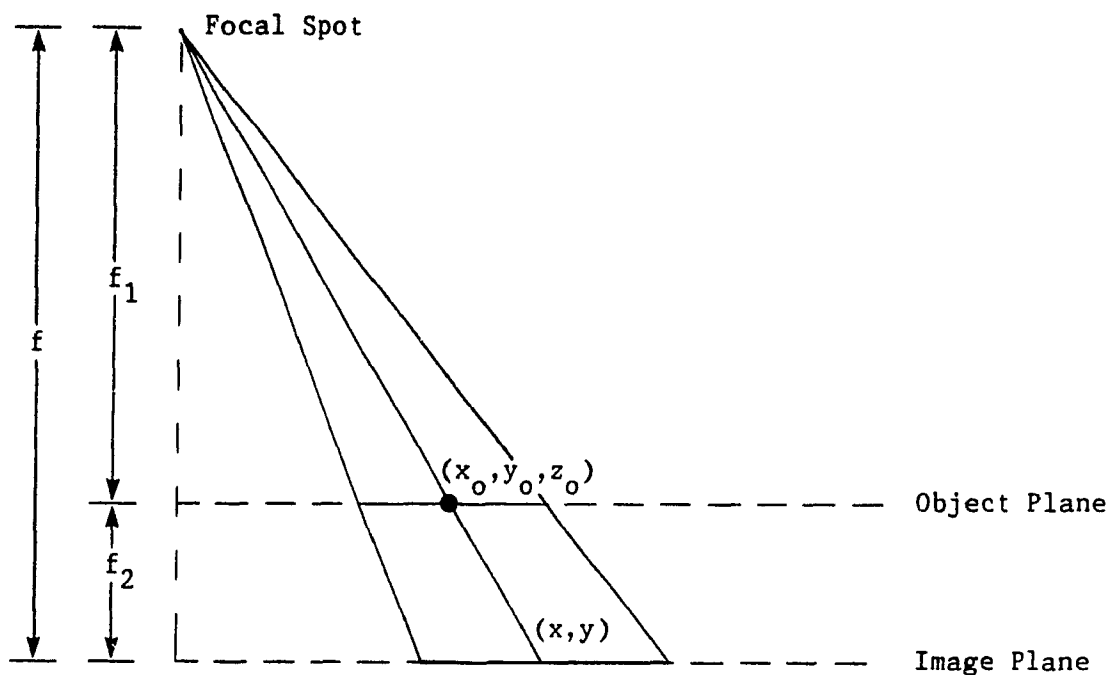
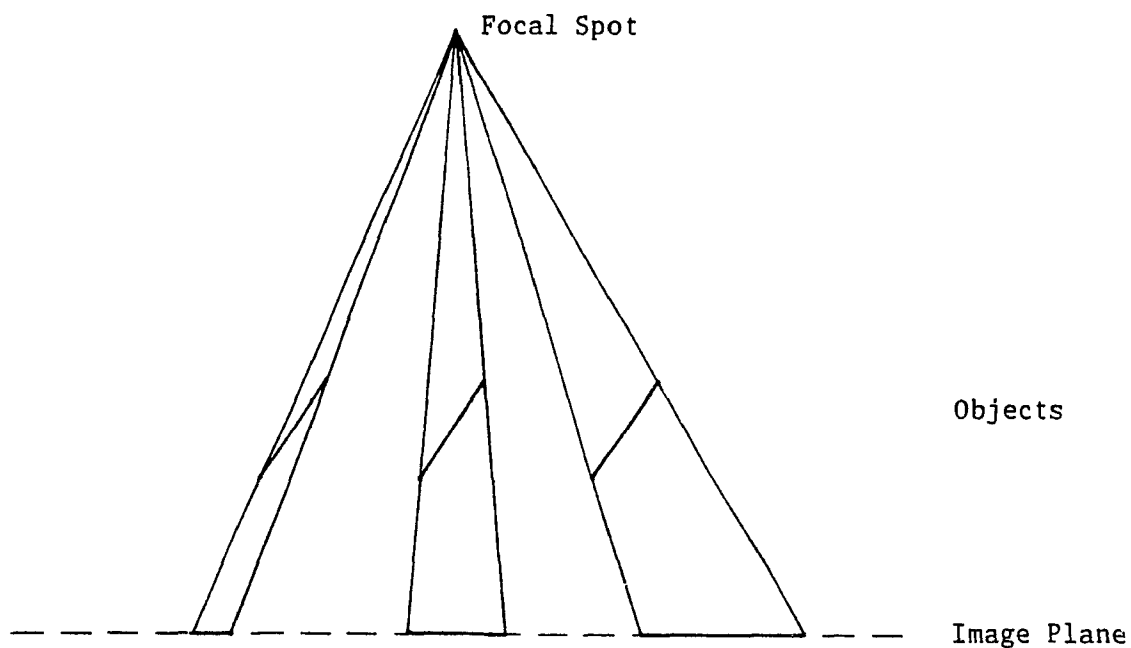


Figure 2.4 Distortion of the shape and size of the image of a tilted object depends on the position of the object in the x-ray beam. (Adapted from Macovski 1983)



to a square focal spot of length  $s$  as a function of magnification  $M$  is given by (McNeil 1966)

$$s_x = s(M-1) [ 1 + (x_o \cot(\theta) / f_1 - s \cot(\theta)) ] \quad (2.8)$$

where  $\theta$  is the target angle and  $x_o$  is the distance from center line to object of interest. For small geometric magnifications ( $\leq 1.5$ ) the second term in (2.8) is sufficiently small that  $s_x$  is effectively spatially invariant. The contribution of the focal spot to resolution  $r_f$  in the object plane for objects on the center line is (Kruger et al. 1981)

$$r_f = M/s(M-1) \quad (2.9)$$

Fig. 2.6 shows the resolution limit set by the finite focal spot size and geometric magnification (2.9). A magnification of at least 1.25 is almost always present due to the geometry of the equipment, though larger geometric magnifications may be used in practice. The choice of a focal spot size in pulsed mode DSA involves a trade-off between the increased geometric unsharpness resulting from a larger focal spot and the decreased patient motion blurring resulting from the higher allowed tube currents and correspondingly shorter exposure time.

From the curves in Fig. 2.6, the effect of focal spot blur becomes important at large magnifications. For large objects, contrast is unaffected by blurring since it merely rounds the edges of the object and does not change its central value. However, for smaller structures the contrast will definitely be affected.

Geometric unsharpness resulting from the finite size of the focal spot can be corrected by deconvolving the focal spot response in cases where magnification cannot be further reduced. The focal response can be extricated from the signal in a manner analogous to correcting for the effects of the collimator response characteristics in CT (Bracewell 1977). The problem with carrying out such a correction is that it is assumed that the focal spot blurring function is spatially invariant which is not always true (2.8).

Figure 2.5 Geometry of vertical plane perpendicular focal spot. (Adapted from McNeil 1966)

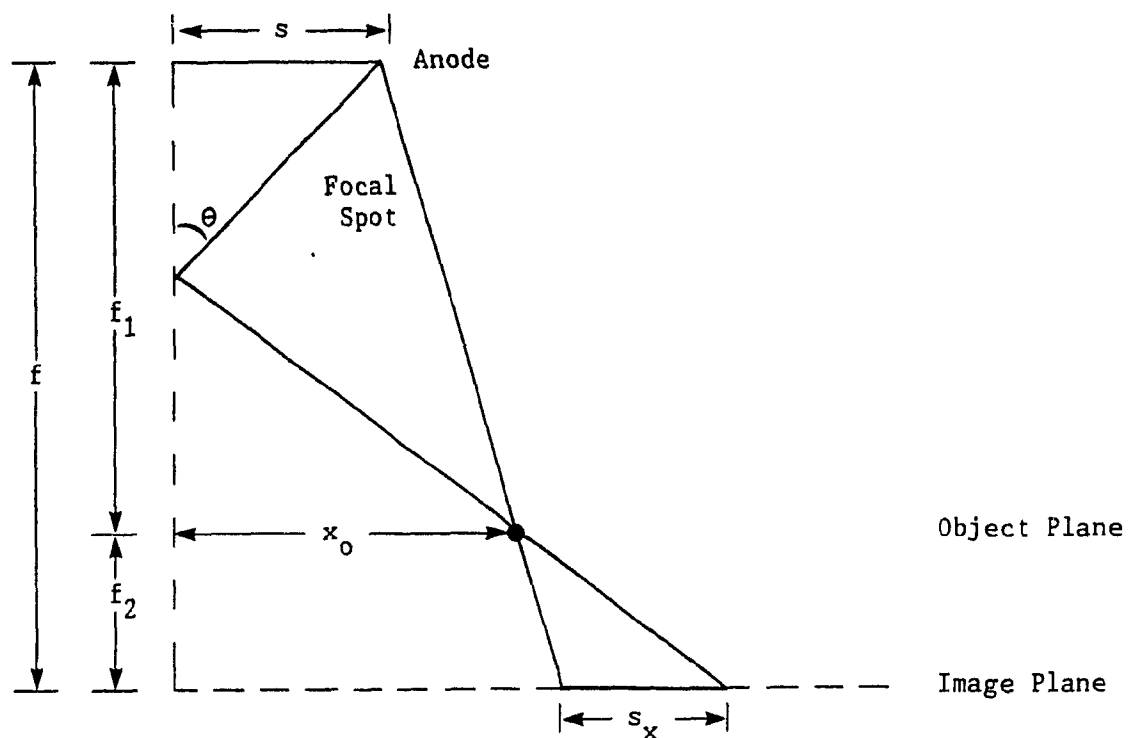
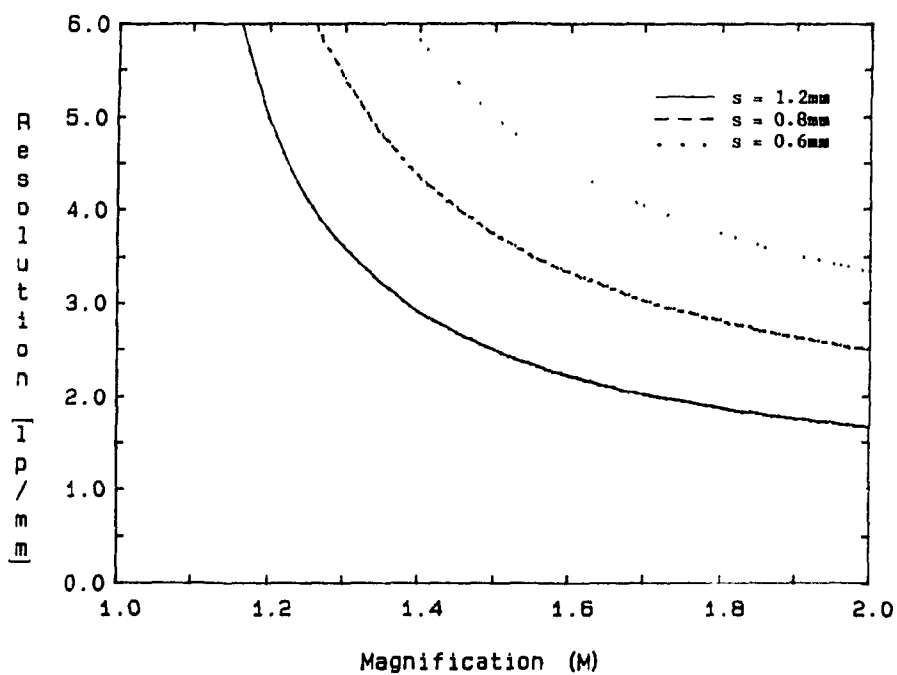


Figure 2.6 Resolution limit of a focal spot of width  $s$  (mm) plotted as a function of magnification ( $M$ ).



### 2.4.3 Noise

A fundamental limit on the detection and measurement of information in the subtraction signal is noise. The presence of noise in the subtraction signal is readily noticeable by fluctuations in image pixel values from one area to another about a regional average. In DSA, noise is an accumulated effect of factors such as Poisson counting statistics, scatter, and additive noise (Macovski 1983). Additive electrical noise is introduced primarily by statistical variations of II-TV camera parameters and ADC converter step non-uniformities (Roehrig et al. 1981).

Each noise component is independent and can be assumed to be comparable in pre- and post-contrast measurements. Hence, the total variance in the subtraction signal, the logarithm of the ratio of two signals (2.4), is given by (Macovski 1983)

$$\sigma^2 = (2/N_t \eta) + (2/N_s \eta) + 2\sigma_a^2 \quad (2.10)$$

where  $\eta$  is the fraction of x-ray photons captured,  $\sigma_a$  represents the standard deviation of the additive noise, and  $N_t$  and  $N_s$  are respectively the mean numbers of transmitted and scattered photons per picture element. Of the two types of noise sources described in (2.10), one of them will dominate a DSA image and limit information extractable as well as image quality. At low detected x-ray exposure, photon noise will dominate. As exposure increases either the system or the digitization noise component will gradually dominate the photon statistics. In this case noise reduction techniques such as frame integration are needed. Frame integration reduces  $\sigma$  by  $(k)^{1/2}$  where  $k$  is the number of frames averaged together.

### 2.4.4 X-ray scatter and veiling glare

Images acquired from x-ray image intensifiers are degraded by the acceptance of scattered radiation and by veiling glare. The result of both scatter and glare is to produce spatially non-uniform video black level errors that lead to a reduction in the measured object contrast (Shaw et al. 1982; Nalcioğlu et al. 1983). Of the two effects, x-ray scatter dominates (Riederer et al. 1981; Shaw et al. 1982).



Attempts to reduce the detrimental effect of scatter have included geometric techniques (§2.3.2), deconvolution techniques (Shaw et al. 1982; Boone 1986; Naimuddin et al. 1987; Love and Kruger 1987; Siebert and Boone 1988), iterative deconvolution techniques (Fahimi and Macovski 1989), and the use of scanning lead bars (Shaw and Plewes 1985). Deconvolution techniques have also been proposed to correct for veiling glare (Shaw et al. 1982; Seibert et al. 1985).

#### 2.4.5 Sampling

In practice, the spatial resolution is dominated by the focal spot size (§2.4.2) and sampling (i.e. the pixel resolution). The process of sampling affects the spatial frequency content of an image by limiting its spatial resolution and in circumstances of inadequate sampling, the creation of artificial structures or 'aliasing.' The effect of sampling on the spatial resolution is described below. A description of aliasing and its consequences can be found in Legault (1973) and Bracewell (1978).

The pixel size depends on the display matrix and on the diameter of the image in the patient plane. The latter is determined by the active input-phosphor size and geometric magnification. For a given maximum resolution  $r_{\max}$ , the sampling intervals  $\Delta x$  and  $\Delta y$  needed in order to avoid aliasing is specified by the Nyquist sampling theorem (Nyquist 1928) as

$$K/2W = 1/2\Delta x = 1/2\Delta y \geq r_{\max} \quad (2.11)$$

where  $K$  is the number of pixels along each side of the square image matrix and  $W$  is the width in the detector plane of the digitized image. The noise or uncertainty in measured pixel coordinates due to the spatial quantization  $\Delta x$  and  $\Delta y$  is respectively (Stearnes 1975)

$$\sigma_{\Delta x}^2 = \Delta x^2/12 \quad \text{and} \quad \sigma_{\Delta y}^2 = \Delta y^2/12 \quad (2.12)$$

In the object plane the spatial resolution limit due to the image matrix is given as  $(KM/2W)$ . Fig. 2.7 illustrates the effect of these parameters on the spatial resolution limit in the object plane for typical display

Figure 2.7 Resolution limit of a  $K \times K$  image matrix plotted as a function of magnification ( $M$ ). A field size of  $W = 153\text{mm}$  is assumed. The resolution limit of a  $1.2\text{mm}$  focal spot is also plotted.

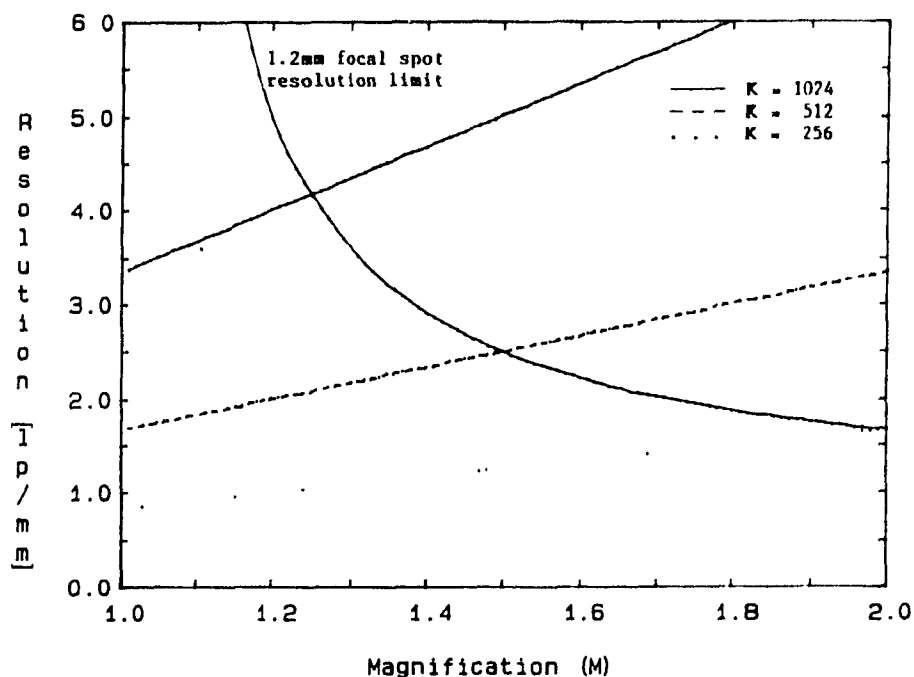
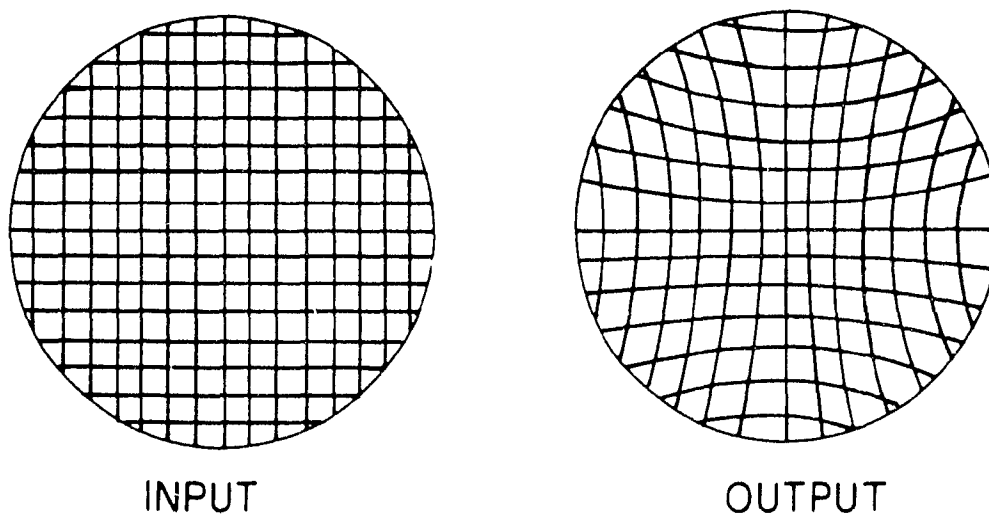


Figure 2.8 Pin-cushion distortion by the image intensifier of a square cm-grid. (Adapted from Casperson 1976)



matrices used in DSA: 256x256, 512x512, and 1024x1024. From Fig. 2.7 the optimum resolution occurs at the magnification where the resolution limits due to finite sampling and focal spot blur become equal (i.e.  $s(M-1) = 2\Delta x = 2\Delta y$ ).

#### 2.4.6 Pin-cushion distortion

Some image intensifiers produce images with a noticeable 'pin-cushion' distortion. In addition to the curvature of the input phosphor, sources of this distortion include poor electron optics, influence of stray magnetic fields on electrons, and poor optics in the recording camera (Christensen et al. 1972). The result of this distortion is that image size, shape, and absorption information are functions of field location (Caspersen et al. 1976).

The level of pin-cushion distortion is usually assessed from an image of a cm-grid which is positioned against the input screen (Fig. 2.8). Typically, grid spacing magnification is observed to increase the further away it is from the center of the image. There are two common approaches to correct for pin-cushion distortion.

The first approach is based on the assumption that the distortion is radially symmetric about the center of the image intensifier and that the relative magnification of a pixel's position can be determined from its radius. Either an empirically determined analytical function of the radius (Brown et al. 1977) or stored relative magnification factors for a single radial line (Alderman 1981) can be then used to correct for the distortion.

The other approach is based on the assumption that the grid spacing at the image center is undistorted and that this spacing can be used as the basis to estimate the 'ideal' or undistorted positions of all other grid intersections. For each intersection point the difference between observed and estimated position is computed and stored as a correction vector. Correction vectors for points between grid intersections can be determined by means of a bilinear interpolation between the correction vectors of the four neighboring intersection points (Kooijman et al. 1982; see also

Chakraborty 1987). Of the two approaches, the latter is preferred because the distortion in the image intensifier used in this work could not be approximated by a simple analytic function.

#### 2.4.7 Patient motion

A basic postulate of DSA is that all images are geometrical projections of the same object. This is violated if there is any movement of the body during examination. Motion produces a misregistration of mask and live signals and results in an inexact cancellation of background signal.

Current DSA machines with capability of pulse exposure (1 to 10 per sec) can take an examination in as little 2-5 seconds. In cases where very small focal spots are used, reducing power output requires longer exposure intervals. Any motion during this interval will result in blurring. Although physiologic motion (e.g. cardiac contraction, respiration) is not necessarily a difficulty with cerebral examinations, involuntary head motion would lead to registration artifacts. The effect of motion in DSA is generally a loss of contrast and spatial resolution.

Two techniques commonly used to reduce motion artifacts are 're-masking' and 'pixel-shifting.' Re-masking is the process by which an observer selects a mask and live image pair that gives the best subtracted image (Kruger and Riederer 1984). Alternatively, some types of motion artifacts can be removed by pixel-shifting or re-registration. This technique involves shifting one image until it matches the other to provide optimal artifact cancellation (Venot and Leclerc 1984). Re-registration can also be achieved by using 'spatial-warp' techniques (Pickens et al. 1987).

#### 2.5 Conclusion

This chapter has reviewed the relationship between the measured subtraction signal in a DSA image and the actual vessel-contrast thickness of iodine at image formation. Underlying physical processes in image formation, detection, and processing impose limitations on the measured subtraction signal. The measured signal is affected by several sources: the

beam energy and shape, photon and system noise, x-ray scatter and image intensifier veiling glare, spatial sampling, image intensifier spatial distortion, and patient motion. The relative importance of these sources of non-linearities depends on what use is to be made of the subtracted image. Applications can be categorized as either diagnostic or quantitative.

The diagnostic value of DSA is well established and depends essentially on factors that affect detectability in an image such as noise, resolution, and inherent object contrast. Image quality is dependent on the proper adjustment of geometric magnification, pixel size, beam quality, and radiation exposure at the image intensifier input. There are several limitations to the use of DSA (Crummy et al. 1982). First is the reduced spatial resolution of DSA ( $2-3 \text{ lp mm}^{-1}$ ) in comparison to film angiography ( $10 \text{ lp mm}^{-1}$ ). Secondly, the inability to perform simultaneous biplane examinations is disadvantageous. This is due to the cost of having two separate imaging chains and the increase in the amount of scatter radiation which reduces the quality of the images. Lastly, the field size of current image intensifiers (270 mm) limits both examinations in some areas and the use of magnification techniques. Using larger image intensifiers (359 - 411 mm) is costly and would require the typical  $512 \times 512$  image matrix to be upgraded to at least  $1024 \times 1024$  in order to avoid image degradation from occurring.

Examples of the quantitative information available from DSA are three-dimensional (3-d) coordinates of points identified in stereo or biplane image pairs, the geometrical measurements of projected features, the most common being vessel mid-lines and diameters, cross sectional areas and volumes of blood vessels, and blood flow measurements. The measurement of 3-d coordinates of points from DSA image pairs is basically limited to spatial quantization noise in the measured coordinates in each image. The noise in measured coordinates associated with spatial sampling is random and can be reduced by increasing spatial sampling or by increasing geometric magnification to a limit set by the focal spot size of the x-ray tube used. Image coordinates may also be distorted by the image intensifier. Error in measured coordinates due to image intensifier pin-cushion distortion is deterministic. Distortion is usually smallest at the center of the image and

increases towards the edge. Image pin-cushion distortion can usually be corrected by simple image mapping techniques.

Image processing techniques to recover vessel information, such as mid-lines and diameters, and to measure object contrast require that some physical features of the vessel being imaged (e.g. shape, position, contrast etc.) be detectable and have a 'faithful' correspondence in the measured signal. The most common limitation to such techniques is vessel projection superposition and foreshortening. For techniques that attempt to measure object contrast in a subtracted image, or reconstruct object contrast tomographically from a given number of DSA projections, system linearity is important. Degradation of linearity is primarily a result of beam hardening, scatter, and veiling glare. When photon statistics are good, system noise will limit the precision of the subtracted signal.

There are really few strategies to deal with system non-linearities. The simplest solution is to re-design the detector system eliminating or reducing the source of error to within tolerable limits for the desired application. A more expedient solution is to directly correct for these errors by either avoiding or compensating for them. However, it is simpler to describe these effects than it is to physically separate them from other errors and then correct them. The other possibility is to use image processing techniques that are sufficiently robust to tolerate these sources of error.

## CHAPTER THREE

### GEOMETRIC RECONSTRUCTION FROM DSA IMAGE PAIRS: METHOD

#### 3.1 Introduction

Methods of reconstructing three-dimensional (3-d) vessel geometry from either stereo or biplane pairs of digital subtraction angiograms (DSA) were reviewed in §1.4.2. The conditions under which these methods are applicable are different from those found in cerebral DSA. The nature of the reconstruction problem in cerebral DSA is described in §3.2. There are two important and related aspects of this problem. The first is image coordinate measurement errors which are no longer negligible when digital angiograms are used for stereo reconstruction. The other aspect is the difficulty in finding corresponding vessels between widely spaced views, particularly biplane angiograms. This correspondence problem is often the result of trying to reduce the effect of measurement error by increasing the angular separation between views. The correspondence problem for widely spaced views exists whether or not some attempt is made to compensate for measurement error. The problem of finding correspondences between angiograms from different views is discussed in §3.3.

§3.4 describes a new interactive technique for finding correspondences between vessels in biplane angiograms. In the proposed method the 3-d coordinates of a vessel's center-line is reconstructed from a pair of lateral stereo DSA images. This first reconstruction is re-projected into the anterior-posterior (AP) image of the biplane pair and used to aid the observer in selecting the corresponding vessel. The corresponding vessels from the biplane images are then used in the final reconstruction. Chapter 4 describes the experiments and the results obtained in the evaluation of this method.

#### 3.2 Problems in 3-d vessel reconstruction from cerebral DSA images

Reconstructing the 3-d geometry of an object from differences in its

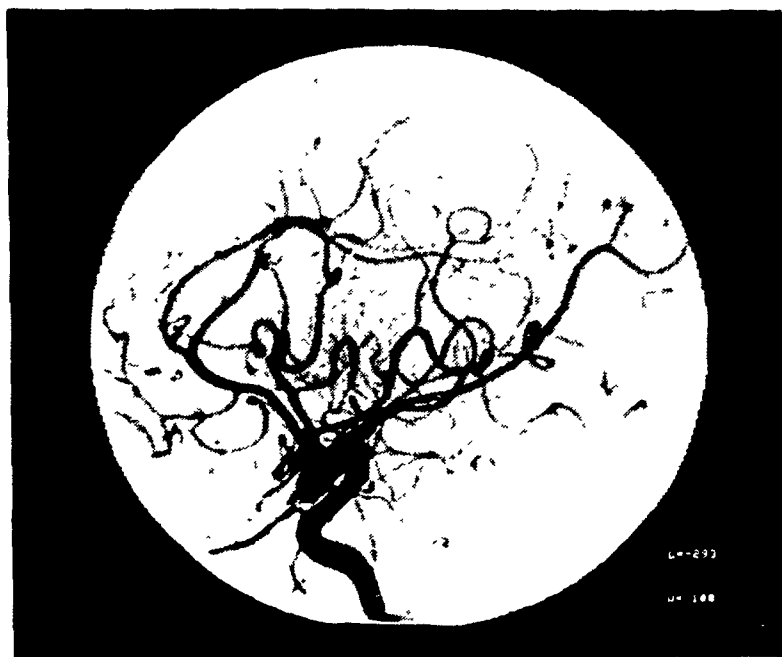
measured image coordinates, or disparity, between their projections in different views involves two aspects. They are the selection of readily distinguishable object points as candidates for matching and the definition of criteria for deciding which matches are correct (Barnard and Thompson 1980). Problems associated with meeting these requirements in reconstruction of vessels from cerebral DSA stereo and biplane images are considered below.

The first step towards matching of points in different views is the identification of the projections of the cerebral vessels in each angiogram by segmentation. Segmentation is the process of partitioning an image into distinct meaningful regions. As blood vessels are generally thin and elongated structures, points along the medial axis or center-line of a vessel in an angiogram would adequately describe its structure and be suitable candidates for matching (Vignaud and Korach 1973). However automatic segmentation or manual tracking of vessels in angiograms is not a trivial problem due to system non-linearities (§2.4) and vessel superposition and foreshortening in projection. The latter depends on both the 3-d structure of the vascular system and its projections. In comparison to other systems, such as the coronary vessels, the cerebral vasculature is complex. The pattern of vessel superposition and foreshortening in cerebral angiograms of lateral and anterior-posterior views is shown in Fig. 3.1, regions where vessel tracking or segmentation would be ambiguous are indicated. Of the two projections, the vessels in the anterior-posterior angiogram are the more difficult to segment.

Most methods of vessel segmentation (§3.4.5) are intended for simpler vessel geometries than expected in cerebral angiograms. Their application in cerebral DSA would not be reliable and pose too many difficulties to be clinically practical. The preferred means of tracking vessels is still the human observer. The perceptual skills of the observer are often the only means of resolving ambiguities that are encountered in tracking vessels.

Given the traced vessels from two different views, the next step is finding a matching between the sets of traced center-line points from each image. Points from both images should be matched if they are image plane projections of the same object point. The problem is to determine which





a) Lateral view



b) Anterior-posterior view

Figure 3.1 Orthogonal DSA images with examples of vessel superposition and foreshortening indicated.

image point pairs to use and to choose the basis for deciding which matches are correct. The possible projections considered for matching are restricted by the geometry of the stereotactic frame (§3.4.3.1) to either stereo or biplane views.

It was pointed out in §1.4.2.1 that both manual and computer techniques for matching stereo angiograms are possible. With manual techniques, the observer views the images stereoscopically and tracks in 3-d the perceived vessel depth using a stereo cursor. The primary limitation of manual techniques is the time consuming aspect of correspondence point entry. Most automated systems have attempted to overcome this limitation by finding matches between segmented stereo images computationally.

Correspondence algorithms have been based on the similarity of local point properties between stereo pairs and the point's local relationship to neighboring vessel points, such as 'continuity of disparity' (§1.4.2.1). Except for vessels whose medial axes lie either in the direction of disparity or perpendicular to the plane of projection in one of the images, most vessels in angiograms can be matched unambiguously. However, the accuracy of reconstruction can be poor in stereo analysis of digital angiograms. The uncertainty in the measurements of the matched set of image coordinates, due to both incorrect tracking and the finite pixel size of a digital angiogram, is no longer negligible (Suetens et al. 1983). At least a 30 degree angular separation between views is necessary before the distance between the location of the object point and its reconstruction becomes equal to the pixel width in the image (Blume 1984). The loss of accuracy due to measurement error can also be reduced by increasing the geometric magnification (Sherlock and Aitken 1980). Sherlock and Aitken showed that the reduction in the magnitude of reconstruction error was proportional to the increase in geometric magnification. However, the short focal lengths (~110 cm) and small image intensifier field sizes (~154-270 mm) of the c-arm unit used in this work made magnification techniques impractical for stereotactic applications.

The other possibility is to match vessel traces between more widely spaced views such as biplane images (Fig. 3.1). The biplane angiograms are

often not similar, and only major vessel features such as forks and junctions may be identifiable in both views. A number of methods for matching orthogonal views described in §1.4.2.2 take advantage of these features. The common approach has been to construct a 'tree' or 'graph' description of the segmented vasculature using major vessel features as 'node' points. Next, the nodes of these graphs in the two views are matched on the basis of their relationships with other nodes in the graph. Having established correct correspondence between the nodes, the individual trace points along paths or branches connecting the nodes are then matched. This method of finding corresponding branches is limited by the complexity of the 3-d vascular system. It assumes that an angiogram pair can be described by tree structures or graphs that are different but have essentially the same relational structure between node points. Where this is possible, such as in cardioangiograms, this method has demonstrated success (§1.4.2.2).

For cerebral angiograms shown in Fig. 3.1, it can be observed that the projections of the 3-d vessel system are too complex to be completely described by the same node points and tree structure relationships in each view. Such vessel features such as forks and junctions which constitute node points may be visible in one view but not the other. This makes it difficult not only to match nodes but to subsequently identify corresponding lateral vessel branches in an anterior-posterior angiogram. There is obviously a need to overcome this limitation.

In order to perform any matching between biplane cerebral angiograms, 'a priori' information about how the vessels are structured in 3-d is needed. The approach proposed is based on the thesis that although the vessel reconstruction from lateral stereo image pairs is generally inaccurate for stereotactic planning, it may provide a good estimate of the vessel's 3-d geometry. Given the x-ray beam geometry for the anterior-posterior projection, the reconstructed vessel can be re-projected into the anterior-posterior image. The biplane images are now in a format which provides direct comparison of vessels. Taking advantage of prior knowledge that the vessel's center-line points are ordered and connected, the vessel reconstructed from the stereo images should exhibit recognizable structure on re-projection in the anterior-posterior view in spite of reconstruction

errors. The observer then selects the vessel that resembles the re-projected one. Point correspondence between matched branches is then established using a computer algorithm described in the following section.

### 3.3 Vessel trace correspondence principle

Given the 2-d center-line traces of the same vessel in two different views, the correspondence problem is simplified to finding the match between any point along the trace of the vessel in one view with the matching view of the second trace. The possible approaches to this correspondence problem are discussed in §3.3.1. §3.3.2 describes the proposed correspondence algorithm.

#### 3.3.1 Background

The nature of the correspondence problem in matching vessels in angiogram pairs of different views depends on the 3-d complexity of the vessels and their projections. These aspects of the vessel correspondence problem are discussed in §3.3.1.1. In previous work, vessel correspondence algorithms have been based either on correlation of similarities in the vessel traces or on a construction of a system of 2-d and 3-d rays from the view transformation data (§3.4.3.2) of each view. The use of rays or 'auxiliary' lines is referred to as 'ray- or 'back- projection' (MacKay et al. 1982; Mol et al. 1986). The use of correlation and ray-projection approaches are described in §3.3.1.2 and §3.3.1.3.

##### 3.3.1.1 Vessel correspondence problem

Fig. 3.2 shows a 3-d line curve projected onto images 'A' and 'B,' where the sampled points of the projected curve are given by  $(x_a, y_a)_n$ ,  $n=1,2,\dots,N$  and  $(x_b, y_b)_m$ ,  $m=1,2,\dots,M$  respectively. The shift or 'disparity' between corresponding points assigned to  $(x_a, y_a)_n$ ,  $n=1,2,\dots,N$  is given by  $(\Delta x, \Delta y)_n$ ,

$$(\Delta x, \Delta y)_n = (x_b - x_a, y_b - y_a)_{n,m} \quad (3.1)$$

Disparate image pairs may be produced either by rotation of the x-ray

Figure 3.2 Illustration of projection geometry used in the correspondence and reconstruction problems. Projection of line  $\overline{S_a P_a}$  into image 'B' is the 'auxiliary' line of  $P_a$ .

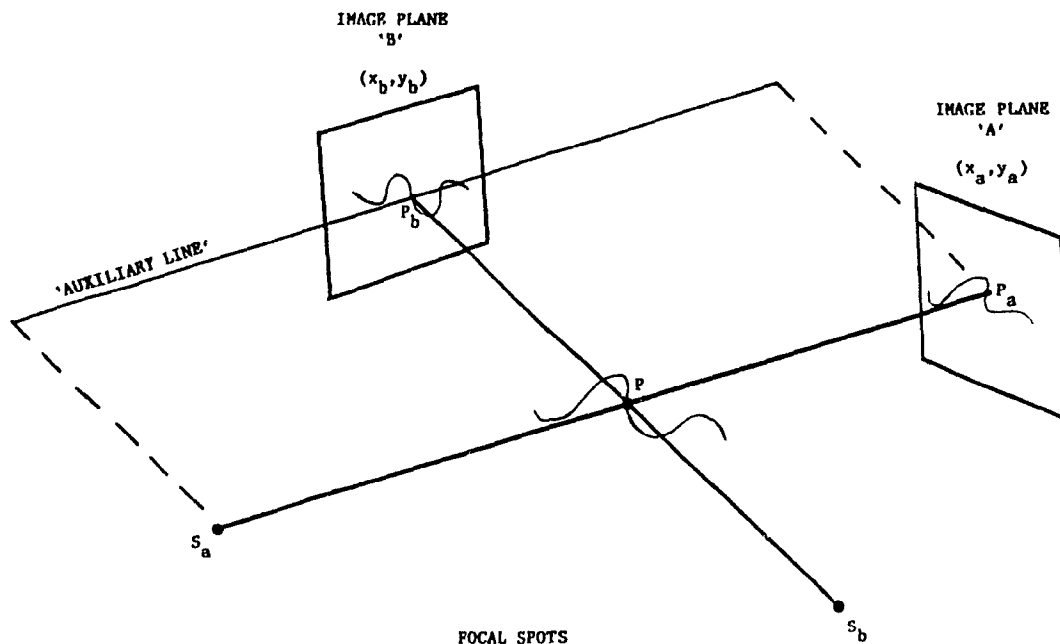
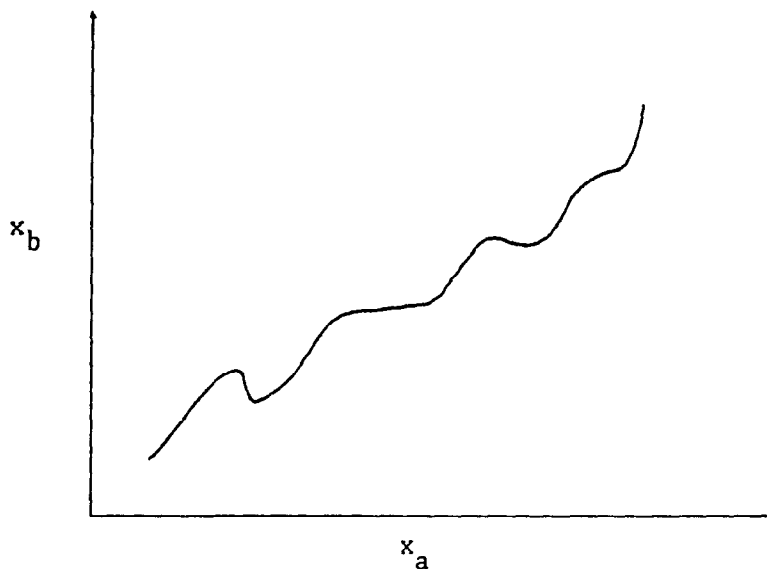


Figure 3.3 Relationship of  $x_a$  to  $x_b$ , where  $x_a$  and  $x_b$  are the 'x' pixel coordinates of a projected vessel in image 'A' and 'B' respectively (see Fig. 3.2).



source-image detector assembly creating an angular separation between views or by a lateral translation of the assembly or x-ray source. The distance translated is called the 'stereo shift.' Rotation of the source-detector assembly is the method of choice with the c-arm unit used in this work.

The central problem in determining correspondences between the sample points of vessel traces is that, except for branching points, there are few 'exact' point correspondences between them. Because of the arbitrary orientation of the 3-d vessels, the sampled projected vessels will have different numbers of points in each view. This becomes more evident as the angular separation or stereo shift distance is increased. This problem can be better explained by looking at a plot of  $x_a$  versus  $x_b$  of known point correspondences for a single vessel branch (Fig. 3.3). In Fig. 3.3, zero, negative, or infinite slopes in the relationship between  $x_a$  and  $x_b$  give rise to points that are unavailable for matching.

Negative slopes mean that a vessel overlaps itself either completely or partially in one of the two images. This makes matching difficult because there is more than one match possible. By keeping the angle between view pairs small, as in the case with stereo pairs, the instances of vessel superimposition occurring in just one of the images can be reduced. The chance of superimposition by other projected vessels still remains a problem.

Zero or infinite slopes mean that the x-ray source in one of the two views is looking directly down a vessel, and the vessel is completely foreshortened. As a result one point may map onto many points. Depending on the 3-d vasculature of interest, there is often a preferred view where the complex pattern of vessel superimposition and foreshortening can be minimized. In the case of cerebral vasculature, this is the lateral view (Vignaud et al. 1979).

As the angle separating the image pair increases, spatial correlation between vessel traces is lost. Superimposition and foreshortening of vessels make each image of the pair different as is the case with the biplane cerebral angiograms in Fig. 3.1.

### 3.3.1.2 Correlation-based algorithms

Most existing algorithms for matching images from stereo views of the same object surface incorporate the technique of 'pixel correlation' (Levine et al. 1973; Mori et al. 1973; Yakimovsky and Cunningham 1978; Frei et al. 1980; Barnard and Thompson 1980). Fig. 3.4 illustrates the principle of pixel correlation for a stereo image pair. Given a small windowed region in the left image centered at  $(x_1, y)$ , the object of pixel correlation is to find the matching region in the right image. A measure of 'agreement' between the image content of the two windowed regions is calculated by means of cross-correlation, or a similar technique. A match is found when the measure of agreement reaches a maximum. However, when these image pairs are angiograms, images in corresponding windows are not likely to be the same (e.g. windows a, b, and c in Fig. 3.5). This is an important limitation in the use of traditional correlation-based methods.

Instead of correlating windows in both images, characteristics of the vessel trace in both views may be compared. Algorithms for correlating vessel trace features have been proposed by Hoffmann et al. (1987) and Suetens et al. (1983). Both algorithms are discussed below.

Hoffmann's algorithm is based on comparing background-subtracted vessel profiles in stereo-magnified image pairs (Doi et al. 1976; 1983). As a vessel in one image is being tracked, a vessel profile is obtained along a line perpendicular to the tracking direction (Hoffmann et al. 1986). This profile is then compared to a set of candidate track point profiles along the stereoscopic image shift line in the other image. Agreement is measured by computing the root-mean-square (RMS) differences between profiles of the given track point and the set of candidate points. The track point of the profile in the set that gives the lowest RMS difference is selected as the corresponding point.

This algorithm assumes that the vessel profiles are invariant in the stereo image pair. This does not hold if the profiles are of vessels that are foreshortened or obscured in only one of the images, or if misregistration artifacts are present. Furthermore, ambiguities may still

Figure 3.4 Principle of image-window pixel correlation.  $x_l$  and  $x_r$  lie on a common 'y' or the stereo shift line in the left and right images of the stereo pair.

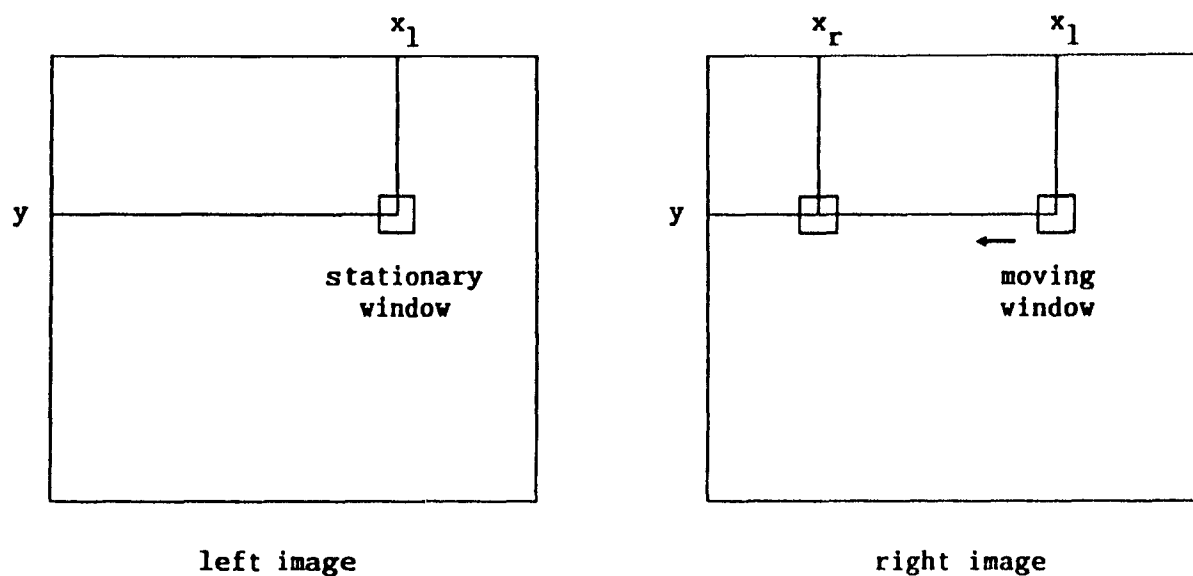
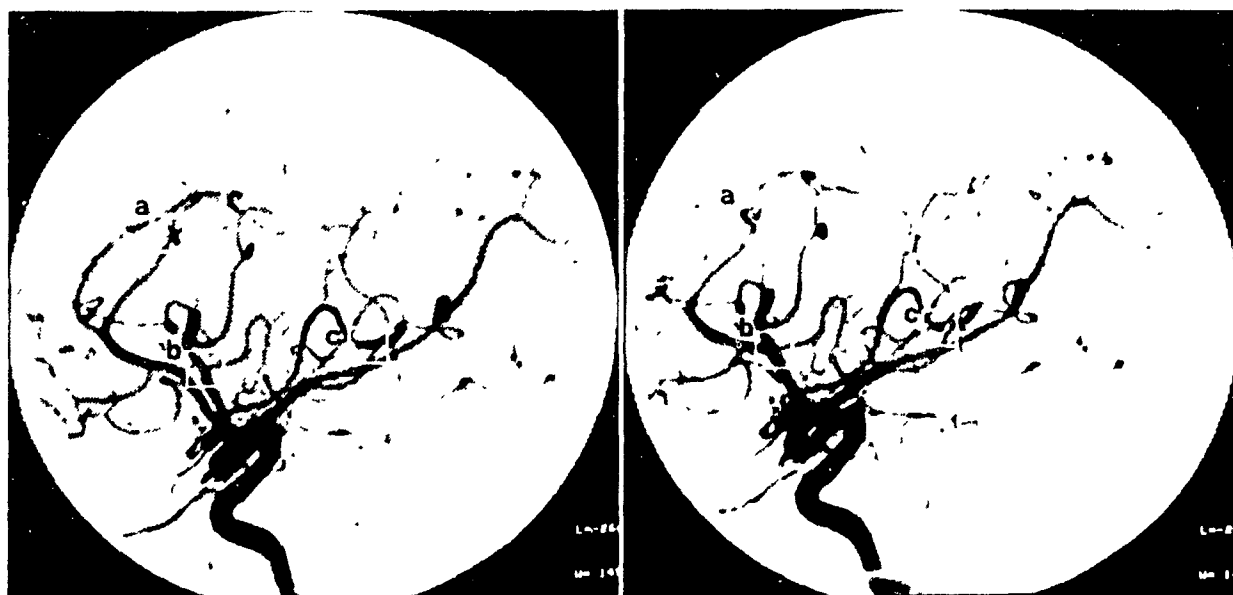


Figure 3.5 Stereoscopic pair of DSA images with corresponding windows indicated.





arise because most points in the trace are not 'discrete' in the sense that they can be easily distinguished from their neighbors. Suetens et al. (1983) addressed this problem by incorporating a global mechanism into the correspondence algorithm to find a preferred set of matches.

Their algorithm begins with matching points between a stereo pair of vessel traces on the basis of similarity of local vessel characteristics for each point pair. Each sample point in the trace belongs to a characteristic vessel segment of a distinct orientation, width, and intensity. They found that this alone is not sufficient to establish all correspondences. A preferred set of matches is found by an iterative process (Barnard and Thompson 1980) of evaluating different sets of point pairings and selecting the one set whose disparities are the most 'consistent.' Consistency is a measure of how well the disparity of a match 'conforms' to its neighboring matches and is a consequence of the continuity of real world surfaces. Suetens' algorithm (1983) for finding correspondences between stereo image pairs produced by a stereo shift technique is described below.

For each vessel track point in the left image,  $(x_a, y_a)_n$ , a set  $L$  of disparity vectors of possible matches is constructed in the other image. Points in the right image are selected as possible matches if they are within a distance  $s_r$  of two horizontal lines from the 'y' coordinate of the considered point in the left image. Let  $\vec{l}_i = (\Delta x, \Delta y)_i$  be a disparity vector in  $L$  that can be assigned to the point  $(x_a, y_a)$  and let  $p(\vec{l}_i)$  be an estimate of its likelihood. The initial probabilities  $p^0(\vec{l}_i)$  are based on a measure of similarity between local vessel features at track points in the left and right images,

$$p^0(\vec{l}_i) = w(\vec{l}_i)(1 - p^0_\emptyset) / \sum_i w(\vec{l}_i) \quad (3.2)$$

where  $w(\vec{l}_i)$  is a measure of similarity for  $\vec{l}_i$ .  $w(\vec{l}_i)$  is given by

$$w(\vec{l}_i) = 1 / (1 + a_1 |\Delta_o(\vec{l}_i)| + a_2 |\Delta_w(\vec{l}_i)| + a_3 |\Delta_{in}(\vec{l}_i)|) \quad (3.3)$$

where  $a_1$ ,  $a_2$ , and  $a_3$  are constants and where  $\Delta_o(\vec{l}_i)$  is the difference between the orientation values of the considered vessel segments at points in the left and right images,  $\Delta_w(\vec{l}_i)$  is the difference between their widths, and  $\Delta_{in}(\vec{l}_i)$  is the difference between their intensity values. The

probability that point  $(x_a, y_a)$  in the left image does not correspond to any point in the right is  $p_{\emptyset}^0$ ,

$$p_{\emptyset}^0 = 1 - \max_i [w(l_i^{\rightarrow})] \quad (3.4)$$

These probabilities are iteratively modified by applying the requirement of consistency. For each possible match nearly the same disparities are searched for among the neighbors. If there are any found, the possibility of this match increases. Consistency requires  $p^{k+1}(l_i^{\rightarrow})$ ,  $k=0,1,\dots$ , to increase if many neighboring points have a high probability of having disparity  $l_j^{\rightarrow}$  that makes

$$|| l_i^{\rightarrow} - l_j^{\rightarrow} || \leq \psi_1 \quad (3.5)$$

where  $\psi_1$  is an appropriate threshold (e.g.  $\psi_1=2$  in Suetens et al. 1983). Otherwise,  $p^{k+1}(l_i^{\rightarrow})$  should decrease. The consistency condition is given by

$$|| l_i^{\rightarrow} - l_j^{\rightarrow} || = \max [ |\Delta x_i - \Delta x_j|, |\Delta y_i - \Delta y_j| ] \quad (3.6)$$

A point  $(x_a, y_a)_n$  is considered a neighbor of  $(x_a, y_a)$  if there is a continuous path of track points between them consisting of no more than  $K$  points (e.g.  $K=5$  in Suetens et al. 1983). Only those candidates consistent with their neighbors can survive through several iterations of 'relaxation.' 'Relaxation labeling' is a technique introduced by Rosenfeld et al. (1976) and Zucker (1976). The basic principle of relaxation labeling is to perform ambiguity reduction by applying iterated parallel operations.

The following rule is used to update  $p^k(l_i^{\rightarrow})$ :

$$p^{k+1}(l_i^{\rightarrow}) = p^{k+1}(l_i^{\rightarrow}) / (p_{\emptyset}^k + \sum_i p^{k+1}(l_i^{\rightarrow})) \quad (3.7)$$

where

$$p^{k+1}(l_i^{\rightarrow}) = p^k(l_i^{\rightarrow}) [Q + Gv^k(l_i^{\rightarrow})] \quad (3.8)$$

and

$$\left. \begin{aligned} v^k(l_i^{\rightarrow}) &= \sum_{n:} \left( \sum_{l_j^{\rightarrow}:} p_n^k(l_j^{\rightarrow}) \right) \\ n: & (x_a, y_a)_n \text{ near } (x_a, y_a), (x_a, y_a)_n \neq (x_a, y_a) \\ l_j^{\rightarrow}: & || l_i^{\rightarrow} - l_j^{\rightarrow} || \leq \psi_1 \end{aligned} \right\} \quad (3.9)$$

In (3.9)  $p_n^k(l_j^{\rightarrow})$  is the probability that  $(x_a, y_a)_n$  in the left image has disparity  $l_j^{\rightarrow}$  after the  $k^{\text{th}}$  iteration. The probability that no match exists is updated by

$$p_{\emptyset}^{k+1} = p_{\emptyset}^k / ( p_{\emptyset}^k + \sum_i p_i^{k+1}(l_i^{\rightarrow}) ) \quad (3.10)$$

The convergence characteristics of the model are influenced by a damping parameter  $Q$  and gain parameter  $G$ , in Suetens et al. (1983)  $Q=0.3$  and  $G=0.4$ .

After each iteration the algorithm purges those matches with a probability less than 0.01. Iteration stops when the probability values reach a steady state, but in practice it is stopped after 10 to 20 iterations (Barnard and Thompson 1980; Suetens et al. 1983). Points that have a disparity with probability greater than 0.7 are considered to be matched.

Suetens et al. (1983) demonstrated the feasibility of this algorithm on an x-ray stereo image pair of a test object composed of a skull and a number of copper wires. The weak point of their technique is not the algorithm but with vessel tracking and feature extraction. Stereo angiogram pairs that are not collected 'simultaneously' or that contain foreshortened and superimposed vessels make vessel tracking and subsequent measurement of features difficult. In cerebral angiography such images are common.

### 3.3.1.3 Ray-based algorithms

Finding correspondences using ray-projection is based on the assumption that a point in one view will map to a line segment in the image plane for any other view. Hence, the corresponding image of the point in the desired view will ideally be found at some position along this line (Fig. 3.2). The correspondence search is then limited to displacements along this auxiliary line or back-projected ray (MacKay et al. 1982; Potel et al. 1983). The ray-projection approach has been used in a wide variety of applications in the solution of the correspondence problem (Kim et al. 1982; MacKay et al. 1982; Potel et al. 1983; Blume 1984; Barba et al. 1987).

There are two potential problems associated with the use of the ray-projection algorithm. The first is that although intersection of the back-projected ray with the trace in the second view is necessary for correspondence, it is not sufficient. The back-projected ray can in fact cross a trace at several locations as shown in Fig. 3.2. Blume (1984) suggests that 'a priori' knowledge be used to resolve the ambiguous correspondences. 'A priori' knowledge can take the form of previously determined correspondence (Barba et al. 1987). The other problem is that in the presence of measurement inaccuracies, geometric distortion, and object motion, the auxiliary line of a point may not intersect the corresponding point in the trace of the conjugate image. Instead correspondence can be selected on the basis of how close the 3-d lines of candidate matching points intersect (Parker et al. 1985;1986;1987). The methods of Parker et al. (1985;1986;1987) and Barba et al.(1987) are discussed below.

Barba et al. (1987) use previously determined correspondences to resolve multiple matches between vessel traces from biplane angiograms. Their correspondence algorithm begins with a selection of two consecutive track or 'seed' points on the vessel trace in image 'A' whose auxiliary lines intersect a tracked vessel in the other image 'B' only once. The projected vessel length is then calculated from the Euclidean distance between the two intersection points. Next, for each track point in image 'A,' starting from the seed points and working uniformly along one direction of the tracked vessel, a corresponding auxiliary line in image 'B' is computed. The track point within 1.5 times the projected vessel length of the previous intersection is selected, and this length is updated. The procedure is repeated in the other direction along the vessel away from the seed points.

This method depends on unambiguous matches and vessel connectivity to resolve ambiguous matches. In the presence of measurement noise, unambiguous matches may potentially be incorrect and result in reconstruction errors. Since previous correspondences are used, such errors would be propagated in the reconstruction through the rest of the trace.

In Parker et al. (1985;1986;1987) a set of measures of how 'close' 3-d

lines from a possible match of point pairs intersect and vessel connectivity are used to determine matches. This method is used to match vessel traces from a pair of gated coronary angiograms separated by about 90 degrees. Their method begins with an observer selecting as nodes the start and stop points of vessel branches in the tree. Given a pair of vessel branch traces, a set of matches for each point in the longer trace with each point in the shorter trace is constructed. For each pair of matched points, two lines in 3-d are constructed, and the distance of the segment between the points of closest approach between the two lines is computed (Fig. 3.6). The reconstructed coordinates are taken at the midpoint of this segment. The squared value of the distance of each pair,  $d_{mn}^2$ , is represented by the matrix  $M(m,n)$  (Fig. 3.7). The top left and bottom right indices of the matrix represent the known correspondences of the start and stop end points of the vessel branch trace in each view. The smaller the squared distance value the more likely that the pair of points it represents are in correspondence. This reduces the problem of finding the best set of matches to finding the minimum cost path from the upper left corner of the 'likelihood' matrix to the lower right. The values in  $M(m,n)$  are updated by rows starting from  $n = 2$ ,

$$M(m,n) = M(m,n) + \min_u ( M(m-u,n-1) ) \quad (3.11)$$

$$u: ( -\Delta m, \dots, -1, 0, 1, \dots, \Delta m )$$

where the connectivity constraint requires that indices of subsequent matches can differ by at most  $|\Delta m|$  from indices of previous matches. For each row element of  $M(m,n)$  the path chosen by the search algorithm from the previous row is stored as a pointer. The final path of index pairing is then specified by the bottom right index of the matrix (i.e. known stop end points of the vessel branch traces). The pointer at this matrix element indicates the path to the element in the previous row. 'Chaining' together the pointers row by row this way, the final path is constructed. This search process is referred to as 'dynamic programming.' Other related applications of dynamic programming have been described in Pope et al. (1984;1985) and Parker and Pryor (1982).

If the start and stop node points of a pair of vessel branches are not known, the final path can be specified by the minimum value in the last row

Figure 3.6 The minimum distance  $d_{mn}^2$  between two lines corresponding to the paired points  $(x_a, y_a)_n$  and  $(x_b, y_b)_m$ . (After Parker et al. 1986)

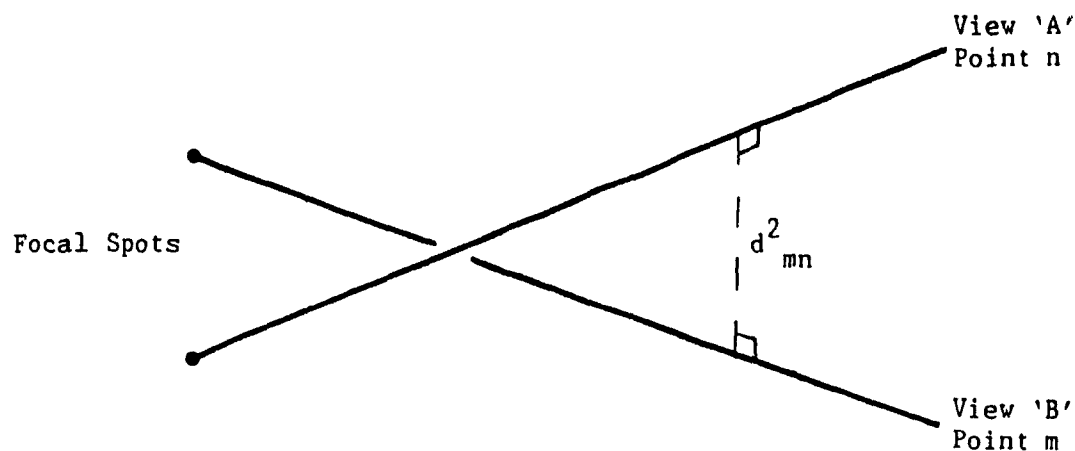
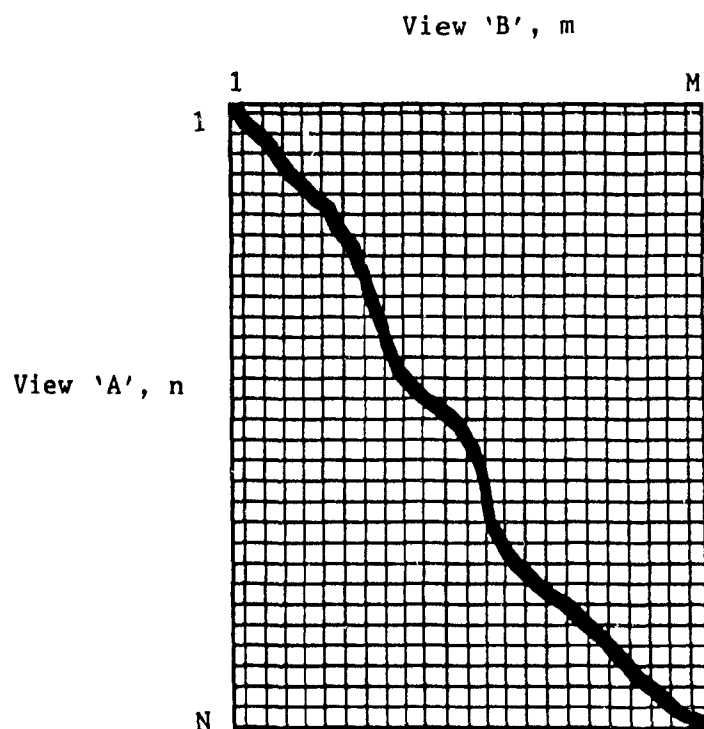


Figure 3.7 The likelihood matrix of minimum distances  $d_{mn}^2$  between the line of the  $n^{\text{th}}$  point in a branch in view 'A' paired with the line of the  $m^{\text{th}}$  point in the matching branch in view 'B'. (After Parker et al. 1986)



of  $M(m,n)$ . Difficulties arise if the minimum value appears in more than one row element.

In comparison to the previous method, this method should be less sensitive to measurement noise in the image coordinates of the points being matched, but less flexible to large changes in indices that would reflect vessel foreshortening. Its application in cerebral angiography is not straightforward. Unlike the system of coronary arteries, there are few node points that can be advantageously used.

### 3.3.2 Proposed algorithm

Building on the work of Suetens et al. (1983) and Parker et al. (1985; 1986;1987), an algorithm for automatic matching of points along a matched pair of traces from any pair of views is proposed. The proposed correspondence algorithm is similar to Suetens' et al. (1983), but different in the way candidate points are found and in the how the initial probabilities are estimated and iterated. These three differences are described below.

Ray-projection is used to find an initial set of possible disparities for each point  $(x_a, y_a)$  of trace 'A.' Every point in the vessel trace 'B' is considered as a candidate match if its distance along the normal to the projected ray is less than  $s_r$ . Because of patient re-positioning after rotating the c-arm assembly, the 'y' coordinates of the projected vessels will not necessarily lie on the same horizontal lines.  $s_r$  is adjusted to reflect any inaccuracies in the auxiliary line that may arise from measurement errors.

The second difference is that the initial probabilities are based on the contents of the likelihood matrix (Parker et al. 1985;1986;1987). Since point features cannot be expected to be invariant in non-stereo projections, each disparity in the set is assigned an initial probability based on the distance  $d_{mn}^2$ . A matrix  $M(m,n)$  is constructed of the candidate matches and updated according to  $u: 0,1,...,\Delta m$  in (3.11) in order to avoid ambiguous matches that may result from multiple crossings. Rather than constructing

the final path through the likelihood matrix by chaining, the updated elements of  $M(m,n)$  are used as the initial probability estimates where

$$w(l_i^{\rightarrow}) = 1 / ( 1 + a |M(m,n)| ) \quad (3.12)$$

replaces (3.3). The expected advantage of iterating the initial probabilities in parallel operations is that the level of ambiguity in candidate matches should be reduced further than by chaining.

The last difference in the proposed algorithm is the addition of an ordering constraint to  $l_j^{\rightarrow}$  in (3.9),

$$\begin{aligned} r_{a,i} < r_{a,j} , \quad 0 \leq (r_{b,j} - r_{b,i}) \leq \psi_2 \\ r_{a,i} > r_{a,j} , \quad 0 \leq (r_{b,i} - r_{b,j}) \leq \psi_2 \end{aligned} \quad (3.13)$$

where indices in trace 'A'  $r_{a,i}$  and  $r_{a,j}$  and trace 'B'  $r_{b,i}$  and  $r_{b,j}$  are associated with the disparity vector  $l_i^{\rightarrow}$  and its neighbor  $l_j^{\rightarrow}$  respectively. By this constraint, the rank order of indices of  $l_i^{\rightarrow}$  with its neighbor  $l_j^{\rightarrow}$  in trace 'B' must be the same as in trace 'A.' Since blood vessels are linear and connected objects, it is reasonable to assume that the ordering of track points representing the connected path of a vessel should be preserved in different projections. Of course, should a vessel's 3-d path lie almost entirely along the direction of projection in one of the images being compared then this constraint would be defeated. In the case of the cerebral vessel tree, foreshortening of entire vessel branches is unlikely. The threshold  $\psi_2$  gives the size of the neighborhood of  $l_i^{\rightarrow}$  in trace 'B' where  $l_j^{\rightarrow}$  is allowed. This constraint is important for matching points between biplane vessel traces where except for very simple vessel geometries consistency of disparity does not hold.

### 3.4 Stereo - biplane reconstruction method

It has been proposed in §3.2 that vessels reconstructed from stereo views will often exhibit recognizable structure from which information useful in biplane analysis should be extractable by the observer. In order to take advantage of the observer's insight and to efficiently make use of this prior knowledge, an interactive reconstruction method has been



developed. An overview of the proposed method to reconstruct vessels from stereo and biplane DSA images is outlined in §3.4.1. §3.4.2-3.4.6 describe the design of the algorithms used.

### 3.4.1 Overview of proposed method

The reconstruction procedure uses as input three DSA images, a lateral stereo pair and a single anterior-posterior image of the head and stereotactic frame together. All views are collected by c-arm rotation (§3.4.2). The output of this procedure is a set of 3-d coordinates that represent the center-line positions of the blood vessels in the stereotactic coordinate system. A function chart of the procedure is shown in Fig. 3.8. The ten steps of this procedure are outlined below.

The first step in the procedure is the calibration of the x-ray beam geometry and pin-cushion distortion in the lateral stereo and anterior-posterior DSA images (§3.4.3). The x-ray views are calibrated directly from the images of the stereotactic frame's fiducial markers in the angiograms. The stereotactic frame remains attached to the patient's head during DSA examination. It is then a simple task for the observer to identify the 2-d image coordinates of the markers in an angiogram displayed on a CRT monitor (Peters et al. 1986). Next, the computer uses these measurements to compute the transformation constants between 3-d object space and the 2-d image in each view. The transformation constants are then used later in the reconstruction and re-projection steps of the procedure. Because images suffer from pin-cushion distortion, the images are calibrated to correct for this distortion. A 1cm square wire grid is imaged, and a correction procedure similar to Kooijman's technique (§2.4.6) is used.

Following calibration, the lateral stereo angiograms are displayed stereoscopically in step 2. The stereo image pair is displayed as a red-blue anaglyph on a colour CRT monitor (§3.4.4). This permits the observer to visually select those branches of vessels in both images that are of interest to be reconstructed. The observer proceeds with one vessel branch at a time. In step 3, the selected vessel branch in each angiogram of the stereo pair is manually tracked (§3.4.5).

Figure 3.8 Function chart of reconstruction procedure.

INPUT: Lateral stereo and anterior-posterior stereotactic DSA images

<u>Steps</u>	<u>Performed by</u>
1) Calibration of input images	observer & computer
2) Display stereo lateral images	computer
3) Track branch of vessel projected in the stereo image pair	observer
4) Match stereo vessel traces	computer
5) 3-d reconstruction from stereo pairs	computer
6) Re-project 3-d coordinates to anterior-posterior image	computer
7) Track corresponding vessel branch in anterior-posterior image	observer
8) Match biplane vessel traces	computer
9) 3-d reconstruction from biplane pairs	computer
10) Return to 2) until all vessel branches reconstructed	observer

OUTPUT: 3-d coordinates of tracked vessel

The two sets of 2-d points representing the tracked vessels are matched by the computer in step 4. Image points are paired using the algorithm described previously in §3.3.2. In step 5, the 3-d coordinates of the track points are then reconstructed from the set of matches. The pair of 2-d image coordinates of each point and the calibration data from each view are used to compute the point's 3-d coordinates. Given the calibration data for the anterior-posterior view, the reconstructed 3-d points are then re-projected by the computer and displayed in the anterior-posterior angiogram in step 6 (§3.4.6).

In step 7, the vessel branch in the anterior-posterior angiogram that most resembles the re-projected vessel is selected by the observer. This vessel is then tracked by the observer. Steps 8 and 9 are the same as steps 4 and 5 except that the biplane vessel traces are matched instead of the stereo traces. The final 3-d coordinates are re-computed on the basis of the biplane matches. The procedure is repeated for any number of vessel branches.

#### 3.4.2 Stereo and biplane acquisition of DSA images

Fig. 3.9 illustrates the coordinate system of the data collection model and the notations that are adopted here. Referring to Figs. 3.9 and 3.10, the  $x, y, z$  (cartesian) coordinates are fixed in object space where  $f_1$  is the distance of the x-ray source to P, the object point to be reconstructed, and  $f_2$  is the distance of P to the image intensifier surface. Typically,  $f_1$  is between 70 to 90 cm and  $f_2$  is between 10 to 40 cm. In cerebral DSA, projection images are acquired by rotating a fixed x-ray source-detector or c-arm assembly around the patient's head at variable angles of  $\theta$  and  $\beta$ . In practice  $\beta$  is kept constant (usually  $\beta=90$  degrees) and the c-arm is rotated in  $\theta$ . Lateral and anterior-posterior views are specified by  $\theta=0$  and  $\theta=90$  degrees respectively.

The effect of 3-d space can be created by viewing the stereo image pair on a stereoscopic CRT display system. The various CRT displays systems possible are discussed in §3.4.4.

Figure 3.9 Data collection geometry.

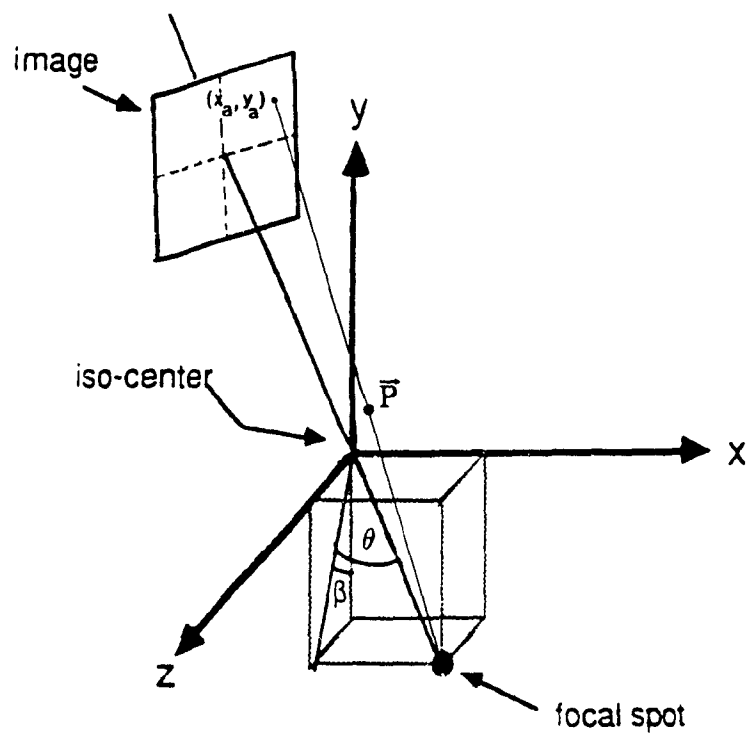
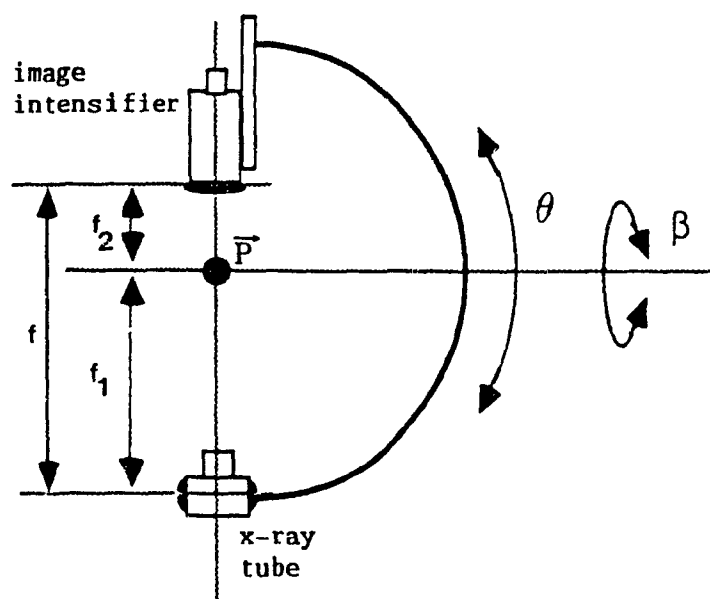


Figure 3.10 Schematic representation of c-arm showing relevant geometric parameters.



### 3.4.3 Calibration

The calibration of the x-ray equipment as it is used in this procedure consists of estimation of both x-ray beam geometry and pin-cushion distortion in the DSA image. A description of the stereotactic frame used in calibrating the x-ray beam is presented in §3.4.3.1, and §3.4.3.2 describes the calibration technique. The correction technique for image pin-cushion distortion is given in §3.4.3.3.

#### 3.4.3.1 Description of the MNI stereotactic frame

The stereotactic frame used at the Montreal Neurological Institute (MNI) (Tipal 1989) is shown in Fig. 3.11 fitted with plexiglass plates on the anterior-posterior (x-axis) and lateral (z-axis) sides. On each plate there are four 0.5mm diameter steel pellet markers at the vertices of a square. The object coordinates of the fiducial markers in lateral and anterior-posterior plates are listed in Table 3.1. The image location of these fiducials in the angiogram is used to calibrate the x-ray beam geometry with respect to the object or stereotactic coordinate system in either anterior-posterior or lateral views. This physical arrangement of fiducial markers at geometric magnifications of 1.25 to 1.5 and a 154 mm image intensifier field size permits a range of  $\pm 7-10$  degree rotation in  $\theta$  from either of the biplane directions. Outside of this range the images will not contain the projections of all fiducial markers necessary for calibration. Although the frame's coordinate system uses the 'left-handed' convention, a 'right-handed' system is assumed throughout the rest of this chapter.

#### 3.4.3.2 X-ray beam geometry calibration

In order to reconstruct points from their images or re-project them into images of different views, the mapping of 3-d object points onto the 2-d image must be determined for each view. The 3-d to 2-d mapping can be modeled by a linear transformation in homogeneous coordinates (Sutherland 1974).

Referring to Fig. 3.9, the projected image plane coordinates of a point

Figure 3.11 Principle axes of stereotactic frame. Fiducial markers are indicated by small arrows.

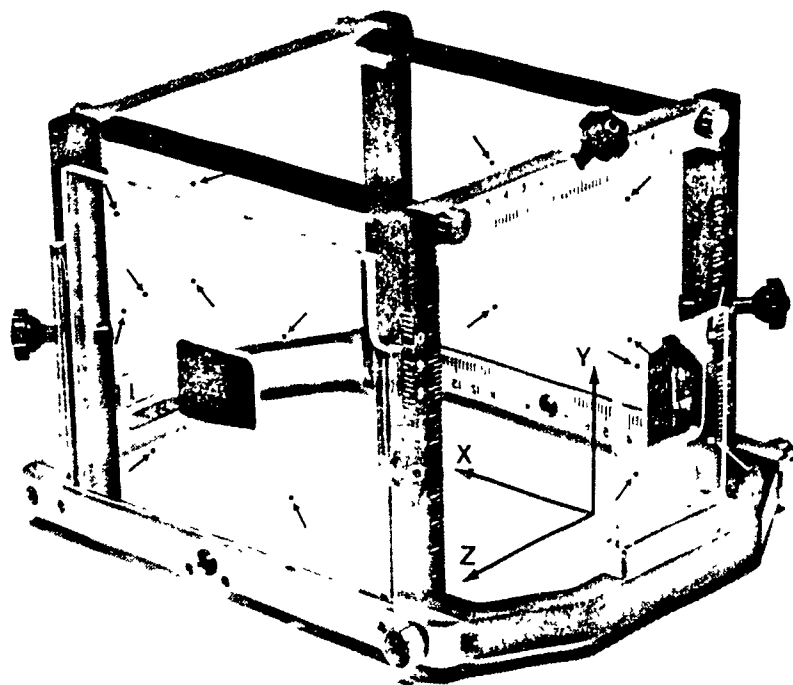


Table 3.1 3-d coordinates of fiducial markers in stereotactic frame.

Fiducial Marker Set	x [cm]	y [cm]	z [cm]
Lateral Proximal Plate	4.0	9.0	-9.0
	11.0	9.0	-9.0
	4.0	3.0	-9.0
	11.0	3.0	-9.0
Lateral Distal Plate	4.0	9.0	9.0
	11.0	9.0	9.0
	4.0	3.0	9.0
	11.0	3.0	9.0
Anterior Plate	-5.0	8.0	2.0
	-5.0	4.0	2.0
	-5.0	8.0	-2.0
	-5.0	4.0	-2.0
Posterior Plate	15.0	8.0	2.0
	15.0	4.0	2.0
	15.0	8.0	-2.0
	15.0	4.0	-2.0

P can be expressed in homogeneous coordinates as  $(x', y', h)$  where  $x = x'/h$  and  $y = y'/h$ . The mapping of point P,  $(x_o, y_o, z_o, 1)$ , onto its image can be then given by

$$(x', y', h) = (x_o, y_o, z_o, 1)[T] \quad (3.14)$$

where  $[T]$  is a  $4 \times 3$  matrix. The advantage of homogeneous coordinates is that a single matrix  $[T]$  can accomplish full coordinate transformation operations on P, such as perspective, rotation, translation, and scaling.

The elements of the transformation matrix  $[T]$  can be determined if the positions of the focal spot and image plane with respect to object space coordinate system are measured directly prior to imaging. The major disadvantage of determining the transformation in this way is that there is no way of knowing if any changes to the geometry have occurred during imaging. Instead the transformation matrix  $[T]$  may be calculated from the knowledge of a set of image projections of known 3-d points. This technique of computing  $[T]$  is called view calibration (Sutherland 1974). If  $T_1^{\rightarrow}$ ,  $T_2^{\rightarrow}$ , and  $T_3^{\rightarrow}$  are the column vectors of  $[T]$ , then each known point gives rise to two equations:

$$\left. \begin{aligned} (x_o, y_o, z_o, 1)(T_1^{\rightarrow} - xT_3^{\rightarrow}) &= 0 \\ (x_o, y_o, z_o, 1)(T_2^{\rightarrow} - yT_3^{\rightarrow}) &= 0 \end{aligned} \right\} \quad (3.15)$$

For  $k$  known points, the corresponding pairs of (3.15) can be represented in matrix form as

$$[A][T'] = t_{43}[B] \quad (3.16)$$

where  $[A]$  is a  $2k \times 11$  matrix,  $[T']$  is a column matrix containing eleven of the twelve elements of the matrix  $[T]$ ,  $[B]$  is a  $2k$  column matrix, and the twelfth matrix element  $t_{43}$  is a scaling factor. This scaling factor is typically set to unity without loss of generality. Eleven equations are needed to solve for  $[T']$  and thus six or more points give rise to an over-determined system which can be solved in a least squares sense using a generalized inverse (Strang 1980),

$$[T'] = ([A]^t[A])^{-1}[A]^t[B] \quad (3.17)$$

The constants of  $[T']$  can be determined if there are at least 6 known 3-d object points in the image with the restriction that no more than four

object points should be coplanar and that no more than three of the imaged points be collinear (Adams 1981). In stereotactic applications, the necessary system of control points is provided by the fiducial plates of the stereotactic frame (§3.4.3.1).

Each plate of the stereotactic frame consists of 4 distributed fiducial markers with known spatial coordinates defining the object space in the frame (Table 3.1). As the stereotactic frame is also imaged during the DSA examination, the result is that the image displays a set of 8 easily identified spots at the periphery of the image (Fig. 3.12). Fig. 3.12a), b), and c) show photographs corresponding to typical DSA mask images of lateral, lateral stereo, and anterior-posterior views of the head and fiducial plates of the stereotactic frame. It is not necessary that the center-line of the x-ray beam be perpendicular to the face of the frame, merely that all 8 of the markers be distinguishable within the image.

The observer using a track-ball controlled graphics cursor enters the position of the 8 fiducial points in each displayed image. The transformation  $[T']$  for each view is computed and stored for later use in the reconstruction and re-projection operations described in §3.4.6.

#### 3.4.3.3 Image pin-cushion distortion correction

DSA images suffer from image pin-cushion distortion and as a result objects near the edges of the image are selectively magnified compared to its size in the center of the field (§2.4.6). The degree of image pin-cushion distortion will depend primarily on the input phosphor curvature and this will be different for each tube manufacturer.

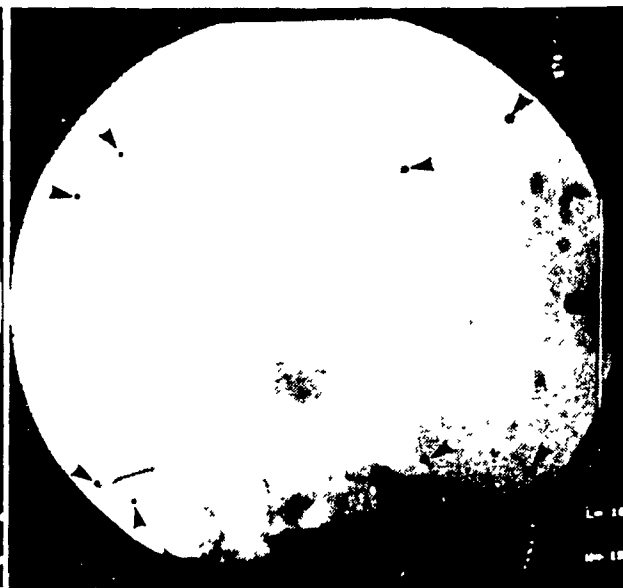
To correct for pin-cushion distortion a plexiglass tablet with an embedded 1cm-grid of copper wires is imaged prior to examination (Fig. 3.13). The distortion patterns for lateral, lateral stereo, and anterior-posterior views shown in Fig. 3.13 are different because of the changing interaction with the earth's magnetic field on the electron optics of the image intensifier as the c-arm assembly is rotated to each view. Since the distortion cannot be described by a simple analytic function,



Figure 3.12 Mask images of the head and the stereotactic frame. Images of the 8 fiducial markers are indicated by small arrows.

a) Lateral view

b) Lateral stereo view



c) Anterior-posterior view

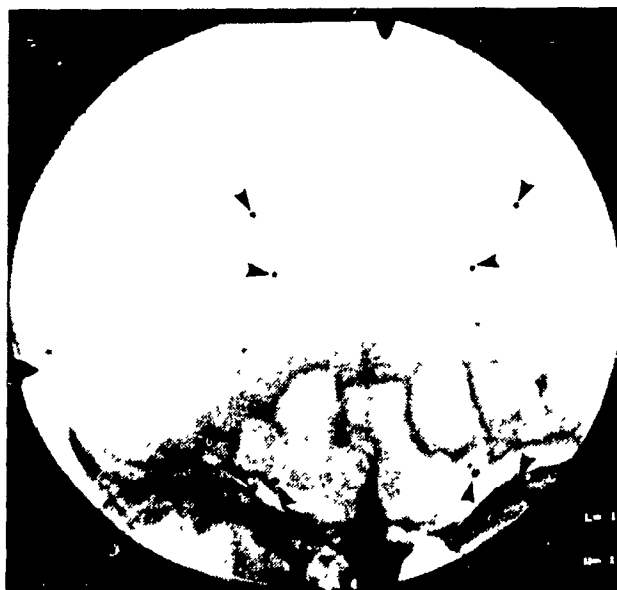
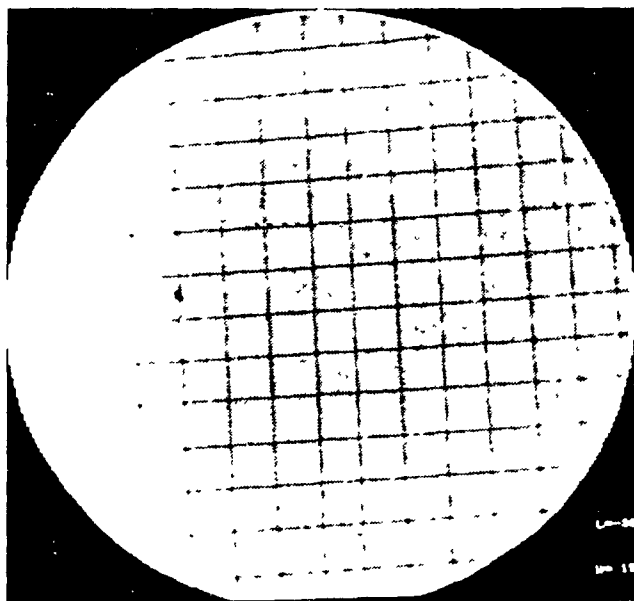
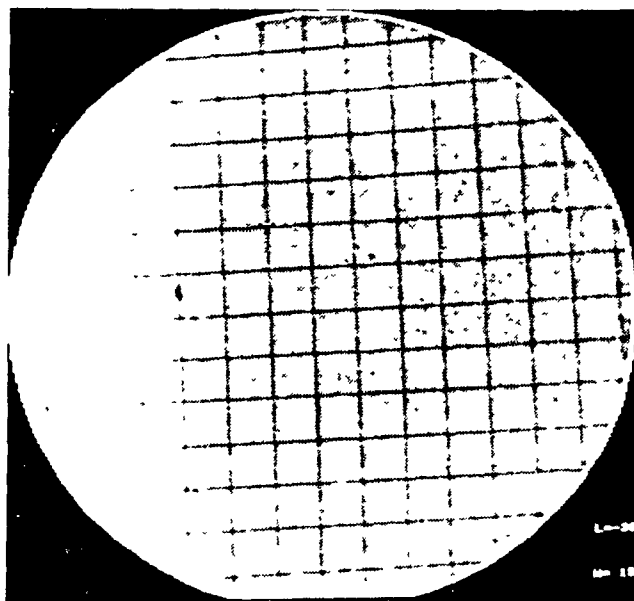


Figure 3.13 Pin-cushion distortion pattern in subtracted images of a cm wire-grid. Grid imaged with a 231mm Philips CsI image intensifier operating in its 154mm mode. The image matrix size is 512 x 512.

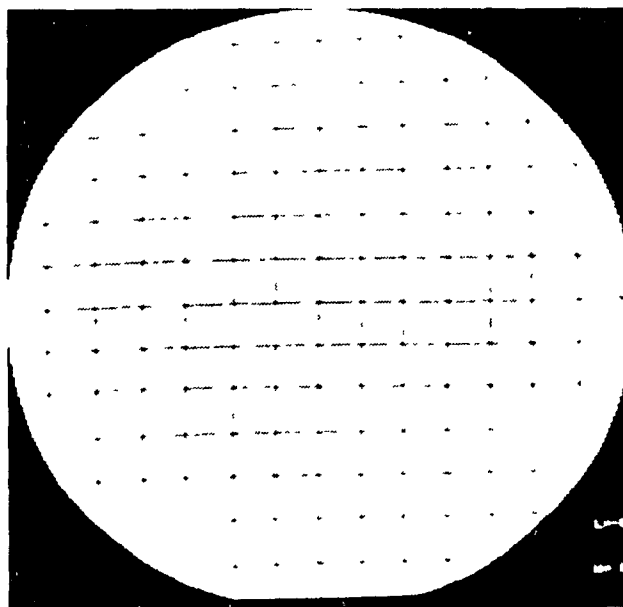
a) Lateral view



b) Lateral stereo view



c) Anterior-posterior view



Kooijman's technique (Kooijman et al. 1982) was chosen from those reviewed in §2.4.6. The implementation of their method is described below.

This technique's implementation is semi-automated. The observer starts by indicating the four corners of the grid square at the center of the image, indicated by the small cross hairs in Fig. 3.14a). The computer then calculates the positions of the undistorted grid intersection points (Fig. 3.14b). To measure the correction vectors, the coordinates of the wire-grid intersections need to be detected. The detection algorithm uses two facts. First, intersections of wires distinguish themselves by a low pixel value compared to the background, and secondly the positions of corresponding ideal and wire grid intersections are in close proximity of each other. Wire-grid intersections are detected by searching the image for a local minimum in a 15x15 window centered at each of the ideal grid intersection positions. The correction vectors are then stored in a look-up table according to the location of the point the correction represents. Fig. 3.14c) shows the correction vector for each wire-grid intersection point.

#### 3.4.4 3-d display of stereo DSA images

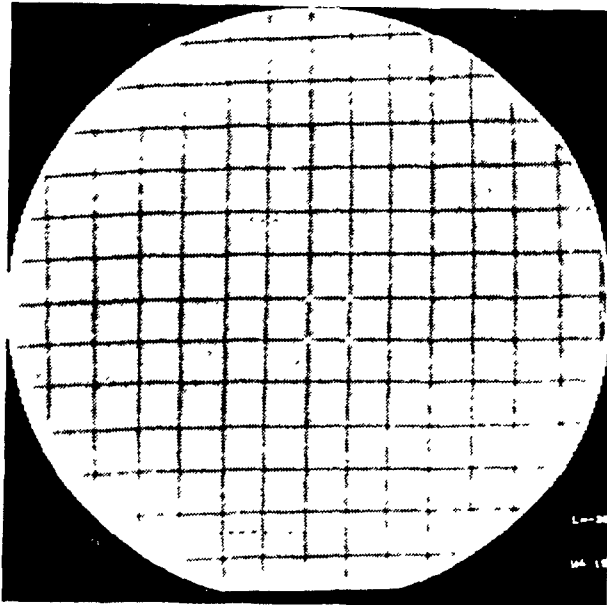
In this work a c-arm rotation technique is used to acquire stereo images in DSA. Fig 1.2 shows photographs of representative stereo digital subtraction angiograms in lateral and anterior-posterior directions. The stereo pair in both anterior-posterior and lateral views is obtained by rotating the c-arm assembly by  $|\Delta\theta|=7$  degrees in each view. The stereoscopic impression of depth created by the resulting image pair was found to be sufficient for the purposes of resolving continuity of vessels at crossings with other vessels.

A number of CRT-based displays for 3-d viewing of stereo angiograms is possible. Fig. 3.15 presents a generic tree of some of the more interesting CRT stereo display systems. These systems do not provide directly viewable stereoscopic images, a special apparatus is required to permit each eye to see only the image intended for it.

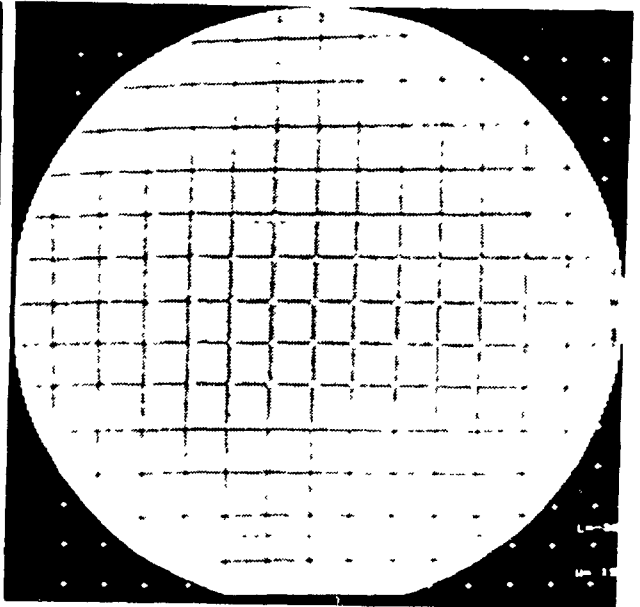
Time parallel systems are characterized by the simultaneous presentation

Figure 3.14 a to c) Step by step illustration of pin-cushion calibration technique.

a) Indication of center square in distorted grid image.



b) Prediction of undistorted grid intersections in image.



c) Computed correction vector at each wire-grid intersection point in the image.

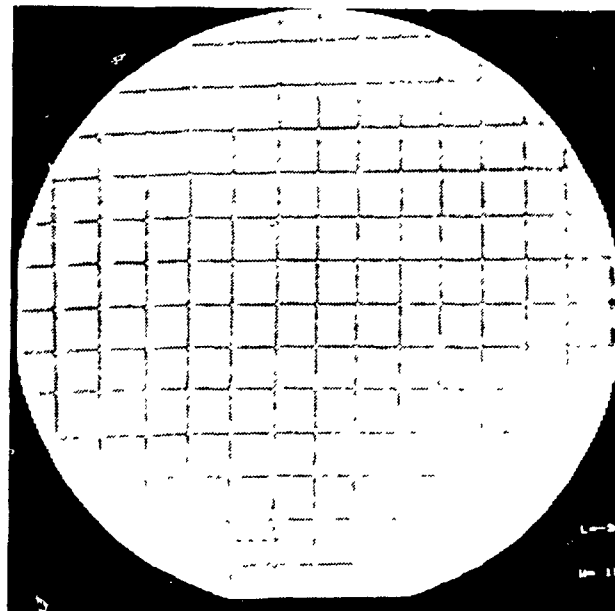
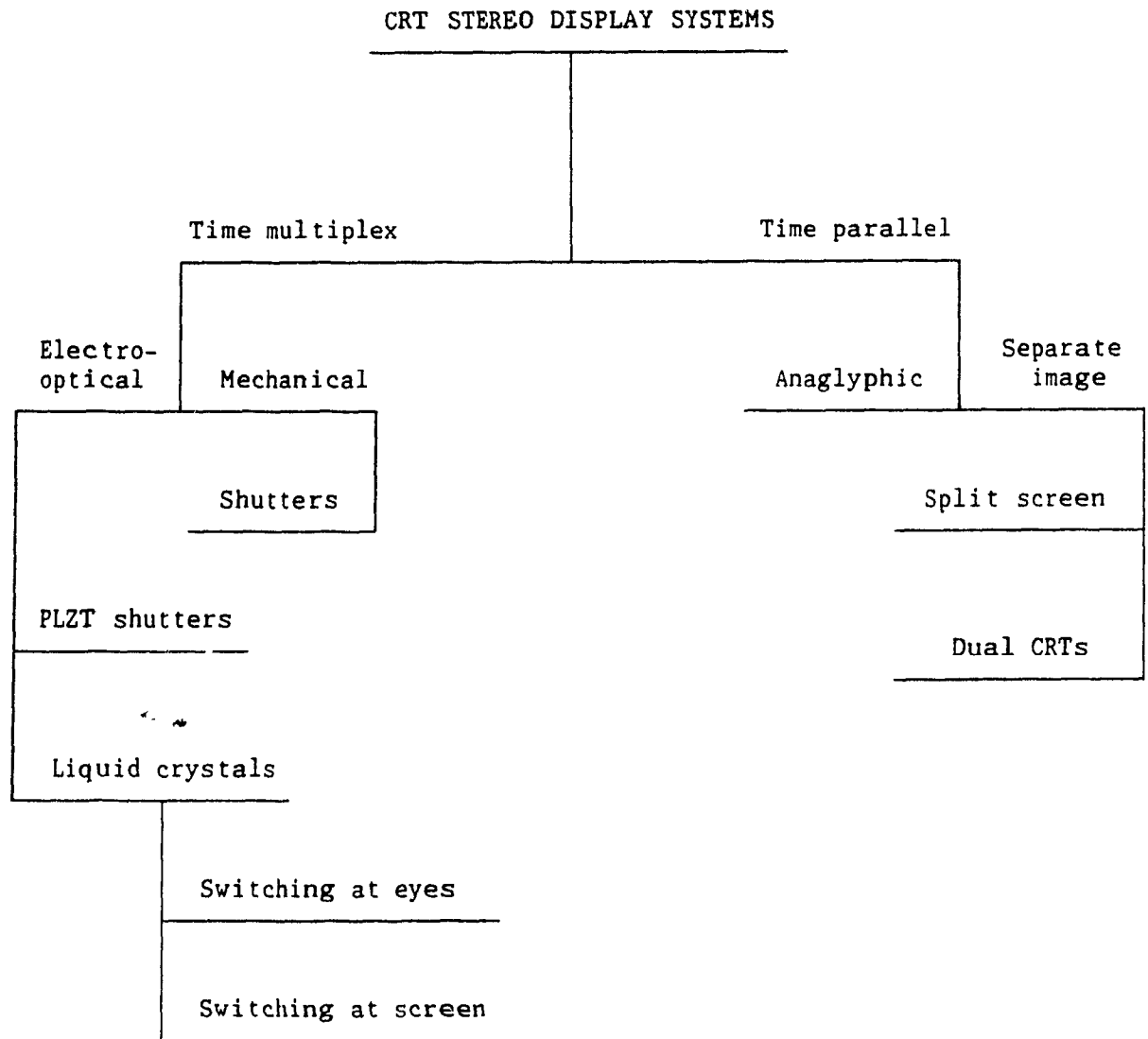


Figure 3.15 Generic tree for CRT stereoscopic display systems. (After Hodges and McAllister 1985)



of left- and right-eye views. A well known example of a time parallel system is the 'anaglyph' display in which the two images of the stereo pair are displayed on the same CRT using complementary colours. The observer then views the images through glasses with filters matching the complementary colours (Von Helmholtz 1925; Wolvin 1967; Ferguson 1968). Other examples of time parallel systems present views side by side on a single CRT screen or on adjacent CRT screens. These systems require either reflective or optical means to deliver the correct view to each eye (Ortony 1970; Sand 1984; Dietz and Kuhn 1980; Herman 1986).

Time multiplexed systems are characterized by rapidly presenting alternate left- and right-eye views on a single CRT display. To synchronize the views to the correct eye a shutter mechanism is employed. Systems have evolved from heavy mechanical shutters (Lane 1982) to lighter weight shutters with faster switching times. The later are typically constructed using either lead lanthanum zirconate titanate (PLZT) electrooptic ceramics or liquid crystal panels (Roese and Turner 1976; Lipton and Meyer 1984; Hodges and McAllister 1985). Alternatively, the shutter mechanism can be placed directly in front of the CRT and the observer views the images through a pair of polarized glasses (Tektronix 1989). An example of the medical application of this display technology is described by Herman (1986).

The inconvenience and restraint of wearing a viewing device has led to the development of autostereoscopic displays. Examples of systems that do not require a special viewing device include: lenticular displays (Meacham 1986) and Fresnel displays (Rudell and Sheima 1983).

Of the different stereo CRT viewing systems considered a colour anaglyph display was selected for this work on the basis of availability, cost, and ease of implementation. A dual monitor/polarizing screen approach was tried and abandoned because of difficulties in matching the brightness and geometrical distortion of the two channels. §3.4.4.1 presents details of the implementation of an anaglyph display system.

#### 3.4.4.1 Implementation of colour anaglyph method

There are essentially two schemes by which a stereo pair can be displayed as an anaglyph. The first is to add the stereo image pair together 'temporally' by switching alternately left and right images and modifying the colour map look-up-table (LUT) according to the display image's designated colour. The colours commonly used in stereo anaglyphs are red and blue. This means of presentation requires a separate image frame buffer for each image or one image frame buffer large enough to accommodate the two images. Furthermore, unless the alternate images are presented at normal frame rates (e.g. 60 cycles per second) the resulting 'flicker' can be disturbing to the observer.

The other method to present anaglyphs on CRTs is to 'spatially' sum the left and right images. The images are processed in order that each image does not change its intensity value when added to the other the images. Processing consists of first selecting  $N/2$  bit range of pixel values from each image where  $N$  is the total number of input bits to the colour map LUTs. In this case the display processor being used (Lexidata 3400, Lexidata Corp.) offers red and blue LUTs of 1024 channels each, hence  $N=10$  and the images must be reduced to 5 bits each. By 'windowing' (§2.3.3) the image, the 5 bits that 'best' represent the angiogram can be selected. Because of different levels of image background in the angiogram, some regions of the image may be thresholded out of the 5 bit image. Next, the red and blue LUTs, each 1024 channels, are divided into 32 bands of 32 channels each. In the red LUTs, each band is linearly ramped with values ranging from 0 to 255 (Fig. 3.16). In the blue LUTs, each band has a level value that starts at 0 for the first band and steps up to 255 for the last band with 31 steps of height 8 between the first and last bands (Fig. 3.16). With both LUTs set, the pixel values of the left image (red LUTs) are divided by 32. The blue image pixel values are scaled to form multiples of 32. Modifying the images and the LUTs in this way allows the images to be overlapped when added to each other. Though the dynamic range in the images is reduced by a factor of 32, this is acceptable for digital subtracted cerebral angiograms. Fig. 3.17 shows an example of angiograms processed for anaglyph presentation.

Figure 3.16 Definition of bit-plane values of colour map look-up-table (LUT) locations for 'Red-Blue' anaglyph image presentation. Green LUTs are set to zero.

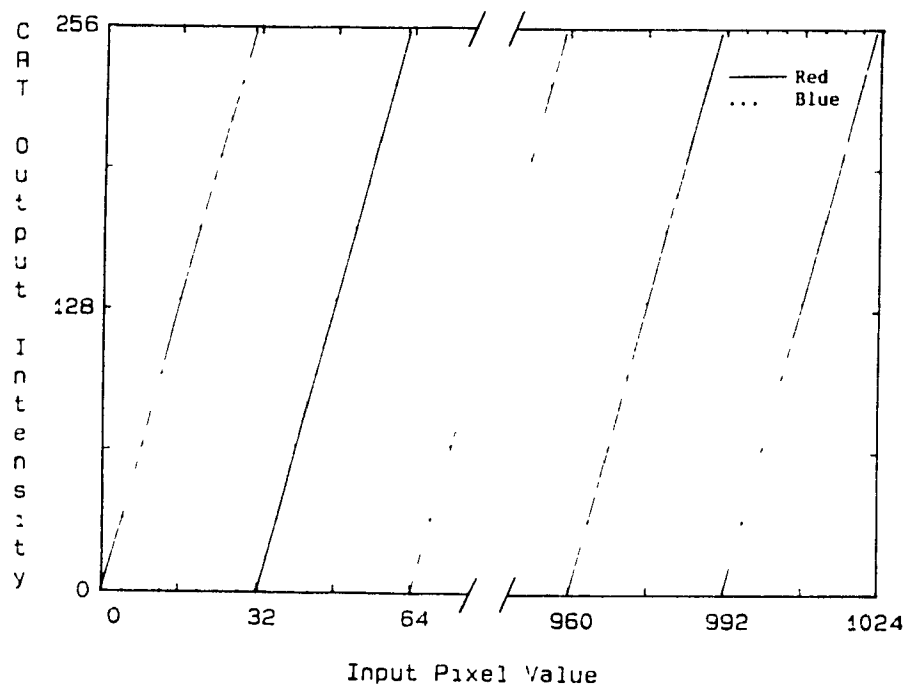
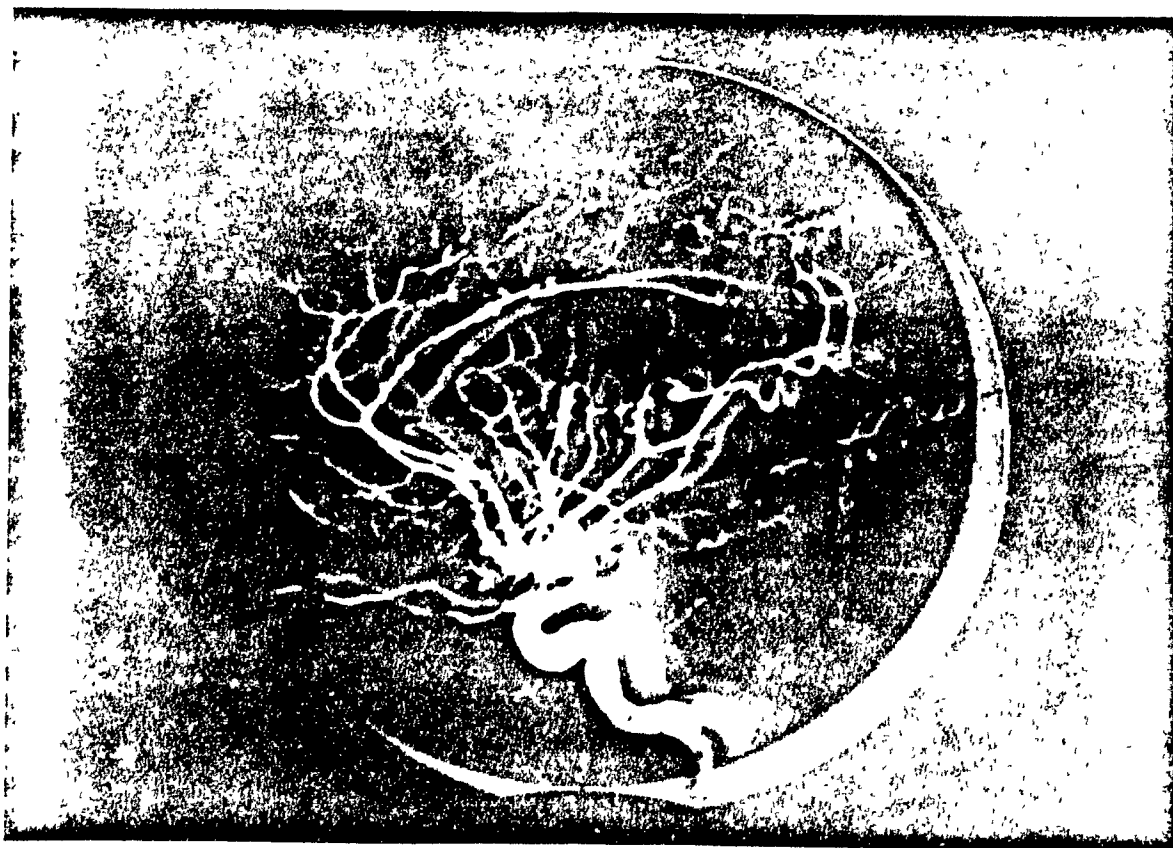


Figure 3.17 Stereoscopic DSA image pair presented as a 'Red-Blue' anaglyph image.





### 3.4.5 Tracking of vessels in DSA images

If complete and homogeneous filling of the artery with contrast agent is assumed, equation (2.4) indicates that the grey-level intensity in the subtraction image is proportional to irradiated vessel thickness. For a circularly-cylindrical artery with its main axis orthogonal to the x-ray beam, this means that the intensity values show a maximum in the center of the projected artery (Brown et al. 1977). This is approximately so in most cases, thus the center-line of a vessel in an angiogram should adequately describe its structure. Furthermore, vessels in angiograms are separated from background by relatively sharp transitions in their grey-level values. The center-line of a vessel may be found either by manually tracing it directly or by computer measurement and tracking of local edge and line attributes of the vessel in the angiogram. Although manual tracing is quite simple, it can be a time consuming if many vessels are to be traced.

Any attempt to automate vessel segmentation in angiograms is faced with problems of noise and the complex 3-d structure of the vessels. Vessels may be obscured at crossings as arteries of the 3-d system intersect in the 2-d projection or vessels may be poorly visible if iodine contrast is low. Usual simple segmentation techniques such as thresholding are not applicable to angiograms (Suetens et al. 1983). This is because the grey-level intensities of vessels are not constrained to a unique range of values. The use of spatially variant thresholds showed little improvement in vessel segmentation (Suetens et al. 1983). Unimodal grey-level profiles are not always sufficient to uniquely characterize vessels in an angiogram, and other features need to be considered in segmentation. In addition to (i) grey-level intensity, other features may include: (ii) grey-level intensity continuity, (iii) linearity, vessels are thin and elongated structures which join to form a tree-like object, or exhibit (iv) 'connectedness.'

Most vessel segmentation techniques reported to date have consisted of the detection and sequential tracking of vessel features (i-iv) in an angiogram. Tracking usually consists of point to point 'line-following' guided by the assumed connectivity of the detected feature(s) in the image of the vessel. Given a point on the vessel center-line, the next point is

searched for in an area expected to contain the continuation. This area can be either a fixed size or adjusted according to previously determined points. A number of such segmentation techniques have been implemented where tracking is guided by local intensity maxima at vessel center-lines (Gerbrands et al. 1982; Stevenson et al. 1987), continuity of vessel contrast profiles (Hoffmann et al. 1986; Kitamura et al. 1988), and continuity of vessel center-line, width, orientation, and intensity (Sun 1989). The task of vessel tracking has also been addressed using dynamic programming techniques (Parker et al. 1985; Dallas and Roehrig 1987).

Such techniques are capable of detecting thin straight vessel segments in an angiogram. Tracking is less reliable for vessels that follow sharp turns, or fold over themselves, and for small vessels where noise is a factor. Segments of such vessels in angiograms may prove to be difficult to extract because it may no longer possess the 'linear' or other features (i-iii) that the detection operators are expecting.

Another approach to the segmentation problem is to separate the vessel detection and tracking operations. Nguyen and Sklansky (1986) describe a technique that attempts to detect all maximum grey-level pixels that may form a vessel's center-line. Only those points with similar attributes are then merged and tracked. At each candidate point, the direction of the vessel segment, vessel boundaries, and grey-level value are measured and stored as local properties attributed to that point. Attributes can be weighted to emphasize certain properties depending on the application. Other examples of this approach are described by Fukui et al. (1980) and Collorec and Coatrieux (1988). The main advantage of this 'bottom-up' approach to vessel segmentation is that it is less sensitive to vessel superposition and foreshortening than the previous 'top-down' approach. However, problems occur with small vessels where grey-level profiles are no longer unimodal, and vessel boundaries may be difficult to detect because of low contrast and noise in the image.

The sources of these limitations occur more frequently in cerebral angiography than in coronary angiography for which most of the described methods were intended. Improved reliability and accuracy in vessel

segmentation techniques are needed before they can be used routinely in clinical studies. Recently, rule-based expert systems have been proposed to guide segmentation of geometrically complex vessels in an attempt to unambiguously detect and identify all vessels (Ritchings et al. 1985; Stansfield 1986; Smets et al. 1988). Although the use of expert systems looks promising, precise tracking of geometrically complex vessels is presently still reserved to the domain of the experienced human observer.

### 3.4.6 Reconstruction and re-projection algorithms

With two images given by transformation matrices  $[T]$  and  $[U]$ , and the coordinates of the corresponding points in each image  $(x_a, y_a)$  and  $(x_b, y_b)$ , the coordinates of the 3-d object point  $(x_o, y_o, z_o)$  can be reconstructed. In addition, re-projection operations on 3-d points are also possible if the desired view transformation matrix  $[T]$  is known. The mathematics of the reconstruction and re-projection operations are described below.

For any  $(x, y)$  and matrix  $[T]$ , (3.15) describes two planes whose intersection gives the equation of a line in 3-d object coordinates along which the real object point must lie. After the transformation matrices  $[T]$  for view 'A' and  $[U]$  for view 'B' are determined and the corresponding point pair  $(x_a, y_a)$  and  $(x_b, y_b)$  is given, the two lines can be constructed whose intersection gives the location of the real point in object space coordinates. The four equations arising from (3.15) can be written in matrix form as

$$\begin{bmatrix} t_{11}-t_{13}x_a & t_{21}-t_{23}x_a & t_{31}-t_{33}x_a \\ t_{12}-t_{13}y_a & t_{22}-t_{23}y_a & t_{32}-t_{33}y_a \\ u_{11}-u_{13}x_b & u_{21}-u_{23}x_b & u_{31}-u_{33}x_b \\ u_{12}-u_{13}y_b & u_{22}-u_{23}y_b & u_{32}-u_{33}y_b \end{bmatrix} \begin{bmatrix} x_o \\ y_o \\ z_o \end{bmatrix} = \begin{bmatrix} t_{43}x_a-t_{41} \\ t_{43}y_a-t_{42} \\ u_{43}x_b-u_{41} \\ u_{43}y_b-u_{42} \end{bmatrix} \quad (3.18)$$

This matrix equation represents a system of 4 equations in 3 unknowns,  $(x_o, y_o, z_o)$ , which can be solved in a least squares sense by a generalized inverse (see 3.17). The transformation matrices can also be used to re-project 3-d points or to locate the auxiliary line of a 2-d point in another view.

Re-projection of a 3-d point  $(x_o, y_o, z_o)$  onto an image described by  $[T]$  can be computed from (3.15),

$$\left. \begin{aligned} x &= (t_{11}x_o + t_{21}y_o + t_{31}z_o + t_{41}) / h \\ y &= (t_{12}x_o + t_{22}y_o + t_{32}z_o + t_{42}) / h \\ h &= (t_{13}x_o + t_{23}y_o + t_{33}z_o + t_{43}) \end{aligned} \right\} \quad (3.19)$$

The display and interaction of 3-d data are discussed further in appendices A and B respectively.

The re-projection or back-projection of a 2-d point in one view onto a line in another view can also be reckoned from (3.18). Since (3.18) represents an over-determined system of 4 equations in 3 unknowns, it would be still possible to solve for  $(x_o, y_o, z_o)$  if one of its rows was dropped. Given  $(x_a, y_a)$  the point of interest in image 'A' and  $(x_b)$  the left edge of the image in 'B' are specified in (3.18), the matching system of 3 equations can be solved for  $(x_o, y_o, z_o)_l$ . This point is then projected through transform  $[U]$  to give  $(x_b, y_b)_l$ , the intersection of the projected 3-d line with the left edge of image 'B.' The process is repeated for the right edge of image 'B' to give  $(x_b, y_b)_r$ . The points  $(x_b, y_b)_l$  and  $(x_b, y_b)_r$  define the auxiliary line of  $(x_a, y_a)$  in image 'B.' In an analogous manner, an auxiliary line between the left and right edges in image 'A' can be constructed when  $(x_b, y_b)$  is specified.

If the two lines corresponding to image coordinate points  $(x_a, y_a)$  and  $(x_b, y_b)$  have parametric equations

$$\left. \begin{aligned} x &= x_1 + j_1 b & x &= x_2 + j_2 c \\ y &= y_1 + g_1 b & y &= y_2 + g_2 c \\ z &= z_1 + k_1 b & z &= z_2 + k_2 c \end{aligned} \right\} \quad (3.20)$$

then the minimum distance  $d$  between them is given by the expression

$$d = \frac{\begin{vmatrix} x_2 - x_1 & y_2 - y_1 & z_2 - z_1 \\ j_1 & g_1 & k_1 \\ j_2 & g_2 & k_2 \end{vmatrix}}{\left( \begin{vmatrix} j_1 & g_1 \\ j_2 & g_2 \end{vmatrix}^2 + \begin{vmatrix} g_1 & k_1 \\ g_2 & k_2 \end{vmatrix}^2 + \begin{vmatrix} k_1 & j_1 \\ k_2 & j_2 \end{vmatrix}^2 \right)^{1/2}} \quad (3.21)$$

where the vertical bars  $||$  denote the determinant of the matrix inside.

## CHAPTER FOUR

### GEOMETRIC RECONSTRUCTION FROM DSA IMAGE PAIRS: IMPLEMENTATION & EVALUATION

#### 4.1 Introduction

This chapter examines the reconstruction method described in chapter 3. Its scope is limited to determining reconstruction error dependence on both measurement errors and the correspondence algorithm.

The accuracy of 3-d point reconstruction from stereo and biplane image pairs depends primarily on the error in the measurements of point and fiducial marker image pixel coordinates, and the assignment of point and marker correspondences. The work of Sherlock and Aitken (1980) details the relationship of reconstruction error to measurement error in x-ray film systems with long focal length (i.e. greater than 2m). Its applicability to digital subtraction angiography (DSA), where focal lengths are short (i.e. between 1-2m), is uncertain. Similarly, the contribution of fiducial image measurement errors to reconstruction error is also not known. For these reasons, the sensitivity of reconstruction to measurement errors is examined under conditions similar to those found in cerebral DSA (see §3.4.2 and §3.4.3.1).

This chapter reports the results of experiments on the sensitivity of reconstruction accuracy to measurement errors in the image coordinates of the target or test points and in the image coordinates of the fiducials (§4.2). §4.3 reports on the results of experiments with the correspondence algorithm, and §4.4 concludes the chapter with a discussion of results and possible further refinements to this method.

#### 4.2 Reconstruction sensitivity to measurement error

This section describes the methodology and results of experiments that examine reconstruction sensitivity to measurement error. The geometry of reconstruction and definitions of error measures are described in §4.2.1 and

§4.2.2 respectively. The possible sources of measurement error are outlined in §4.2.3.

Occurrence of measurement errors in both the image coordinates of the fiducial markers and test points in actual measurements of accuracy make separate examination of these two contributions to reconstruction error difficult. For this reason reconstruction is simulated numerically on a VAX 11/750 computer. §4.2.4 and §4.2.5 respectively report the results of computer simulation experiments on the effect of measurement error in image coordinates of test points and fiducials on reconstruction. These results are compared with actual measurements of accuracy made on a test phantom described in §4.2.6.

#### 4.2.1 Reconstruction coordinate system

Fig. 4.1 sketches the reconstruction coordinate system used throughout this chapter. Referring to Fig. 4.1, a test or target point  $P^{\rightarrow}$  is projected into two images 'A,' and 'B.' The image of  $P^{\rightarrow}$  in each respective view is measured by the coordinates  $(x_a, y_a)_p$  and  $(x_b, y_b)_p$ . The isocenter is designated by point  $O^{\rightarrow}$  located at (7.5cm, 6cm, 0cm) in the stereotactic coordinate system (§3.4.3.1) and is also the point from which the geometric magnification is computed (§2.4.2). For purposes of discussion all references to test point and fiducial marker coordinates are made from the reconstruction coordinate system. The rotation angle of a view or projection is given by  $\theta$  about  $O_y$ , the axis of rotation of the c-arm assembly.

The projections of the lateral and the anterior-posterior fiducial points of the stereotactic frame are given by the image coordinates  $(x_a, y_a)_{lat,j}$  and  $(x_b, y_b)_{ap,j}$  respectively where  $j=1, \dots, 8$ .

#### 4.2.2 Definitions of error measures

Knowledge of the image coordinates of the fiducial markers allows the  $(x, y, z)$  coordinates of point  $P^{\rightarrow}$  to be estimated as  $P_e^{\rightarrow}$  from its image

Figure 4.1 Illustration of the geometry of the x-ray imaging system used in reconstruction.

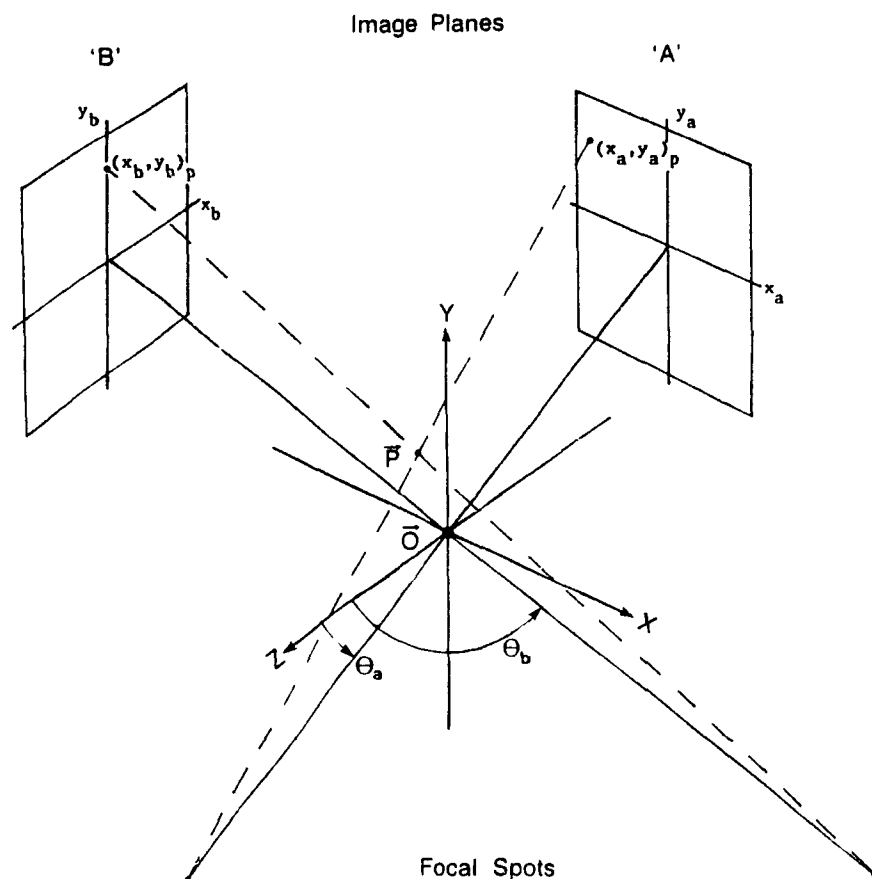


Table 4.1 Pixel widths and corresponding RMS error associated with 256, 512, and 1024 square image matrices for a 154mm image intensifier.

Matrix Size	Pixel Width [mm/pixel]	Uncertainty ±[mm]	RMS error ±[mm]
256 x 256	0.6	0.3	0.17
512 x 512	0.3	0.15	0.087
1024 x 1024	0.15	0.075	0.043



coordinates  $(x_a, y_a)_p$  and  $(x_b, y_b)_p$ . The error in  $P_e^{\rightarrow}$  is denoted by  $\Delta P^{\rightarrow}$ ,

$$\Delta P^{\rightarrow} = P^{\rightarrow} - P_e^{\rightarrow} = (\Delta x, \Delta y, \Delta z) \quad (4.1)$$

where  $\Delta x = x - x_e$ ,  $\Delta y = y - y_e$ ,  $\Delta z = z - z_e$

and by its norm or linear distance error D,

$$D^2 = \Delta x^2 + \Delta y^2 + \Delta z^2 \quad (4.2)$$

The uncertainty with which  $P^{\rightarrow}$  is reconstructed depends on the error in the measured image coordinates of the test point and the fiducial markers. The possible types of measurement errors are discussed in the following section.

#### 4.2.3 Sources of measurement error

Error in the measured image coordinates of projected test and fiducial points can arise from several sources. They are sampling or digitization, observation, correspondence, focal spot blur, image intensifier distortion, and patient motion.

Digitization error occurs because the image is finitely sampled (§2.4.5), hence the precision of the measured image coordinates is fundamentally limited by their pixel size. Table 4.1 lists the three most common pixel sizes for a 154mm image intensifier and their corresponding root-mean-square (rms) error on the assumption that digitization error is random (2.12).

Inaccurate localization of point image coordinates by either the observer or computer introduces error in the reconstruction. Error in the assignment of pixel coordinates is referred to here as observation error. It is expected that the likelihood of this error increases as the image feature (e.g. fiducial points, vessel center-points or lines) to be reconstructed becomes more complicated and observation requires more judgment. The statistical nature of observation error is assumed to be independent and normally distributed (Blume 1984).

Another source of measurement error is correspondence error, the incorrect classification or matching of pixel pairs. The character of this

error depends on the correspondence algorithm used. For the purposes of this section correspondence error is included in the class of observation errors.

The effect of finite focal spot size (§2.4.2) and image intensifier pin-cushion distortion (§2.4.6) also contribute to measurement error. Whereas digitization and observation errors are essentially random, focal spot blur and pin-cushion distortion are systematic. These errors can be minimized by reducing geometric magnification in case of focal spot blur and by using a grid technique (§2.4.6 and §3.4.3.3) for pin-cushion distortion correction.

The last potential source of measurement error is patient movement (§2.4.7). Patient motion during a DSA examination produces registration artifacts which makes it more difficult for the observer or the computer to correctly 'observe' the image coordinates of the fiducials or the vessel center-lines. §2.4.7 outlines the different techniques that can be used to reduce artifacts. Since the fiducial markers also move with patient head motion and providing all fiducial markers are visible in the image, patient motion will not result in any calibration error. Although for individual frames calibration may be different.

Of these types of measurement error, digitization and observation errors are of most concern. These errors are studied in the following sections.

#### 4.2.4 Measurement error in image pair coordinates

The sensitivity of 3-d point reconstruction to measurement error in the target or test point image coordinates can be characterized by general analytical expressions for  $\Delta P^{\rightarrow}$  (§4.2.4.1) and by simulating errors numerically for a known  $P^{\rightarrow}$ ,  $(x_a, y_a)_p$ , and  $(x_b, y_b)_p$  (§4.2.4.2). It is assumed that there are no uncertainties in the image coordinates of the fiducial markers.

##### 4.2.4.1 Theory

The propagation of error can be expressed in terms of a Taylor expansion

of the reconstruction equations or in terms of the root-mean-square error. Both are considered below.

The Taylor expansion to the first order of the coordinates of  $P_e^{\rightarrow}$  about the true or actual values of the image coordinates of point  $P^{\rightarrow}$  is given by

$$\Delta P^{\rightarrow} = \begin{pmatrix} \Delta x \\ \Delta y \\ \Delta z \end{pmatrix} = \begin{pmatrix} \partial x / \partial x_a & \partial x / \partial y_a & \partial x / \partial x_b & \partial x / \partial y_b \\ \partial y / \partial x_a & \partial y / \partial y_a & \partial y / \partial x_b & \partial y / \partial y_b \\ \partial z / \partial x_a & \partial z / \partial y_a & \partial z / \partial x_b & \partial z / \partial y_b \end{pmatrix} \begin{pmatrix} \Delta x_a \\ \Delta y_a \\ \Delta x_b \\ \Delta y_b \end{pmatrix} \quad (4.3)$$

where  $\Delta x_a$ ,  $\Delta y_a$ ,  $\Delta x_b$ , and  $\Delta y_b$  are the uncertainties in the measured image coordinates. The Jacobian matrix evaluated for the special case of  $P^{\rightarrow}$  at the origin and symmetrical projection angles  $\Theta = -\Theta_a = \Theta_b$  (Sherlock and Aitken 1980) is equal to

$$1/(2M) \begin{pmatrix} \sec(\Theta) & 0 & \sec(\Theta) & 0 \\ 0 & 1 & 0 & 1 \\ -\csc(\Theta) & 0 & \csc(\Theta) & 0 \end{pmatrix} \quad (4.4)$$

where  $M$  is the geometric magnification. The dependence of  $\Delta x$  and  $\Delta z$  with the angle of projection are respectively functions of the secant and cosecant of  $\Theta$ ,  $\Delta y$  is independent of  $\Theta$ . From (4.4) it is evident that reconstruction error will be mostly in the 'z' coordinate for projection angles ( $2\Theta$ ) less than 60 degrees and that as  $2\Theta$  approaches 90 degrees,  $\Delta x$  and  $\Delta z$  become equal in magnitude.

$\Delta P^{\rightarrow}$  as expressed by (4.3) gives a pessimistic estimate of reconstruction error. The probability of a number of uncertainties combining in magnitude and direction to give the worst possible result for  $P_e^{\rightarrow}$  is small. For this reason the root-mean-square (rms) error is used. The rms error in  $P_e^{\rightarrow}$  is given by  $P_{rms}^{\rightarrow}$ ,

$$(P_{rms}^{\rightarrow})^2 = \begin{pmatrix} x_{rms}^2 \\ y_{rms}^2 \\ z_{rms}^2 \end{pmatrix} = \begin{pmatrix} \sum_i [(\partial x / \partial d_i) d_{i,rms}]^2 \\ \sum_i [(\partial y / \partial d_i) d_{i,rms}]^2 \\ \sum_i [(\partial z / \partial d_i) d_{i,rms}]^2 \end{pmatrix} \quad (4.5)$$

$d_i: (x_a, y_a, x_b, y_b), i = 1, \dots, 4$

Substituting the known partial derivatives from (4.4),  $P^{\rightarrow}_{rms}$  for the case of  $P^{\rightarrow}$  at the origin and symmetrical projection angles is

$$P^{\rightarrow}_{rms} = 1/(2M) \left[ \begin{array}{c} (x_{a,rms} \sec(\theta))^2 + (x_{b,rms} \sec(\theta))^2 \\ (y_{a,rms})^2 + (y_{b,rms})^2 \\ (x_{a,rms} \csc(\theta))^2 + (x_{b,rms} \csc(\theta))^2 \end{array} \right]^{1/2} \quad (4.6)$$

The dependence of  $x_{rms}$  and  $z_{rms}$  with the angle of projection are functions of the squares of the secant and cosecant of  $\theta$ ,  $y_{rms}$  is independent of  $\theta$ . Still, uncertainty in  $z_e$  is dominant for small angles and as  $2\theta$  approaches 90 degrees,  $x_{rms}$  and  $z_{rms}$  become equal in magnitude.

The partial derivatives used in these equations were derived for the special case of  $P^{\rightarrow}$  at the origin and symmetric projection angles. Sherlock and Aitken (1980) demonstrated that the Jacobian was adequate for points other than  $P^{\rightarrow} = (0,0,0)$ . Their work does not indicate if this also holds true under conditions in DSA of shorter focal lengths and asymmetric angles between projection pairs. These uncertainties are addressed by means of computer simulation experiments.

#### 4.2.4.2 Simulation experiments

The basic simulation experiment consists of substituting the actual numerical values of the image coordinates  $(x_a, y_a, x_b, y_b)$  of  $P^{\rightarrow}$  with  $(x_a \pm \Delta d, y_a \pm \Delta d, x_b \pm \Delta d, y_b \pm \Delta d)$  which are input to the reconstruction algorithm. The values of  $\Delta d$  are found by drawing four separate error terms randomly from a specified distribution of values. For digitization errors,  $\Delta d$  is drawn randomly from a uniform distribution of values  $\pm \Delta d_d$ , and for observation errors,  $\Delta d$  is randomly drawn from a normal distribution of values  $\pm (d_o)_{rms}$ . The reconstructed coordinates of  $P^{\rightarrow}_e$  are then compared to  $P^{\rightarrow}$ , and the residual errors are computed by (4.1). The basic trial is repeated  $N$  times and the rms error in  $P^{\rightarrow}_e$  is given by

$$(P^{\rightarrow}_{rms})^2 = (1/N) \left[ \begin{array}{c} \sum_j (\Delta x_j)^2 \\ \sum_j (\Delta y_j)^2 \\ \sum_j (\Delta z_j)^2 \end{array} \right] \quad (4.7)$$

The errors of the three coordinates are also combined to give a linear distance error  $D_{rms}$  (see 4.2). The angular separation between projection pairs is denoted by  $\Delta\theta$  (i.e.  $\theta_b - \theta_a$ ). Except for the error model described by (4.6), asymmetric incidences are assumed,  $\theta_b$  is varied and  $\theta_a = 0$  degrees.

The error model described by (4.6), the dependence of error on position of  $P^{\rightarrow}$ , on the magnitude of measurement error, and on the geometric magnification are examined using simulation.

#### 4.2.4.2.1 Expt. 1: Comparison of modeled and simulated error

Reconstruction error dependence on separation angle  $\Delta\theta$  for given measurement errors was simulated and compared to the errors calculated directly from (4.6).

Fig. 4.2 shows the dependence of  $D'_{rms}$ , distance error of  $P^{\rightarrow}_{rms}$ , on  $\Delta\theta$  for both digitization and observation errors using (4.6). The geometric magnification was held constant at a value of 1.25 where the focal length was 125cm. In Fig. 4.2a) reconstruction error versus angular separation is plotted for a digitization error of  $\Delta d_d = \pm 0.15\text{mm}$  (i.e. pixel size of 0.3mm) which corresponds to  $(d_d)_{rms} = \pm 0.087\text{mm}$ . Fig. 4.2b) shows the error plot for an observation error of  $\pm 1$  pixel, or  $(d_o)_{rms} = \pm 0.3\text{mm}$ . These error plots are compared to the values obtained by simulation using the same measurement errors for a point  $P^{\rightarrow}$  at the origin.

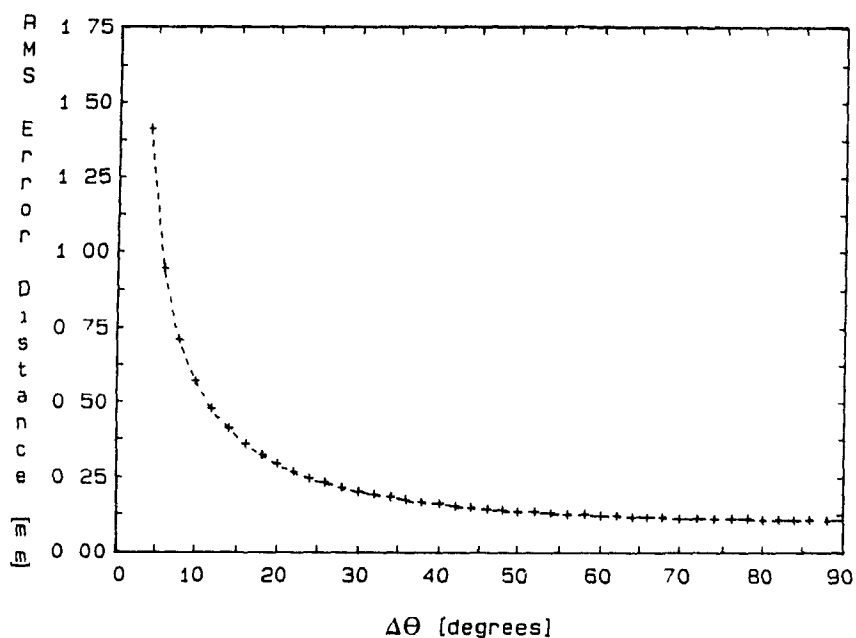
It was found that the difference between reconstruction errors determined analytically and by simulation decreased as the number of trials  $N$  in each simulation increased. The standard deviation in the rms error  $P^{\rightarrow}_{rms}$  is expressed by (Bevington 1969)

$$\sigma_i = P^{\rightarrow}_{rms,i} / (2(N-1))^{1/2} \quad \text{for } i = 1, 2, 3 \quad (4.8)$$

Fig. 4.3 shows the difference between reconstruction errors determined analytically and by simulation for  $N=10,000$  where  $\sigma_i = 0.007(P^{\rightarrow}_{rms,i})$ . Overall, good agreement of simulation with the model is observed in Fig. 4.3. At angles nearing 90 degrees, differences approach the round-off error

Figure 4.2  $D'_{rms}$  (determined analytically) in  $P_e^{\rightarrow}$  at the origin with a) a digitization error of  $(d_d)_{rms} = \pm 0.087\text{mm}$  and b) an observation error of  $(d_o)_{rms} = \pm 0.3\text{mm}$  in image coordinates of  $P^{\rightarrow}$ .

a) Digitization error,  $(d_d)_{rms} = \pm 0.087\text{mm}$



b) Observation error,  $(d_o)_{rms} = \pm 0.3\text{mm}$

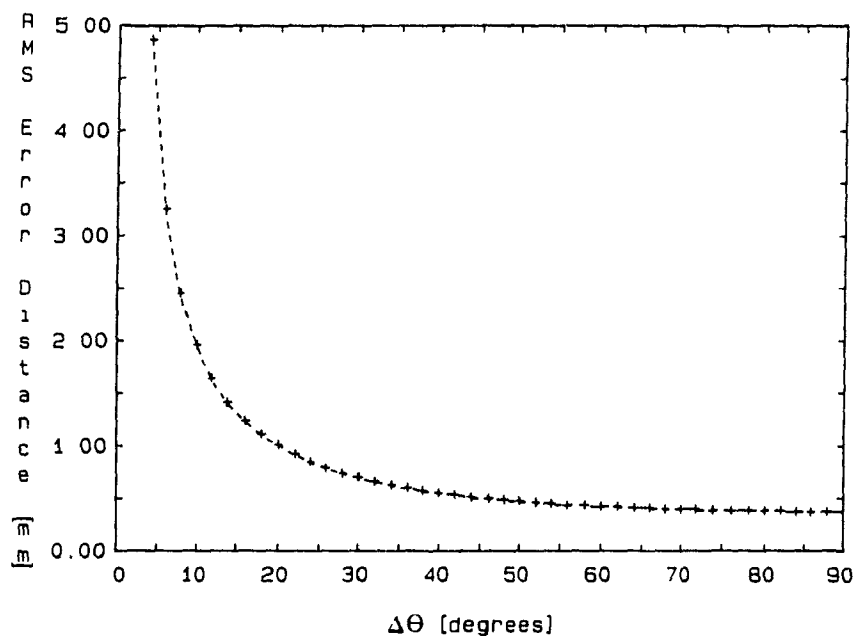
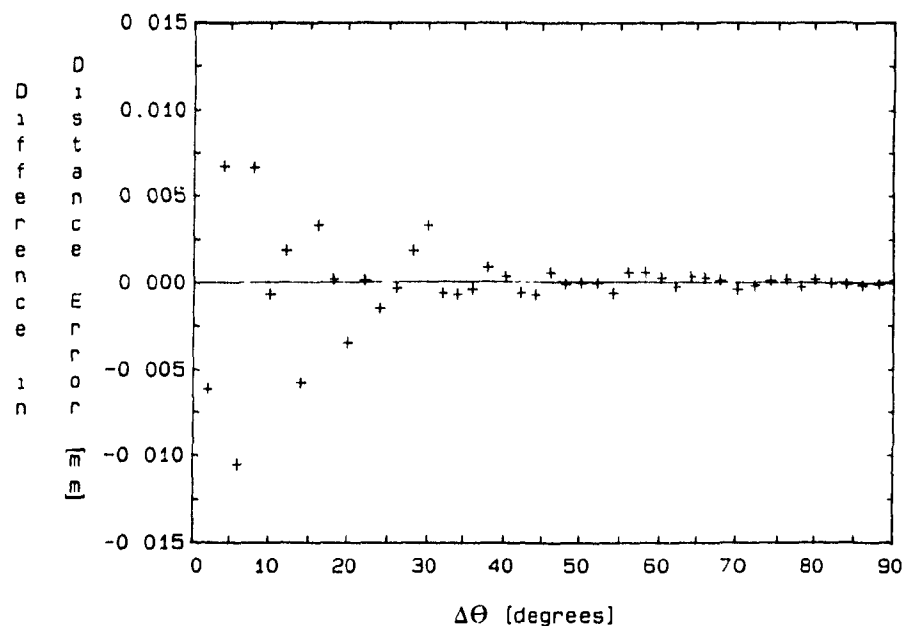
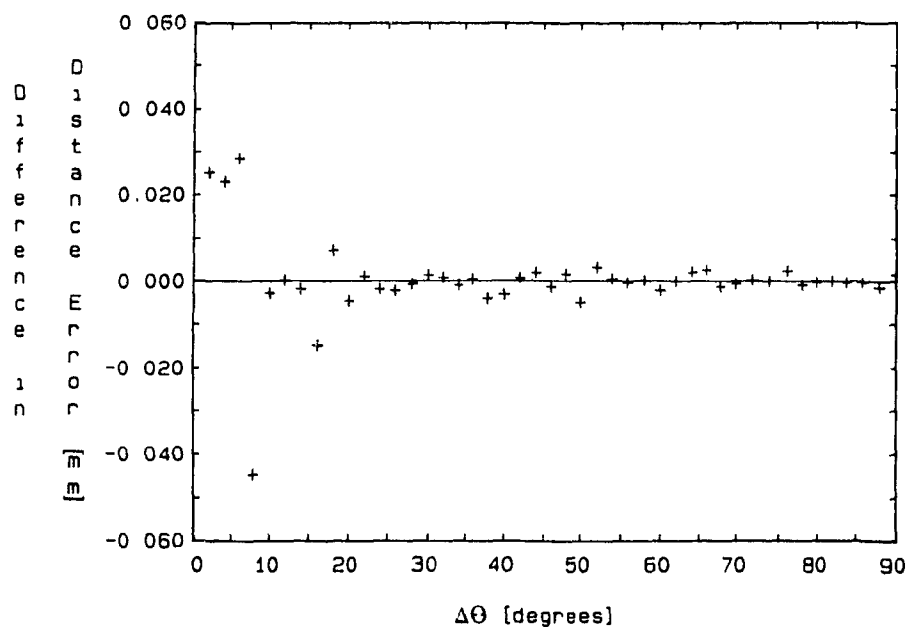


Figure 4.3 Difference between the distance error in  $P_e^{\rightarrow}$  determined analytically and by simulation ( $D'_{rms} - D_{rms}$ ) for  $P^{\rightarrow}$  at the origin given a) a digitization error of  $\Delta d_d = \pm 0.15\text{mm}$  and b) an observation error of  $(d_o)_{rms} = \pm 0.3\text{mm}$  in image coordinates of  $P^{\rightarrow}$ .

a) Digitization error,  $\Delta d_d = \pm 0.15\text{mm}$



b) Observation error,  $(d_o)_{rms} = \pm 0.3\text{mm}$



associated with the reconstruction which was determined to be  $\pm 0.001\text{mm}$  by computing  $D_{\text{rms}}$  for a measurement error equal to zero. At small angles ( $\Delta\theta < 20$  degrees) the differences in Fig. 4.3 are expectedly larger (4.8). Since the magnitudes of these differences are small in comparison to the magnitude of errors being examined, they can be ignored. Consequently  $N$  is set to 10,000 in all simulation experiments described below.

#### 4.2.4.2.2 Expt. 2: Dependence on position

Simulation was used to evaluate the reconstruction error for test points at locations other than the origin. Test points at locations on the line through  $\pm(5\text{cm}, 5\text{cm}, 5\text{cm})$ , representative of stereotactic space, were reconstructed. Rather than simulating measurement error for all angular separations,  $\Delta\theta$  was restricted to 5, 10, 15, and 90 degrees which represent the more likely projections in DSA stereotaxy. The geometric magnification was kept at 1.25 with a focal length of 125 cm. The distance error  $D_{\text{rms}}$  was computed for a typical measurement error consisting of combined digitization error of  $\Delta d_d = \pm 0.15\text{mm}$  and observation error of  $(d_o)_{\text{rms}} = \pm 0.3\text{mm}$ .

Fig. 4.4 shows that reconstruction error is reduced as the test point location moves away from the image plane. As magnification of the test point increases, the measurement error relative to the image coordinates of the point becomes smaller, and consequently reconstruction error is reduced. The percent difference in error between points reconstructed at  $\pm(5\text{cm}, 5\text{cm}, 5\text{cm})$  and the origin is approximately 10% for  $\Delta\theta = 5, 10$ , and 15 degrees and approximately 5% for 90 degrees. These differences are reduced by a factor of two at  $\pm(2\text{cm}, 2\text{cm}, 2\text{cm})$ . For small angles (i.e.  $\Delta\theta < 10$  degrees) and the above stated measurement error magnitudes, reconstruction error dependence on the location of the test point will be important. In contrast, for biplane pairs such differences can be ignored. The reconstruction error in each coordinate for  $P^{\rightarrow}$  at  $\pm(5\text{cm}, 5\text{cm}, 5\text{cm})$  and the origin is listed in Table 4.2. The rms error in each coordinate generally increases for test points closer to the image plane. For angles of  $\Delta\theta$  from 5 to 15 degrees the 'y' rms error component doesn't follow this trend since points away from the origin have image measurement errors that contribute to all three error components unlike measurement errors in (4.6). As the angle between projection pairs



Figure 4.4  $D_{rms}$  in  $P_e^{\rightarrow}$  at different positions given a digitization error of  $\Delta d_d = \pm 0.15\text{mm}$  and an observation error of  $(d_o)_{rms} = \pm 0.3\text{mm}$  in test point image coordinates.

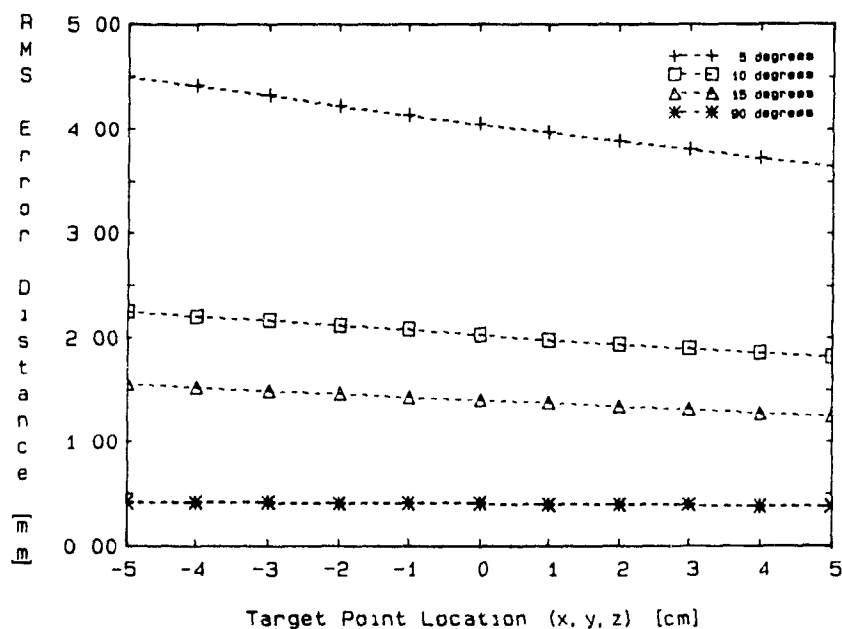


Table 4.2 RMS error in reconstructed coordinates for different angular separations given a digitization error of  $\Delta d_d = \pm 0.15\text{mm}$  and an observation error of  $(d_o)_{rms} = \pm 0.3\text{mm}$  in test point image coordinates.

Angular Separation [deg.]	RMS Error [mm] in Reconstructed Coordinates of Test Points (x,y,z) [mm] at:								
	(-50,-50,-50)			(0, 0, 0)			(50,50,50)		
	x	y	z	x	y	z	x	y	z
5	0.437	0.283	4.50	0.249	0.176	4.05	0.170	0.253	3.64
10	0.344	0.214	2.24	0.249	0.176	2.02	0.182	0.192	1.82
15	0.314	0.199	1.49	0.249	0.176	1.34	0.198	0.178	1.21
90	0.262	0.185	0.265	0.249	0.176	0.252	0.237	0.168	0.240

increases, these cross-contributions become less evident in the error. As expected the  $z_{rms}$  error decreased and the  $x_{rms}$  error increased with increasing  $\Delta\theta$ . At the origin and at  $(-5\text{cm}, -5\text{cm}, -5\text{cm})$  the  $x_{rms}$  error remained constant and decreased respectively with increasing  $\Delta\theta$  which is thought to be due to the asymmetry of the incidence angles of the projection pair.

Reconstruction error dependence on position can be reduced by increasing the focal length. Fig. 4.5 shows  $D_{rms}$  for  $P^{\rightarrow}$  at  $\pm(5\text{cm}, 5\text{cm}, 5\text{cm})$  and the origin reconstructed from projection pairs separated by  $\Delta\theta=5$  degrees with different focal lengths under the same simulation parameters as above. These curves indicate that the focal length should be increased from 125cm to at least 250cm in order to reduce the percent difference between points at  $\pm(5\text{cm}, 5\text{cm}, 5\text{cm})$  and the origin by half to 5%.

#### 4.2.4.2.3 Expt. 3: Dependence on magnitude of measurement error

The effect of changing the magnitude of the measurement error on reconstruction error was simulated. Digitization and observation errors were considered in turn.  $P_{rms}^{\rightarrow}$  was computed for digitization errors of  $\Delta d_d = \pm 0.075, \pm 0.15, \text{ and } \pm 0.3 \text{ mm}$  and for an observation in error by one pixel at each digitization,  $(d_o)_{rms}$  of  $\pm 0.15, \pm 0.3, \text{ and } \pm 0.6 \text{ mm}$  respectively. Points at  $\pm(5\text{cm}, 5\text{cm}, 5\text{cm})$  and the origin were reconstructed from projection pairs separated by  $\Delta\theta=5, 10, 15 \text{ and } 90$  degrees. The geometric magnification was 1.25 and the focal length was 125cm.

It was observed that the reconstruction error is proportional to both types of measurement error at all three test point locations. Table 4.3 lists rms errors in reconstructed coordinates for the worst case,  $P^{\rightarrow}$  at  $(-5\text{cm}, 5\text{cm}, 5\text{cm})$  for  $\Delta\theta=5$  and 90 degrees. The next section considers how the geometric magnification  $M$  can be selected to minimize the error of reconstruction for different magnitudes of measurement error.

#### 4.2.4.2.4 Expt. 4: Dependence on geometric magnification

The effect of changing the geometric magnification on reconstruction error was simulated for reconstruction from projection pairs separated by

Figure 4.5  $D_{rms}$  in  $P_e^{\rightarrow}$  for different focal lengths given a digitization error of  $\Delta d_d = \pm 0.15\text{mm}$  and an observation error of  $(d_o)_{rms} = \pm 0.3\text{mm}$  in test point image coordinates. ( $\Delta\theta = 5\text{degrees}$ )

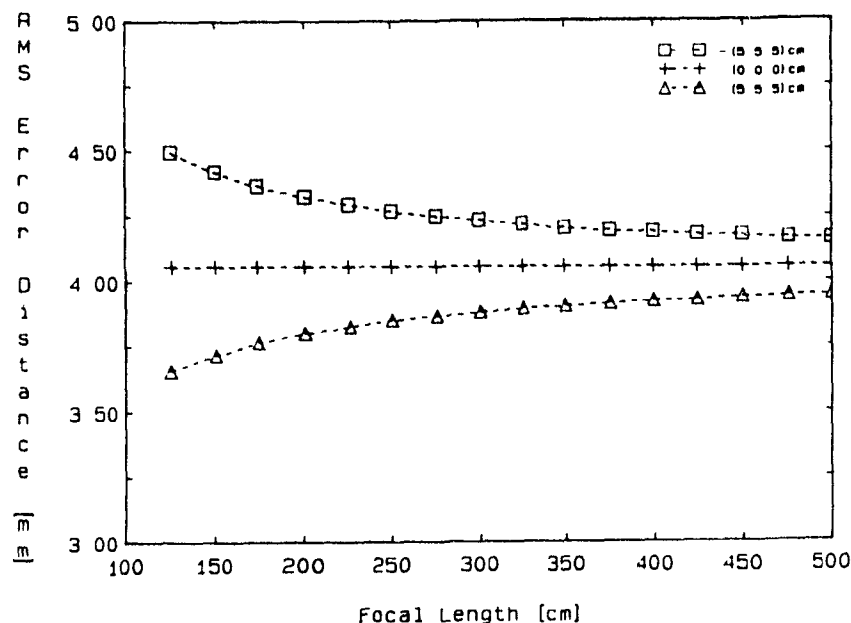


Table 4.3 RMS error in reconstructed coordinates for different magnitudes of digitization and observation errors in test point image coordinates.

Digitization Error [mm]	RMS Error [mm] in Reconstructed Coordinates of Test Point (-50,-50,-50) [mm] at angular separations [deg.] of:					
	5			90		
	x	y	z	x	y	z
0.075	0.061	0.039	0.621	0.036	0.026	0.037
0.15	0.122	0.078	1.24	0.073	0.052	0.073
0.30	0.243	0.156	2.48	0.146	0.103	0.147

Observation Error [mm]	RMS Error [mm] in Reconstructed Coordinates of Test Point (-50,-50,-50) [mm] at angular separations [deg.] of:					
	5			90		
	x	y	z	x	y	z
0.15	0.210	0.136	2.15	0.126	0.089	0.127
0.30	0.420	0.272	4.33	0.252	0.178	0.255
0.60	0.841	0.545	8.60	0.504	0.356	0.510

$\Delta\theta = 5, 10, 15,$  and  $90$  degrees. Geometric magnification was changed by translating the isocenter  $O^{\rightarrow}$  along the focal axis, where the focal length remained at  $125\text{cm}$ .

In order to examine this relationship,  $D_{\text{rms}}$  was measured for a test point,  $-(5\text{cm}, 5\text{cm}, 5\text{cm})$ , at geometric magnifications ranging from  $M = 1.2$  to  $2.0$ . Measurement errors corresponding to a combined digitization and observation error of  $\Delta d_d = \pm 0.15 \text{ mm}$  and  $(d_o)_{\text{rms}} = \pm 0.3 \text{ mm}$  respectively were simulated. Fig. 4.6 shows the results. Table 4.4 lists  $P_{\text{rms}}^{\rightarrow}$  that result for geometric magnifications of  $M = 1.25, 1.5,$  and  $2.0$  at  $\Delta\theta = 5$  and  $90$  degrees. These results indicate that error is approximately proportional to  $(1/M)$ .

There are two limits to how large the geometric magnification can be made in order to reduce reconstruction errors. The first limitation is imposed by the focal spot width (§2.4.2). Referring to Fig. 2.7, a pixel width of  $0.3\text{mm}$  will limit spatial resolution for magnifications up to  $1.5$  when the focal spot width is kept less than  $1.2\text{mm}$ . The other potential limitation is the availability of large image intensifier field sizes, which would be necessary for the fiducial markers to be visible for calibration at increased geometric magnifications. With the current dimensions of the fiducial marker system (§3.4.3.1) and a  $154\text{mm}$  image intensifier, increases in geometric magnification are limited to approximately  $1.33$ . Geometric magnification can be increased further if the dimensions of the fiducial markers are reduced. However, since reconstruction depends on the error in the measurements of the image coordinates of the fiducials as well, a trade-off is expected between fiducial dimensions and reconstruction error. This relationship is considered in the section below.

#### 4.2.5 Measurement error in fiducial image coordinates

In the previous section error in reconstruction was examined assuming there were no errors in the image coordinates of the fiducials. In practice, digitization and observation errors are introduced into the measurements of the fiducial point image coordinates. Since the fiducial markers image as 'points,' observation errors are less likely to occur than in observing vessel center-point image coordinates.

Figure 4.6  $D_{rms}$  in  $P_e^{\rightarrow}$  at  $-(5cm, 5cm, 5cm)$  for different geometric magnifications given a digitization error of  $\Delta d_d = \pm 0.15mm$  and an observation error of  $(d_o)_{rms} = \pm 0.3mm$  in test point image coordinates.

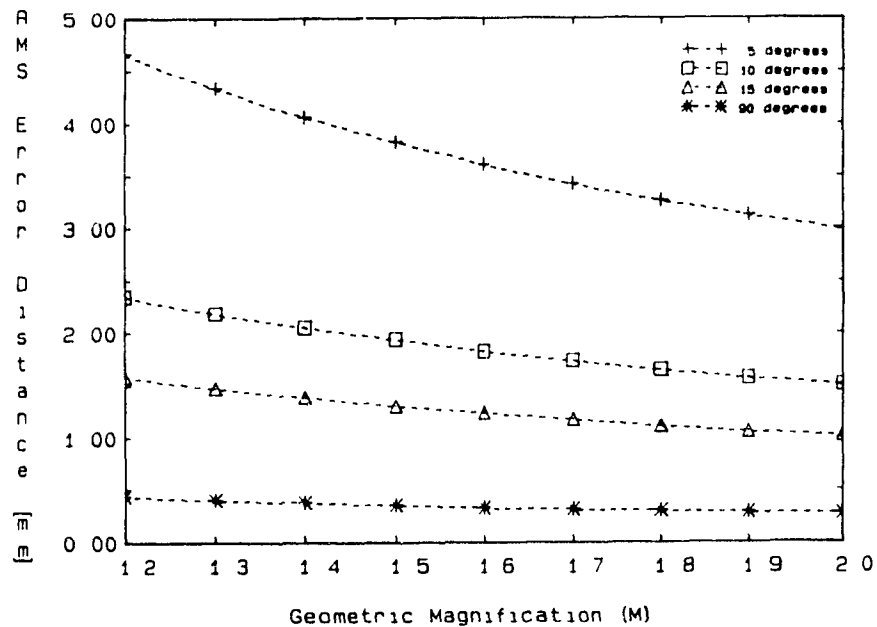


Table 4.4 RMS error in reconstructed coordinates for geometric magnifications of 1.25, 1.5, and 2.0 given a digitization error of  $\Delta d_d = \pm 0.15mm$  and an observation error of  $(d_o)_{rms} = \pm 0.3mm$  in test point image coordinates.

Geometric Magnification	RMS Error [mm] in Reconstructed Coordinates of Test Point $(-50, -50, -50)$ [mm] at angular separations [deg.] of:					
	5			90		
	x	y	z	x	y	z
1.25	0.437	0.283	4.50	0.262	0.185	0.265
1.5	0.401	0.266	3.79	0.221	0.156	0.224
2.0	0.357	0.251	2.97	0.169	0.120	0.171

Instead of deriving an expression for the relationship between reconstruction error and fiducial image coordinate measurement error, it is evaluated by means of simulation. The basic simulation experiment is similar to that described in §4.2.4.2.

#### 4.2.5.1 Simulation experiments

The basic experiment considers only error from the measurements of the fiducial markers in image pairs. Referring to §4.2.1, there are two separate sets of fiducial markers and both are considered.

In each simulation trial the actual numerical values of the image coordinates of the fiducials  $(x_a, y_a)_j$  and  $(x_b, y_b)_j$  are substituted with  $(x_a \pm \Delta d, y_a \pm \Delta d)_j$  and  $(x_b \pm \Delta d, y_b \pm \Delta d)_j$ ,  $j=1, \dots, 8$ . The values of the error terms,  $\Delta d$  for each image coordinate, are found by drawing 32 separate error terms randomly from a specified distribution of values. The reconstructed point coordinates are then calculated, and the residual error in the reconstructed coordinates from the actual values is computed. The trial is repeated  $N=5000$  times, and  $P_{rms}^{\rightarrow}$  is computed by (4.7) where the standard deviation in  $P_{rms}^{\rightarrow}$  is  $0.01(P_{rms}^{\rightarrow})$ . The number of trials was reduced to 5000 from the previous set of simulations, without loss of precision, in order to reduce the long computation times associated with simulating fiducial measurement errors (i.e. 32 versus 4 error terms).

Simulation experiments evaluating reconstruction error dependence on the angle between projection pairs, magnitude of the measurement error, geometric magnification, and fiducial marker system dimensions are described with results below.

##### 4.2.5.1.1 Expt. 1: Dependence on projection angle

The reconstruction error that results from varying only the angle separating the projection pairs was simulated. Projection pairs separated by  $\Delta\theta = 5$  to 15 degrees and  $\Delta\theta = 80$  to 90 degrees, corresponding to the stereo and biplane views of the lateral and anterior-posterior fiducial plates of

the stereotactic frame, were selected for reconstruction. A test point  $P^{\rightarrow}$  at the origin was reconstructed for a digitization error  $\Delta d_d$  of  $\pm 0.15\text{mm}$  and an observation error  $(d_o)_{\text{rms}}$  of  $\pm 0.3\text{mm}$  separately. The geometric magnification was kept at 1.25 for a focal length of 125cm.

Fig. 4.7 shows the resulting error  $P^{\rightarrow}_{\text{rms}}$  due to image coordinate error of the lateral fiducials in projections separated by 5 to 15 degrees. The curves for 'x' and 'y' rms errors remain essentially constant and are very small in comparison to the 'z' rms error curves. Reconstruction error consists predominately of error in the 'z' coordinate which decreases by half from 5 to 10 degrees. These estimates of error are less than the error magnitude resulting from measurement errors in the image coordinates of test points (Fig. 4.2).

Fig. 4.8 shows  $P^{\rightarrow}_{\text{rms}}$  due to image coordinate error in both the lateral and anterior-posterior fiducials in projections separated by  $\Delta\theta=80$  to 90 degrees. The error curves in Fig. 4.8 remain almost constant from 80 to 90 degrees and the magnitude of these errors indicate fiducial error is not as important as test point image coordinate measurement error contributions.

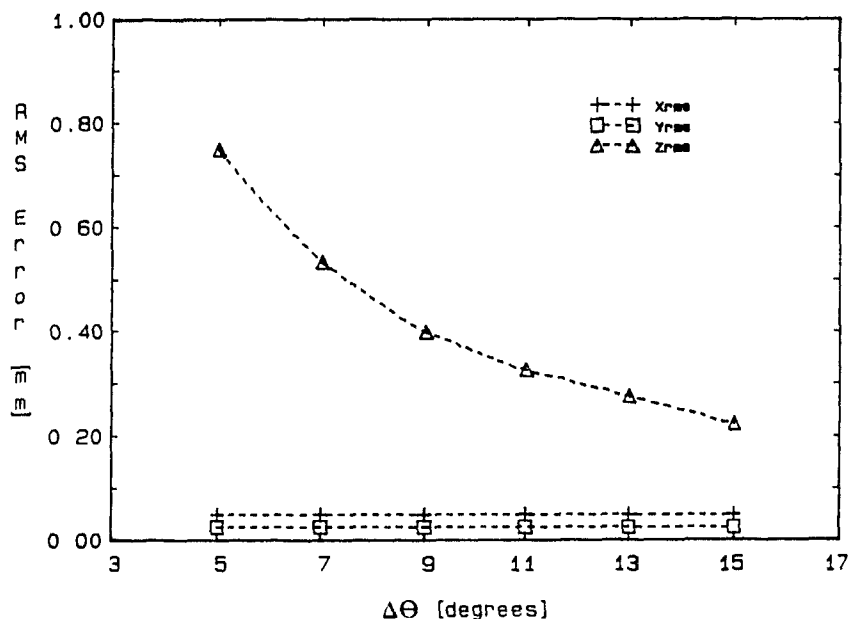
#### 4.2.5.1.2 Expt. 2: Dependence on position

The dependence of reconstruction error on position in stereotactic space was simulated. Points on a line through  $\pm(5\text{cm}, 5\text{cm}, 5\text{cm})$  were reconstructed with lateral fiducial image coordinate errors in projections separated by  $\Delta\theta=5, 10$ , and 15 degrees, and with anterior-posterior and lateral fiducial image coordinate errors in projections separated by  $\Delta\theta=90$  degrees. Measurement error consisted of a digitization error  $\Delta d_d$  of  $\pm 0.15\text{mm}$  and observation error  $(d_o)_{\text{rms}}$  of  $\pm 0.3\text{mm}$ . Geometric magnification remained at 1.25 for a focal length of 125cm.

Fig. 4.9 shows that the distance error  $D_{\text{rms}}$  along the line through  $\pm(5\text{cm}, 5\text{cm}, 5\text{cm})$  is smallest at or near the origin. Error values increase dramatically for those points that lie near or just outside the volume defined by the fiducial markers. Table 4.5 lists the reconstruction error in each coordinate of  $P^{\rightarrow}$  at  $\pm(5\text{cm}, 5\text{cm}, 5\text{cm})$  and the origin. In comparison to

Figure 4.7 RMS error in reconstructed coordinates of  $P_e^{\rightarrow}$  at the origin as a function of angular separation for a) a digitization error of  $\Delta d_d = \pm 0.15\text{mm}$  and b) an observation error of  $(d_o)_{\text{rms}} = \pm 0.3\text{mm}$  in the lateral fiducial image coordinates.

a) Digitization error,  $\Delta d_d = \pm 0.15\text{mm}$



b) Observation error,  $(d_o)_{\text{rms}} = \pm 0.3\text{mm}$

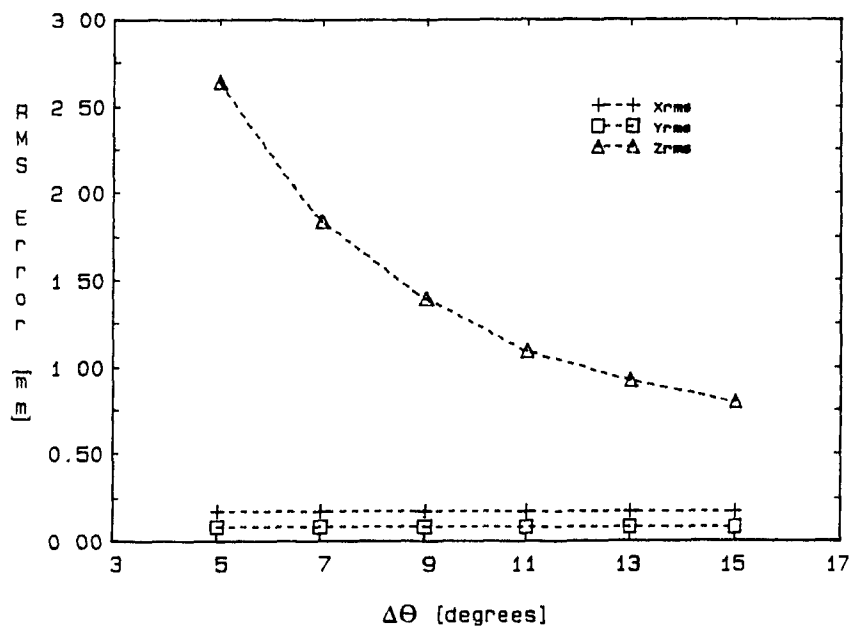
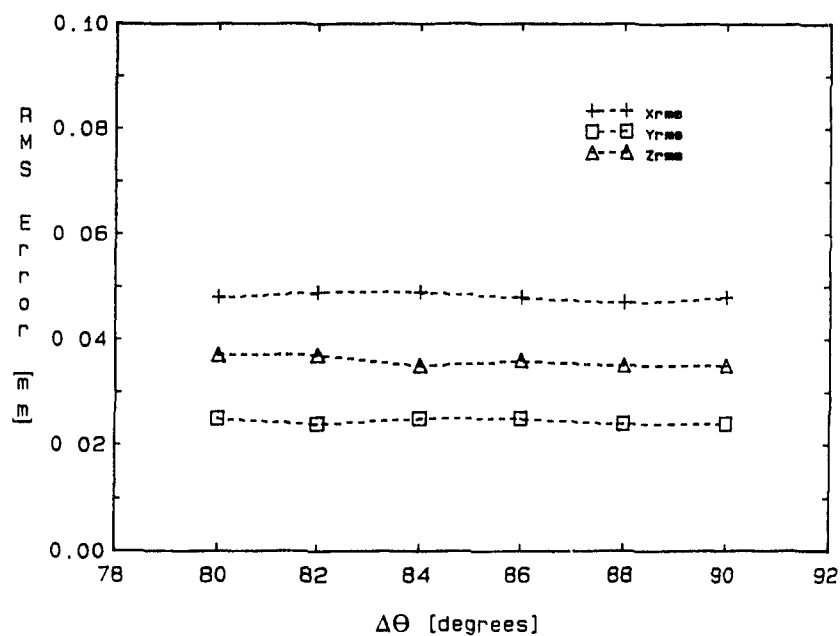




Figure 4.8 RMS error in reconstructed coordinates for  $P_e^{\rightarrow}$  at the origin as a function of angular separation for a) a digitization error of  $\Delta d_d = \pm 0.15\text{mm}$  and b) an observation error of  $(d_o)_{\text{rms}} = \pm 0.3\text{mm}$  in both the lateral and anterior-posterior fiducial image coordinates.

a) Digitization error,  $\Delta d_d = \pm 0.15\text{mm}$



b) Observation error,  $(d_o)_{\text{rms}} = \pm 0.3\text{mm}$

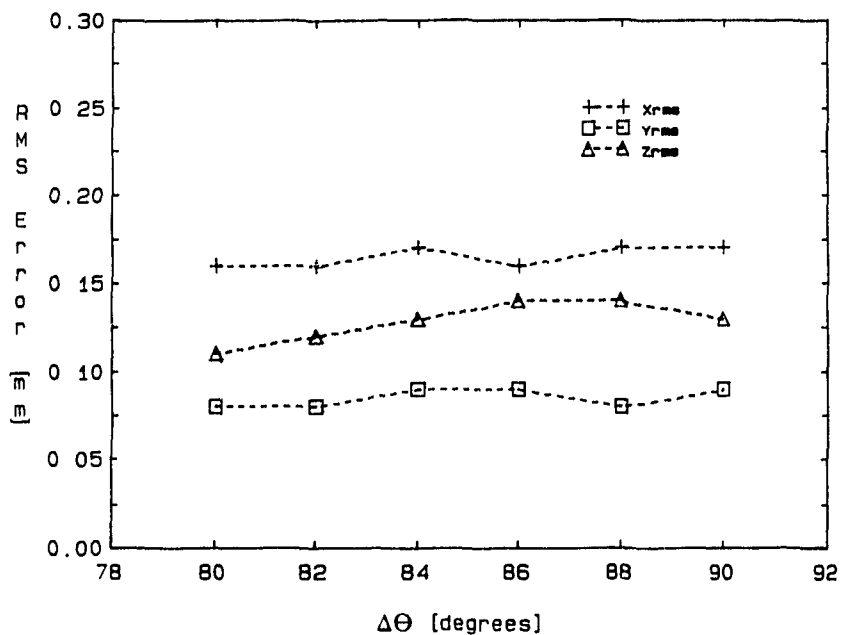


Figure 4.9  $D_{rms}$  in  $P_e^{\rightarrow}$  at different positions given a digitization error of  $\Delta d_d = \pm 0.15\text{mm}$  and an observation error of  $(d_o)_{rms} = \pm 0.3\text{mm}$  in fiducial point image coordinates.

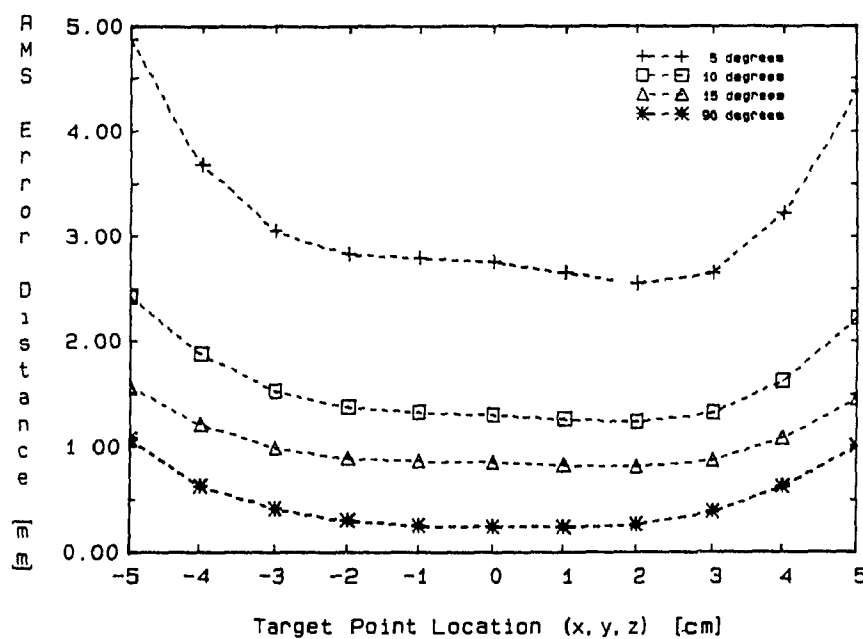


Table 4.5 RMS error in reconstructed coordinates for different angular separations given a digitization error of  $\Delta d_d = \pm 0.15\text{mm}$  and an observation error of  $(d_o)_{rms} = \pm 0.3\text{mm}$  in fiducial point image coordinates.

Angular Separation [deg.]	RMS Error [mm] in Reconstructed Coordinates of Test Points								
	(x,y,z) [mm] at:								
	(-50,-50,-50)			(0, 0, 0)			(50,50,50)		
	x	y	z	x	y	z	x	y	z
5	0.477	0.405	4.78	0.173	0.087	2.74	0.202	0.313	4.39
10	0.352	0.332	2.39	0.173	0.085	1.27	0.220	0.242	2.17
15	0.349	0.322	1.52	0.175	0.085	0.823	0.243	0.221	1.43
90	0.295	0.606	0.832	0.174	0.092	0.145	0.289	0.421	0.875

Table 4.2, reconstruction error at points outside the region of space defined by the fiducial markers can be expected to be larger than errors due to measurement error in the image coordinates of the test points.

It was also found that this dependence on position could not be reduced by increasing the focal length as shown with measurement errors in test point image coordinates. Fig. 4.10 shows the magnitude of  $P_{rms}^{\rightarrow}$  at  $-(5\text{cm}, 5\text{cm}, 5\text{cm})$ ,  $-(2\text{cm}, 2\text{cm}, 2\text{cm})$ , and the origin reconstructed from projection pairs separated by  $\Delta\theta=5$  degrees with different focal lengths under the same simulation parameters. The geometric magnification was kept constant at 1.25. The error plots in Fig. 4.10 remain essentially constant for focal length of 125cm to 500cm.

#### 4.2.5.1.3 Expt. 3: Dependence on measurement error

Reconstruction error dependence on the magnitude of digitization and observation errors was evaluated. In the simulations,  $P_{rms}^{\rightarrow}$  was computed for digitization errors of  $\Delta d_d = \pm 0.075$ ,  $\pm 0.15$ , and  $\pm 0.3$  mm and observation errors of  $(d_o)_{rms} = \pm 0.15$ ,  $\pm 0.3$ , and  $\pm 0.6$  mm. Three test points,  $P^{\rightarrow}$  at  $\pm(5\text{cm}, 5\text{cm}, 5\text{cm})$  and the origin, were reconstructed with lateral fiducial image coordinate errors in projections separated by  $\Delta\theta = 5$ , 10, and 15 degrees, and with anterior-posterior and lateral fiducial image coordinate errors in projections separated by  $\Delta\theta=90$  degrees. The geometric magnification was kept at 1.25 for a focal length of 125cm.

$P_{rms}^{\rightarrow}$  was found to be proportional to both types of measurement error at all three test point locations. Table 4.6 lists  $P_{rms}^{\rightarrow}$  for a test point at  $-(5\text{cm}, 5\text{cm}, 5\text{cm})$  for  $\Delta\theta = 5$  and 90 degrees.

#### 4.2.5.1.4 Expt. 4: Dependence on geometric magnification

Error was computed in reconstruction from projection pairs separated by  $\Delta\theta = 5$ , 10, 15, and 90 degrees at different values of geometric magnification for a fixed focal length of 125cm. The measurement error consisted of a combined digitization error  $\Delta d_d$  of  $\pm 0.15$  mm and observation error  $(d_o)_{rms}$  of  $\pm 0.3$  mm in both the lateral and anterior-posterior fiducial image

Figure 4.10  $D_{rms}$  in  $P_e^{\rightarrow}$  for different focal lengths given a digitization error of  $\Delta d_d = \pm 0.15\text{mm}$  and an observation error of  $(d_o)_{rms} = \pm 0.3\text{mm}$  in fiducial point image coordinates. ( $\Delta\theta = 5$  degrees)

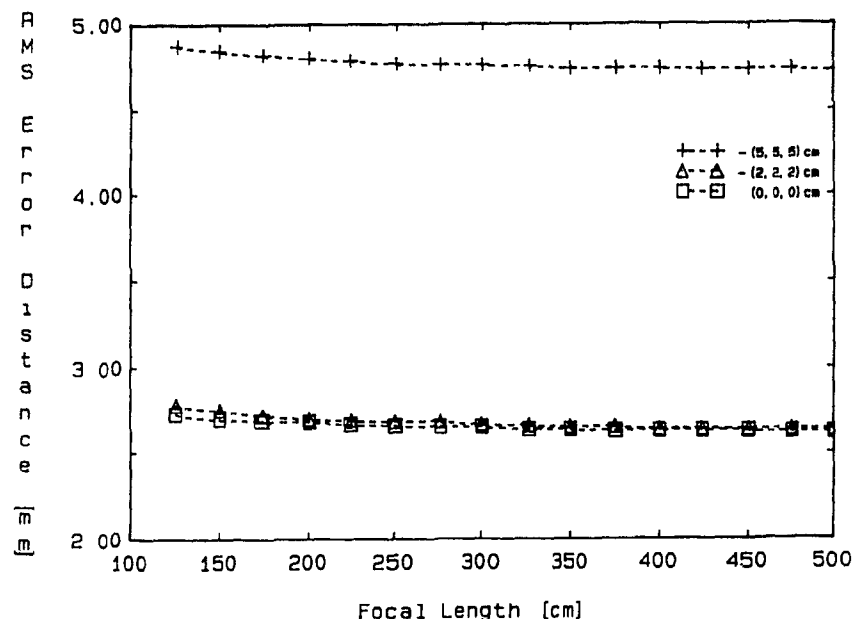


Table 4.6 RMS error in reconstructed coordinates for different magnitudes of digitization and observation errors in fiducial point image coordinates.

Digitization Error [mm]	RMS Error [mm] in Reconstructed Coordinates of Test Point (-50,-50,-50) [mm] at angular separations [deg.] of:					
	5			90		
	x	y	z	x	y	z
0.075	0.067	0.055	0.675	0.041	0.084	0.116
0.15	0.135	0.110	1.35	0.082	0.169	0.232
0.30	0.270	0.221	2.70	0.163	0.337	0.465

Observation Error [mm]	RMS Error [mm] in Reconstructed Coordinates of Test Point (-50,-50,-50) [mm] at angular separations [deg.] of:					
	5			90		
	x	y	z	x	y	z
0.15	0.229	0.190	2.30	0.142	0.291	0.399
0.30	0.458	0.380	4.59	0.284	0.582	0.799
0.60	0.916	0.761	9.20	0.568	1.16	1.60

coordinates.

Fig. 4.11 shows  $D_{rms}$  in the reconstruction of a test point at  $-(5cm, 5cm, 5cm)$  for geometric magnifications from  $M=1.2$  to  $2.0$ . The error in each coordinate of the test point reconstructed at  $\Delta\theta=5$  and  $90$  degrees is listed in Table 4.7. In this data reconstruction error is approximately proportional to  $(1/M)$ .

#### 4.2.5.1.5 Expt. 5: Dependence on fiducial dimensions

In this experiment the effect of changing the 3-d spatial distribution of the fiducial markers in both pairs of plates on reconstruction error was considered. Three test points,  $P^{\rightarrow}$  at the origin,  $-(2cm, 2cm, 2cm)$ , and  $-(5cm, 5cm, 5cm)$ , were reconstructed with a combined digitization error  $\Delta d_d$  of  $\pm 0.15mm$  and observation error  $(d_o)_{rms}$  of  $\pm 0.3mm$  in the fiducial image coordinates. Projection pairs separated by  $\Delta\theta=5, 10, 15$ , and  $90$  degrees were considered. The geometric magnification was kept at  $1.25$  for a focal length of  $125cm$ .

Results are listed for projection pairs separated by  $\Delta\theta=5$  and  $90$  degrees as representative of the range of error expected. Table 4.8 lists the distance errors  $D_{rms}$  that result when the size of the square formed by the fiducials in the lateral and anterior-posterior plates was changed. The depth or the distance between fiducial plates was held constant at  $20cm$ . The error at the origin remained constant for both projection pairs at  $\Delta\theta=5$  degrees (i.e.  $2.30 \pm 0.02mm$ ) and  $\Delta\theta=90$  degrees (i.e.  $0.22 \pm 0.01mm$ ). For test points near or outside the region of 3-d space defined by the fiducial markers, errors can be large. These errors are reduced as the size of fiducial distribution increases to include these points.

The effect of changing the distance between the pairs of lateral and anterior-posterior fiducial plates is presented in Table 4.9. The size of the square made by the fiducials in each plate is fixed at  $8cm$ . Changing the distance between plates produced changes in the reconstruction at only the test point at  $-(5cm, 5cm, 5cm)$ , error at the other test points remained essentially constant. For projection pairs separated by  $\Delta\theta=5$  degrees, the

Figure 4.11  $D_{rms}$  in  $P_e^{\rightarrow}$  at  $-(5cm, 5cm, 5cm)$  for different geometric magnifications given a digitization error of  $\Delta d_d = \pm 0.15mm$  and an observation error of  $(d_o)_{rms} = \pm 0.3mm$  in fiducial point image coordinates.

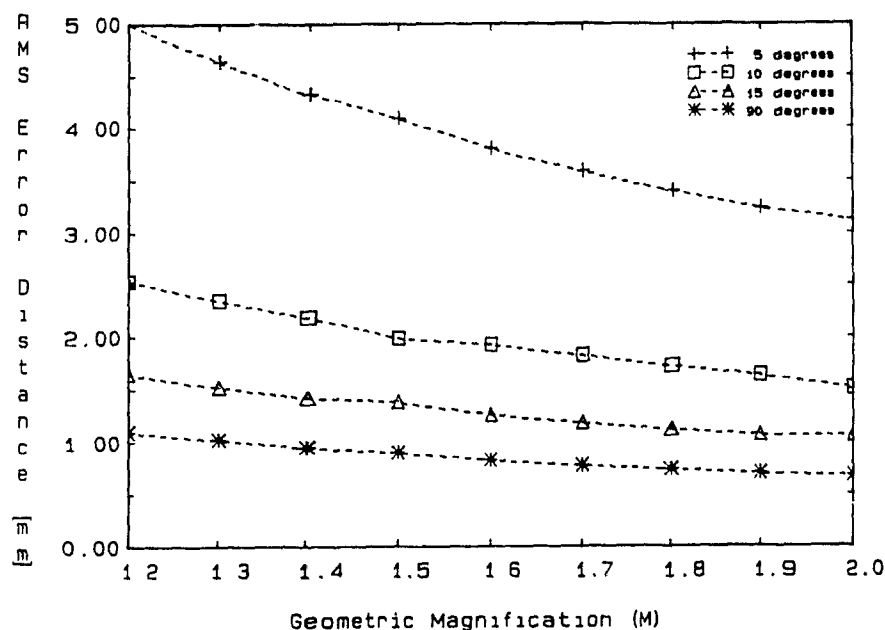


Table 4.7 RMS error in reconstructed coordinates for geometric magnifications of 1.25, 1.5, and 2.0 given a digitization error of  $\Delta d_d = \pm 0.15mm$  and an observation error of  $(d_o)_{rms} = \pm 0.3mm$  in fiducial point image coordinates.

Geometric Magnification	RMS Error [mm] in Reconstructed Coordinates of Test Point $(-50, -50, -50)$ [mm] at angular separations [deg.] of:					
	5			90		
	x	y	z	x	y	z
1.25	0.477	0.405	4.78	0.296	0.604	0.832
1.5	0.432	0.356	4.02	0.244	0.512	0.688
2.0	0.374	0.312	3.04	0.184	0.394	0.496

Table 4.8  $D_{rms}$  in  $P_e^{\rightarrow}$  that result when the size of the square formed by the fiducials in both the lateral and anterior-posterior plates is varied.

Width of Square [mm]	Distance Error [mm] in Reconstructed Coordinates of Test Point (x,y,z) [mm] at:			
	(-20,-20,-20)		(-50,-50,-50)	
	$\Delta\theta = 5$	$\Delta\theta = 90$	$\Delta\theta = 5$	$\Delta\theta = 90$
40	3.09	0.337	13.1	1.42
60	2.57	0.262	6.31	0.676
80	2.49	0.245	4.17	0.438
100	2.47	0.239	3.38	0.342
120	2.46	0.236	3.05	0.299

Table 4.9  $D_{rms}$  in  $P_e^{\rightarrow}$  that result when the distance between the pairs of lateral and anterior-posterior plates is varied.

Distance between plates [mm]	Distance Error [mm] in Reconstructed Coordinates of Test Point (x,y,z) [mm] at:	
	(-50,-50,-50)	
	$\Delta\theta = 5$	$\Delta\theta = 90$
40	4.75	0.465
60	4.39	0.441
80	4.25	0.437
100	4.17	0.438
120	4.13	0.438

error magnitude at the origin was  $2.30 \pm 0.02\text{mm}$  and at  $-(2\text{cm}, 2\text{cm}, 2\text{cm})$  was  $2.5 \pm 0.02\text{mm}$ . For projection pairs separated by  $\Delta\theta=90$  degrees, the error magnitude at the origin was  $0.22 \pm 0.01\text{mm}$  and at  $-(2\text{cm}, 2\text{cm}, 2\text{cm})$  was  $0.25 \pm 0.01\text{mm}$ . Table 4.9 shows that reconstruction error decreases when the fiducial geometry is increased to a volume that contains the test point. In comparison to Table 4.8, sensitivity to change in the fiducial geometry is more significant in the lateral dimensions (i.e. in the direction of disparity measurements).

#### 4.2.6 Physical determination of accuracy: phantom test

In order to measure reconstruction error under typical examination conditions, stereo and biplane projections of a test object composed of steel beads were imaged and used to reconstruct the 3-d coordinates of each bead. The reconstructed coordinates were compared to the actual coordinates, determined physically by stereotactic instruments, and the mean residual error and standard deviation were then computed.

##### 4.2.6.1 Description of experiment

The test object was made up of 25 spherical steel beads, ranging in diameter from 0.9 to 1.2mm, mounted to the surface of a plexiglass plate. These 25 beads were arranged in a square 1cm grid pattern (Fig. 4.12). This plate was attached by wires to the frame so as to center the plate in the proximal lateral half and later in the distal lateral half of the frame. The 3-d coordinates of each bead were determined by a biopsy needle that was attached to the frame by calibrated side bars. Table 4.10 lists the measured 3-d coordinates of the beads with respect to the stereotactic coordinate system. The spatial distribution of the fiducial markers is given in Table 3.1 where the center of the region defined by these markers is at  $(7.5\text{cm}, 6\text{cm}, 0\text{cm})$ . Although the 'x' and 'y' coordinates of the frame's side bars are calibrated in 2mm divisions, it was possible to visually interpolate to within 1mm steps reliably. The minimum uncertainty of the measurements listed in Table 4.10 is  $(\pm 0.5\text{mm}, \pm 0.5\text{mm}, \pm 0.25\text{mm})$ .

Images of the frame with test beads were recorded on a Technicare DR-960



Figure 4.12 Plan of test phantom consisting of 25 beads spaced on a 1cm square grid. Bead positions are indexed for reference with Table 4.10.

```

      '1  '2  '3  '4  '5
      '6  '7  '8  '9 '10
      '11 '12 '13 '14 '15
      '16 '17 '18 '19 '20
      '21 '22 '23 '24 '25
  
```

Table 4.10 Actual 3-d coordinates of test beads in the stereotactic frame.

Bead No.	Actual Coordinates Of Test Beads ( $\pm .05\text{cm}$ , $\pm .05\text{cm}$ , $\pm .025\text{cm}$ )					
	Distal Lateral			Proximal Lateral		
	X	Y	Z	X	Y	Z
1	5.0	7.9	2.85	6.9	7.8	-0.20
2	5.7	7.9	2.20	7.6	7.8	-0.90
3	6.5	7.9	1.50	8.3	7.8	-1.60
4	7.2	7.9	0.90	9.0	7.8	-2.20
5	8.0	7.9	0.25	9.7	7.8	-2.90
6	5.0	6.9	2.85	6.9	6.8	-0.20
7	5.8	6.9	2.20	7.6	6.9	-0.90
8	6.5	6.9	1.50	8.3	6.8	-1.55
9	7.2	6.9	0.90	9.0	6.8	-2.20
10	8.0	6.9	0.30	9.7	6.8	-2.90
11	5.0	6.0	2.85	6.9	5.8	-0.20
12	5.7	6.0	2.20	7.6	5.8	-0.90
13	6.5	6.0	1.55	8.3	5.8	-1.50
14	7.2	5.9	0.90	9.1	5.8	-2.20
15	8.0	5.9	0.30	9.8	5.8	-2.90
16	4.9	5.0	2.90	7.0	4.8	-0.10
17	5.7	5.0	2.20	7.7	4.8	-0.85
18	6.5	5.0	1.60	8.4	4.9	-1.50
19	7.2	5.0	0.90	9.1	4.9	-2.20
20	8.0	5.0	0.30	9.8	4.9	-2.80
21	4.9	4.1	2.90	7.0	3.9	-0.10
22	5.7	4.1	2.25	7.7	3.9	-0.80
23	6.5	4.1	1.60	8.4	3.9	-1.50
24	7.2	4.0	0.90	9.1	3.9	-2.20
25	7.9	4.0	0.30	9.9	3.9	-2.90

DSA unit interfaced to a Philips CsI 154mm/231mm image intensifier and were digitized to 10 bits and sampled on a 512x512 matrix. A large focal spot of 1.2mm width (nominal) was used. Three projections of the frame were imaged, spaced  $\Theta = 0, 7, \text{ and } 90$  degrees. The focal length was 125cm and the geometric magnification was approximately 1.25 in each projection. To correct for pin-cushion distortion (§3.4.3.3) a 1cm-grid was left fixed to the face of the image intensifier during the entire imaging procedure. With the image intensifier operating in 154mm mode, the pixel size for the 512x512 matrix is approximately 0.3mm.

Figs. 4.13, 4.14, and 4.15 show images of the test beads in the proximal lateral half of the frame recorded at  $\Theta = 0, 7, \text{ and } 90$  degree projections respectively. Similarly Figs. 4.16, 4.17, and 4.18 show different projection images of the test beads in the distal lateral half of the frame. Images in Figs. 4.13-18a) show the observed 2-d coordinates of the beads and fiducial markers designated by the white dots and cross hairs respectively. In Figs. 4.13-18b) the computed correction vectors are shown superimposed at intersections of the cm-grid.

In all of these images the 2-d coordinates of the beads and fiducial markers were selected by an observer using a track-ball controlled graphics cursor where the cursor was placed over the center of the image of the beads and fiducial markers.

#### 4.2.6.2 Results

The results of reconstruction are summarized in Table 4.11 where image coordinates of the beads and fiducials markers were not corrected for pin-cushion distortion and in Table 4.12 after corrections.

From both tables the mean error in 'x' and 'y' coordinates was determined to be approximately  $0.5 \pm 0.5$ mm which reflects the uncertainty of the physical measurements. The mean error in the 'z' coordinate was found to be  $0.5 \pm 2.0$ mm in the stereo reconstructions and  $0.5 \pm 0.3$ mm in biplane reconstructions. These values are within the range of errors predicted in Tables 4.3 and 4.6. For digitization errors of  $\pm 0.15$ mm and an observation

Figure 4.13 DSA images of test bead phantom (proximal lateral) and 1cm correction grid in  $\theta = 0$  degree projection.

a) fiducial markers and beads selected

b) correction vectors indicated

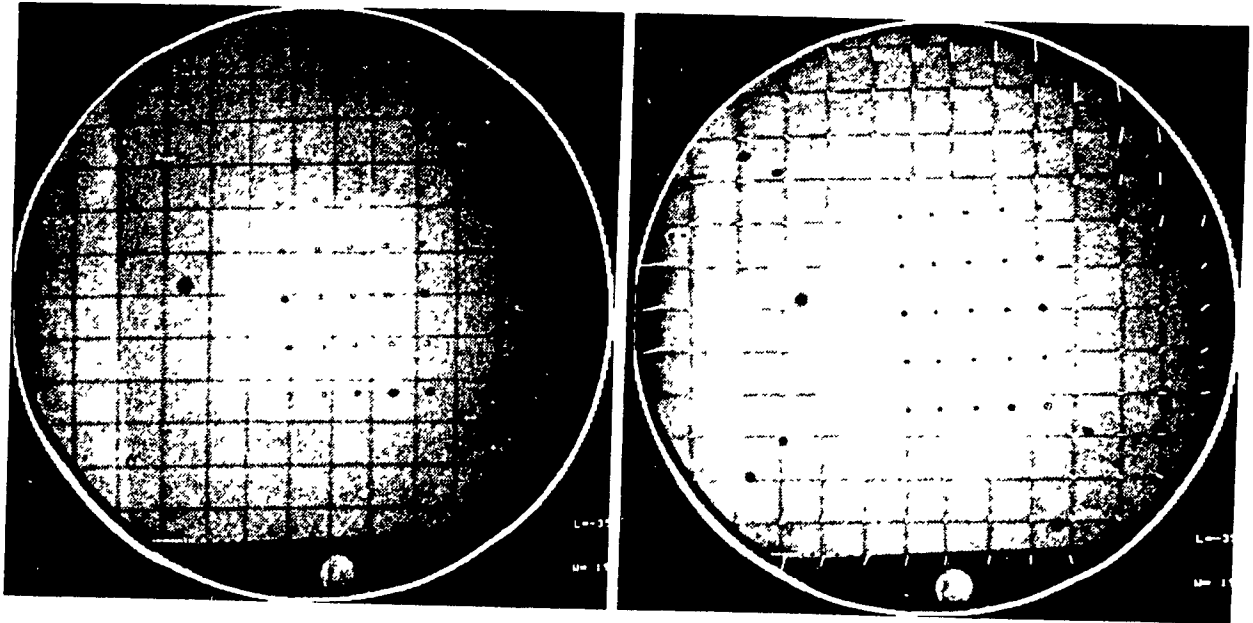


Figure 4.14 DSA images of test bead phantom (proximal lateral) and 1cm correction grid in  $\theta = 7$  degree projection.

a) fiducial markers and beads selected

b) correction vectors indicated

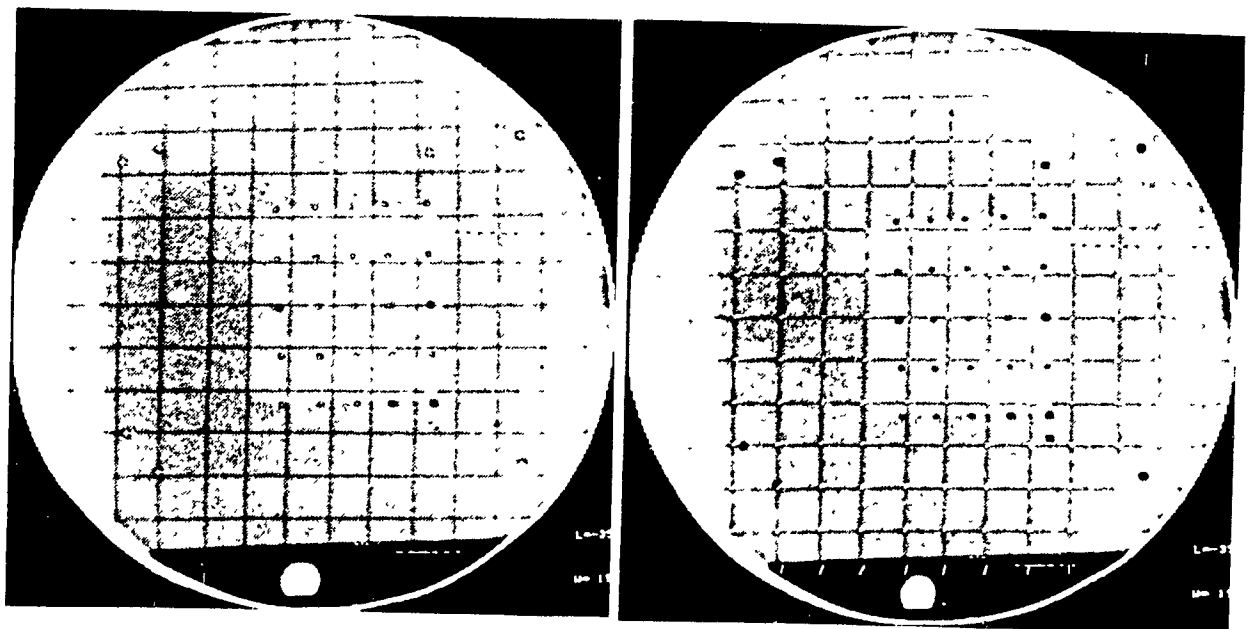


Figure 4.15 DSA images of test bead phantom (proximal lateral) and 1cm correction grid in  $\theta = 90$  degree projection.

a) fiducial markers and beads selected

b) correction vectors indicated

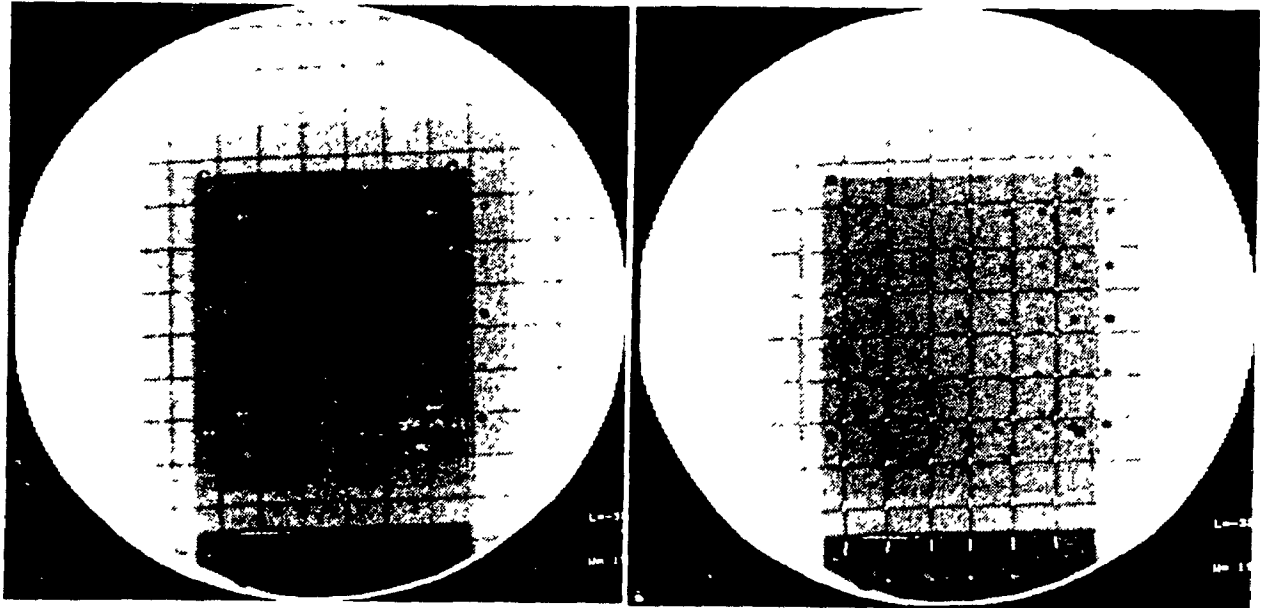


Figure 4.16 DSA images of test bead phantom (distal lateral) and 1cm correction grid in  $\theta = 0$  degree projection.

a) fiducial markers and beads selected

b) correction vectors indicated

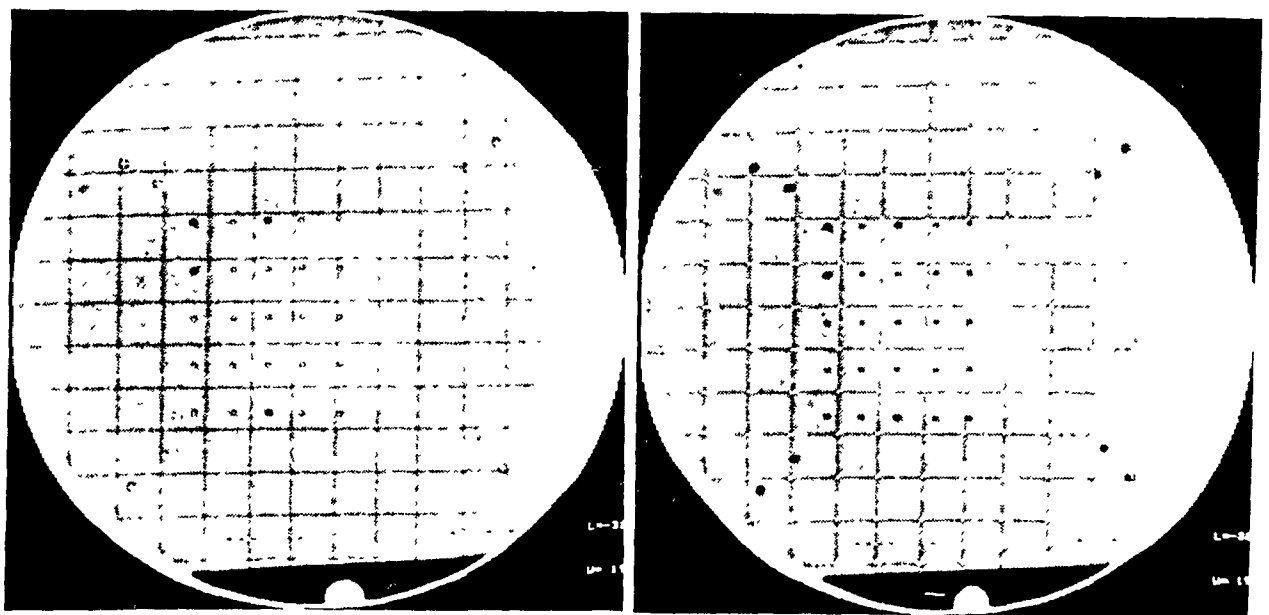


Figure 4.17 DSA images of test bead phantom (distal lateral) and 1cm correction grid in  $\theta = 7$  degree projection.

a) fiducial markers and beads selected

b) correction vectors indicated

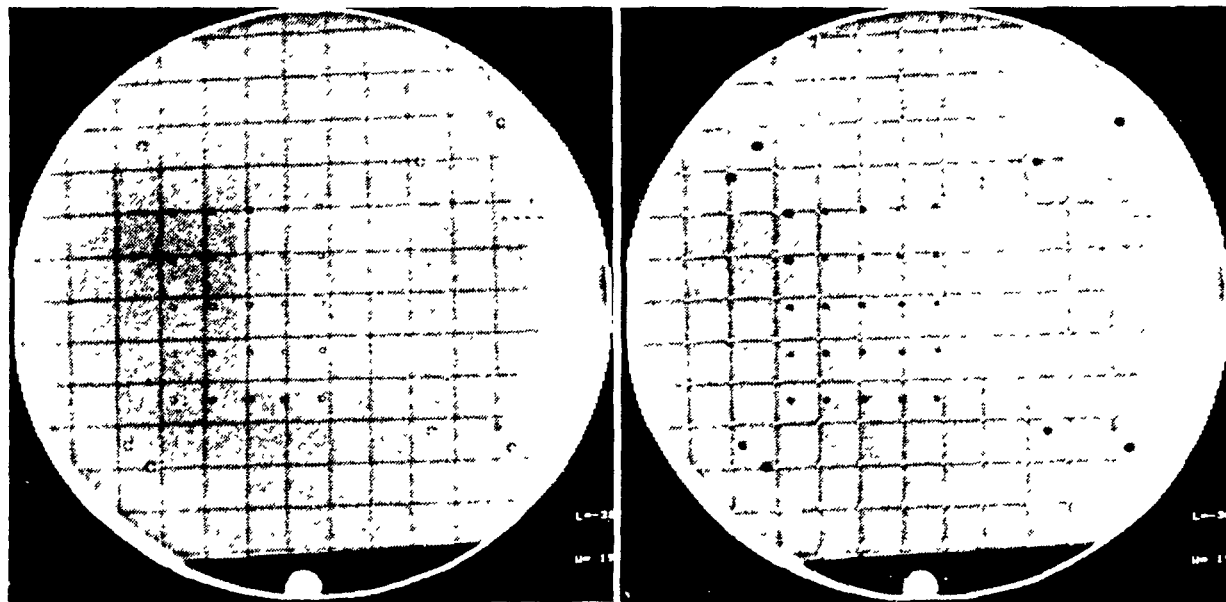


Figure 4.18 DSA images of test bead phantom (distal lateral) and 1cm correction grid in  $\theta = 90$  degree projection.

a) fiducial markers and beads selected

b) correction vectors indicated

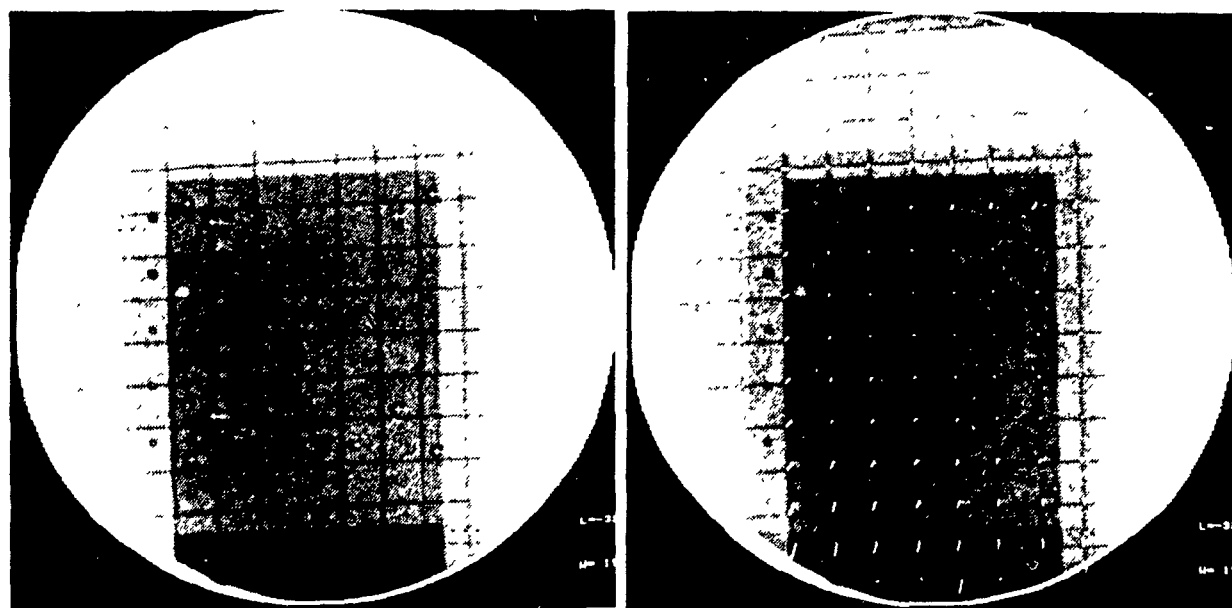


Table 4.11 Residual errors resulting from a comparison of actual and calculated values of coordinates of test beads without pin cushion distortion correction.

Residual Error [mm] in Reconstructed Coordinates of Test Beads (no pin-cushion correction)									
		Angular Separation [deg.]		X mean $\pm \sigma$		Y mean $\pm \sigma$		Z mean $\pm \sigma$	
Proximal lateral	7	0.4	0.6	0.3	0.6	-0.5	1.7		
	90	0.4	0.6	0.3	0.7	0.2	0.2		
Distal lateral	7	0.1	0.5	-0.3	0.5	0.3	1.5		
	90	0.4	0.6	-0.3	0.4	0.4	0.3		

Table 4.12 Residual errors resulting from a comparison of actual and calculated values of coordinates of test beads after pin cushion distortion correction.

Residual Error [mm] in Reconstructed Coordinates of Test Beads (after pin-cushion correction)									
		Angular Separation [deg.]		X mean $\pm\sigma$		Y mean $\pm\sigma$		Z mean $\pm\sigma$	
Proximal lateral	7	0.5	0.6	-0.1	0.5	-0.5	2.0		
	90	0.5	0.5	0.1	0.6	-0.3	0.2		
Distal lateral	7	-0.5	0.5	-0.4	0.5	0.5	1.8		
	90.	-0.5	0.5	-0.2	0.5	0.5	0.2		

error of  $\pm 1$  pixel in both the image coordinates of test points and fiducials, the error in 'z' at the origin of the frame is expected to be  $\pm 4.7\text{mm}$  and  $\pm 0.3\text{mm}$  for stereo and biplane reconstructions respectively.

It was by this method that the frame's calibrated horizontal side-bars were found to be misaligned. The 'x' coordinate mean error in this case was found to be biased at 2mm.

Contrary to expectations, pin-cushion distortion correction did not result in a reduction in reconstruction error (Tables 4.11-12). A possible explanation is that for this method of correction any potential gain is offset by introduction of measurement errors associated with the computation of the correction vectors. This would be the case especially for those test beads near the center of the image whose locations are slightly distorted (see Figs 4.13-18b). Another possible explanation for why reconstruction error changes little with image pin-cushion correction is that a first-order correction for the linear component of the distortion occurs through the calibration of the fiducial markers.

Tables 4.11 and 4.12 show that reconstruction errors for beads located in the lateral proximal and distal halves of the frame are almost the same. The observed invariance of reconstruction error with position is probably due to the effects of measurement error in the fiducials and test point image coordinates averaging out the reconstruction error.

#### 4.2.7 Summary

Experiments describing the relationship between reconstruction error and measurement error in fiducial and test point image coordinates have been performed and analyzed. Reconstruction errors were found to be proportional to measurement error magnitude and inversely proportional to geometric magnification for both errors in fiducial and test point image coordinates. For reconstruction of points at or near the isocenter, measurement error in the test point image coordinates dominates reconstruction error. Measurement error in the fiducial marker image coordinates becomes important when test points are located outside the volume defined by the system of fiducial

markers.

Results from test point image coordinate error experiments showed agreement with (4.6) derived from Sherlock and Aitken's work (1980). However, these equations do not describe the dependence of error at locations other than the origin. Errors change as much as  $\pm 10\%$  of the values at the origin, and the actual error depends on the geometric magnification of the test point and the focal length. In the case of fiducial image coordinate errors, dependence on position varies with the location of the point with respect to the fiducial volume. Points outside the volume defined by the fiducial markers have large reconstruction errors. These errors can be reduced by increasing the size of the pattern of fiducial markers.

Physical determination of reconstruction accuracy from image pairs of test beads for 7 and 90 degree separations demonstrated errors less than (1mm,1mm,2.5mm) and (1mm,1mm,0.7mm) respectively. Although these error values represent the best possible reconstruction, since observation errors are minimal, the potential for large errors exists for angular separations around 5 degrees. The magnitude of reconstruction error is best reduced by using finer digitizations, at least 0.15mm/pixel. This would still permit using projections separated by small angles which is necessary for finding correspondences between conjugate pixels. When this is not possible or practical, reconstruction error should be reduced by increasing angular separation. Changing angular separation from 5 to 10 degrees reduces reconstruction error by about half. A minimum of at least 10 degrees separation is then necessary and can be achieved with stereotactic DSA by using symmetric projections ( $\theta = \theta_b = -\theta_a$ ). Any potential reduction in reconstruction error is limited by the difficulty of finding correspondences in more widely spaced projection pairs. The next section examines observation error associated with the proposed correspondence algorithm (§3.3.2).

#### 4.3 Reconstruction sensitivity to correspondence error

The other potential source of reconstruction error is the mismatching of vessel trace points between views. Both vessel topology and the algorithm by



which correspondence is established contribute to this error. This section describes the methodology and results of experiments that examine both aspects of error in the correspondence algorithm described in §3.3.2.

§4.3.1 examines the sensitivity of the correspondence measure for known point-pairs to measurement errors in the point-pair and fiducial marker image coordinates. In §4.3.2 the results of matching simulated vessel traces are presented, and §4.3.3 describes the results of matching actual vessel traces from DSA image pairs. §4.3.4 concludes with a summary.

#### 4.3.1 Correspondence measure sensitivity to measurement error

The likelihood that a point-pair is in correspondence is based on the 'closeness' or distance between the intersection of 3-d lines from these point-pairs (§3.3.1.3). This assumption is examined. Computer simulation was used to calculate the probability distributions of these distances for different magnitudes of digitization and observation errors in the image coordinates of the point-pairs and fiducial markers (§4.3.1.1.1-3).

##### 4.3.1.1 Simulation experiments

The basic simulation experiment is similar to that described in §4.2.4.2 and §4.2.5.1 previously. A 3-d test point was reconstructed with error terms in the image coordinates of the test point and fiducial markers. The error terms were randomly drawn from a specified distribution of values. On reconstruction the distance  $d_{mn}$  between the intersection of the 3-d lines was computed (§3.4.6). The basic trial was repeated  $N$  times and a normalized histogram of  $d_{mn}$  was computed. The width of each histogram bin was 0.01 mm. From this probability distribution, the final estimate of the distance value  $d_{mn}$  is given by the 'median' value of the distribution. The median of a probability distribution is defined here as the value  $d_{med}$  for which larger and smaller values of  $d_{mn}$  are equally probable (Bevington 1969). This measure was chosen because the distribution was found to be skewed.

The dependence of  $d_{mn}$  on the magnitude of digitization and observation

errors in the image coordinates of the point-pair and fiducial markers was examined by simulation. In each of these simulation experiments the basic trial was repeated 5,000 times, for which the round-off error associated with  $d_{mn}$  was determined to be  $\pm 0.005$  mm. This estimate of error was determined by computing  $d_{mn}$  in the absence of measurement errors. Since values of  $d_{mn}$  are compared with values from other match pairs that differ by one to three pixels in their disparities, the results of the simulations for a test point  $P^{\rightarrow}$  at the origin should be generalizable for other locations. In these experiments only asymmetric incidences were considered.

#### 4.3.1.1.1 Expt. 1: Dependence on angular separation

The dependence of  $d_{mn}$  on angular separation was simulated for digitization errors of  $\Delta d_d = \pm 0.15$  mm in the image coordinates of the test point and fiducial markers individually. The test point  $P^{\rightarrow}$  was reconstructed from image pairs separated by angles of  $\Delta\theta = 5, 10, 15$ , and 90 degrees.

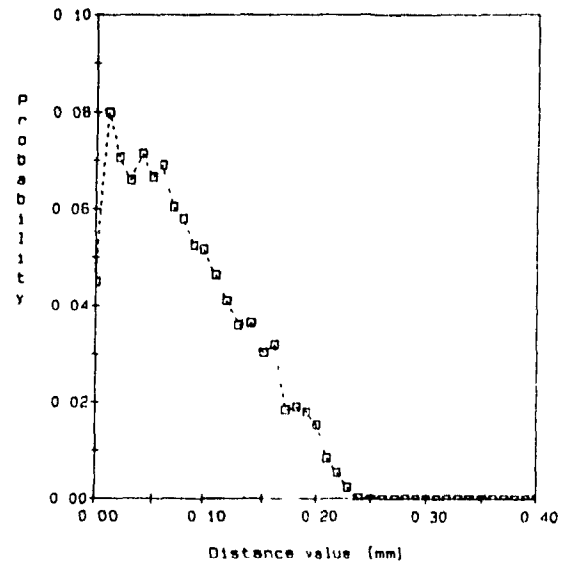
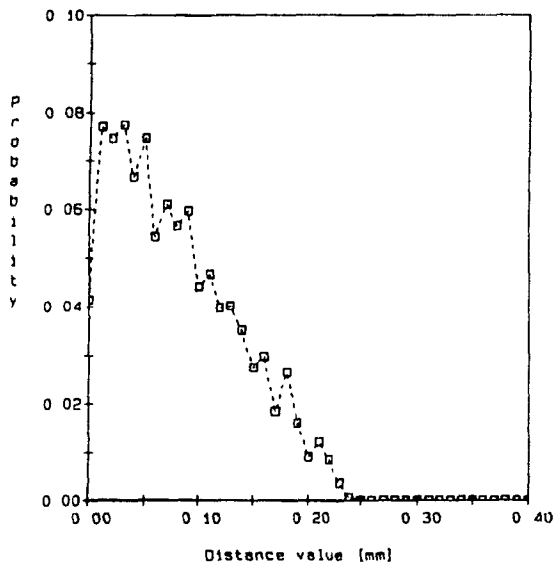
Fig. 4.19 shows the normalized histograms of  $d_{mn}$  for errors in the image coordinates of the test point. The maximum value in the histograms is observed at a value of  $d_{mn}$  other than zero. This bias is thought to be due to the combination of round-off error in the reconstruction calculations and in histogram 'binning.' It is also noted that the distributions and their median values do not change significantly with increased angular separation. Invariance in  $d_{med}$  with angular separation is explained by taking into account that the projection pair is separated by rotation  $\Delta\theta$  about the y-axis. For this recording geometry, errors in the 'y' image coordinates will affect  $d_{mn}$  more than errors in the 'x' image coordinates of the test point.

The normalized histograms of  $d_{mn}$  for errors in image coordinates of the fiducial markers are shown in Fig. 4.20. Observations made for Fig. 4.19 hold for Fig. 4.20. As expected the median values from this source of error are smaller.

Figure 4.19 Probability distributions of  $d_{mn}$  for angular separations of a) 5, b) 10, c) 15, and d) 90 degrees, given a digitization error of  $\Delta d_d = \pm 0.15 \text{ mm}$  in the test point image coordinates.

a) 5 degrees,  $d_{med} = 0.07 \pm 0.01 \text{ mm}$ .

b) 10 degrees,  $d_{med} = 0.07 \pm 0.01 \text{ mm}$ .



c) 15 degrees,  $d_{med} = 0.07 \pm 0.01 \text{ mm}$ .

d) 90 degrees,  $d_{med} = 0.07 \pm 0.01 \text{ mm}$ .

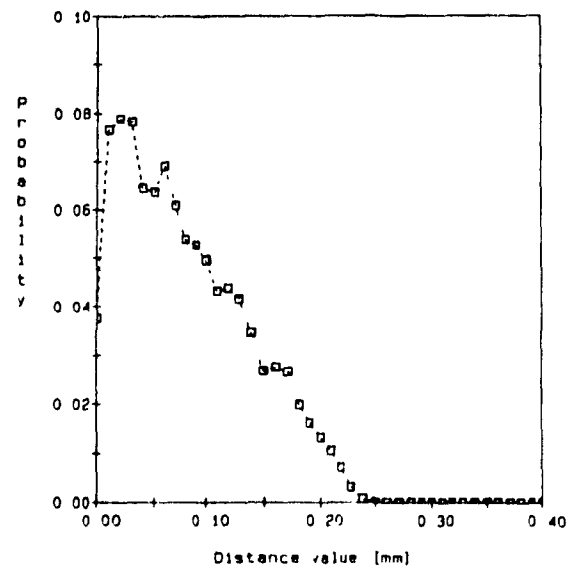
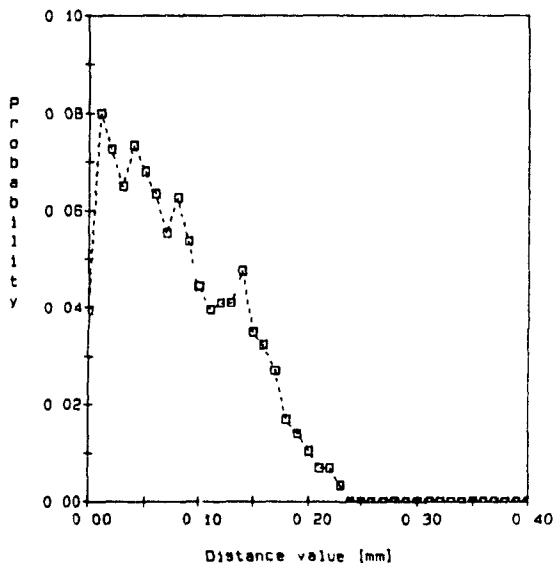
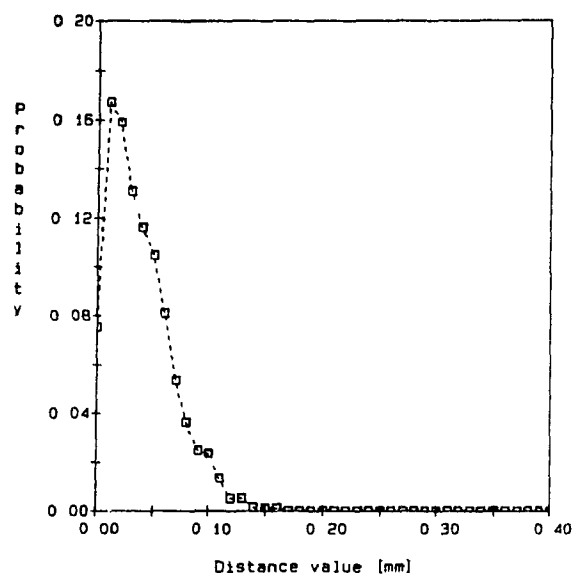
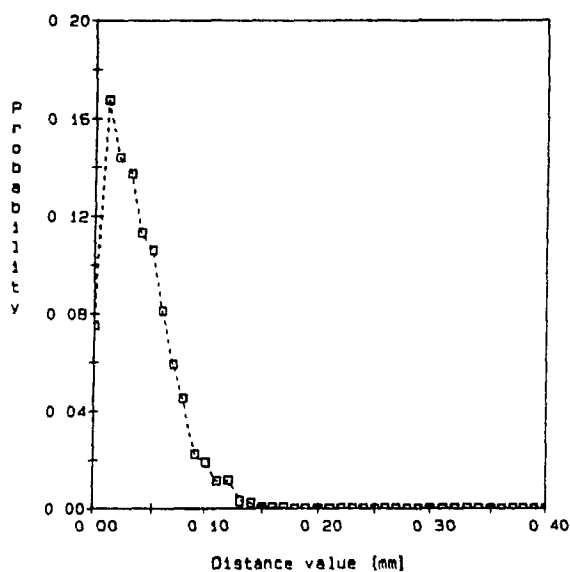


Figure 4.20 Probability distributions of  $d_{mn}$  for angular separations of a) 5, b) 10, c) 15, and d) 90 degrees, given a digitization error of  $\Delta d_d = \pm 0.15 \text{ mm}$  in the fiducial marker image coordinates.

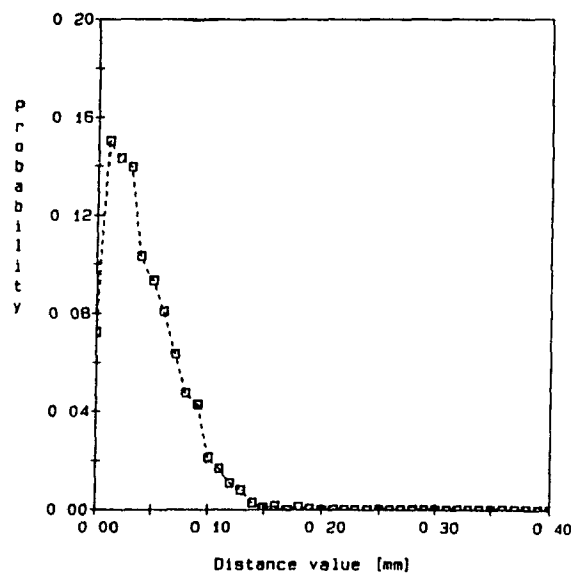
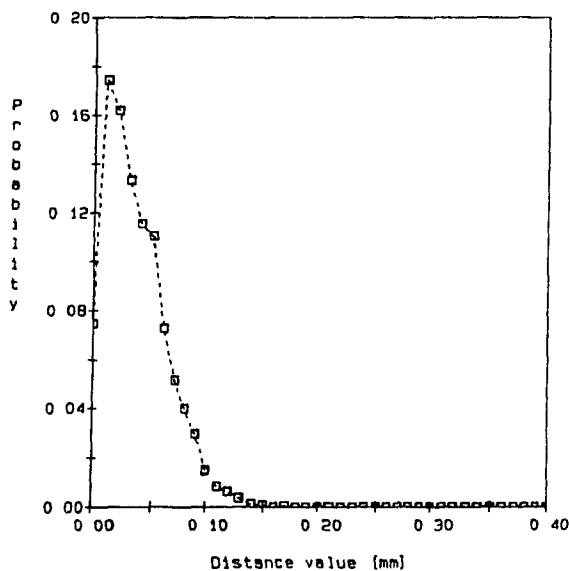
a) 5 degrees,  $d_{med} = 0.03 \pm 0.01 \text{ mm}$ .

b) 10 degrees,  $d_{med} = 0.03 \pm 0.01 \text{ mm}$ .



c) 15 degrees,  $d_{med} = 0.03 \pm 0.01 \text{ mm}$ .

d) 90 degrees,  $d_{med} = 0.03 \pm 0.01 \text{ mm}$ .



#### 4.3.1.1.2 Expt. 2: Dependence on magnitude of measurement error

The effect of different magnitudes of measurement error on  $d_{mn}$  was simulated. Measurement errors in the image coordinates of the test point pairs and fiducial markers were considered separately and in combination. The test point  $P^{\rightarrow}$  was reconstructed from image pairs separated by an angle of  $\Delta\theta = 5$  degrees.

Table 4.13 lists the median values  $d_{med}$  for different magnitudes of digitization and observation errors in the test point image coordinates only. Values of  $d_{med}$  indicate that  $d_{mn}$  is proportional to the magnitude of measurement error and will be sufficiently different so that observation errors can be discriminated.

Table 4.14 lists the median values  $d_{med}$  for different magnitudes of digitization and observation errors in the fiducial marker image coordinates only. As expected  $d_{mn}$  is proportional to the magnitude of measurement error and is approximately half of the values in Table 4.13.

Tables 4.15-4.17 list the median values  $d_{med}$  resulting from observation errors in image coordinates under different conditions of measurement error in the fiducial marker image coordinates. Digitization error was  $\pm 0.15$  mm in both the test point and fiducial marker image coordinates. As the observation error in the fiducial marker image coordinates increases, Table 4.15 shows that differences in  $d_{med}$  between different magnitudes of observation errors in the test point image coordinates decrease. Tables 4.16 and 4.17 show the contribution of observation errors in the 'x' and 'y' test point image coordinates respectively. The results in Tables 4.16 and 4.17 indicate that  $d_{mn}$  will primarily reflect observation errors in the 'y' image coordinates for this image-recording geometry. However, reconstruction error is predominately due to error in the 'x' image coordinates.

#### 4.3.2 Error sensitivity of correspondence algorithm

The disparity and reconstruction errors associated with the correspondence algorithm described in §3.3.2 were estimated by matching

Table 4.13 Median values of  $d_{mn}$  for different magnitudes of digitization and observation errors in test point image coordinates.

Digitization error $\Delta d_d$ [mm]	Observation error $(d_o)_{rms}$ [mm]	Median of $d_{mn}$ $d_{med} \pm 0.01$ [mm]
0.15	0.0	0.07
0.3	0.0	0.14
0.0	0.3	0.23
0.0	0.6	0.45
0.15	0.3	0.24
0.15	0.6	0.46

Table 4.14 Median values of  $d_{mn}$  for different magnitudes of digitization and observation errors in fiducial marker image coordinates.

Digitization error $\Delta d_d$ [mm]	Observation error $(d_o)_{rms}$ [mm]	Median of $d_{mn}$ $d_{med} \pm 0.01$ [mm]
0.15	0.0	0.03
0.3	0.0	0.06
0.0	0.3	0.11
0.0	0.6	0.22
0.15	0.3	0.12
0.15	0.6	0.23

Table 4.15 Median values of  $d_{mn}$  for different magnitudes of observation errors in the test point and the fiducial marker image coordinates. Digitization error,  $\Delta d_d = \pm 0.15$  mm.

Fiducial Marker Image Coordinate Error $(d_o)_{rms}$ [mm]	Test Point Image Coordinate Error $(d_o)_{rms}$ [mm]	Median of $d_{mn}$ $d_{med} \pm 0.01$ [mm]
0.0	0.0	0.08
0.0	0.3	0.24
0.0	0.6	0.45
0.3	0.0	0.13
0.3	0.3	0.26
0.3	0.6	0.47
0.6	0.0	0.23
0.6	0.3	0.32
0.6	0.6	0.49

Table 4.16 Median values of  $d_{mn}$  for different magnitudes of observation errors in the test point 'x' image coordinate and in the fiducial marker image coordinates. Digitization error,  $\Delta d_d = \pm 0.15$  mm.

Fiducial Marker Image Coordinate Error ( $d_o$ ) <sub>rms</sub> [mm]	Test Point Image Coordinate Error ( $d_o$ ) <sub>rms</sub> [mm]	Median of $d_{mn}$ $d_{med} \pm 0.01$ [mm]
0.0	0.0	0.03
0.0	0.3	0.03
0.0	0.6	0.03
0.3	0.0	0.12
0.3	0.3	0.12
0.3	0.6	0.13

Table 4.17 Median values of  $d_{mn}$  for different magnitudes of observation errors in the test point 'y' image coordinate and in the fiducial marker image coordinates. Digitization error,  $\Delta d_d = \pm 0.15$  mm.

Fiducial Marker Image Coordinate Error ( $d_o$ ) <sub>rms</sub> [mm]	Test Point Image Coordinate Error ( $d_o$ ) <sub>rms</sub> [mm]	Median of $d_{mn}$ $d_{med} \pm 0.01$ [mm]
0.0	0.0	0.08
0.0	0.3	0.24
0.0	0.6	0.47
0.3	0.0	0.14
0.3	0.3	0.27
0.3	0.6	0.47

computer-generated stereo and biplane images of a 3-d piece-wise constant curve. Details of the experiment and algorithm parameters are described in §4.3.2.1 and §4.3.2.2-3 present the results.

#### 4.3.2.1 Method

Sampled 3-d piece-wise constant curves were projected using transformation matrices calibrated from actual DSA images (§3.4.3). The points in the lateral trace ( $\theta=0$  degrees) were then matched to the points in the lateral stereo ( $\theta=7$  degrees) and anterior-posterior traces ( $\theta=90$  degrees). The parameters used in the algorithm for stereo pairs were  $s_r=4$ ,  $\Delta m=2$  for the initial correspondence and for relaxation labeling:  $K=2$ ,  $Q=0.3$ ,  $G=0.4$ ,  $\psi_1=2$ , and  $\psi_2=2$ . Parameters for biplane matching were the same except for  $\psi_1$ , the constraint of disparity continuity was not applied. a  $|M(m,n)|$  ranged from 0 to 10, and the algorithm was stopped after 20 iterations. When  $p_0 \geq 0.75$ , the corresponding trace point was not reconstructed. Reconstruction by this algorithm is referred to as method (II).

Results of the correspondence search were evaluated by comparing the estimated and actual disparity values by using both mean error (i.e. actual-estimated) and worst case (W) differences. The worst case for differences between actual,  $\Delta x$ , and estimated,  $\Delta x_e$ , disparities for 'x' is given by

$$W = \max_{1 \leq i \leq n} | \Delta x_i - \Delta x_{e,i} | \quad (4.9)$$

The worst case difference for 'y' disparities is similarly defined. The reconstruction that results from a particular set of trace point correspondences is also evaluated by comparison to the known 3-d coordinates of the piece-wise constant curve using mean and worst case differences.

For comparison, the mean and worst case differences in the disparities and reconstructions were computed for the correspondences after 'chaining' the initial estimates (see §3.3.1.3). This is denoted as method (I).

§4.3.2.2 and §4.3.2.3 present results of the correspondence search and



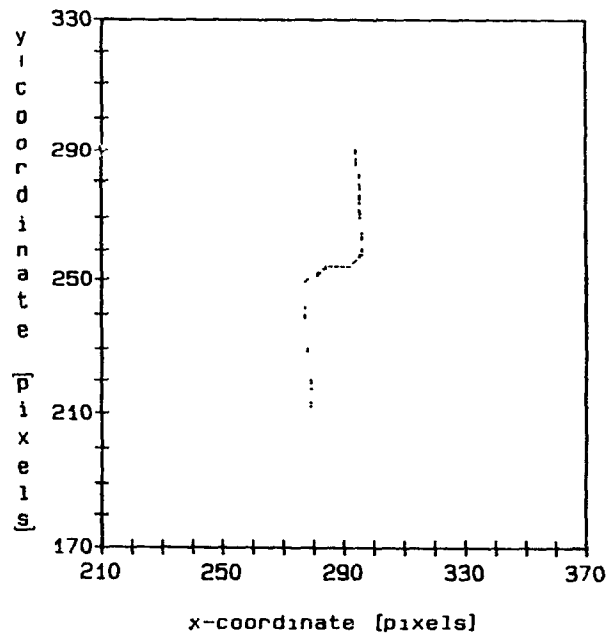
reconstruction for two examples of 3-d curves that are typical of the geometrical complexities of vessels found in the cerebral vasculature.

#### 4.3.2.2 Example 1

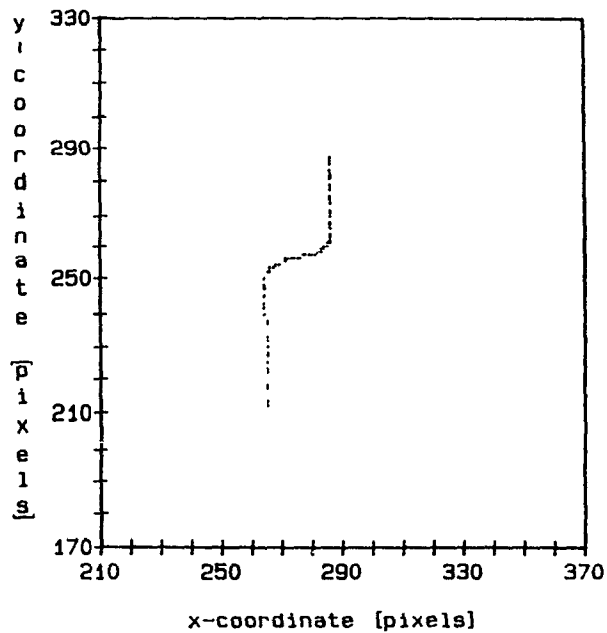
Fig. 4.21 shows plots of a 3-d curve projected into lateral, lateral stereo, and anterior-posterior views. The traces consist of 72, 77, and 83 sample points in the lateral, lateral stereo, and anterior-posterior images respectively.

Tables 4.18-19 list the mean and worst case differences in the disparities and reconstructions that result from matching between the stereo pair of traces (Fig. 4.21a) and b)). The differences in disparity and reconstruction indicate that relaxation (method II) of the initial estimates of correspondence reduces the worst case value. The worst case error is found to occur along horizontal sections of the trace where matching is ambiguous. This is seen in Fig. 4.22b) and c) where the results of stereo reconstruction have been re-projected into the anterior-posterior view. Fig. 4.22a) shows the re-projection of the reconstruction from the known correspondences in the stereo trace pair and represents the results of a 'best-case' reconstruction.

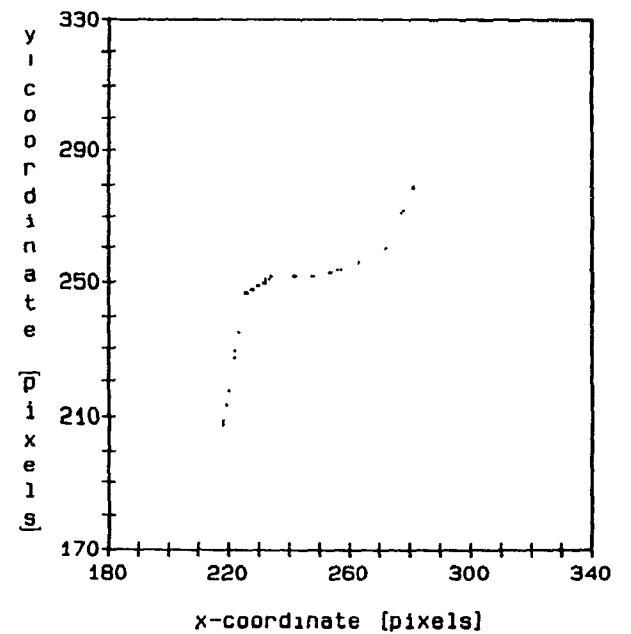
The mean and worst case differences in disparities and reconstructions that result from matching between biplane trace pairs (Fig. 4.21a) and c)) are listed in Tables 4.20-21. In the biplane case, improvements similar to the stereo case are observed in the disparities and reconstructions, but are smaller in magnitude. Again the worst-case reconstruction is observed along the horizontal sections. Given the magnitude of these errors it is difficult to observe them on re-projection, instead a plot of the relationship between indices of the lateral and anterior-posterior trace points (§3.3.2) is preferred (Fig. 4.23). The known correspondences are compared to those estimated by chaining (method I) and by relaxation labeling (method II) in Fig. 4.23a) and b) respectively. Deviations from the known correspondences in these plots are largely due to incorrect matching along projected horizontal sections. Overall, the results of relaxation labeling render a better estimate of correspondences than does chaining the initial estimates alone.



a) Lateral



b) Lateral stereo



c) Anterior-posterior

Figure 4.21 Drawings of a) lateral, b) lateral stereo, and c) anterior-posterior projections of a 3-d piece-wise constant curve (Example 1).

Table 4.18 Error in disparity associated with correspondences determined by methods I and II for stereo trace pair 1.

Correspondence Method	Disparity Error in [pixels]					
	mean $\pm \sigma$				worst case	
	$\Delta x$		$\Delta y$		$\Delta x$	$\Delta y$
I	-0.6	1.1	2.5	1.5	4	5
II	-0.5	0.8	1.9	1.3	2	4

Table 4.19 Error in coordinate reconstruction associated with the known correspondences, and correspondences determined by methods I and II for stereo trace pair 1.

Correspondence Method	Reconstruction Error in [mm]		
	mean $\pm \sigma$		worst case
	z		z
Actual	3.2	2.8	8.0
I	7.7	2.9	13.8
II	6.9	1.7	10.1

Table 4.20 Error in disparity associated with correspondences determined by methods I and II for biplane trace pair 1.

Correspondence Method	Disparity Error in [pixels]					
	mean $\pm \sigma$				worst case	
	$\Delta x$		$\Delta y$		$\Delta x$	$\Delta y$
I	-0.3	2.2	-0.6	1.2	8	3
II	-0.3	1.9	-0.6	1.2	6	3

Table 4.21 Error in coordinate reconstruction associated with the known correspondences, and correspondences determined by methods I and II for biplane trace pair 1.

Correspondence Method	Reconstruction Error in [mm]		
	mean $\pm \sigma$		worst case
	z		z
Actual	0.0	0.1	0.4
I	-0.2	0.5	1.8
II	-0.2	0.4	1.4

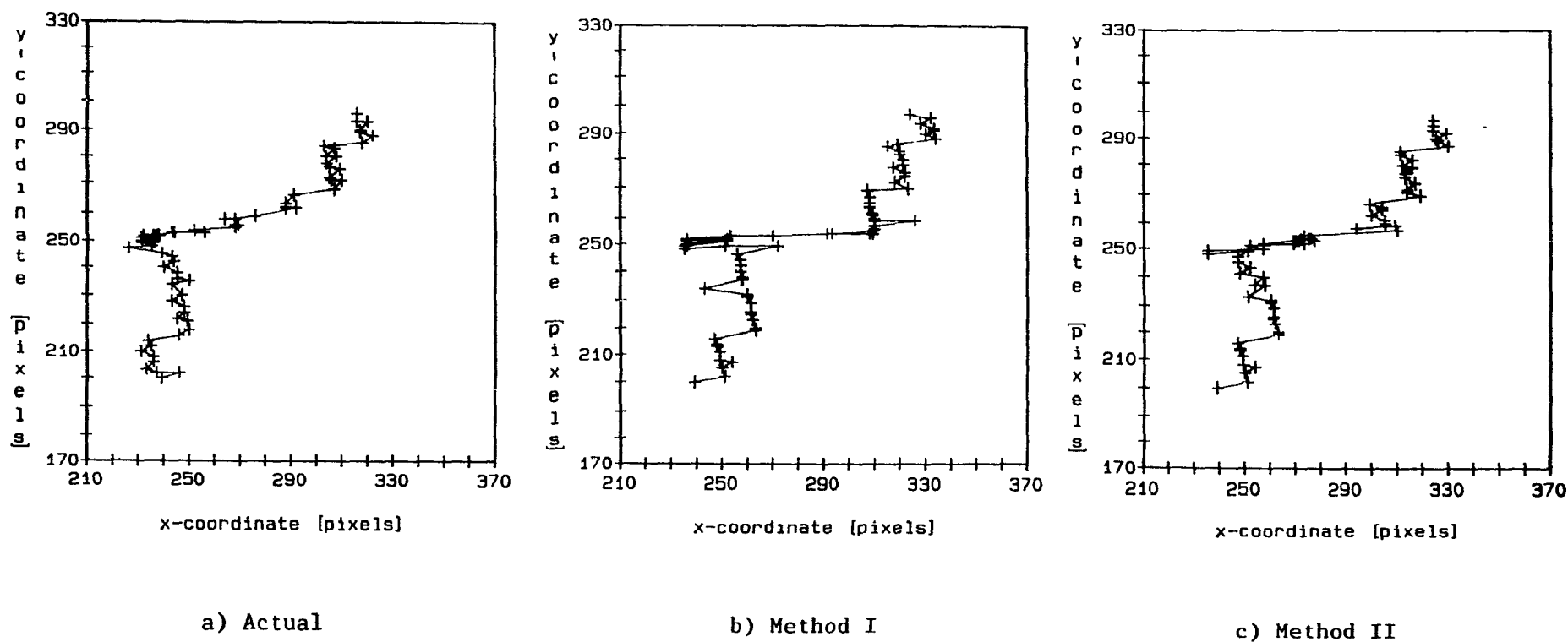
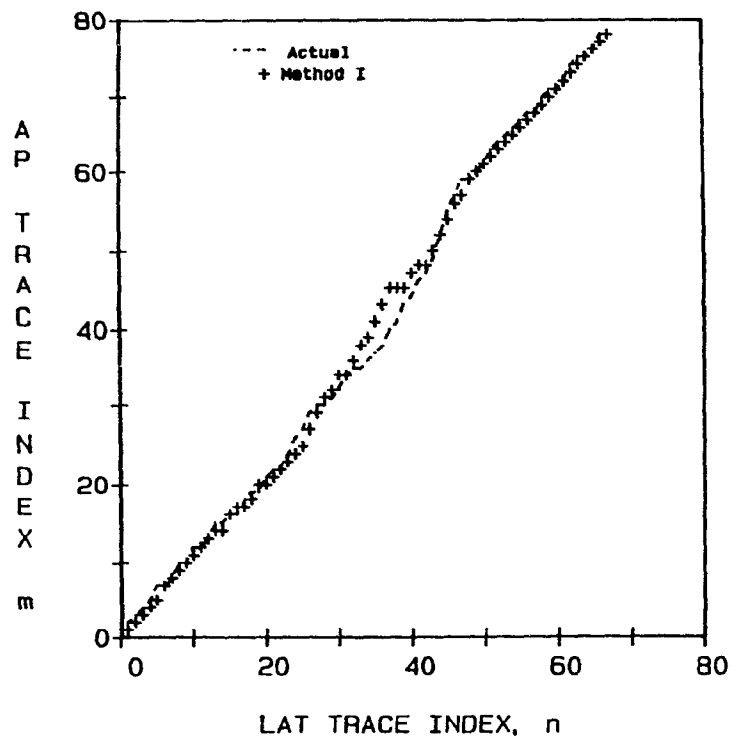
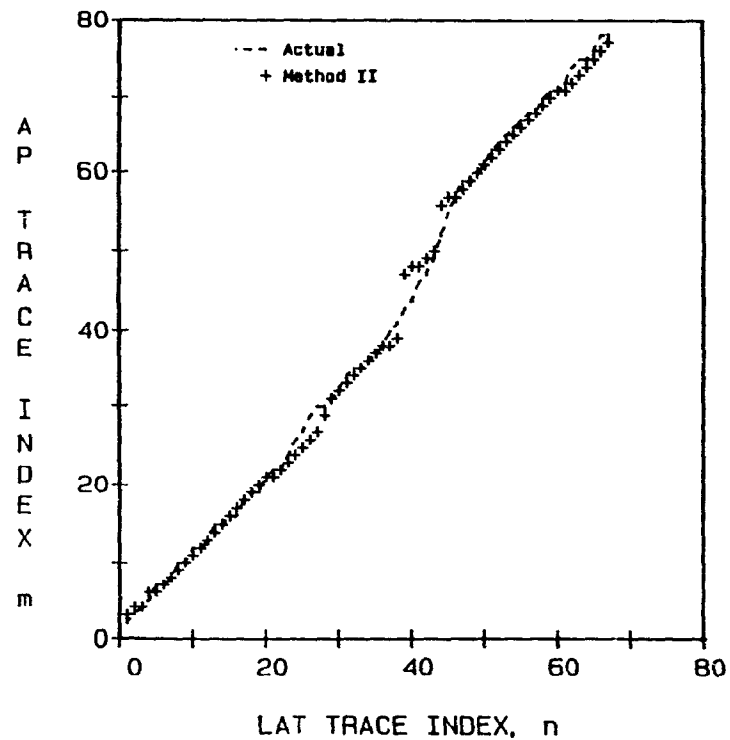


Figure 4.22 Anterior-posterior view re-projection of stereo reconstruction in Example 1 trace pair from a) actual correspondences, and correspondences determined by b) method I and c) method II.



a) Method I



b) Method II

Figure 4.23 Plot of indices between lateral and anterior-posterior traces in Example 1 comparing known correspondences with those determined by a) method I and b) method II.

#### 4.3.2.3 Example 2

A more complex 3-d curve was considered. Fig. 4.24 shows plots of the curve's lateral, lateral stereo, and anterior-posterior projections. The projected curve in the lateral, lateral stereo, and anterior-posterior images consists respectively of 161, 160, and 160 sample points.

Tables 4.22-23 list the mean and worst case differences in the disparities and reconstructions that result from matching between the stereo pair of traces (Fig. 4.24a) and b)). Anterior-posterior re-projections of these reconstructions are shown in Fig. 4.25. The mean and worst case differences in disparities and reconstructions that result from matching between biplane trace pairs (Fig. 4.24a) and c)) are listed in Tables 4.24-25. The plots of correspondence between indices of the lateral and anterior-posterior trace points are shown in Fig. 4.26.

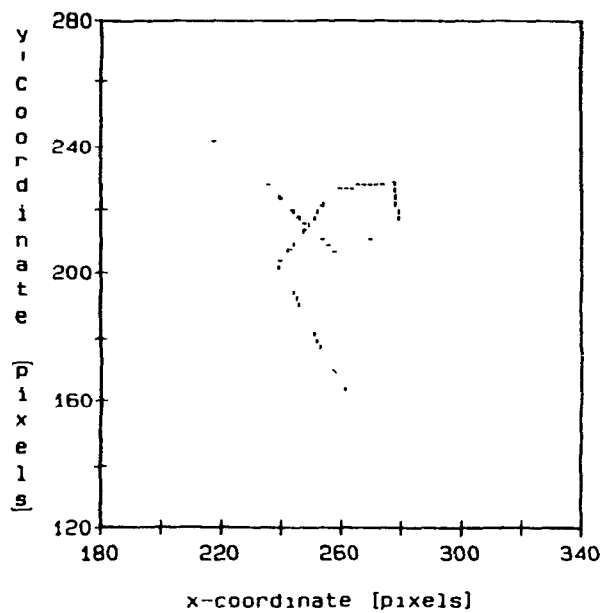
Results of matching stereo and biplane traces again show an improvement in correspondence and reconstruction error with the application of relaxation labeling (method II) under constraints of continuity and connectivity. Correspondence errors occur primarily along the projected horizontal sections of the trace.

#### 4.3.3 Application to cerebral DSA

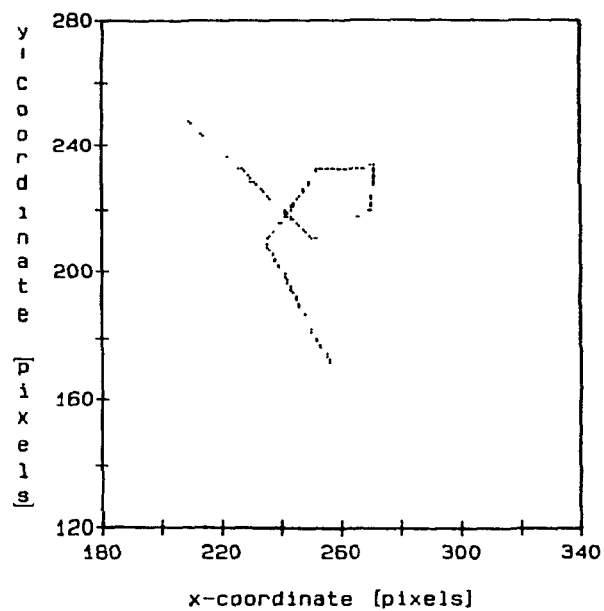
Two examples of the application of the correspondence algorithm to vessel traces from DSA image pairs are presented. §4.3.3.1 summarizes the method used to collect the DSA images and extract the vessel traces. §4.3.3.2-3 presents two vessels reconstructed from its stereo and biplane projections using the procedure described in §3.4.

##### 4.3.3.1 Method

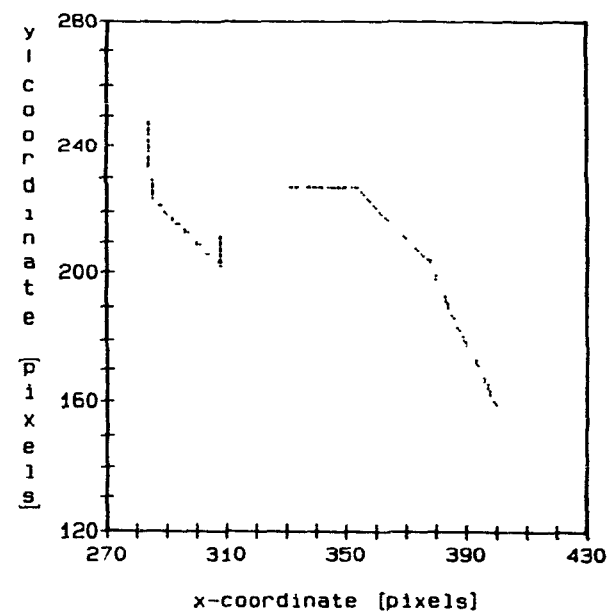
DSA images of a patient fitted with a stereotactic frame were collected at three projections  $\theta \approx 0, 7, \text{ and } 90$  degrees on a Technicare DR-960 DSA unit interfaced to a Philips CsI 154mm/231mm image intensifier operating in 154mm mode. All images were digitized to 10 bits and sampled on a 512x512



a) Lateral



b) Lateral stereo



c) Anterior-posterior

Figure 4.24 Drawings of a) lateral, b) lateral stereo, and c) anterior-posterior projections of a 3-d piece-wise constant curve (Example 2).

Table 4.22 Error in disparity associated with correspondences determined by methods I and II for stereo trace pair 2.

Correspondence Method	Disparity Error in [pixels]					
	mean $\pm \sigma$				worst case	
	$\Delta x$		$\Delta y$		$\Delta x$	$\Delta y$
I	-2.0	1.0	-0.9	2.2	5	4
II	-1.8	0.9	-0.7	2.0	4	4

Table 4.23 Error in coordinate reconstruction associated with the known correspondences, and correspondences determined by methods I and II for stereo trace pair 2.

Correspondence Method	Reconstruction Error in [mm]			
	mean $\pm \sigma$		worst case	
	z		z	
Actual	1.3	2.1	9.1	
I	7.5	2.6	14.2	
II	6.8	2.1	12.9	

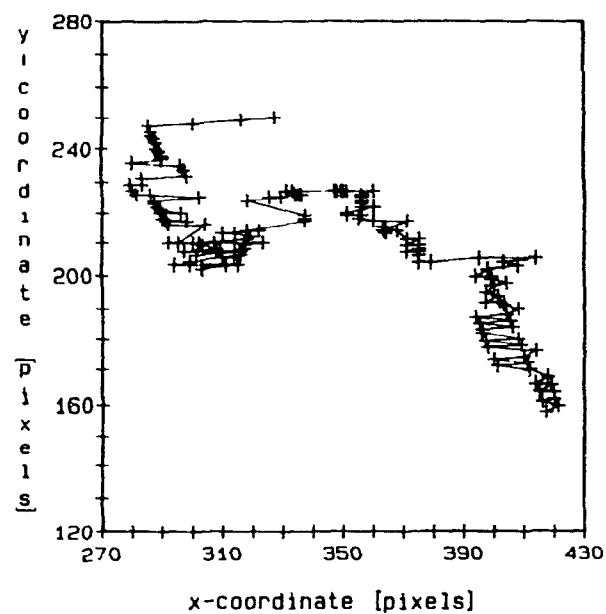
Table 4.24 Error in disparity associated with correspondences determined by methods I and II for biplane trace pair 2.

Correspondence Method	Disparity Error in [pixels]					
	mean $\pm \sigma$				worst case	
	$\Delta x$		$\Delta y$		$\Delta x$	$\Delta y$
I	1.0	2.7	0.2	1.0	13	2
II	0.4	2.2	0.1	1.0	11	2

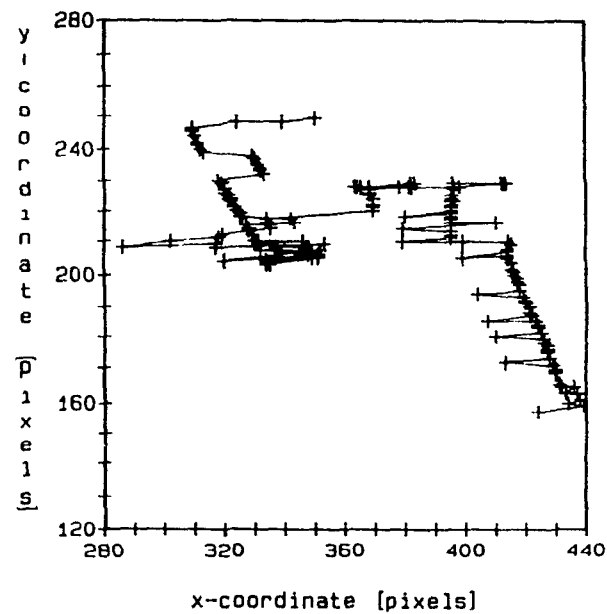
Table 4.25 Error in coordinate reconstruction associated with the known correspondences, and correspondences determined by methods I and II biplane trace pair 2.

Correspondence Method	Reconstruction Error in [mm]			
	mean $\pm \sigma$		worst case	
	z		z	
Actual	0.0	0.1	0.2	
I	-0.2	0.6	2.7	
II	-0.2	0.5	1.3	

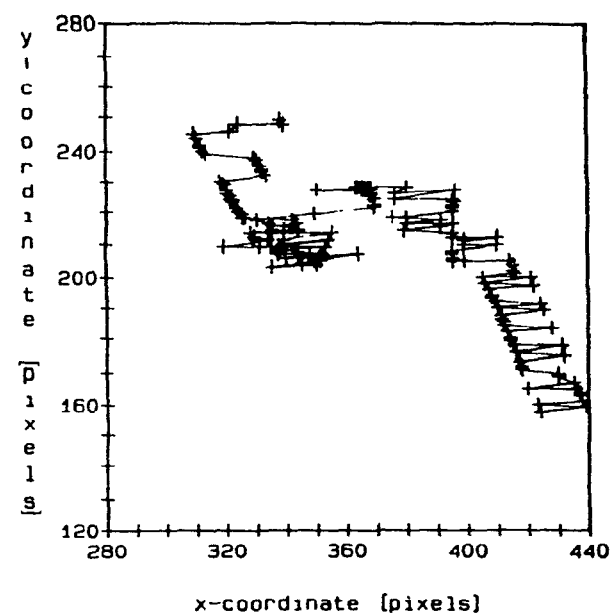




a) Actual

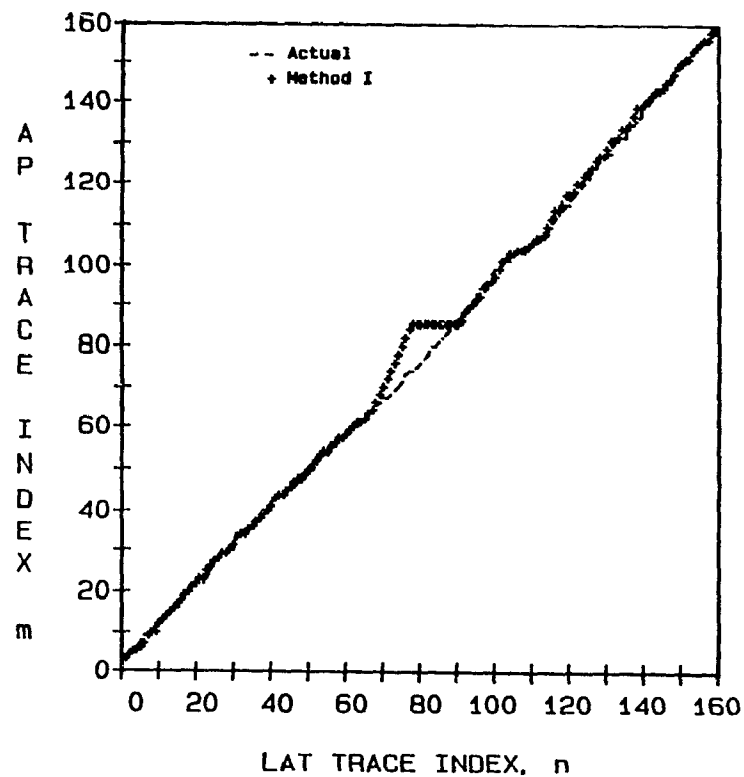


b) Method I

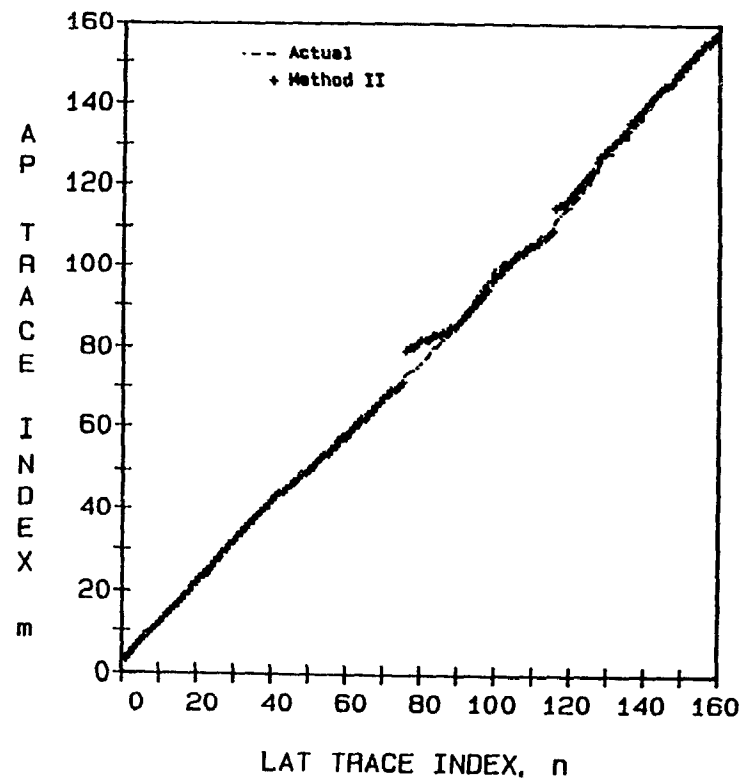


c) Method II

Figure 4.25 Anterior-posterior view re-projection of stereo reconstruction in Example 2 trace pair from a) actual correspondences, and correspondences determined by b) method I and c) method II.



a) Method I



b) Method II

Figure 4.26 Plot of indices between lateral and anterior-posterior traces in Example 2 comparing known correspondences with those determined by a) method I and b) method II.

matrix. A focal spot of 1.2mm width (nominal) was used. The focal length was approximately 120cm, and geometric magnification was approximately 1.25 in each projection. Images were transferred for processing onto a VAX 11/750.

Vessels' center-lines were sampled manually. Sampling of vessels that are superimposed or greatly foreshortened was performed by the observer viewing the images stereoscopically (§3.4.4). By these means matching vessel traces from stereo views were selected. The anterior-posterior trace was found after the stereo pairs were reconstructed and re-projected into the anterior-posterior view. The vessel that most resembles the re-projection was selected and tracked.

The correspondence algorithm proposed in §3.3.2 was used to find the matches between vessel trace points in stereo and biplane images. From the paired trace points the 3-d vessel coordinates were estimated. The parameters used in the algorithm for stereo pairs were  $s_r=10$  and  $\Delta m=4$  for the initial correspondence, and for relaxation:  $K=2$ ,  $Q=0.3$ ,  $G=0.4$ ,  $\psi_1=3$ , and  $\psi_2=3$ . Parameters for biplane matching were the same, except for  $\psi_1$  which was not used. The range of  $a|M(m,n)|$  was from 0 to 10 and the algorithm was stopped after 20 iterations. When  $p_\theta \geq 0.75$ , the corresponding trace point was not reconstructed.

Two examples of vessel traces matched and reconstructed from stereo and biplane images are presented. In each example the lateral trace points were matched to points in the lateral stereo and the anterior-posterior traces. There were no trace point pairs with  $p_\theta \geq 0.75$ , and all paired points were reconstructed.

#### 4.3.3.2 Example 1

Figs. 4.27a) and b) show a stereo pair of vessel traces which were matched. The resulting matched vessel trace points were used to reconstruct the vessel shown re-projected in the anterior-posterior DSA image (Fig. 4.27c). Fig. 4.27d) shows the vessel that most resembles the re-projection in Fig. 4.27c).

The differences between traces in Fig. 4.27c) and d) are larger than

Figure 4.27 Example 1: Illustration of a vessel reconstructed from lateral stereo DSA images a) & b). The reconstructed trace is re-projected into the AP image in c) for comparison with the trace of the actual vessel in d). In a), b), and d) every 5th point in the trace is drawn. The reconstructed points in c) are denoted by 'plus' signs and are joined by lines.

a) Tracked vessel in lateral image



b) Tracked vessel in lateral stereo image



c) AP re-projection



d) Tracked vessel in AP image

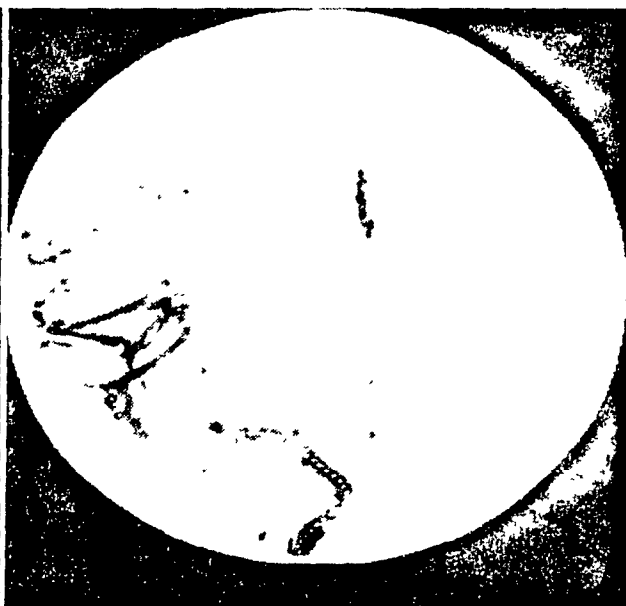
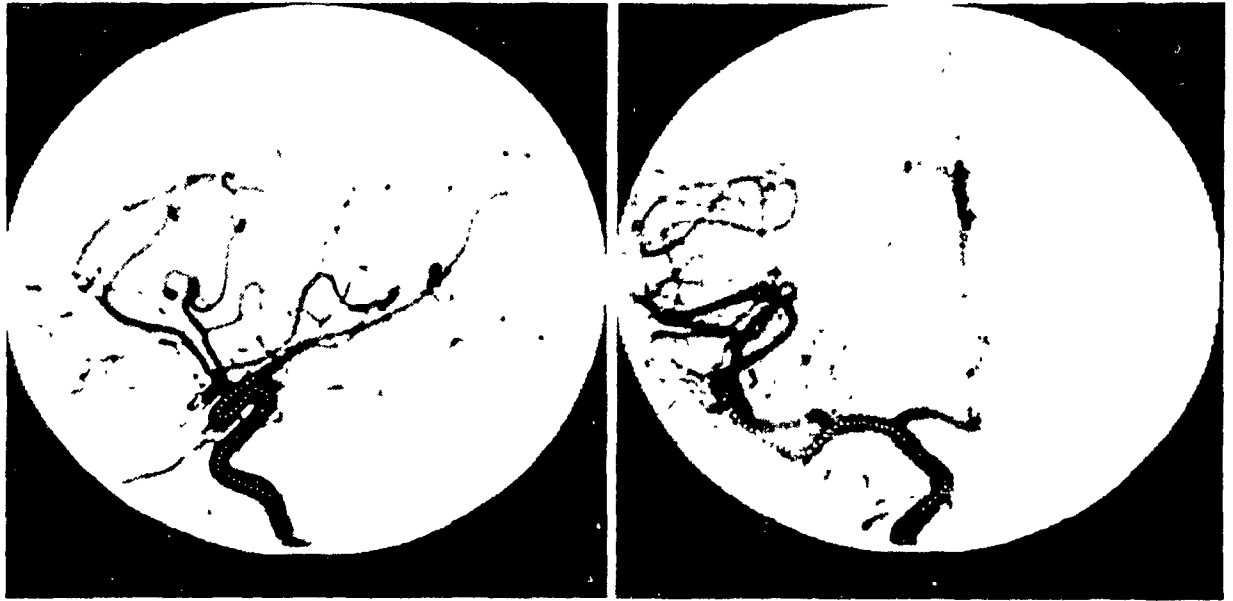


Figure 4.28 Example 1: Illustration of a vessel reconstructed from biplane DSA images a) & b). The AP re-projection of the reconstructed trace is shown in c) for comparison with the actual vessel trace d). In a) and b) every 5th point in the trace is drawn.

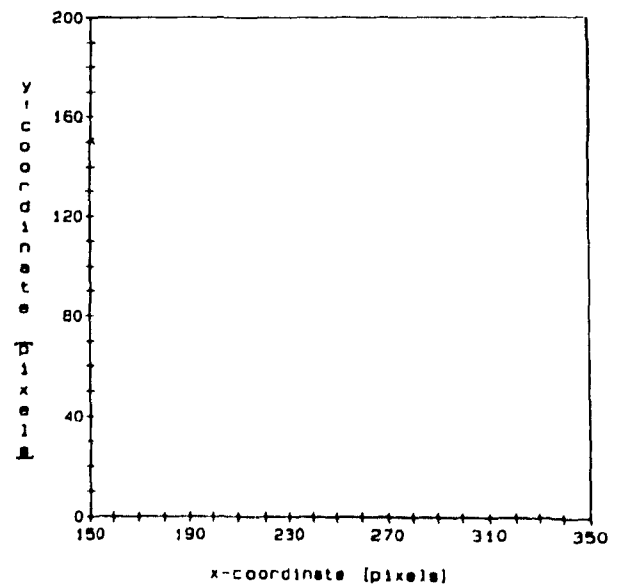
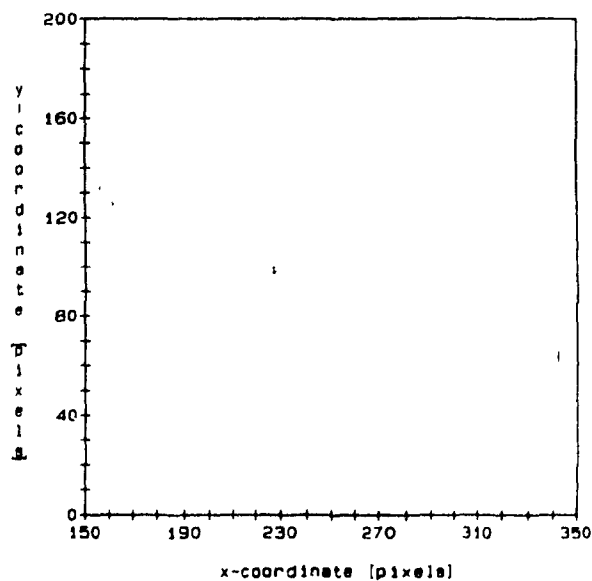
a) Tracked vessel in lateral image

b) Tracked vessel in AP image



c) AP re-projection

d) Actual AP vessel trace



what would be expected on the basis of the simulation experiments. What is different in this case is the addition of measurement error from the tracking process. Errors in the sampled vessel are probably larger than  $\pm 1$  pixel. As expected the largest correspondence errors occur along the projected horizontal sections of the traces.

Figs. 4.28a) and b) show the traces from the lateral and anterior-posterior images which were matched and used to reconstruct the vessel indicated. Fig. 4.28c) shows the reconstructed vessel re-projected into the anterior-posterior view. Both the original and re-projected traces are plotted to better illustrate their differences. On comparing these traces, large gaps are seen between reconstructed points. This results when the vessel trace being matched is foreshortened (e.g. the lateral trace in this case).

#### 4.3.3.3 Example 2

Figs. 4.29 and 4.30 illustrate the sequence of reconstruction of a vessel from lateral stereo and biplane DSA images respectively.

Fig. 4.29c) shows the anterior-posterior re-projection of the stereo reconstructed vessel. In comparison to Fig. 4.29d), there are large errors at points where the vessel in the lateral DSA image is foreshortened and folds over itself. The vessel was tracked incorrectly in those segments and consequently reconstruction artifacts such as the 'loop' in Fig. 4.29c) arose.

The result of biplane reconstruction shown in Fig. 4.30c) exhibits the same errors as seen with the previous example. Segments of the vessel in the lateral DSA image that are almost completely foreshortened do not match well with the points in the anterior-posterior trace. Mismatching occurs because there is no longer one to one mapping between the points in the trace pair, and the indices in the anterior-posterior trace differ by more than  $\psi_2$ . For both examples, the resulting gaps in the reconstruction can be approximated by linear interpolation because these vessel sections are almost straight.

Figure 4.29 Example 2: Illustration of a vessel reconstructed from lateral stereo DSA images a) & b). The reconstructed trace is re-projected into the AP image in c) for comparison with the trace of the actual vessel in d). In a), b), and d) every 5th point in the trace is drawn. The reconstructed points in c) are denoted by 'plus' signs and are joined by lines.

a) Tracked vessel in lateral image

b) Tracked vessel in lateral stereo image



c) AP re-projection

d) Tracked vessel in AP image



Figure 4.30 Example 2: Illustration of a vessel reconstructed from biplane DSA images a) & b). The AP re-projection of the reconstructed trace is shown in c) for comparison with the actual vessel trace d). In a) and b) every 5th point in the trace is drawn.

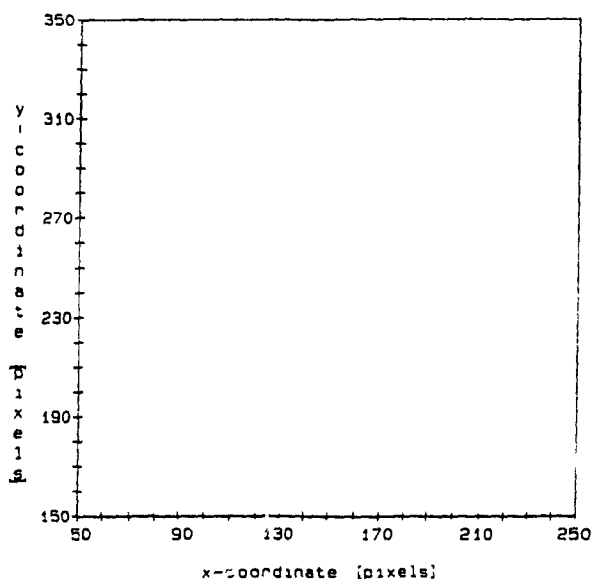
a) Tracked vessel in lateral image



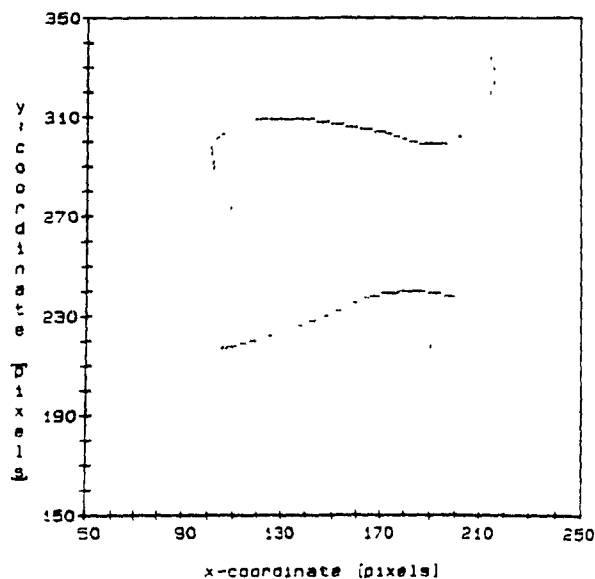
b) Tracked vessel in AP image



c) AP re-projection



d) Actual AP vessel trace





#### 4.3.4 Summary

In this section reconstruction sensitivity to correspondence error was studied. Particularly, the sensitivity of correspondence to measurement errors and the correspondence errors that result from matching simulated and actual vessel traces were considered.

Simulation experiments showed that the correspondence estimate based on the distance between 3-d intersecting rays from the point-pair it represents was proportional to the measurement error in the point-pair and fiducial marker image coordinates. However, there are two limitations associated with this correspondence measure. First, as the observation error in the fiducial marker image coordinates increases, correspondence estimates are no longer proportional to measurement error in the point-pair image coordinates. Differences in the correspondence estimates originating from observation errors in the point-pair image coordinates decrease. The other limitation is that the correspondence estimate does not reflect differences between point-pairs that have the same 'y' disparities (for this recording geometry). This means that ambiguities will occur when points from horizontal sections of traces are matched.

Matching experiments with simulated stereo and biplane projections of 3-d piece-wise constant curves demonstrated that the proposed technique of relaxation labeling of initial correspondences follows global trends in disparity continuity and vessel connectivity better than using a chaining technique. The mean error in the estimated disparities ranges from 1 to 3 pixels after several iterations of relaxation labeling. Expectedly large errors occur when horizontal and/or foreshortened sections of the traces are matched. These errors in disparity, however, are smaller than those appearing from chaining the initial correspondence estimates alone.

The computing time associated with finding the initial correspondences and refining them by relaxation labeling depends on the number of points in each trace, the number of possible matches found for each point, and the number of iterations. For examples 1 (i.e. ~75 points) and 2 (i.e. ~160 points), the computing time to match stereo traces was approximately 0.25

and 1.2 minutes respectively on a VAX-750.

Results of matching stereo and biplane vessel traces from DSA images were similar to those from matching 3-d curve traces. Matching vessel traces from DSA images involved an additional source of error, an observation error associated with the vessel tracking process. Even with stereoscopic views it is difficult to manually track the vessel center-line where the vessel folds on itself. The combination of tracking error and vessel foreshortening produce artifacts in reconstruction from stereo pairs. Vessel reconstruction from biplane pairs had gaps in it corresponding to those sections of vessel in the anterior-posterior image that appear foreshortened in the lateral image. Fortunately, these sections are straight and can be approximated by linear interpolation.

#### 4.4 Conclusions

In this chapter the factors that influence geometric reconstruction of the vessel center-line from stereo and biplane images were examined. These factors were vessel trace point and fiducial marker image coordinate errors and correspondence errors.

The sensitivity of reconstruction to measurement error was shown to depend primarily on the angular separation between the image pair, image pixel size, and the geometric magnification. Reconstruction error was found to be proportional to the image pixel size and inversely proportional to the geometric magnification. Increasing angular separation between views from 5 to 15 degrees drastically decreases the reconstruction error, but will result in an image pair where the stereoscopic impression of depth is distorted. For larger angular separations the improvement in reconstruction decreases. The contribution to reconstruction error from error in the fiducial marker coordinates becomes important when test points are outside the volume defined by the system of fiducial markers.

Reconstruction sensitivity to correspondence error depends on the correspondence algorithm and the vessel topology. The correspondence algorithm has a mean error in disparity that ranges from 1 to 3 pixels. It

was found to be limited in finding matches between horizontal sections of vessel traces and between vessel traces where one of the vessels is foreshortened and superimposed on itself. Part of the problem with superimposed vessels is that they are difficult to track correctly.

The results of reconstructing vessel traces from stereo DSA images showed how large reconstruction error can be when correspondence errors are taken into account. In spite of these errors, the anterior-posterior re-projection of the stereo reconstruction is sufficient to determine the vessel to which it corresponds. Biplane reconstruction of vessel traces showed errors primarily due to vessel foreshortening in one of the images. The missing reconstruction points that result may be approximated by linear interpolation.

In stereotactic operations it is important to avoid blood vessels. By the proposed technique the vessels can be reconstructed and an unobstructed path through the vascular structure plotted. In light of the above results, this will be possible providing the errors associated with the reconstructed vessels are taken into account.

There are basically two ways in which geometric vessel reconstruction can be improved. The first and most obvious is to minimize the influence of the error sources by increasing the image matrix size and geometric magnification. The other is to directly reduce the error associated with vessel tracking, especially in vessels that are self-superimposed, and with the correspondence algorithm. In order to improve on the correspondence algorithm, the possibility that a vessel trace point may match into several points in the conjugate trace should be considered. In addition, other measures of correspondence that could be used to resolve ambiguities that arise from matching points from horizontal sections of traces should be investigated.

## CHAPTER FIVE

### ITERATIVE 3-D RECONSTRUCTION OF VASCULAR IMAGES FROM A FEW VIEWS

#### 5.1 Introduction

An alternate means of reconstructing the 3-d coordinates of vessels from its projections is computed tomography. §5.2 reviews the relevant image reconstruction theory. It would be advantageous and practical if the number of projections used in image reconstruction were kept small (e.g. 4 to 16 projections, especially the 4 views constituting a stereo pair). However, when fewer than the required projections are used in image reconstruction, the reconstructed images tend to be severely contaminated by streak artifacts. The problem of streak artifacts is discussed in §5.3 and §5.4. §5.5 proposes a method to recognize and discount these artifacts by using 'a priori' information about the blood vessels. The proposed method reconstructs a 3-d vascular network in a series of 2-d sections by back-projection and summation of the projections followed by non-linear iterative deconvolution of the summated image. The reconstruction method is tested on both numerical examples and a 3-d wire phantom resembling vasculature. The results are presented in §5.6 and §5.7 respectively, and the chapter is summarized in §5.8.

#### 5.2 Reconstruction theory overview

##### 5.2.1 Preliminaries

"Computed tomography (CT) is a technique by which each slice of the object can be viewed in total isolation, that is, with complete freedom of clutter from adjacent slices" (Barrett and Swindell 1981). CT consists of the reconstruction of a density image from computations on transmission measurements whose paths are restricted to lie within the plane or slice of interest through the object. The actual quantity reconstructed is the x-ray linear attenuation coefficient (Brooks and Di Chiro 1976). The way in which a cross section is reconstructed depends on both the x-ray beam geometry and the measurement system.

The simplest reconstruction procedure arises when the x-ray beam geometry is parallel, and the detectors respond to only those x rays arriving from within a desired thin section of space (Fig. 5.1). It is also assumed here that the material properties of the object are time-invariant.

Fig. 5.2 illustrates the image and Fourier space coordinate systems that are adopted here. The  $x, y$  (cartesian) and  $r; \theta$  (polar) coordinates describe image space. Similarly the  $u, v$  (cartesian) and  $\rho; \phi$  (polar) coordinates describe Fourier space. In image space the  $\xi, \eta$  (cartesian) coordinates can be rotated by  $\phi$  about the origin with respect to the  $x, y$  coordinates.  $\lambda(r; \theta)$  and  $\lambda(\xi, \eta)$  are defined to be the image density of the cross section, in polar and cartesian coordinates respectively, to be reconstructed.

Transmission measurements taken from the object in  $\phi$  direction along lines parallel to the  $\eta$  axis are sets of projections  $f(\xi; \phi)$ ,

$$f(\xi; \phi) = - \log \left( \frac{\Phi_d}{\Phi_0} \right) = \int_{-\infty}^{\infty} \lambda(\xi, \eta) d\eta \quad (5.1)$$

where the fluence of the x-ray beam measured at the detector,  $\Phi_d$ , is related to the incident photon fluence,  $\Phi_0$ , by the linear attenuation coefficients of the object  $\lambda(\xi, \eta)$ . Given a set of measured projections  $f(\xi; \phi)$ , the object  $\lambda(r; \theta)$  can be reconstructed from its projections. There are two conceptually different approaches to the image reconstruction problem. The first approach is the transform method (Bates and Peters 1971; Peters 1973; Lewitt 1983; Louis and Natterer 1983). The other approach consists of algebraic techniques, also known as iterative methods (Gordon and Herman 1974; Herman and Lent 1976; Censor 1981; 1983). Transform and algebraic techniques are reviewed in §5.2.2 and §5.2.4 respectively. §5.2.3 comments on the sampling requirements of transform reconstruction methods.

### 5.2.2 Transform reconstruction methods

The 'projection theorem' relates the projections to the Fourier

Figure 5.1 Parallel x rays propagating through a thin object section  $\lambda(r; \theta)$  towards a detector array.

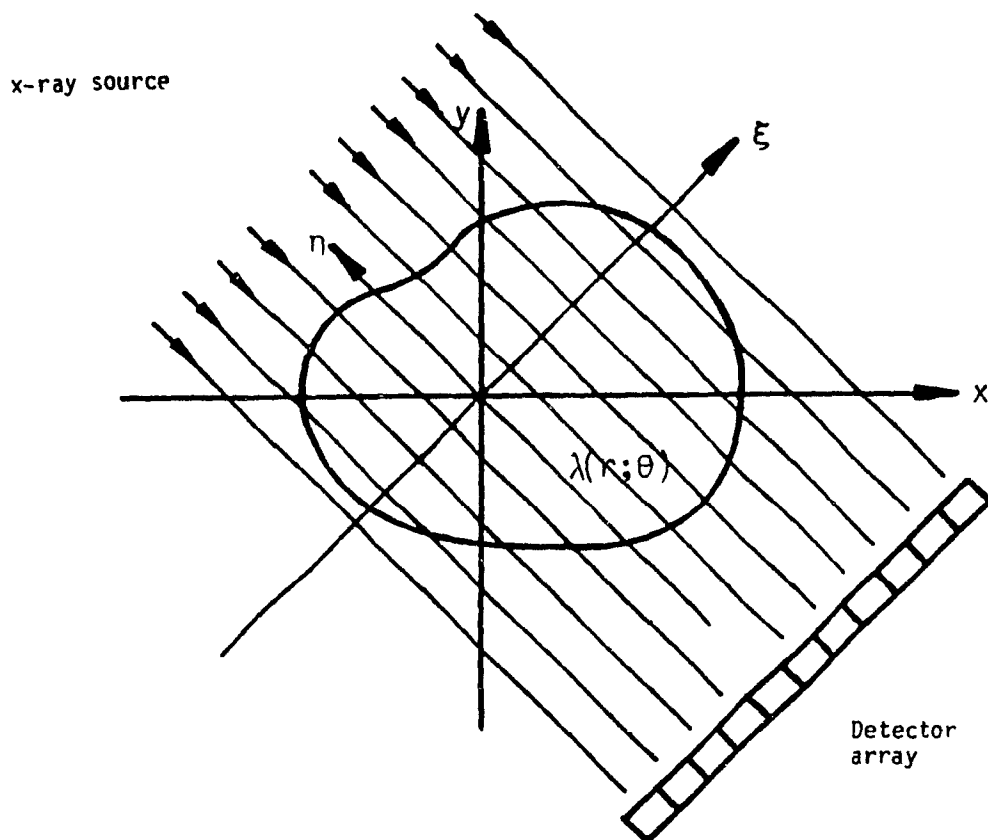
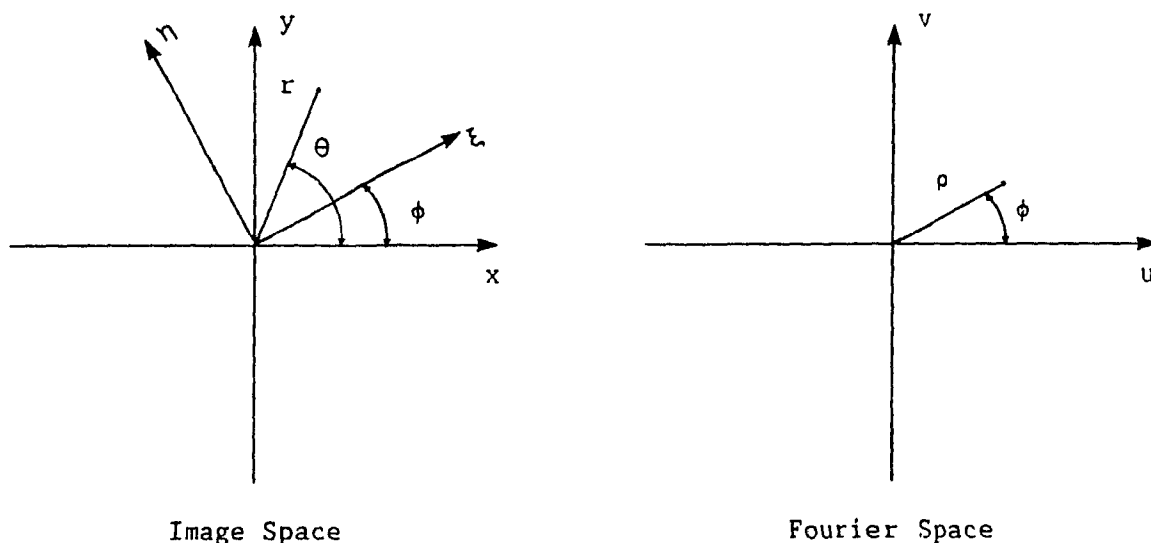


Figure 5.2 Image and Fourier space coordinate geometry used for the reconstruction method.



transform of the density,

$$\Lambda(\rho; \phi) = \int_{-\infty}^{\infty} f(\xi; \phi) \exp \left( i2\pi\rho\xi \right) d\xi \quad (5.2)$$

where  $i = \sqrt{-1}$ . The Fourier inverse of (5.2) is

$$f(\xi; \phi) = \int_{-\infty}^{\infty} \Lambda(\rho; \phi) \exp \left( -i2\pi\rho\xi \right) d\rho \quad (5.3)$$

The way the projection theorem (5.2) can be used for image reconstruction is described in the following section.

#### 5.2.2.1 Reconstruction by direct inversion

If the value of  $\Lambda(u,v)$  is known for all  $(u,v)$  then the density  $\lambda$  can be reconstructed by

$$\lambda(x,y) = \iint_{-\infty}^{\infty} \Lambda(u,v) \exp \left( -i2\pi(ux + vy) \right) du dv \quad (5.4)$$

Given measured projections  $f(\xi; \phi)$ , only certain values of  $\Lambda(u,v)$  can be calculated. According to (5.2)  $\rho; \phi$  space is built up by sets of 1-d transforms of projections along radial lines as shown in Fig. 5.3 for the case of 6 projections. The function to be transformed must be sampled on a rectangular grid. In order to do so requires an interpolation from polar to cartesian coordinates. This reconstruction method is summarized by the following

$$\lambda(x,y) = \lambda(r; \theta) = \int_0^{2\pi} \int_0^{\infty} \Lambda(\rho; \phi) \exp \left( -i2\pi\rho r \cos(\theta - \phi) \right) \rho d\rho d\phi \quad (5.5)$$

and is referred to as 'direct Fourier inversion' (Bracewell 1956). The chief difficulty with this method is the need for very accurate interpolation from polar to cartesian coordinates in Fourier space. Interpolation in Fourier space can be avoided when back-projection is the basis of reconstruction. In back-projection, interpolation is in image space. The radial blurring in the image that results from back-projection and the techniques to compensate for

Figure 5.3 Fourier transform of projections indicated by solid radial lines. Dots indicate the location of the set of samples which completely define  $\Lambda(u,v)$ .

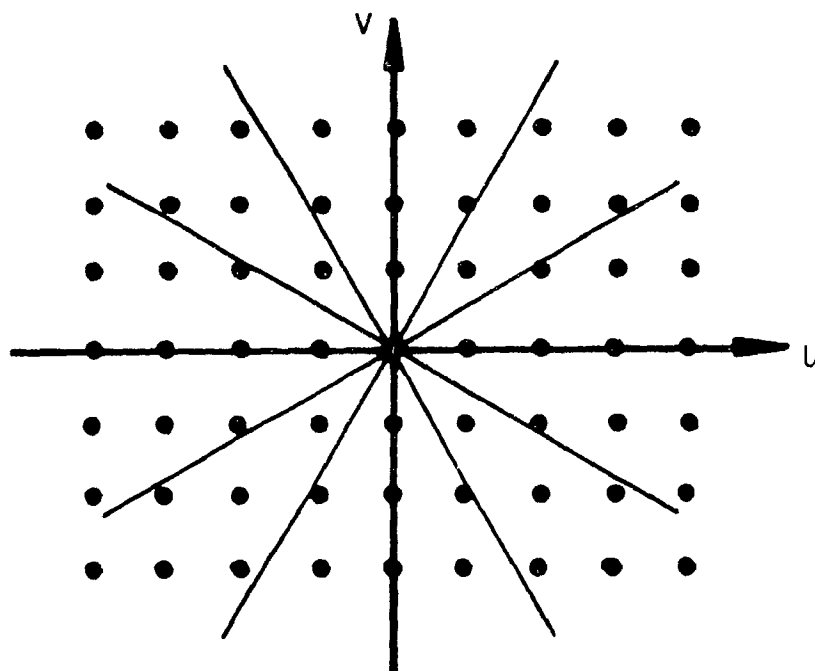
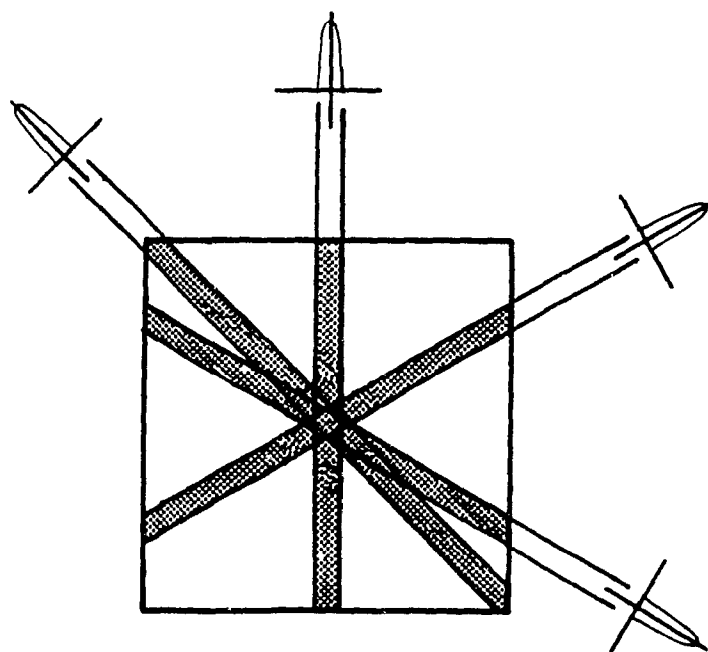


Figure 5.4 Back-projection of four projections of a small circular region of high density.





it are described below.

### 5.2.2.2 Simple back-projection

Let  $\lambda'(r; \theta)$  denote the reconstructed image density after 'back-projection'

$$\lambda'(r; \theta) = \int_0^\pi f(r \cos(\theta - \phi); \phi) d\phi \quad (5.6)$$

The back-projection operation consists of simply smearing each projection across image space along the directions in which they were measured. The density of each point in the image is then estimated by summing all rays intersecting at that point. The resulting image is often referred to as a 'layergram' (Bates and Peters 1971). Fig. 5.4 shows the back-projection of projections of a small circular region of high density, where the overlapping projections give rise to radially dependent blurring on which the true image is superimposed. Each point in the reconstructed image is blurred, since it consists of the superposition of each projected ray passing through the true object at that point. This blurring can be characterized as follows.

Substituting (5.3) into (5.6) gives

$$\lambda'(r; \theta) = \int_0^{2\pi} \int_0^\infty \rho^{-1} \Lambda(\rho; \phi) \exp \left[ -i2\pi r \rho \cos(\theta - \phi) \right] \rho d\rho d\phi \quad (5.7)$$

Rewriting (5.7) gives

$$\lambda'(r; \theta) = F_2 \{ \rho^{-1} \Lambda(\rho; \phi) \} = F_2 \{ \rho^{-1} \} * \lambda(r; \theta) \quad (5.8)$$

where  $F_2\{\}$  denotes a two-dimensional Fourier transform, and  $*$  is the symbol for convolution adopted here. The inverse transform of  $\rho^{-1}$  is  $r^{-1}$  (Bates and Peters 1971). The interpolation problem is further discussed by Smith et al. (1973), Peters (1973), and Crowther et al. (1970).

### 5.2.2.3 Filtered back-projection

Radial blurring can be compensated basically in two ways. The first

method is known as 'convolution back-projection,'

$$f'(\xi; \phi) = F_1\{ |\rho| \} * f(\xi; \phi) = \int_{-\infty}^{\infty} q(\xi - \xi') f(\xi'; \phi) d\xi' \quad (5.9)$$

where  $q$  is a convolving function and is defined to be such that its inverse Fourier transform approximates  $|\rho|$ . The technique of convolution back-projection is discussed in detail by Bracewell and Riddle (1967), Ramachandran and Lakshminarayanan (1971), Shepp and Logan (1974), and Lewitt et al. (1978).

The convolving function  $q(r)$  is approximated by calculating the inverse Fourier transform of  $|\rho|_r = |\rho|W(\rho)$ , where  $W(\rho)$  is a window function. Instead of the 'ramp' filter  $|\rho|$ , an apodized function  $|\rho|_r$  is used since it would handle noisy data better. Examples of two commonly used window functions are  $W_{RL}$  (Ramachandran and Lakshminarayanan 1971),

$$W_{RL}(\rho) = \begin{cases} 1, & |\rho| \leq \rho_{\max} \\ 0, & |\rho| > \rho_{\max} \end{cases} \quad (5.10)$$

and  $W_{SL}$  (Shepp and Logan 1974),

$$W_{SL}(\rho) = \begin{cases} |\text{sinc}(\rho/2\rho_{\max})|, & |\rho| \leq \rho_{\max} \\ 0, & |\rho| > \rho_{\max} \end{cases} \quad (5.11)$$

where  $\rho_{\max}$  is the upper limit on the frequency (i.e. cut-off frequency) that can be meaningfully reconstructed.

An alternative method of compensating for radial blurring is based on deconvolving  $r^{-1}$  from  $\lambda'(r; \theta)$ ,

$$\lambda(r; \theta) = F_2\{ |\rho| F_2\{ \lambda'(r; \theta) \} \} \quad (5.12)$$

(5.12) is referred to as 'rho-filtered back-projection,' derived in detail by Bates and Peters (1971). (5.12) can also be implemented by modifying each of the projections  $f(\xi; \phi)$  in Fourier space before back-projection (Bracewell and Riddle 1967; Ramachandran and Lakshminarayanan 1971). Both space and Fourier approaches are used in practice and are numerically equivalent.

The expressions describing the different reconstruction methods presented are in continuous forms and have to be replaced by approximate expressions in order to implement them digitally. This is discussed in the next section.

### 5.2.3 Sampling requirements

In practice, projections are measured at  $N$  discrete angles, and each projection has  $M$  samples. The requirements of  $\xi$  and  $\phi$  sampling are commented on in §5.2.3.1 and §5.2.3.2 respectively.

#### 5.2.3.1 $\xi$ sampling

The sampled projection is defined by

$$f_S(\xi; \phi) = d \sum_{m=-\infty}^{\infty} f(md; \phi) \delta(\xi - md) \quad (5.13)$$

where  $\delta(\cdot)$  is the Dirac delta function, and  $d$  is the sample spacing. If the image is known to exist within a circle of diameter  $D$  then the number of samples per projection is  $M = D/d$ . Given the Nyquist sampling criterion is satisfied (i.e.  $\Lambda(\rho; \phi)$  is negligible for  $|\rho| > 1/2d$ ), then there will be no aliasing error in the projection samples (Lewitt et al. 1978).

In the case of convolution back-projection, (5.9) becomes

$$f'_S(\xi; \phi) = f'(jd; \phi) = d \sum_{m=-\infty}^{\infty} q((j-m)d) f(md; \phi), \quad j = 0, \pm 1, \dots \quad (5.14)$$

The filter array elements of the convolving function  $q()$  corresponding to  $|\rho|W_{RL}(\rho)$  and  $|\rho|W_{SL}(\rho)$  are

$$q_{RL}(kd) = \begin{cases} 1/4d^2 & , k = 0 \\ 0 & , k \neq 0 \text{ and even} \\ -1/(\pi^2 d^2 k^2) & , k \text{ odd} \end{cases} \quad (5.15)$$

and

$$q_{SL}(kd) = -2/d^2 \pi^2 (4k^2 - 1), \quad k = 0, \pm 1, \pm 2, \dots \quad (5.16)$$

### 5.2.3.2 $\phi$ sampling

Since there are only a limited number of projections measured, the back-projection operation (5.6) has to be evaluated by some numerical procedure. Given projections measured at  $N$  angles equally spaced throughout an interval of  $\pi$  radians, (5.6) is usually rewritten to become a sum containing one value from each projection,

$$\lambda_N'(r; \theta) = \frac{\pi}{N} \sum_{n=1}^N f_s(r \cos(\theta - \phi_n); \phi_n) \quad (5.17)$$

where  $N = \pi/\Delta\phi$  and  $\phi_n = n\Delta\phi$ . In order to achieve a resolution equal to  $2d$ , the minimum number of  $N$  projections required is then given by (Crowther et al. 1970)

$$N = \pi D/2d \quad (5.18)$$

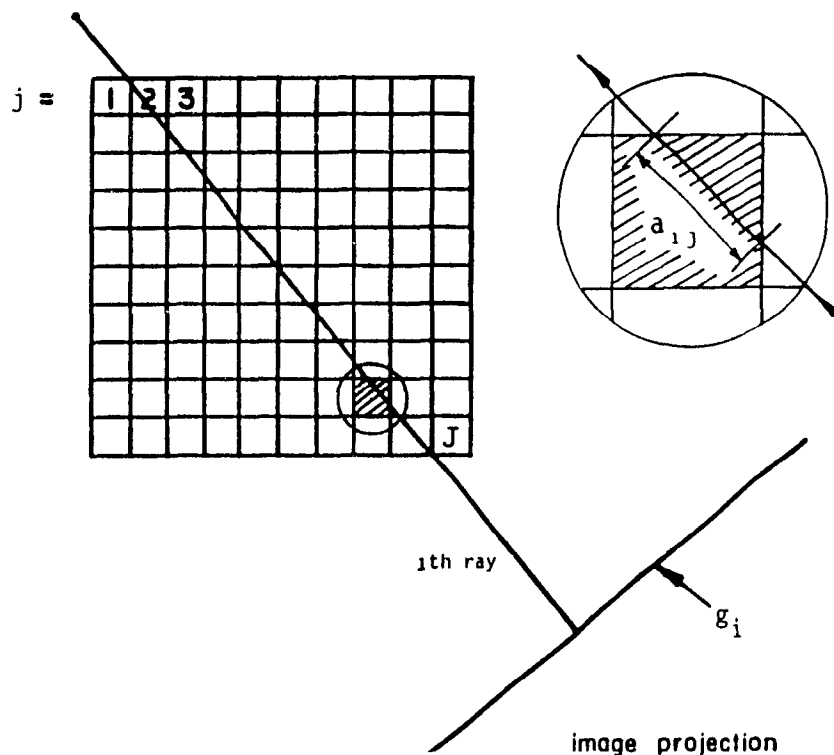
If there is insufficient  $\phi$  sampling, aliasing errors and interpolation errors, referred to as 'clutter,' result in the reconstruction (Smith et al. 1973). The problem of image reconstruction from a few projections (i.e. 4 to 16 projections) is further discussed in §5.3.

## 5.2.4 Algebraic reconstruction methods

### 5.2.4.1 Fundamentals

Algebraic reconstruction methods differ fundamentally from transform methods in that the image reconstruction problem is 'discretized' at the very beginning. Fig. 5.5 shows image space defined as a square array of pixels that encloses the object cross section to be reconstructed. The density within the  $j^{\text{th}}$  square ( $1 \leq j \leq J$ ) is assigned a value  $\lambda_j$ . The image projections  $g_i$  of the square array are defined as a strip integral over the image with the area of the strip defined by the  $i^{\text{th}}$  ray. The total number of rays in all projections is equal to  $I$ . Referring to Fig. 5.5,  $a_{ij}$  is the length of intersection of the  $i^{\text{th}}$  ray with the  $j^{\text{th}}$  pixel for all  $i$  and  $j$ , and represents the contribution of the  $j^{\text{th}}$  pixel to the total attenuation along the  $i^{\text{th}}$  ray. The image projection  $g_i$  is defined as a finite sum of

Figure 5.5 The image projection  $g_i$  shown as an integral of  $\lambda_j$  along the  $i$ th ray. Detail on the right shows the  $i$ th ray passing through the  $j$ th pixel.



density contributions along the  $i^{\text{th}}$  ray path,

$$g_i = \sum_{j=1}^J a_{ij} \lambda_j \quad i = 1, \dots, I \quad (5.19)$$

Given a set of measured projections  $f_i$ , the solution set  $\{\lambda_j\}$  is sought to the equations

$$f_i = \sum_{j=1}^J a_{ij} \lambda_j \quad i = 1, \dots, I \quad (5.20)$$

#### 5.2.4.2 Matrix inversion

(5.20) represents a series of  $I$  linear equations in  $J$  unknowns for which a solution should be attainable by inverting the matrix  $a_{ij}$ ,

$$\lambda_j = \sum_{i=1}^I (a_{ij})^{-1} f_i \quad (5.21)$$

In practice the number of elements in  $a_{ij}$  is large which leads to prohibitive computation times and makes inversion more sensitive to noise in the projection data (Barrett and Swindell 1981). These reasons have prompted the development of iterative methods for image reconstruction.

#### 5.2.4.3 Iterative reconstruction methods

Solutions to (5.20) are based on the 'method of projections' (Kaczmarz 1937). These iterative methods seek the solution that will maximize in some sense the similarity between the set of measured projections  $f_i$  and the image projections  $g_i$ .

Following Barrett and Swindell (1981) a typical iterative algorithm consists of the following steps:

- (i) Assume an initial image  $\lambda_j$ .
- (ii) Compute image projections  $g_i$  by (5.19).
- (iii) Compare  $g_i$  to measured projections  $f_i$ .
- (iv) Compute correction factors and update  $\lambda_j$  values.
- (v) Repeat from (ii) with new iterations, or end with final image.

A common example of an iterative reconstruction algorithm is algebraic reconstruction techniques (ART) introduced by Gordon et al. (1970). In ART, differences between the measured and computed projections (i.e.  $f_i - g_i$ ) are assigned to all image pixels within the  $i^{\text{th}}$  ray. For this reason ART is sometimes called a 'ray by ray' reconstruction method. Update of  $\lambda_j$  is repeated  $k$  times for the whole set of projections until convergence is attained. The algorithm is said to be 'constrained' if 'a priori' information is incorporated. The most common constraints employed are image positivity and image extent (see §5.3.2). 'Unconstrained' ART has been shown to converge for consistent equations (5.20) to the solution with the smallest variance (Herman et al. 1973). If one attempts to solve a set of equations such as (5.20) which are inconsistent, unconstrained ART improves at first then gets progressively worse (Gilbert 1972).

In contrast to ART methods is a scheme referred to as simultaneous iterative reconstruction technique (SIRT) (Gilbert 1972). In SIRT each image pixel is corrected by using data from all the rays simultaneously at each iteration. This 'point by point' approach makes reconstruction less sensitive to measurement errors in the projection data (Gilbert 1972). A variation on SIRT is iterative least squares technique (ILST) (Goitein 1972).

Recast as a problem in terms of optimization theory, the solution to (5.20) can also be found that maximizes its entropy (e.g.  $S(\lambda_j) = -\lambda_j \log(\lambda_j)$ ). This solution can be thought of as being the least biased while still being consistent with the given projection data (Minerbo 1979). The choice of entropy ensures image positivity and maximizes the smoothness of the reconstruction. Examples of implementation of the maximum entropy approach are discussed by Minerbo (1979), who refer to it as 'MENT,' Lent (1977), Frieden (1980) and Smith and Grandy (1985).

### 5.2.5 Comparison between transform and algebraic reconstruction methods

The relative merits of transform and algebraic reconstruction methods depend on practical considerations: application, the range of views, and the number of views. For a fixed recording geometry, and when the number of samples per projection and azimuthal sampling are satisfied in the sense of §5.2.3, transform methods are preferred. Algebraic techniques are deemed more adaptable to non-standard reconstruction problems, such as situations where the projections are incomplete (Oppenheim 1977). This is probably due to the functional being optimized which imposes subjective constraints on the reconstructed images (Heffernan and Bates 1982). In addition to this, iterative techniques allow explicit 'a priori' object knowledge to be easily introduced into the reconstruction procedure. In this way iterative techniques become flexible in handling new reconstruction problems.

### 5.3 Reconstruction from a few views

This section is concerned with the problem of reconstructing an image

when the number of measured projections  $N$  is much less than required by (5.18). It is assumed that each projection contains sufficient ray-sums to satisfy the sampling constraints set out in §5.2.3.1.

In absence of measured projections, reconstruction by methods described in §5.2.2.1 - §5.2.2.3 leads to artifacts in the reconstruction image (Hanson 1982a). Consider the case where the image is a two-dimensional delta function located at the origin,  $\lambda(x,y) = \delta(x)\delta(y)$ , and its 2-d Fourier transform is  $\Lambda(u,v)=1$ . The back-projection reconstruction of  $\lambda(x,y)$  from 5, 10, and 20 projections evenly spaced in an interval of  $\pi$  radians is shown in Fig. 5.6b)-d) respectively. The relief plots show a distorted or 'dirty' delta function elongated along the directions of projection. This streaking or star-pattern artifact can be thought of as being superimposed on the true image. Fig. 5.7 illustrates this point, where Figs. 5.7b)-d) show images of a numerical phantom in Fig. 5.7a) reconstructed by back-projection of 5, 10, and 20 evenly spaced projections. Approaches to the problem of few projections are reviewed in §5.3.1.

In spite of streaking some objects in the reconstructed image can be inferred from its form and structure (Fig. 5.7). The streaking artifact is particularly serious for objects that are relatively smaller in size and contrast. The former observation indicates the possibility of using 'a priori' knowledge about form and structure regarding the object's density distribution in reconstruction. §5.3.2 discusses the role of 'a priori' information.

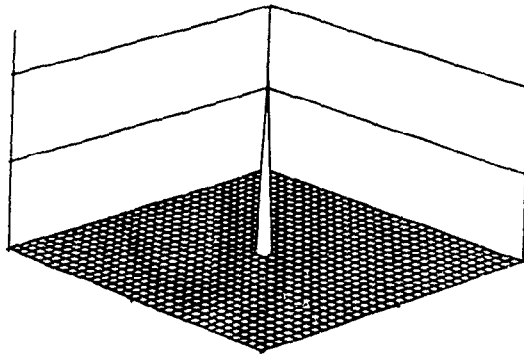
### 5.3.1 Previous work

Algorithms for image reconstruction from a few projections can be grouped into three approaches: methods which use conventional transform algorithms applied to an augmented set of projections, methods that incorporate into the reconstruction scheme global image constraints, or 'a priori' knowledge about the type of image expected to be reconstructed.

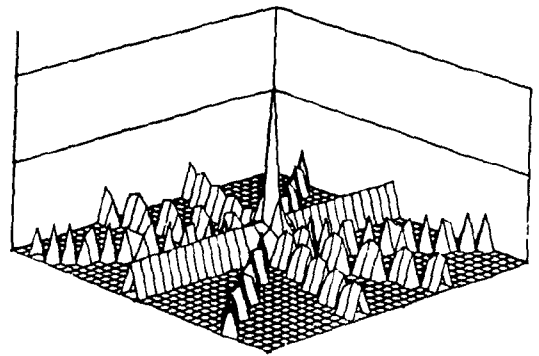


Figure 5.6 a) point source object and its reconstruction by back-projection from b)  $N=5$ , c)  $N=10$ , and d)  $N=20$  projections.

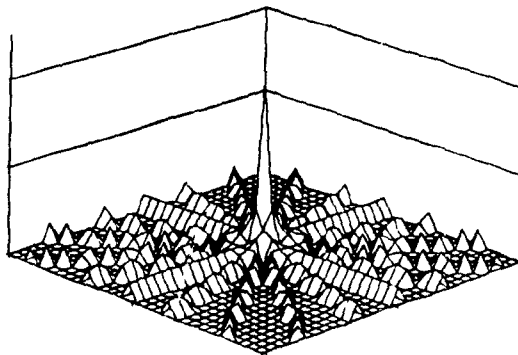
a) Point source object



b)  $N = 5$



c)  $N = 10$



d)  $N = 20$

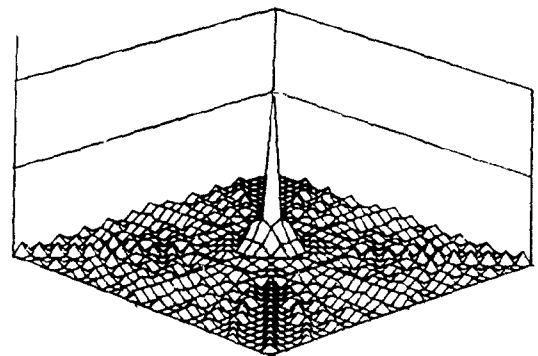
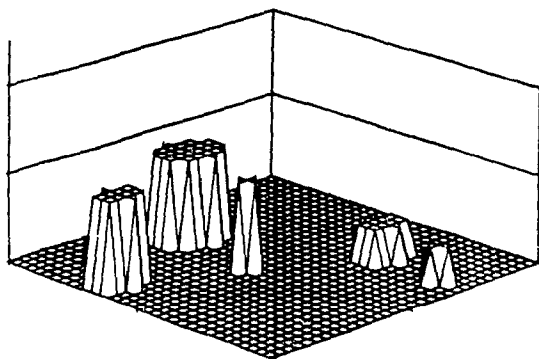
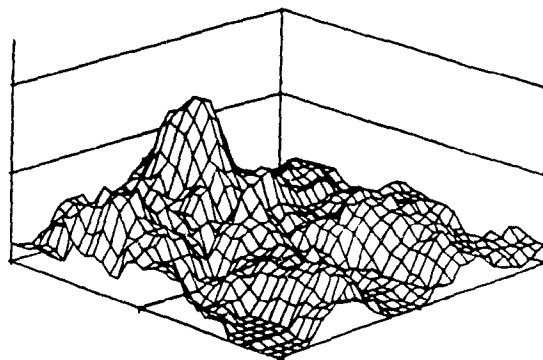


Figure 5.7 Illustration of streak artifacts due to back-projection reconstruction: a) original object, and its reconstruction from b)  $N=5$ , c)  $N=10$ , and d)  $N=20$  projections evenly spaced over  $\pi$  radians.

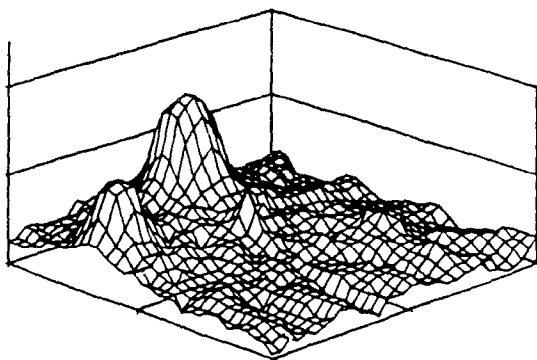
a) Original object



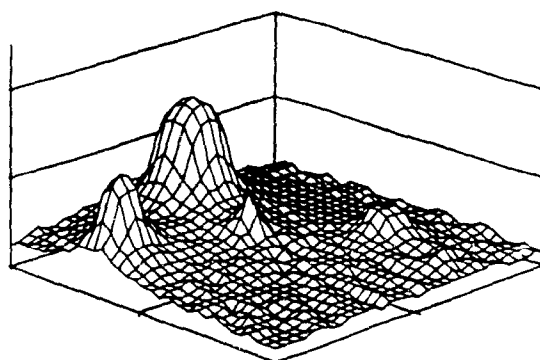
b)  $N = 5$



c)  $N = 10$



d)  $N = 20$



### 5.3.1.1 Interpolation of missing projections

The first approach is to analytically compute the missing projections from the known measured projections. The advantage of such an approach is that it enables the transform reconstruction methods to be applied. As discussed in §5.2.3, transform methods require that the projection set be complete in the number of projections and the number of samples in each projection. Given incomplete projections, it is necessary to estimate the missing projection values.

Much of the reported work on interpolating missing projections has been described for the related problem of limited angular range of views in which a range of projections is not measured. Inouye (1979) estimates the projections in the missing range by fitting a Fourier series to the measured projections (see also Wagner 1979). However, this method leads to large differences in reconstructed images if there is any noise in the projection data. Generally the process of completing missing projections results in reconstruction artifacts, since the interpolated projections are inconsistent with the object being reconstructed (Oppenheim 1977; Heffernan and Bates 1982). An analytic treatment of this problem is given by Davison (1983) who showed that the problem of computing missing projections is ill-conditioned, and therefore, the data must be extremely accurate to yield a successful reconstruction. This result cannot be circumvented in absence of strong 'a priori' constraints on the unknown density distribution of the object being reconstructed.

In an attempt to limit reconstruction artifact Gerchberg's algorithm (Gerchberg 1974) has been implemented to estimate missing projections in CT (Tam and Perez-Mendez 1981; Sato et al. 1981; Heffernan and Bates 1982; Nassi et al. 1982). Gerchberg's algorithm is an iterative scheme which successively applies constraints in frequency domain and image space. Unlike algebraic techniques, any errors introduced in the iterative process are not corrected and would build up with successive iterations (Heffernan and Bates 1982).

### 5.3.1.2 Application of global image constraints

Another approach to image reconstruction in the face of missing projections is to employ iterative techniques which place global constraints on the image. The iterative approach can provide a solution based on the given projection values and does not require that any missing values be estimated. In this sense iterative methods are better suited than transform methods to the problem of reconstruction from a few projections. Examples of such methods are SIRT, ART, and MENT. These methods have proved to reduce artifacts when there are limited projections available (Oppenheim 1977; Heffernan and Bates 1982). An example of this approach is an implementation of MENT for vascular reconstruction by Spears et al. (1988).

Spears et al. (1988) used MENT to reconstruct coronary arterial trees 'in vitro' from 6 to 18 cine angiographic views (equally spaced over  $\pi$ ). The choice of entropy leads to global smoothing and thus, reduces the amount of streaking in the final reconstructed image. They found that the number of projections necessary for an acceptable reconstruction depends greatly on the complexity of the anatomic structure of the vessels. This is to be expected since the reconstructed image reflects only the 'statistical' structure imposed by the available measured projections.

### 5.3.1.3 Application of 'a priori' image information

The last approach to the problem of missing projections is to use 'a priori' information about the type of image expected to be reconstructed.

This approach has been successful in the application of limited-view computed tomography to non-destructive materials testing. Hanson (1982b) showed empirically the extent of improvement in reconstruction from limited views when it is known 'a priori' that the image is a collection of specific shapes. Their approach first fits model parameters in a least squares sense to the available projections. The fitted model is then used as the initial estimate in an ART-type algorithm (see also Rougee et al. 1988). In another example, Heffernan and Robb (1985) were able to reconstruct images from few projections where the reconstruction is a sample of a well defined image.

Garden and Bates (1984) presented a general technique to estimate the type of image expected in reconstruction. Available 'a priori' information about the image structure is revealed by direct reconstruction. Their algorithm takes advantage of the observation that in spite of streak artifacts, structure and boundaries of objects in the reconstructed image are recognizable to humans. Garden and Bates mathematically argued that as the size of the object extent increases it becomes more recognizable in the reconstructed image. Their algorithm is as follows.

From the measured projections an image is reconstructed by convolution back-projection. Visually boundaries of regions that appear divided in the reconstructed image are traced out by cursor. The computer calculates the average density inside each region and forms a 'piece-wise constant' image consisting of the selected regions whose pixel values are set to the region's average. The piece-wise constant image is re-projected along directions of the original projections, and the computed projections are then subtracted from the originals. The difference is reconstructed by convolution back-projection and visually checked for any remaining useful information. If visual inspection of the difference image reveals that its amplitude is everywhere negligible, then the piece-wise constant image is taken to be the best estimate of the original object. Otherwise, the difference image is added to the piece-wise constant image, and the operator re-traces new boundaries. This interactive process is repeated until the operator decides that the amplitude of the difference image is negligible. The iterative nature of this approach provides the facility for redefining the 'a priori' constraints after each iteration. After two to four iterations the reconstructed image resembles the true object.

### 5.3.2 'A priori' image information

'A priori' knowledge is usually based on the perceptive experience that certain object patterns and structure are recognized as acceptable in a given context, whereas others are not possible and are thus strongly rejected. The most common 'a priori' constraints invoked in reconstruction algorithms are image positivity, in the radiographical context density is

always positive, and image extent, the smallest convex region or regions in image space which encloses the image. If the properties of the material making up the cross section are known, interval constraints on the density values can also be imposed. Other 'a priori' constraints based on image estimates of size, shape, and boundary locations are also possible (Rossi and Willsky 1983).

The application of 'a priori' constraints in reconstruction algorithms is basically 'ad hoc,' depending largely on the object being reconstructed. In the case of image reconstruction from projections of opacified blood vessels, several 'a priori' assumptions are made about the object and the reconstruction problem.

Let the 3-d object to be reconstructed be partitioned into a stack of  $L$  mutually parallel axial sections where the density of the  $l^{\text{th}}$  object cross section is described by  $\lambda_l(x,y)$ . It is assumed that  $\lambda_l(x,y)$  is reconstructed from the corresponding rows of each of the  $N$  planar projections. Since only single sections are being considered, the 'l' subscript is dropped for reasons of convenience. The problem under consideration has the following form:

- (A) Object  $\lambda(x,y)$  consists of  $J$  regions of opacified vessels of finite extent surrounded by empty background:

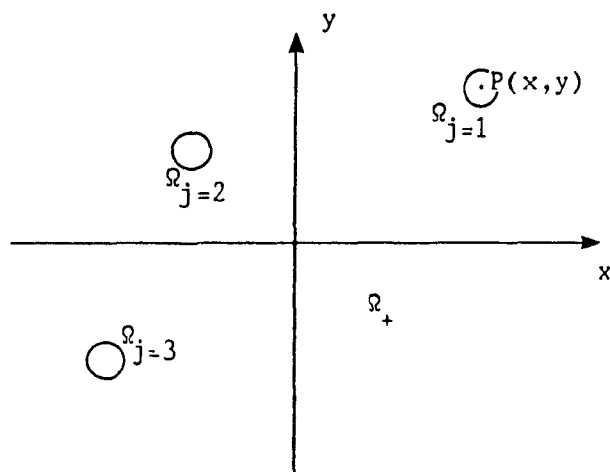
$$\lambda(x,y) = \begin{cases} k_j, & P \in \Omega_j, \{k_j \in \mathbb{R}: j=1,2,\dots,J\} \\ 0, & P \in \Omega_+ \end{cases} \quad (5.22)$$

where  $P$  is a point in image space  $\Omega$  as shown in Fig. 5.8. Image space  $\Omega$  is partitioned into two non-intersecting regions  $\Omega_+$  and  $\Omega_-$ .  $\Omega_+$  represents background and  $\Omega_-$  the  $J$  non-intersecting regions of finite extent  $\Omega_j$ :

$$\Omega_- = \bigcup_{j=1}^J \Omega_j \quad (5.23)$$

- (B) The density of piece-wise constant regions  $\Omega_-$  should always be positive,  $k_j \geq 0$ .

Figure 5.8 Notation and coordinate system for piece-wise constant image.



(C) The opacified vessels within each object section are continuous with vessels in the adjacent cross sections or slices.

(D) The reconstructed image  $\lambda'_N$  is related to the true image by

$$\lambda'_N(x,y) = \text{star}_N(x,y) * \lambda(x,y) \quad (5.24)$$

where the star-function (Smith et al. 1973) is given by

$$\text{star}_N(r; \theta) = \frac{2\pi}{Nr} \sum_{n=1}^N \{ \delta(\theta - \phi_n) + \delta(\theta - \phi_n + \pi) \} \quad (5.25)$$

$\delta(\cdot)$  denotes the Dirac delta function. The star-function can be thought of as the point spread function (PSF) associated with the unfiltered back-projection reconstruction from  $N$  finite projections at  $\{\phi_N\}$ . The star-function is given by the reconstruction of a single point using (5.17) and is superimposed at the original point. Fig. 5.6 gives examples of  $\text{star}_N(x,y)$  for different numbers of projections.

(E) As an initial approximation, the locations of maxima in the reconstructed image  $\lambda'_N(x,y)$  (i.e. the centers of star-patterns) generally correspond to regions of opacification  $\Omega_j$  in the original object  $\lambda(x,y)$  when these regions are 'point-like' and have the same high densities.

## 5.4 Problem statement

Given a data set consisting of a small number of projections of the vessels in the brain, the problem of reducing artifacts in the back-projection image can be solved using 'a priori' object knowledge listed in §5.3.2 (A)-(E). In addition to 'a priori' object knowledge, it is assumed that the vessel in anatomical cross section can be approximated as being 'point-like.' The general problem can be posed; given  $\{f, \phi_n, N\}$  and the above 'a priori' assumptions, estimate  $\lambda(x, y)$  by selectively reducing the star-pattern artifacts in  $\lambda'_N$ , the streaked reconstructed image, within some specified region  $\Omega_-$  of image space.

A streaked image results when a reconstruction algorithm is applied to the few measured projections,

$$\lambda_N = R_N\{f_s(\xi; \phi_n)\} \quad (5.26)$$

where the reconstruction operator  $R_N\{.\}$  is linear and invariant throughout the image plane. The reconstruction operator considered here is simple back-projection (5.17). The streaked reconstructed image is modeled by

$$\lambda_b(x, y) = \iint_{\Omega_-} \lambda_e(x', y') \text{star}_N(x-x', y-y') dx' dy' \quad (5.27)$$

where  $\lambda_e$  is the estimate of the true image. The actual streaked image  $\lambda'_N$  is always non-ideal in the sense

$$\lambda'_N(x, y) = \lambda_b(x, y) + d(x, y) \quad (5.28)$$

where  $d(x, y)$  is the difference or residual image and includes additive noise and any differences between the actual streaked image  $\lambda'_N$  and the model  $\lambda_b$  (5.27).

The problem can be restated; given both  $\lambda'_N$  as defined by (5.26) and  $\lambda_b$  in the form defined by (5.27), estimate  $\lambda$  to within limits set by the residual  $d$ . The estimate of the true image  $\lambda_e$  is constructed by a solution method that minimizes the residual  $d$ ,



$$d(x,y) = \left| \lambda'_N(x,y) - \iint_{\Omega_-} \lambda_e(x',y') \text{star}_N(x-x',y-y') dx' dy' \right| \quad (5.29)$$

to within limits set by the noise level in  $\lambda'_N$ . In the next section a solution to (5.29) is proposed that consists of subtractively deconvolving  $\text{star}_N$  from  $\lambda'_N$  at only those points that are centers of star-patterns.

## 5.5 Reconstruction method

The problem of selectively removing star-pattern artifacts from the reconstructed image is addressed by a subtractive deconvolution technique known as 'Clean.' Clean was introduced by Högbom (1974) to restore radio-source maps reconstructed from incomplete observations that suffered from star-pattern type artifacts. This algorithm was demonstrated to be very successful with images of radio-sources that are essentially blank sky with widely distributed point-source components. The position and amplitudes of these point-source components are determined by a simple iterative procedure which is described in §5.5.1. The idea of star-pattern removal in emission tomography was applied by Muellehner and Wetzel (1971). They experienced poor results since the objects being reconstructed were too large and extended for successful restoration. As a consequence of both the similarity of the reconstruction problem described in §5.4 to Högbom's and that blood vessels in an anatomical cross section may be approximated as point-sources, the extension of Clean to medical imaging of blood vessels is investigated. The application of the Clean algorithm is described in §5.5.2 and details of its implementation are presented in §5.5.3.

### 5.5.1 CLEAN algorithm

The notion of how subtractive deconvolution, in particular Clean, arises is presented. Let  $G(x,y)$  and  $G'(x,y)$  represent the true and degraded images of the same object respectively. It is assumed that each point in  $G$  exists at only a single data point and can be regarded as a 'true' impulse. In contrast, each point in  $G'$  exists at a sequence of points and is considered a 'spread' impulse. It follows that given the point spread function (PSF), known or estimated 'a priori,' each data point in  $G'$  can be reduced down to some residual level by successively subtracting out each of the spread

impulses.

Subtractive deconvolution is appropriate when the true image is composed of isolated points, and when the main effect of the PSF is to reduce contrast rather than resolution (Bates and McDonnell 1986). Högbom's cleaning algorithm is specifically suited for this class of images. The Clean algorithm operates in the image plane and fits the 'a priori' model of the true image to the observed projections. The cleaning algorithm is described below using Högbom's graphic terminology.

The algorithm begins with a degraded or 'dirty' image  $G^{(0)}$ , the recoverable or 'clean' image  $G_e^{(0)}$  which is initially empty, and the synthesized PSF or 'dirty beam.' Each time the dirty beam (i.e. a spread impulse) is subtracted out from the dirty image the clean image takes on the value of the true impulse at the appropriate position. The clean image becomes the true image after all the subtractions have been completed. The iterative process by which images  $G^{(k=0)}$  and  $G_e^{(k=0)}$ , where  $k$  denotes the iteration number, are updated consists of the following steps:

- (i) Locate the maximum in  $G^{(k)}$  and determine its amplitude  $P$ .
- (ii) Add to  $G_e^{(k)}$  a point-source at this location of amplitude  $\alpha P$ , where  $\alpha$  is the loop gain.
- (iii) Convolve the dirty beam with a point-source of amplitude  $\alpha P$  at this location.
- (iv) Compute  $G^{(k+1)}$  by subtracting the result of this convolution from  $G^{(k)}$ .
- (v) Update  $k \rightarrow k+1$  and return to (i) unless  $G^{(k+1)}(x,y) < c$  for all  $(x,y)$ , where  $c$  is the convergence criterion.
- (vi) Convolve the clean image  $G_e^{(k)}$  by the ideal PSF to obtain a smooth clean image.
- (vii) Add the residual  $G^{(k+1)}$  to the smooth clean image.

Steps (i), (ii), (v), and (vi) are at control of the observer. If the maxima in the degraded image are located at the same positions as the true impulses then cleaning will determine the amplitudes from these positions.

The user selects the loop gain and the convergence criterion. The loop gain may range between 0 and 1. If the image has an impulsive character, the loop gain can be as large as unity so as to reduce the number of iterations. For images consisting of extended components, a small loop gain is necessary and more iterations are required.

The convergence or stopping criterion is based on an estimate of noise in  $G^{(0)}(x,y)$  and is set close to the average of background values. In those cases where the noise level is comparable to the amplitudes of the point-sources in  $G'$ , cleaning is not successful. Performance of Clean not only depends on noise levels, but on the shape of the PSF. If the PSF is wide, it is more likely that the maxima in the degraded image are not located at the same positions as the true impulses. In this circumstance, cleaning proceeds from wrong positions, and the cleaned image bears no resemblance to the true image (Bates et al. 1982). The use of an ideal PSF in step (vi) takes into account that it is not possible to resolve image features beyond a limit, that is, the PSF is of finite width. In practice this step is essentially a 'cosmetic' operation (Bates and McDonnell 1986).

In cases where the residual can be reduced to zero and the true image consists of a collection of point-sources whose number is less than half of the observed visibility samples in Fourier domain, Clean will then converge to the correct solution (Schwarz 1978). Thus, if there is sufficient 'a priori' knowledge of the true image, the image components can be located and their amplitudes determined. When the true image does not consist of 'point-like' objects, cleaning will tend to be inefficient. A generalized approach to subtractive deconvolution of a wide class of blurred images is described by Bates et al. (1982;1984).

### 5.5.2 Modified Clean (MCLEAN) algorithm

The problem of reconstructing 2-d axial sections of blood vessels from a few subtracted angiograms is similar to Högbom's problem in two ways. Firstly, it is similar in the sense that the true image can be approximated by widely distributed point-like objects. Secondly, the maxima of star-patterns in the degraded image  $\lambda'_N$  formed by back-projection (5.17)

generally correspond to regions of opacification in the true image. In this case the dirty beam is described by the star-function (5.25).

The algorithm used to determine both the regions of opacification in the streaked reconstructed image  $\lambda'_N$  and their amplitudes is based on Clean. It is referred to here as 'Mclean.' Rather than subtracting out the star-function from the dirty image  $\lambda'_N$  as in steps (iii & iv) of §5.5.1, the computed projections  $g_s(\xi; \phi_n)$  of the selected peak point are used to subtract from the measured projections  $f_s(\xi; \phi_n)$ . The updated version of the dirty image is then formed by back-projecting the modified measured projections. Both forms of implementing the subtractive deconvolution step are numerically equivalent, but the latter form lends itself to comparison with other iterative algorithms.

Reconstruction of the original object is achieved by the following steps for each section in the 3-d object:

- (i) Set  $k \rightarrow 0$ . Introduce empty clean image  $\lambda_e^{(k)}$ , and dirty image  $\lambda'_N^{(k)}$  computed from projections  $f_s^{(k)}(\xi; \phi_n)$  as defined by (5.17).
- (ii) Locate the maximum in  $\lambda'_N^{(k)}$  and determine its amplitude  $P$ .
- (iii) Add to  $\lambda_e^{(k)}$  a point-source at this location of amplitude  $\alpha P$ .
- (iv) Compute  $g_s^{(k)}(\xi; \phi_n)$  of the point-source corresponding to  $\alpha P$ .
- (v) Update  $f_s^{(k+1)}(\xi; \phi_n) \leftarrow f_s^{(k)}(\xi; \phi_n) - g_s^{(k)}(\xi; \phi_n)$  at each data point.
- (vi) Compute  $\lambda'_N^{(k+1)}$  from  $f_s^{(k+1)}(\xi; \phi_n)$  as defined by (5.17).
- (vii) Update  $k \rightarrow k+1$  and return to (ii) unless  $\lambda'_N^{(k+1)} < c$  for all  $(x, y)$ .

In step (ii) the search regions for maxima are restricted to the finite extent of the image, an estimate of  $\Omega$ . The proposed algorithm then proceeds to determine amplitudes from the positions found by the search.

Mclean is primarily different from algebraic algorithms (see §5.2.4.3) in that deconvolution is selective and based on 'a priori' object knowledge. As demonstrated by Garden and Bates (1984) and Heffernan and Robb (1985), the more accurate the 'a priori' estimate of the true object is, the more probable the final reconstructed image will resemble the true image. The

extent of agreement is limited by the 'a priori' information available and ultimately to the measured projections. This method will not recover information lost because of the incompleteness of the projection set.

### 5.5.3 Implementation

The implementation of back- and re-projection operations, and determination of image extent are described in §5.5.3.1, §5.5.3.2, and §5.5.3.3 respectively.

#### 5.5.3.1 Back-projection algorithm

In the back-projection operation values from  $f_s(\xi; \phi_n)$  are assigned to elements of a 2-d matrix of square pixels representing the reconstructed section  $\lambda'$ . There are basically two ways to implement the back-projection operation.

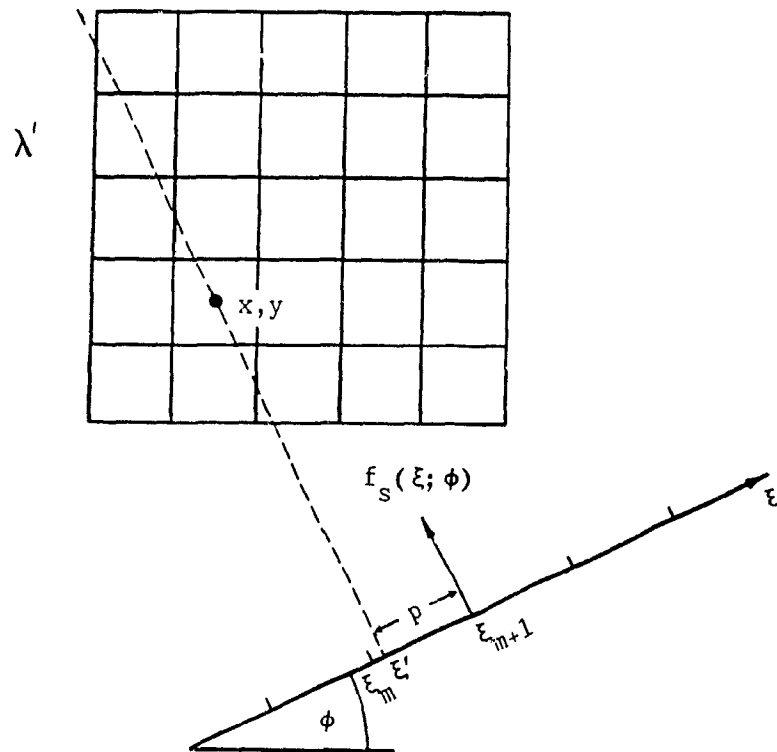
The first method is to assign a fraction of the value of point  $f_s(\xi; \phi_n)$  being back-projected in a manner similar to (5.21). In the other method, the value appropriate to the ray that passes exactly through the center of each image pixel is computed from the projection data. Referring to Fig. 5.9, if the contribution to the  $x, y^{\text{th}}$  point in  $\lambda'$  from  $f_s(\xi; \phi_n)$  being considered is  $f_s(\xi'; \phi_n)$  where  $\xi_m \leq \xi' \leq \xi_{m+1}$ , then the value of the reconstructed grid point is updated by the rule

$$\lambda'_{x,y} = \lambda'_{x,y} + p f_s(\xi_m; \phi_n) + (1-p) f_s(\xi_{m+1}; \phi_n) \quad (5.30)$$

where  $p$  is the fraction of the interval between  $f_s(\xi_m; \phi_n)$  and  $f_s(\xi_{m+1}; \phi_n)$  defined by the intersection with the  $\xi$ -directed vector  $f_s$  of a perpendicular dropped to the  $x, y^{\text{th}}$  point in  $\lambda'$ .

Peters' (1981) back-projection scheme using linear interpolation between sample points of the projection is adopted here. The advantage offered by this scheme is the convenience with which it can be inverted to provide re-projection.

Figure 5.9 Center of each pixel is re-projected to the measured projection and pixel value is assigned as a weighted sum of the two samples of  $f_s$  closest to the re-projected point.



#### 5.5.3.2 Re-projection algorithm

Re-projection can be performed by the inverse operation of either of the two back-projection schemes outlined in §5.5.3.1. The first method based on predetermined weights of the image array is characterized by (5.19).

The second method assigns values from the  $x, y$  grid to sample points of the projection. Referring to Fig. 5.9, the  $x, y^{\text{th}}$  point is re-projected and its immediate neighbors in the sampled projection are updated by

$$\left. \begin{aligned} g_s(\xi_m; \phi_n) &= g_s(\xi_m; \phi_n) + p\lambda'_{x,y} \\ g_s(\xi_{m+1}; \phi_n) &= g_s(\xi_{m+1}; \phi_n) + (1-p)\lambda'_{x,y} \end{aligned} \right\} \quad (5.31)$$

This re-projection algorithm is essentially the inverse of the back-projection procedure (5.30). However, this re-projection scheme will result in large oscillatory errors at angles where grid points are strongly aligned (Peters 1981). These errors can be corrected by using a scaling function

$g_c(\xi; \phi),$

$$g_s'(\xi; \phi_n) = g_s(\xi; \phi_n) / g_c(\xi; \phi_n) \quad (5.32)$$

The correction function is specified by computing  $g_s/g_s'$  of a known object density distribution, such as a uniform square, for all desired angles of  $\{\phi_n\}$  (Peters 1981).

### 5.5.3.3 Estimation of image extent

The extents of the sub-images (i.e.  $\Omega$  by 5.22) in the layergram are estimated by setting values of those points in the image to zero if it has a corresponding 'null ray,' otherwise its value is preset to some arbitrary (non-zero) level (Heffernan and Bates 1982).

A null ray is defined to be any straight line through image space along which the integral of the density is zero. Hence, the image is zero along the null ray since the image density cannot be negative (Brooks and Di Chiro 1976). The resulting image gives an estimate of the extents of the sub-images. These extents are collectively referred to here as the 'image extent' or the image 'mask.' The computed mask image  $\lambda_m(x,y)$  is defined as

$$\lambda_m(x,y) = \begin{cases} 0, & \text{if } \min_n [f_s(\xi'; \phi_n)] \leq 0 \\ 1, & \text{otherwise} \end{cases} \quad (5.33)$$

where  $\xi'$  is the projected position of  $(x,y)$  along  $f_s(\xi; \phi_n)$ . The estimation of the image extent by (5.33) is possible because the object is sparse.

## 5.6 Computational experiments

Since the proposed reconstruction algorithm (§5.5.2) does not lend itself to simple analytical expressions, an empirical approach is taken to gain understanding of its effects.

To evaluate the reconstruction method, its performance was simulated on a computer using analytically defined projections of 2-d sections that are representative of the types of density distributions which are measured in

cerebral DSA. §5.6.1 describes the 2-d phantoms used and the method for generating the phantoms' projections. Incomplete projections are then simulated by deleting the appropriate projections from the complete set. Next, reconstruction from the remaining projections is performed using the Mclean algorithm (§5.5.2). Finally, the reconstructed section is compared with the original section using distance measures described in §5.6.2. For comparison results from two other reconstruction methods are examined. The first method (I) consists of convolution back-projection (§5.2.2.3) where a Shepp-Logan filter is used (5.16). The other method (II) takes the filtered layergram reconstructed by method (I) and sets the image to zero outside its known extent. The extent of the image is specified by its mask as defined in §5.5.3.3. The Mclean algorithm is designated as method (III). The three reconstruction algorithms were implemented in Fortran-77 on a Digital Equipment Corp. VAX 11/750 computer equipped with a Lexidata image display and utilizing the VMS operating system.

§5.6.3 describes the basic image reconstruction experiment. For each method both the number of projections and the magnitude of noise in the projections are varied. The results of reconstruction using methods I, II, and III are presented in §5.6.3.1-3 respectively.

#### 5.6.1 Simulation of projection data

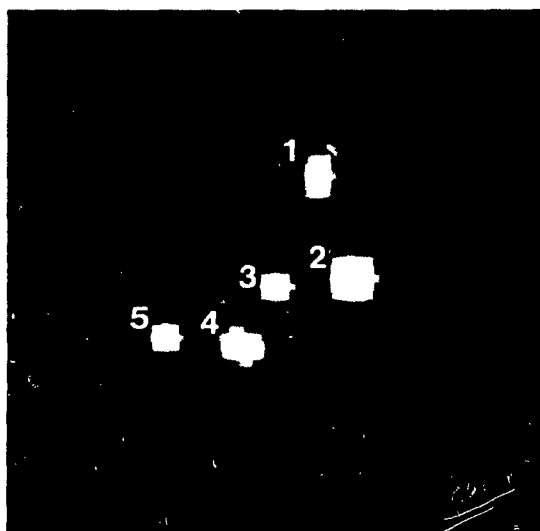
Figs. 5.10a)-c) show computer generated images of 'typical' 2-d cross sections of a 3-d density distribution of opacified blood vessels. All images are displayed in a 64x64 pixel matrix where densities of zero or less are represented by black and densities of 20 or over are represented by white. Densities between 0 and 20 are 'windowed' or mapped linearly onto 256 different grey levels (see 2.5). Although the original images are between 0 and 10 (see Tables 5.1-3), the display window is larger in order to account for possible 'overshoots' in the reconstructed images. Each of the computer generated phantoms contains sufficient structure to permit reconstruction to be evaluated realistically.

The simulated vascular cross sections in each of the images in Fig. 5.10 consist of elliptical boundaries enclosing regions of given density. Fig.

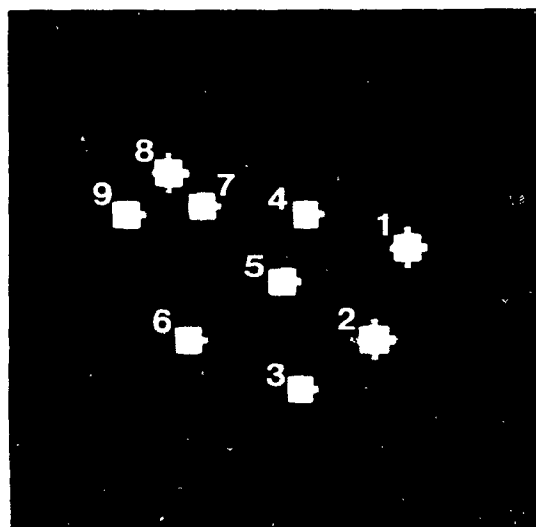


Figure 5.10 a)-c) Grey-scale images of computer generated phantoms. Phantoms consist of ellipses of various densities superimposed on a zero background. Images are windowed between 0 and 20. See Tables 5.1-3 for a list of component ellipses of phantoms shown below.

a) Phantom A



b) Phantom B



c) Phantom C

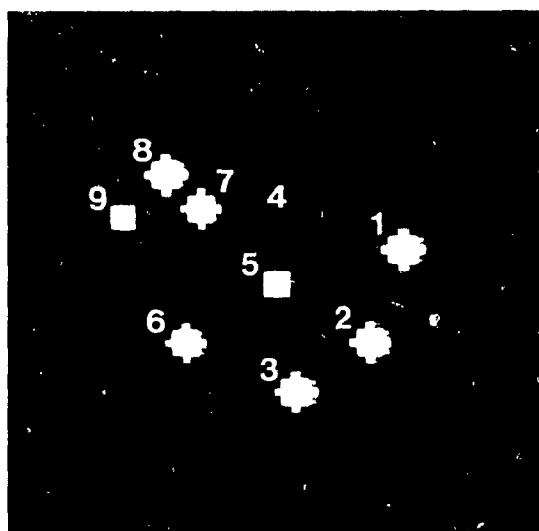


Table 5.1 Component ellipses of phantom A (see Fig. 5.10a).  $\psi$  is the angle between the major and x axes.

Ellipse	Coord. of the center (x,y)	A Major Axis	B Minor Axis	$\psi$ Rotation Angle	k Grey Level
1	38, 20	3	2	80	9
2	42, 32	3	3	0	11
3	33, 33	2	2	0	10
4	29, 49	3	2	165	12
5	20, 39	2	2	0	10

Table 5.2 Component ellipses of phantom B (see Fig. 5.10b).  $\psi$  is the angle between the major and x axes.

Ellipse	Coord. of the center (x,y)	A Major Axis	B Minor Axis	$\psi$ Rotation Angle	k Grey Level
1	48, 29	2	2	0	10
2	44, 40	2	2	0	10
3	35, 46	2	2	0	9
4	36, 25	2	2	0	8
5	33, 33	2	2	0	9
6	22, 40	2	2	0	8
7	24, 24	2	2	0	8
8	20, 20	2	2	0	10
9	15, 25	2	2	0	9

Table 5.3 Component ellipses of phantom C (see Fig. 5.10c)  $\psi$  is the angle between the major and x axes.

Ellipse	Coord. of the center (x,y)	A Major Axis	B Minor Axis	$\psi$ Rotation Angle	k Grey Level
1	48, 29	2	2	0	10
2	44, 40	2	2	0	10
3	35, 46	2	2	0	9
4	36, 25	2	2	0	2
5	33, 33	2	2	0	5
6	22, 40	2	2	0	8
7	24, 24	2	2	0	8
8	20, 20	2	2	0	10
9	15, 25	2	2	0	5

5.10a) shows a section consisting of 5 objects that are different in shape and size (Table 5.1). Figs. 5.10b) and c) illustrate sections where there are many (i.e. 9) disk shaped objects. Fig. 5.10c) (Table 5.3) is different from Fig. 5.10b) (Table 5.2) in that there are larger differences between object densities. Images in Fig. 5.10 a), b), and c) are referred to here as phantoms 'A,' 'B,' and 'C' respectively.

The projections of the test phantoms are computed analytically rather than re-projecting (§5.5.3.2) the digitized images. This avoids the problem of biasing the test of the algorithm by using the same procedure to determine the projections as for the reconstruction (Crowther and Klug 1971; Smith et al. 1973). Fig. 5.11 illustrates a projection of an ellipse where the density distribution is

$$\lambda(x,y) = \left. \begin{aligned} & k, \quad \text{for} \quad \frac{x^2}{A^2} + \frac{y^2}{B^2} \leq 1 \quad (\text{inside the ellipse}) \\ & = 0, \quad \text{otherwise} \quad (\text{outside the ellipse}) \end{aligned} \right\} \quad (5.34)$$

The expression for the relationship between  $\lambda(x,y)$  (5.34) and its projection  $f(\xi;\phi)$  is given by (Rosenfeld and Kak 1982)

$$f(\xi;\phi) = \left. \begin{aligned} & \frac{2kAB}{a^2(\phi)} \sqrt{a^2(\phi) - \xi^2} \quad \text{for} \quad |\xi| \leq a(\phi) \\ & = 0 \quad \text{for} \quad |\xi| > a(\phi) \end{aligned} \right\} \quad (5.35)$$

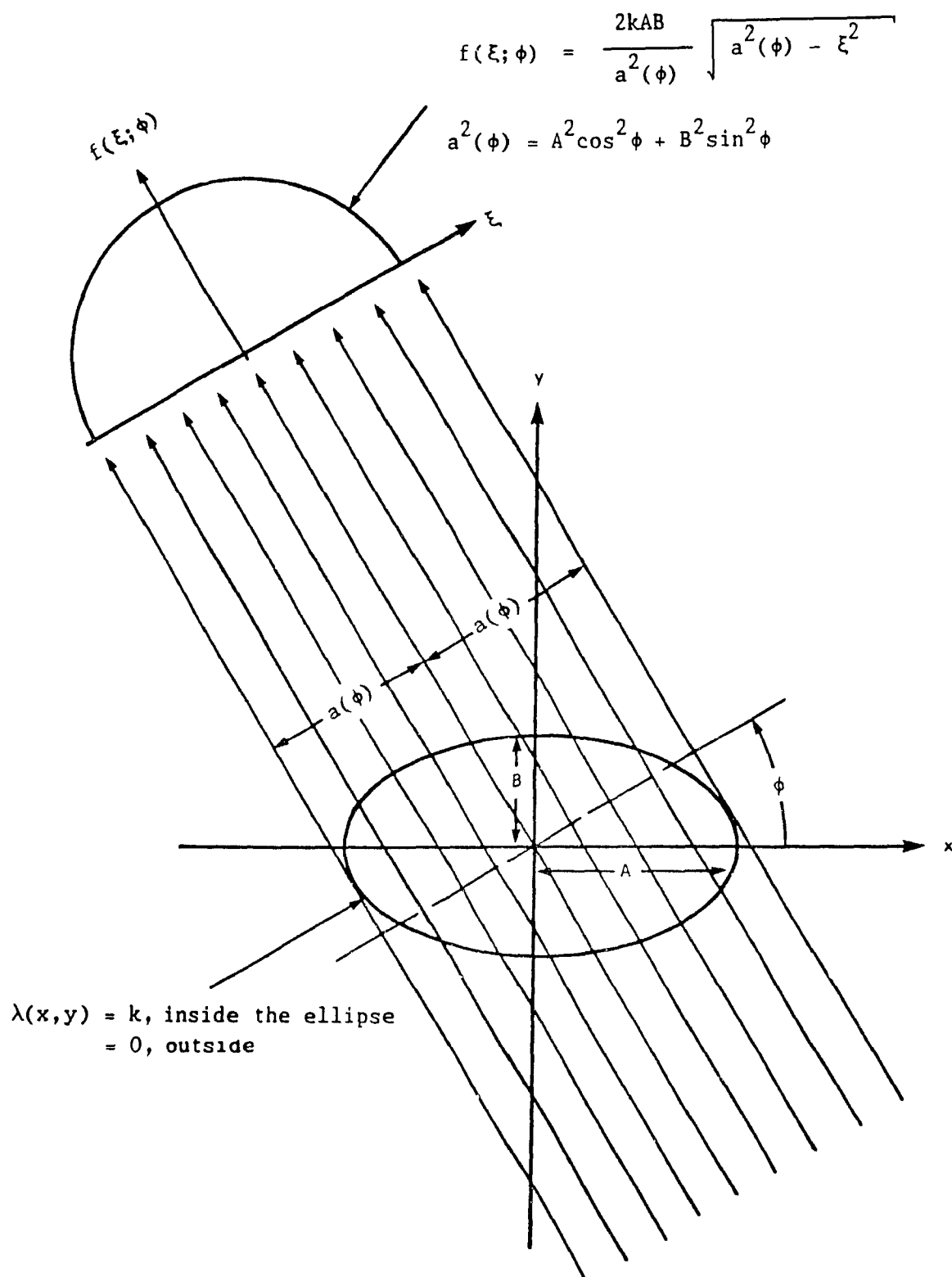
$$\text{where } a^2(\phi) = A^2 \cos^2 \phi + B^2 \sin^2 \phi \quad (5.36)$$

The projection of an image composed of a number of ellipses is simply the sum of the projections for each of the ellipses. Projections of the 2-d computer phantom are produced along 180 angles evenly spaced over  $\pi$  radians. Each simulated projection consists of 128 samples (§5.2.3.1).

### 5.6.2 Comparison criteria

It is often difficult to evaluate the quality of reconstruction and assess artifacts quantitatively from visual inspection of grey scale images alone. For this reason a conventional root-mean-square error criterion is

Figure 5.11 Illustration of a projection of an ellipse. (After Rosenfeld and Kak 1982)



adopted. Following Heffernan and Bates (1982) the 'distance' between the reconstructed image  $\lambda_e$  and the original image  $\lambda$  is given by the total error

$$E^2(T, \Omega) = \iint_{\Omega} [ \lambda_e(x,y) - \lambda(x,y) ]^2 d\Omega \quad (5.37)$$

where  $T$  represents the Roman numeral identifying the reconstruction method, and  $\Omega$  is partitioned into convex image regions  $\Omega_-$  and background  $\Omega_+$  (see 5.22 and 5.23). The computed error in the region of the image extent reflects the distance in pixel values between actual and reconstructed object regions, whereas the background error measure indicates the amount of artifact removed in reconstruction. The error criterion associated with a reconstruction (Heffernan and Bates 1982) is introduced as

$$\epsilon(T, \Omega) = E(T, \Omega) / E(I, \Omega) \quad (5.38)$$

which compares any of the reconstruction methods with method (I). This error criterion is taken as a measure of reconstruction accuracy.

### 5.6.3 Basic experiment

The basic experiment consists of reconstructing images from  $N$  given projections of a phantom. The reconstructed images are then compared to the corresponding true images visually and by computing the error criterion (5.38). The total error resulting from method I reconstruction using  $N=5$  projections serves as the basis of comparison in (5.38). In cerebral DSA 5 projections are reasonably achievable in practice. Each experiment also considers the effect of noise in the projections on reconstruction error. This experiment is performed for phantoms A, B, and C using reconstruction methods I, II, and III.

Reconstruction accuracy or error is expected to depend on both the number of given projections and on the degree to which the given projections are representative of the complete set. Images are reconstructed from 4, 5, 10, 15, and 20 projections evenly spaced over  $\pi$  radians. To investigate the feasibility of reconstruction from biplane stereo pairs, projections are taken at angles  $\phi = 0, 10, 90, \text{ and } 100$  degrees. The set of biplane stereo

projections is denoted by  $N = 4S$ . All possible sets of  $N$  projections are formed by incrementing the starting angle in one degree steps over a span of  $(180/N)$  degrees. Images are then reconstructed from all possible sets of  $N$  projections and the mean total error (5.37) is computed and reported as a fraction of the mean total error for 5 given projections (5.38). Similarly reconstruction from all possible stereo biplane projection pairs are also evaluated in this manner.

The major factor expected to affect reconstruction accuracy is projection noise. Both object dependent and additive noise are introduced to the projections. Object dependent noise in each projection is simulated by multiplying the true projection values by a random number with Gaussian distribution of mean 1 and standard deviation  $\sigma_m$ . Phantoms are reconstructed from simulated projections with  $\sigma_m = 5$  and 10% noise. Noise values drawn randomly from a Gaussian distribution of mean 0 and standard deviation  $\sigma_a$  are also added to the true projection. In these reconstruction experiments additive noise levels of  $\sigma_a = 1$  and 5 are considered. Fig. 5.12 shows an example of a true projection (e.g. phantom C,  $\phi=60$  degrees) corrupted by multiplicative (i.e.  $\sigma_m=10\%$ ) and additive (i.e.  $\sigma_a=5$ ) noise. Multiplicative and additive noise are expected to propagate errors into the object-layergram isometry and the computed image extent of the layergram.

Tables listing the error in phantom reconstructions are only presented for phantom C which were found to be representative of results for the other phantoms in each of the three methods.

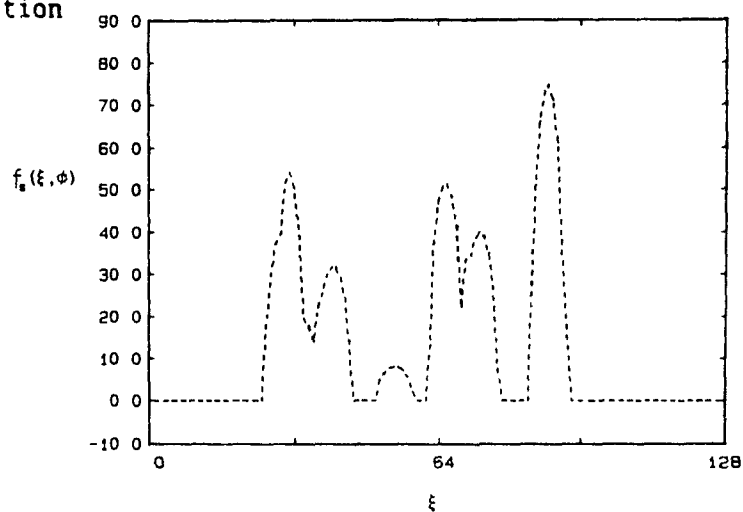
#### 5.6.3.1 Method I: Convolution back-projection

Phantoms A, B, and C were reconstructed by convolution back-projection using a Shepp-Logan filter where the cut-off frequency is defined by the Nyquist sampling frequency (§5.2.2.3). Figs. 5.13, 5.14, and 5.15 show the results of applying this method when there are  $N$  given projections of the test phantoms A, B, and C respectively.

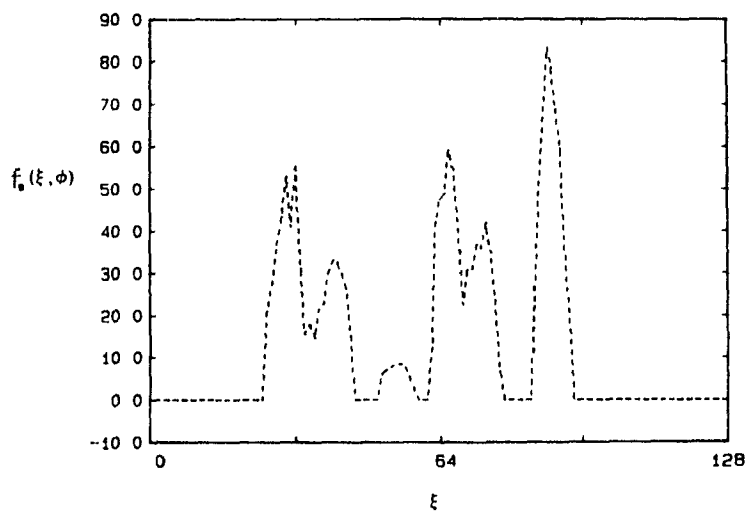
Figs. 5.13-15 a)-c) show that angular aliasing and clutter (§5.2.3.2) dominate images reconstructed by four and five projections. Streak artifacts

Figure 5.12 a) Projection at angle  $\phi=60$  degrees of phantom C degraded by b) multiplicative noise,  $\sigma_m=10\%$ , and c) additive noise,  $\sigma_a=5$ .

a) Original projection



b)  $\sigma_m=10\%$



c)  $\sigma_a=5$

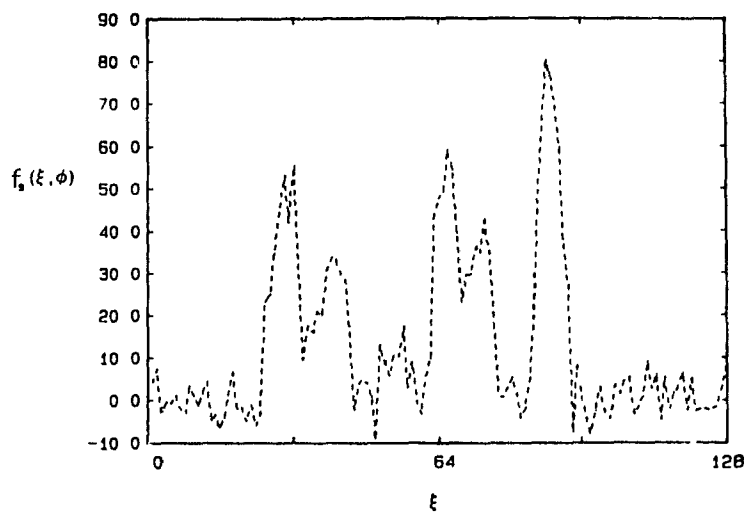
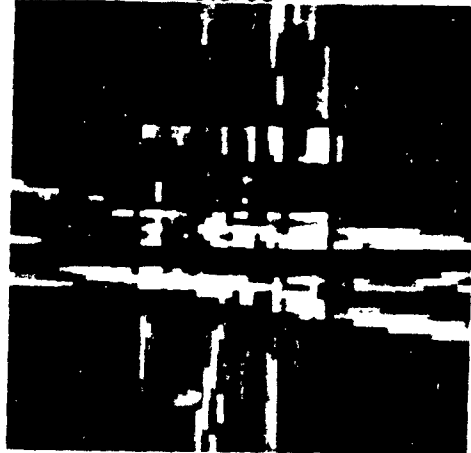
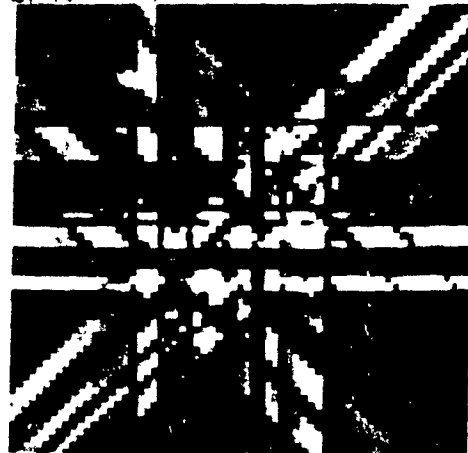


Figure 5.13 Reconstruction of phantom A using method I (convolution back-projection) from  $N$  given projections. Images are windowed between 0 and 20.

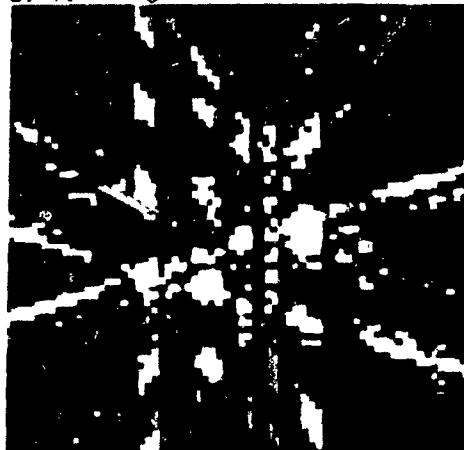
a)  $N = 4$  stereo



b)  $N = 4$



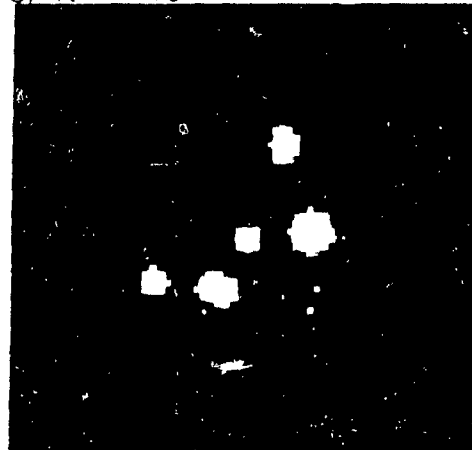
c)  $N = 5$



d)  $N = 10$



e)  $N = 15$



f)  $N = 20$

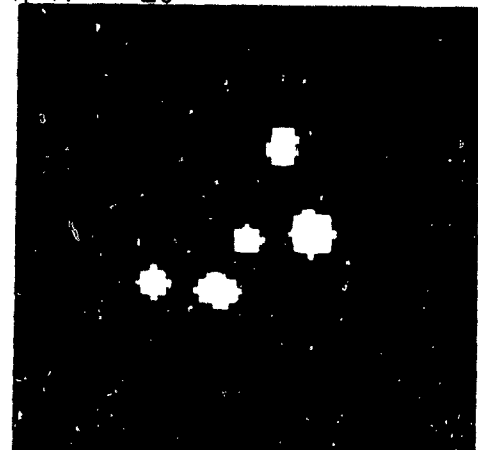
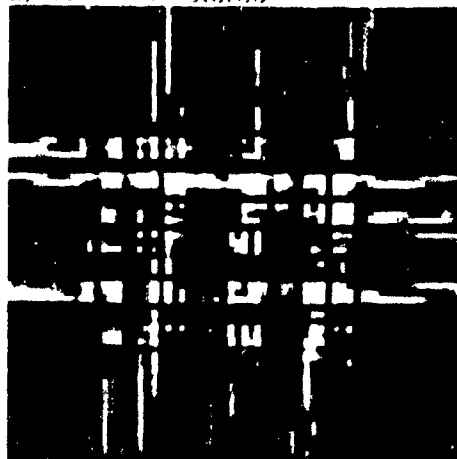


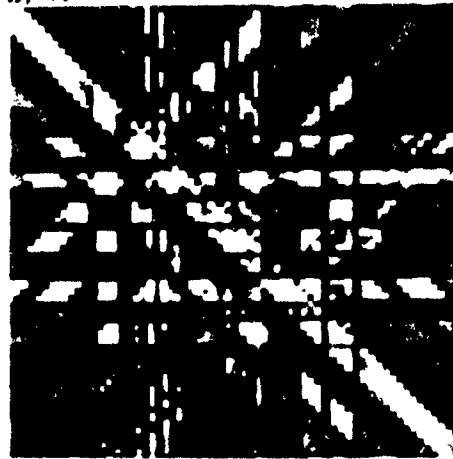


Figure 5.14 Reconstruction of phantom B using method I (convolution back-projection) from  $N$  given projections. Images are windowed between 0 and 20.

a)  $N = 4$  stereo



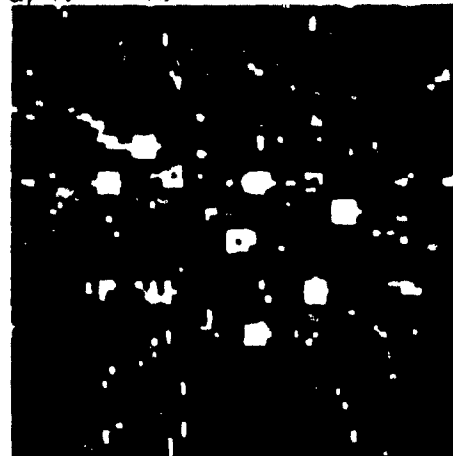
b)  $N = 4$



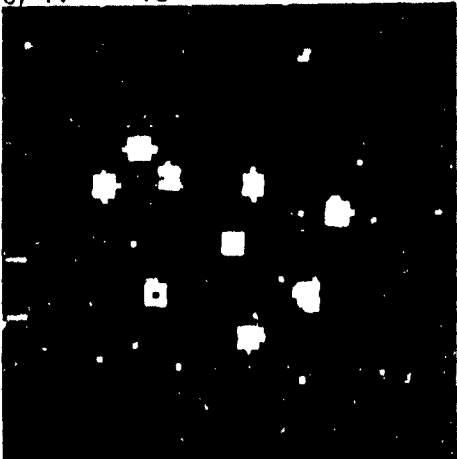
c)  $N = 5$



d)  $N = 10$



e)  $N = 15$



f)  $N = 20$

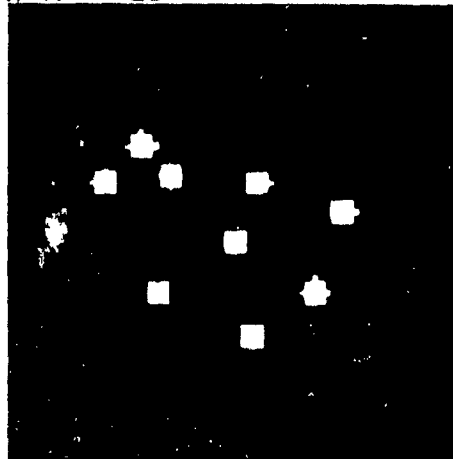
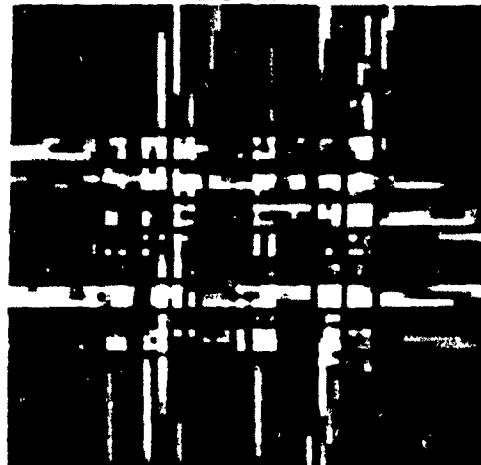
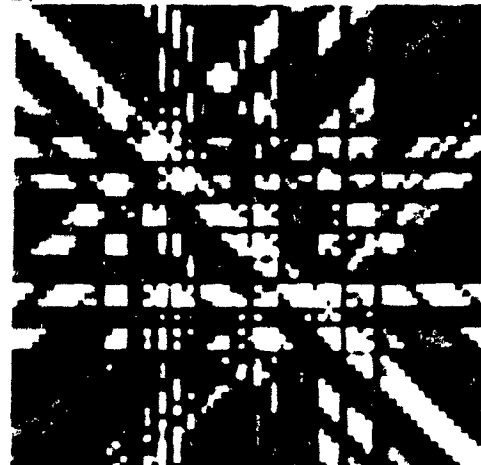


Figure 5.15 Reconstruction of phantom C using method I (convolution back-projection) from  $N$  given projections. Images are windowed between 0 and 20.

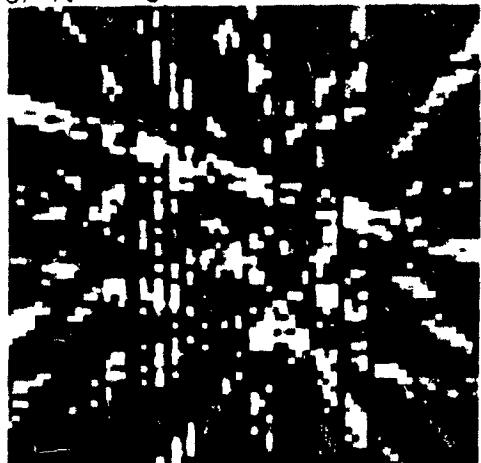
a)  $N = 4$  stereo



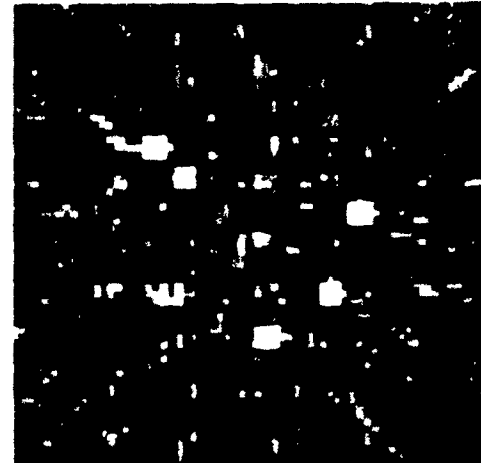
b)  $N = 4$



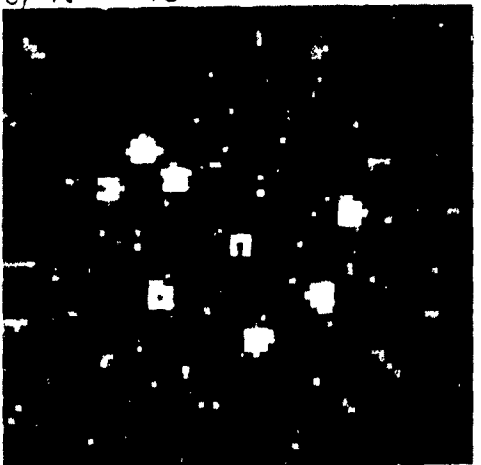
c)  $N = 5$



d)  $N = 10$



e)  $N = 15$



f)  $N = 20$

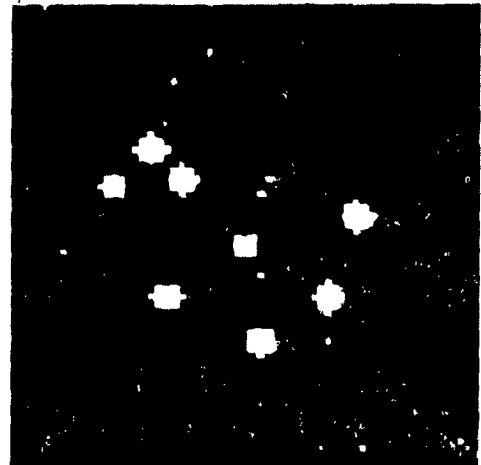


Table 5.4 Error criteria for method I, using different numbers of given projections (N) applied to phantom C. ( $\Omega_+$ , image background;  $\Omega_-$ , image extent)

N Projections	Number of Projection Sets	$\epsilon(I, \Omega_+)$		$\epsilon(I, \Omega_-)$	
4S	80	1.16	$\pm .09$	1.2	$\pm .2$
4	45	1.15	$\pm .07$	1.1	$\pm .1$
5	36	1.0		1.0	
10	18	.65	$\pm .04$	.65	$\pm .04$
15	12	.47	$\pm .03$	.49	$\pm .04$
20	9	.37	$\pm .02$	.38	$\pm .03$
32	6	.23	$\pm .01$	.28	$\pm .03$
64	3	.09	$\pm .01$	.20	$\pm .02$

Table 5.5 Error criteria for method I, using different numbers of given projections (N) and different levels of projection noise ( $\sigma_m$ ) applied to phantom C. ( $\Omega_+$ , image background;  $\Omega_-$ , image extent)<sup>m</sup>

N Projections	$\sigma_m = 5\%$				$\sigma_m = 10\%$			
	$\epsilon(I, \Omega_+)$		$\epsilon(I, \Omega_-)$		$\epsilon(I, \Omega_+)$		$\epsilon(I, \Omega_-)$	
4S	1.19	$\pm .09$	1.3	$\pm .2$	1.27	$\pm .09$	1.4	$\pm .2$
4	1.18	$\pm .08$	1.2	$\pm .1$	1.26	$\pm .08$	1.3	$\pm .2$
5	1.03	$\pm .08$	1.06	$\pm .09$	1.12	$\pm .08$	1.2	$\pm .1$
10	.67	$\pm .04$	.70	$\pm .05$	.72	$\pm .04$	.83	$\pm .07$
15	.49	$\pm .03$	.54	$\pm .05$	.54	$\pm .03$	.66	$\pm .05$
20	.38	$\pm .02$	.40	$\pm .04$	.42	$\pm .02$	.48	$\pm .04$

Table 5.6 Error criteria for method I, using different numbers of given projections (N) and different levels of projection noise ( $\sigma_a$ ) applied to phantom C. ( $\Omega_+$ , image background;  $\Omega_-$ , image extent)<sup>a</sup>

N Projections	$\sigma_a = 1$				$\sigma_a = 5$			
	$\epsilon(I, \Omega_+)$		$\epsilon(I, \Omega_-)$		$\epsilon(I, \Omega_+)$		$\epsilon(I, \Omega_-)$	
4S	1.2	$\pm .1$	1.2	$\pm .2$	1.3	$\pm .1$	1.4	$\pm .2$
4	1.2	$\pm .1$	1.1	$\pm .1$	1.3	$\pm .1$	1.3	$\pm .1$
5	1.0	$\pm .1$	1.0	$\pm .1$	1.2	$\pm .1$	1.2	$\pm .1$
10	.65	$\pm .04$	.65	$\pm .06$	.78	$\pm .04$	.81	$\pm .06$
15	.48	$\pm .03$	.49	$\pm .04$	.59	$\pm .03$	.65	$\pm .05$
20	.37	$\pm .02$	.38	$\pm .03$	.48	$\pm .03$	.52	$\pm .04$

combine in the reconstructed images to appear as false or pseudo objects that can not be distinguished from true objects. As the number of projections used in reconstruction is increased, the level of artifact decreases. It then becomes possible on the basis of object 'a priori' knowledge (see §5.3.2) to distinguish between pseudo and true objects. Streak artifacts in images reconstructed from 10 and more projections (see Figs. 5.13-15 d)-f)) have lower grey level or pixel values and are different in extent by comparison to the reconstructed objects. All objects in the phantom reconstructions can be identified with exception of the fourth object of phantom C (see Table 5.3). The pixel value of this reconstructed object is within the range of background or artifact pixel values. Although images reconstructed from 15 and 20 projections are sufficient to identify and locate phantom objects, the extent and pixel values of these structures are poorly reconstructed.

Table 5.4 lists the error criteria for reconstructions of phantom C from N given projections with no noise. This table shows that the level of error in image background decreases quickly with increasing numbers of projections used in reconstruction. Unlike visual inspection of the reconstructions, the image background error criterion does not indicate how artifacts are spatially distributed.

The error in the regions of the image extent is seen to decrease slowly with increasing numbers of projections in Table 5.4. This is a direct consequence of the incompleteness of the projection set. Reconstruction from noisy projections shows moderate increases in both errors in the image extent and background (see Tables 5.5 and 5.6).

#### **5.6.3.2 Method II: Masked convolution back-projection**

Given the piece-wise constant nature of the object to be reconstructed (see §5.3.2), a scheme to reduce reconstruction artifacts by image extent constraints 'a posteriori' was investigated. The scheme incorporating image extent information after convolution back-projection is referred to here as 'masked convolution back-projection' or method II.

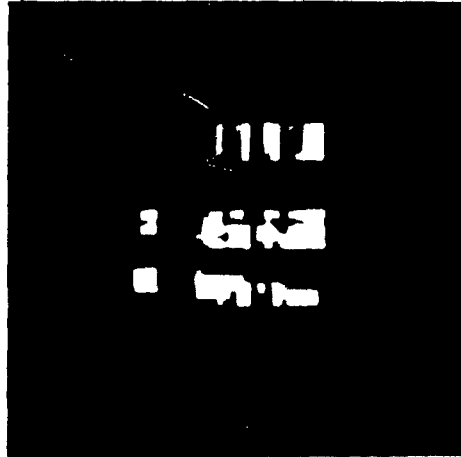
Masked convolution back-projection consists of computing the image extent (§5.5.3.3) from  $N$  given projections and then using the image extent to mask the corresponding filtered layergram. All image pixels in the filtered layergram outside the computed image extent are set to zero value.

Figs. 5.16, 5.17, and 5.18 illustrate the application of method II to test phantoms A, B, and C respectively for  $N$  given projections. Comparing images in Figs. 5.16-18 to the corresponding images in Figs. 5.13-15 show the degree to which the computed image extent improves reconstruction. Figs. 5.16-18 a) and b) show the improvement in images reconstructed from four evenly spaced projections over that from biplane stereo projections. The former set of projections can be thought to be a better representation of the complete projection set than the latter. As the number of projections equals the number of piece-wise constant objects in the section, a little artifact remains (see Figs. 5.16c) and 5.17-18d)). After reconstruction of phantoms from 15 and 20 projections almost all pseudo objects are masked out (see Figs. 5.16-18 e) and f)).

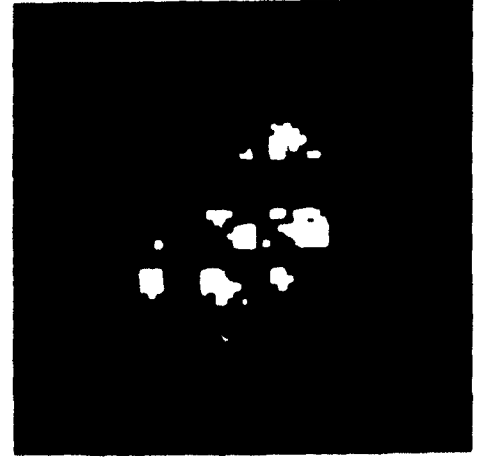
Table 5.7 shows error in the image background decreases with increasing numbers of given projections. The error in image background decreases quickly to small levels, but not to zero. Fewer projections are required to reduce background error to negligible levels than would be achieved by method I (e.g.  $N=10$  vs.  $N=64$  in Table 5.4). In contrast the error in the image extent decreases slowly. Both non-zero image background levels and larger error levels in the image extent are due to incorrectly computed image extents. This affects reconstruction by masking out regions of the true image extent and by retaining some pixels from the background. The remaining portion of image extent changes very little with the number of projections which accounts for the almost constant error in image extent. The inclusion of background image pixels accounts for non-zero image background levels. Error in the computation of image extent is thought to be due to insufficient numbers of projections. Uniform angular sampling of projections is important as shown by the differences between background errors in images reconstructed from 4 equally spaced views and stereo biplane views. These results also support observations made above about Figs. 5.16-18 a) and b).

Figure 5.16 Reconstruction of phantom A using method II (masked convolution back-projection) from  $N$  given projections. Images are windowed between 0 and 20.

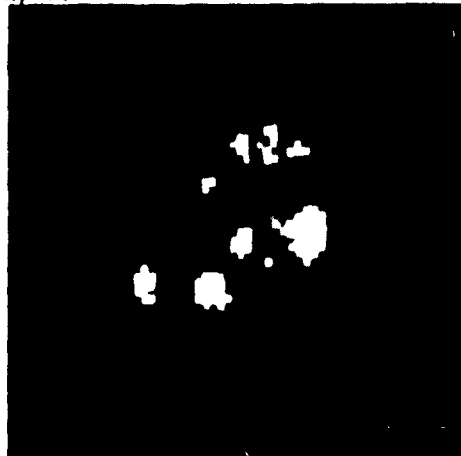
a)  $N = 4$  stereo



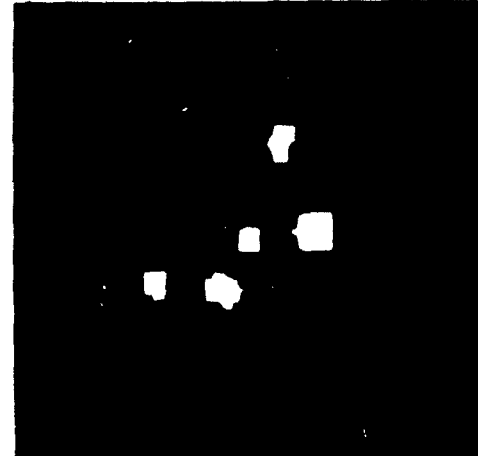
b)  $N = 4$



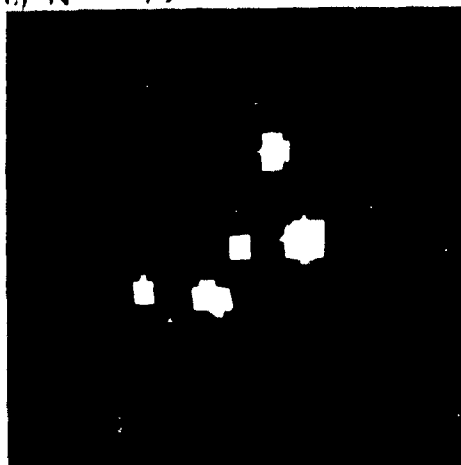
c)  $N = 5$



d)  $N = 10$



e)  $N = 15$



f)  $N = 20$

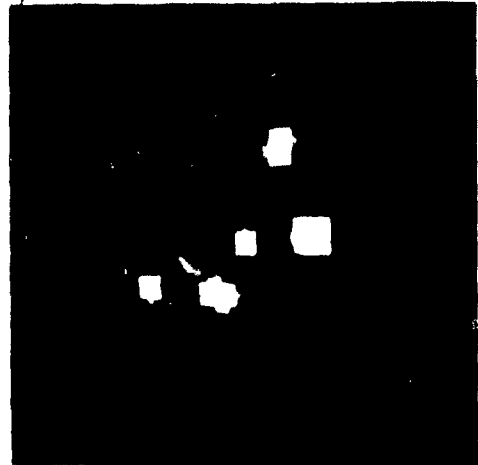
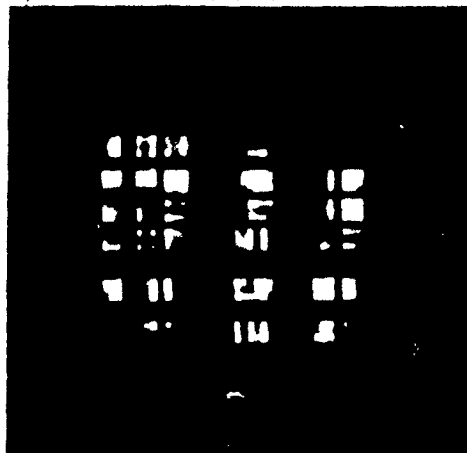
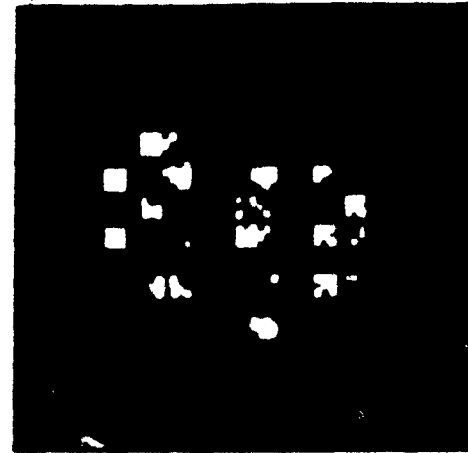


Figure 5.17 Reconstruction of phantom B using method II (masked convolution back-projection) from  $N$  given projections. Images are windowed between 0 and 20.

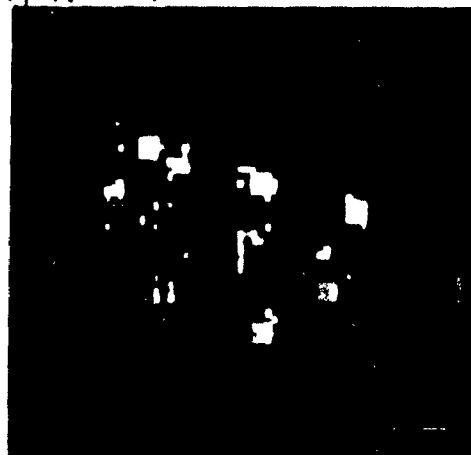
a)  $N = 4$  stereo



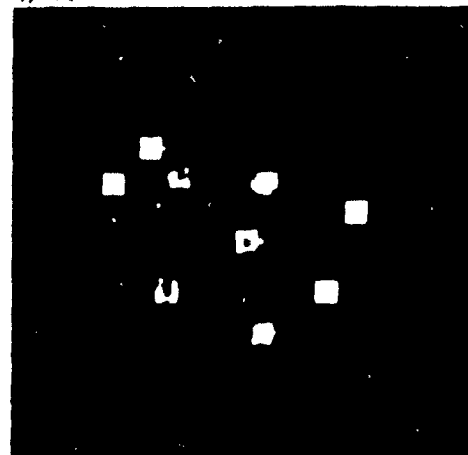
b)  $N = 4$



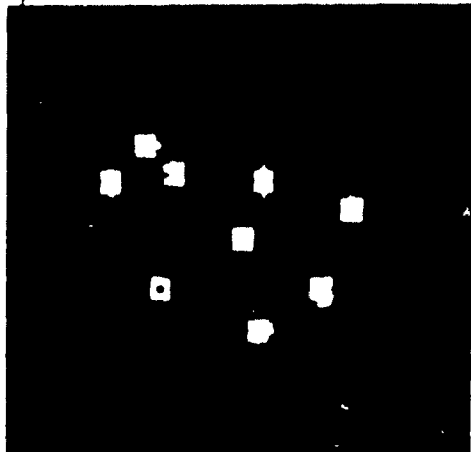
c)  $N = 5$



d)  $N = 10$



e)  $N = 15$



f)  $N = 20$

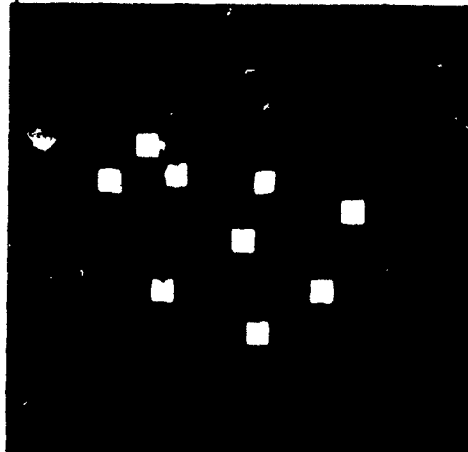
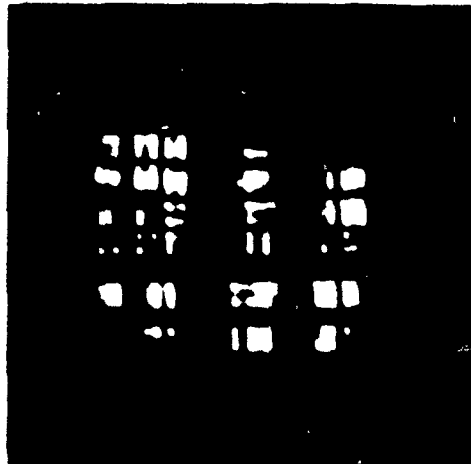
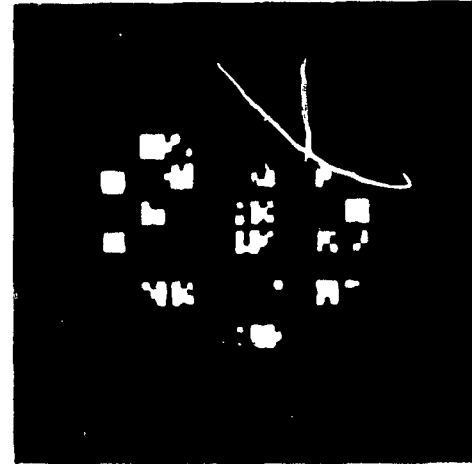


Figure 5.18 Reconstruction of phantom C using method II (masked convolution back-projection) from N given projections. Images are windowed between 0 and 20.

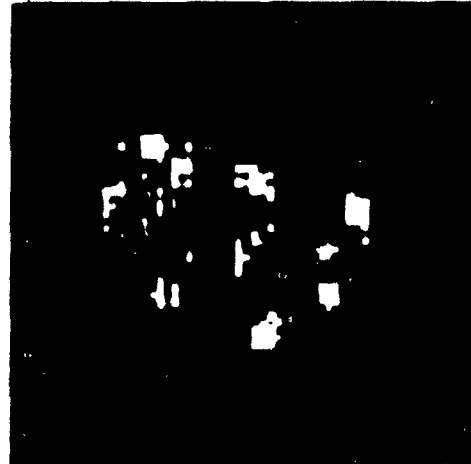
a) N = 4 stereo



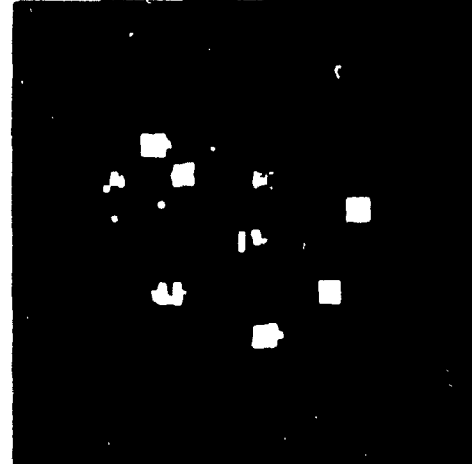
b) N = 4



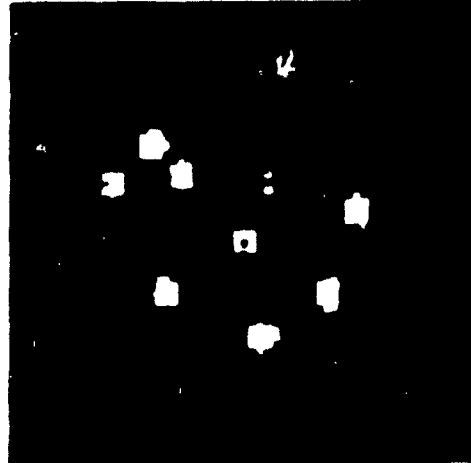
c) N = 5



d) N = 10



e) N = 15



f) N = 20

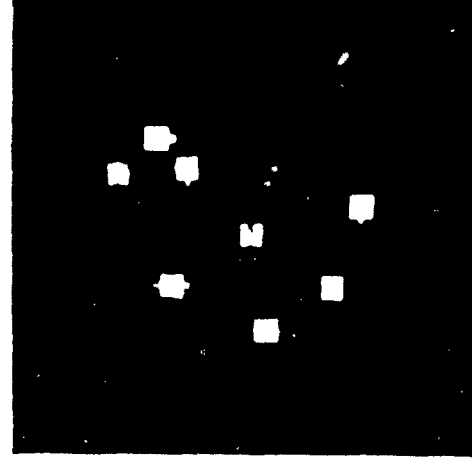




Table 5.7 Error criteria for method II, using different numbers of given projections (N) applied to phantom C. ( $\Omega_+$ , image background;  $\Omega_-$ , image extent)

N Projections	Number of Projection Sets	$\epsilon(\text{II}, \Omega_+)$	$\epsilon(\text{II}, \Omega_-)$
4S	80	.63 $\pm$ .06	1.2 $\pm$ .2
4	45	.46 $\pm$ .06	1.1 $\pm$ .1
5	36	.31 $\pm$ .05	1.01 $\pm$ .07
10	18	.06 $\pm$ .02	.69 $\pm$ .05
15	12	.02 $\pm$ .01	.59 $\pm$ .05
20	9	.01 $\pm$ .01	.54 $\pm$ .05

Table 5.8 Error criteria for method II, using different numbers of given projections (N) and different levels of projection noise ( $\sigma_m$ ) applied to phantom C. ( $\Omega_+$ , image background;  $\Omega_-$ , image extent)<sup>m</sup>

N Projections	$\sigma_m = 5\%$		$\sigma_m = 10\%$	
	$\epsilon(\text{II}, \Omega_+)$	$\epsilon(\text{II}, \Omega_-)$	$\epsilon(\text{II}, \Omega_+)$	$\epsilon(\text{II}, \Omega_-)$
4S	.64 $\pm$ .06	1.3 $\pm$ .2	.67 $\pm$ .06	1.4 $\pm$ .2
4	.47 $\pm$ .06	1.2 $\pm$ .1	.53 $\pm$ .06	1.3 $\pm$ .01
5	.32 $\pm$ .05	1.05 $\pm$ .08	.35 $\pm$ .06	1.20 $\pm$ .09
10	.06 $\pm$ .02	.74 $\pm$ .06	.07 $\pm$ .02	.85 $\pm$ .07
15	.02 $\pm$ .01	.62 $\pm$ .06	.03 $\pm$ .01	.71 $\pm$ .06
20	.01 $\pm$ .01	.55 $\pm$ .06	.02 $\pm$ .01	.60 $\pm$ .06

Table 5.9 Error criteria for method II, using different numbers of given projections (N) and different levels of projection noise ( $\sigma_a$ ) applied to phantom C. ( $\Omega_+$ , image background;  $\Omega_-$ , image extent)<sup>a</sup>

N Projections	$\sigma_a = 1$		$\sigma_a = 5$	
	$\epsilon(\text{II}, \Omega_+)$	$\epsilon(\text{II}, \Omega_-)$	$\epsilon(\text{II}, \Omega_+)$	$\epsilon(\text{II}, \Omega_-)$
4S	.89 $\pm$ .06	1.2 $\pm$ .2	.99 $\pm$ .07	1.4 $\pm$ .2
4	.84 $\pm$ .06	1.1 $\pm$ .2	.95 $\pm$ .07	1.3 $\pm$ .1
5	.66 $\pm$ .06	1.0 $\pm$ .1	.76 $\pm$ .06	1.2 $\pm$ .1
10	.28 $\pm$ .03	.67 $\pm$ .06	.32 $\pm$ .03	.80 $\pm$ .07
15	.14 $\pm$ .02	.54 $\pm$ .06	.16 $\pm$ .02	.66 $\pm$ .06
20	.07 $\pm$ .01	.48 $\pm$ .06	.09 $\pm$ .02	.61 $\pm$ .06

Error values listed in Table 5.8 indicate that phantoms reconstructed from projections with  $\sigma_m = 5\%$  and  $10\%$  noise result in images slightly less faithful than from projections with no noise. In the presence of additive noise, a large increase in image background error is observed, especially for the case of  $N \leq 15$  projections. This is expected since the method of computing the image extent relies on the use of null-rays (see §5.5.3.3), and additive noise in the projections would reduce the number of these rays available.

#### 5.6.3.3 Method III: Mclean

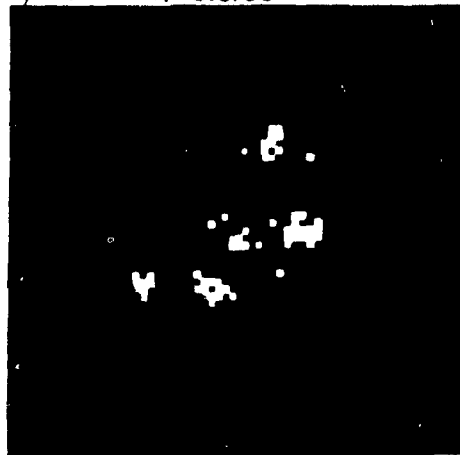
Results of applying method III to different numbers of projections of phantoms are presented. The gain was set to  $\alpha = 0.3$ , and the convergence criterion  $c$  was calculated by taking the average of all image pixel values outside the computed extent in the initially formed layergram. The effect of gain and convergence criterion settings on reconstruction error is discussed later in §5.6.3.3.1.

Figs. 5.19, 5.20, and 5.21 show the results of reconstruction from noiseless projections of phantoms A, B, and C respectively using Mclean. In Figs. 5.19-21 a) and b), images of phantoms reconstructed from 4 equally spaced views are superior to those images reconstructed from biplane stereo views. Biplane stereo data renders a poorer reconstruction since it introduces more false object points. This is in part due to better isometry between the true image and the layergram from 4 equally spaced projections. This layergram is less cluttered (see Figs. 5.16-18 a) and b)) than the layergram formed from biplane stereo projections. Another factor is the larger differences in image pixel values of the layergram between true and pseudo objects than in the biplane stereo layergram. With exception of sections consisting of a very few objects (i.e. less than 5 objects) there is a lack of sufficient information in the stereo projections to form an adequate layergram for cleaning. These results indicate that Mclean requires the number of given projections to be at least equal to the number of the objects in the section (for these types of phantoms).

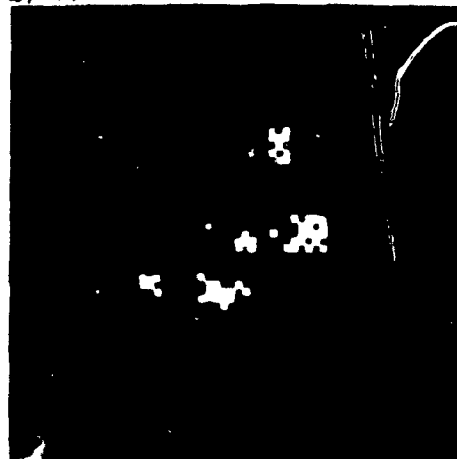
Results also indicate that when object regions consist of relatively the

Figure 5.19 Reconstruction of phantom A using method III (McLennan) from  $N$  given projections. Images are windowed between 0 and 20.

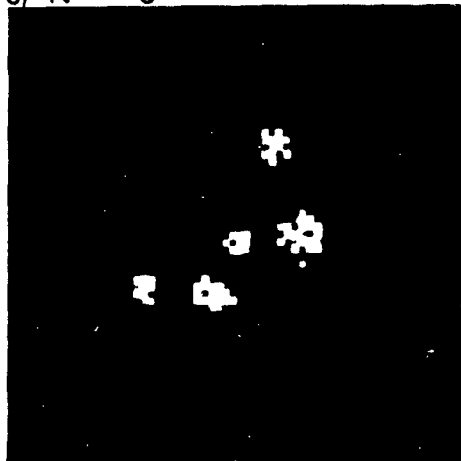
a)  $N = 4$ , stereo



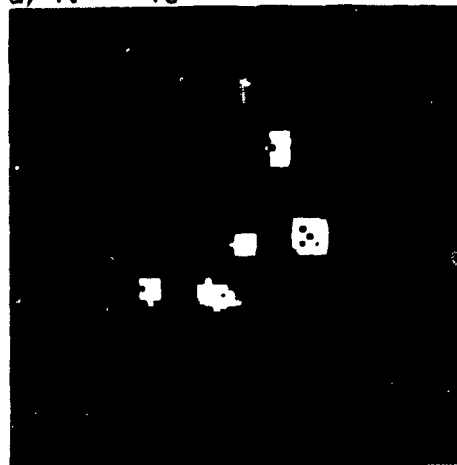
b)  $N = 4$



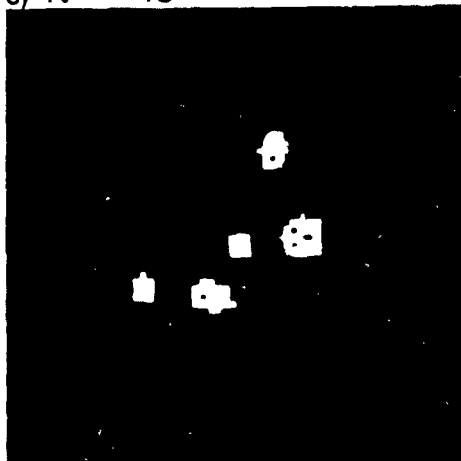
c)  $N = 5$



d)  $N = 10$



e)  $N = 15$



f)  $N = 20$

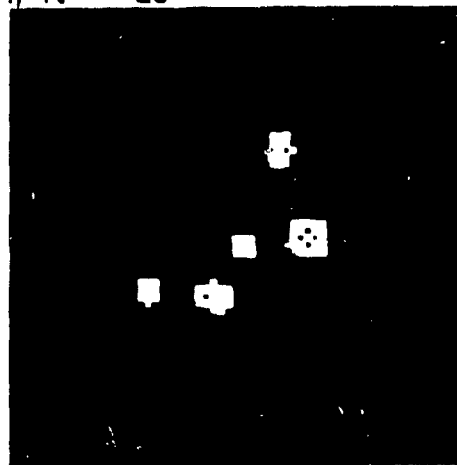
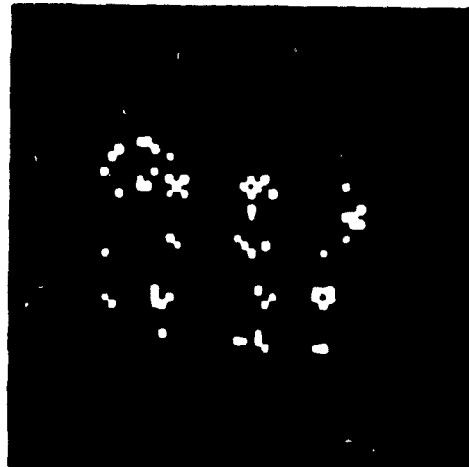


Figure 5.20 Reconstruction of phantom B using method III (McLennan) from  $N$  given projections. Images are windowed between 0 and 20.

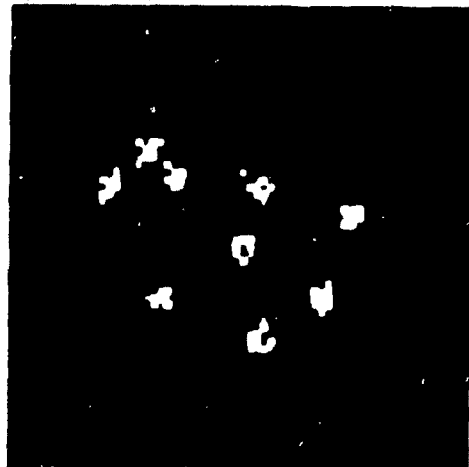
a)  $N = 4$  stereo



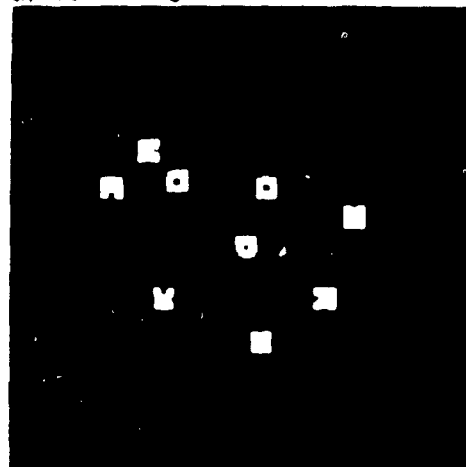
b)  $N = 4$



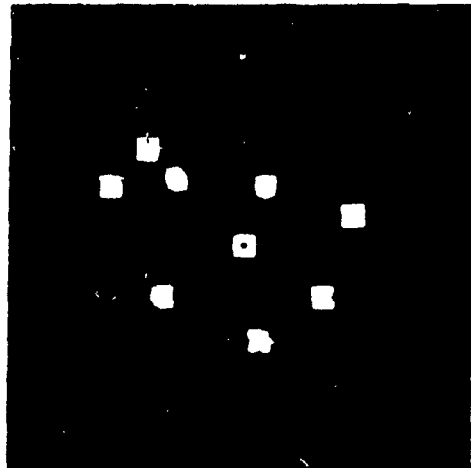
c)  $N = 5$



d)  $N = 10$



e)  $N = 15$



f)  $N = 20$

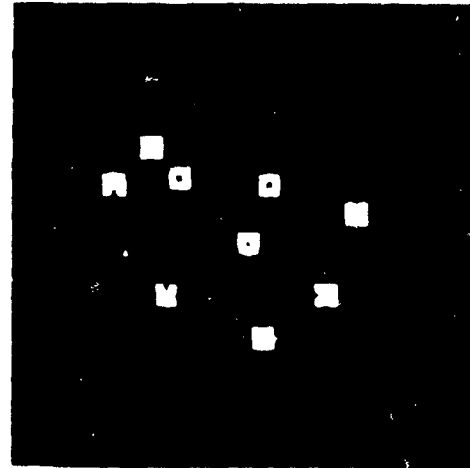
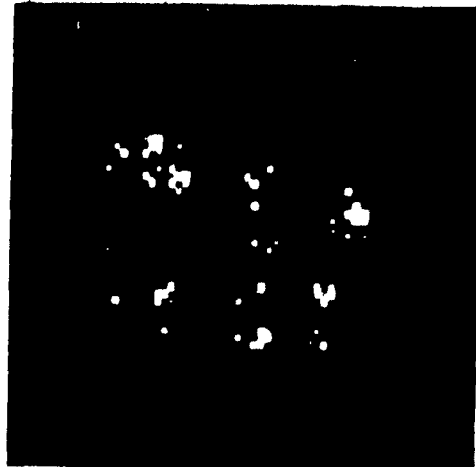
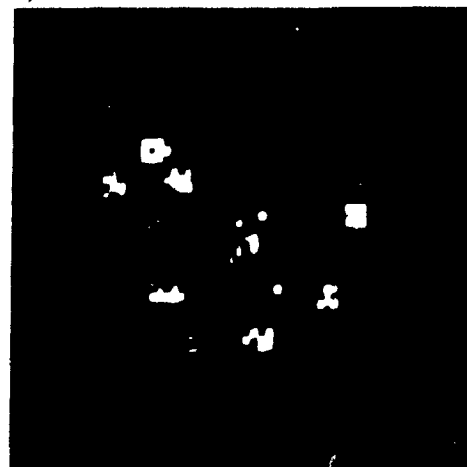


Figure 5.21 Reconstruction of phantom C using method III (McLean) from  $N$  given projections. Images are windowed between 0 and 20.

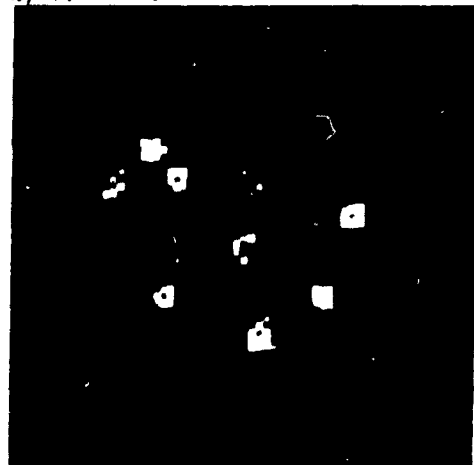
a)  $N = 4$  stereo



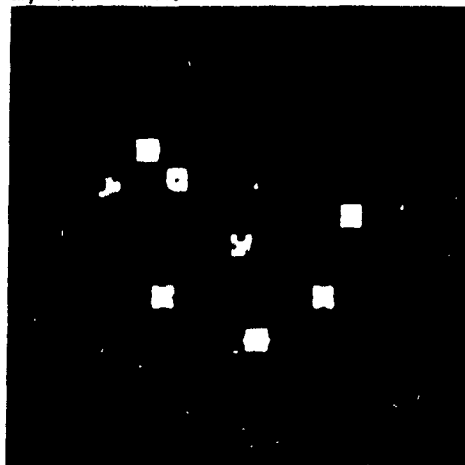
b)  $N = 4$



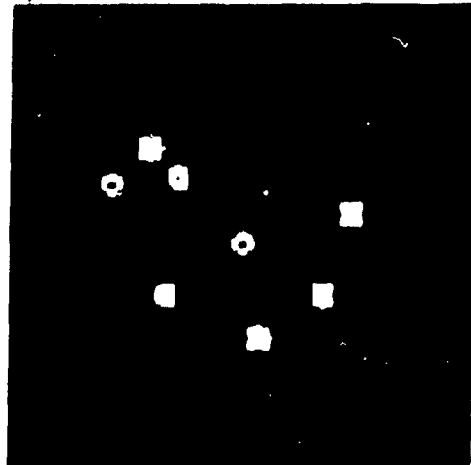
c)  $N = 5$



d)  $N = 10$



e)  $N = 15$



f)  $N = 20$

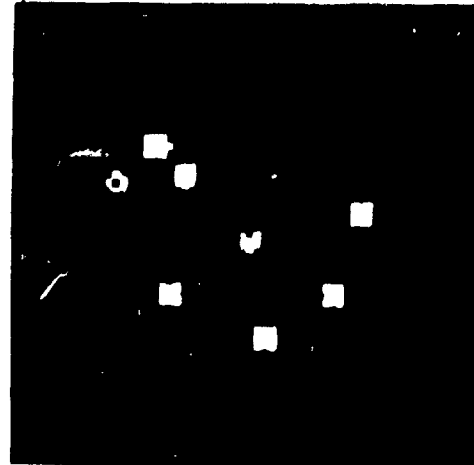


Table 5.10 Error criteria for method III, using different numbers of given projections (N) applied to phantom C. ( $\Omega_+$ , image background;  $\Omega_-$ , image extent)

N Projections	Number of Projection Sets	$\epsilon(\text{III}, \Omega_+)$	$\epsilon(\text{III}, \Omega_-)$
4S	80	.30 $\pm$ .07	1.7 $\pm$ .1
4	45	.18 $\pm$ .05	1.5 $\pm$ .1
5	36	.09 $\pm$ .02	1.3 $\pm$ .1
10	18	.01 $\pm$ .01	1.01 $\pm$ .06
15	12	.0	.95 $\pm$ .06
20	9	.0	.92 $\pm$ .06

Table 5.11 Error criteria for method III, using different numbers of given projections (N) and different levels of projection noise ( $\sigma_m$ ) applied to phantom C. ( $\Omega_+$ , image background;  $\Omega_-$ , image extent)<sup>m</sup>

N Projections	$\sigma_m = 5\%$		$\sigma_m = 10\%$	
	$\epsilon(\text{III}, \Omega_+)$	$\epsilon(\text{III}, \Omega_-)$	$\epsilon(\text{III}, \Omega_+)$	$\epsilon(\text{III}, \Omega_-)$
4S	.30 $\pm$ .07	1.7 $\pm$ .1	.31 $\pm$ .08	1.8 $\pm$ .1
4	.18 $\pm$ .05	1.5 $\pm$ .1	.19 $\pm$ .05	1.7 $\pm$ .1
5	.09 $\pm$ .02	1.3 $\pm$ .1	.10 $\pm$ .02	1.5 $\pm$ .1
10	.01 $\pm$ .01	1.07 $\pm$ .07	.01 $\pm$ .01	1.20 $\pm$ .08
15	.0	1.01 $\pm$ .06	.0	1.07 $\pm$ .08
20	.0	.98 $\pm$ .06	.0	1.02 $\pm$ .06

Table 5.12 Error criteria for method III, using different numbers of given projections (N) and different levels of projection noise ( $\sigma_a$ ) applied to phantom C. ( $\Omega_+$ , image background;  $\Omega_-$ , image extent)<sup>a</sup>

N Projections	$\sigma_a = 1$		$\sigma_a = 5$	
	$\epsilon(\text{III}, \Omega_+)$	$\epsilon(\text{III}, \Omega_-)$	$\epsilon(\text{III}, \Omega_+)$	$\epsilon(\text{III}, \Omega_-)$
4S	.28 $\pm$ .06	1.7 $\pm$ .1	.30 $\pm$ .07	1.8 $\pm$ .1
4	.18 $\pm$ .05	1.5 $\pm$ .1	.21 $\pm$ .05	1.7 $\pm$ .1
5	.09 $\pm$ .02	1.3 $\pm$ .1	.14 $\pm$ .02	1.5 $\pm$ .1
10	.0	1.07 $\pm$ .06	.02 $\pm$ .02	1.20 $\pm$ .08
15	.0	1.04 $\pm$ .06	.0	1.10 $\pm$ .07
20	.0	1.02 $\pm$ .06	.0	1.06 $\pm$ .06

same densities, Mclean is successful in reconstructing these regions. Objects with densities  $\leq 50\%$  of the maximum in a section are poorly reconstructed by Mclean. The reconstruction of object 4 in phantom C is an example of Mclean's inability to entirely recover objects whose amplitudes are near background values in the layergram (Fig. 5.21).

In comparison to the results of method II, the number of pseudo objects is significantly reduced by method III for the case of 4 and 5 projections. Consequently, true objects can be more readily distinguished from the pseudo objects. The reconstructed images in Figs. 5.19-21 are also observed to be lumpy and have holes. This reconstruction artifact is expected since the objects being reconstructed by Mclean are extended in shape and not of point-like extent (Bates et al. 1982; 1984).

Table 5.10 lists the error criteria for reconstructed phantom C. The error in image background is much less than errors in the corresponding cases reconstructed by method II. This is because Mclean begins with an empty reconstruction image and ends before image pixel values of the remaining true objects become comparable to the values of the pseudo objects. As the number of projections increases, the level of image background error decreases (see Table 5.4), and Mclean becomes better at distinguishing between true and pseudo objects. The amount of improvement over images reconstructed by method II can be seen by comparing images of Figs. 5.19-21 and Figs. 5.16-18.

The error values of reconstructed image extent are worse than in images reconstructed by methods I and II. This happens because cleaning terminates on the convergence parameter which is set slightly above noise levels in the image. Hence, Mclean terminates before all image points are found, and as a result, error in the image extent is large because of missing object points. Lowering the convergence parameter would reduce error in the reconstructed image extent but at the expense of an increased error in image background. Using more projections results in a marginal reduction in the image extent error.

Table 5.11 shows results of Mclean with levels of  $\sigma_m = 5\%$  and  $10\%$  noise

in the projections. Error values for both image extent and background increase little with increasing noise levels in projections. Table 5.12 shows similar results for the case of additive noise. This indicates that Mclean is primarily guided by the maxima of the star-pattern artifacts in the layergram. The computed extent does little to constrain the iterative process of subtractive deconvolution. In comparison to method II, Mclean offers an advantage when  $N$  is very small and the projections are noisy (i.e. the image extent is difficult to estimate).

#### 5.6.3.3.1 Selection of gain parameter

To examine the effect of gain on the accuracy and convergence of Mclean, phantom C was reconstructed from 5 noiseless projections using gains ranging from  $\alpha = 0.1$  to 0.9. Results presented for phantom C are representative for phantoms A and B.

Table 5.13 shows the error in both image extent and background increases with increasing gain. The convergence parameter is set equal to the average of image background values. As gain is increased, fewer iterations are required and fewer points are found. From this table a gain of  $\alpha = 0.3$  was selected since it offered a good trade-off between accuracy and computational speed (i.e. the number of iterations).

Table 5.13 Error criteria for method III, using 5 given projections and different gains ( $\alpha$ ) applied to phantom C. ( $\Omega_+$ , image background;  $\Omega_-$ , image extent)

Gain $\alpha$	Number of Iterations	$\epsilon(\text{III}, \Omega_+)$		$\epsilon(\text{III}, \Omega_-)$	
0.1	300	.06	$\pm .01$	1.06	$\pm .09$
0.2	150	.07	$\pm .01$	1.1	$\pm .1$
0.3	100	.09	$\pm .02$	1.3	$\pm .1$
0.4	75	.12	$\pm .02$	1.7	$\pm .1$
0.5	60	.15	$\pm .03$	2.1	$\pm .1$
0.6	50	.18	$\pm .04$	2.5	$\pm .1$
0.7	45	.21	$\pm .06$	2.9	$\pm .2$
0.8	35	.24	$\pm .08$	3.3	$\pm .2$
0.9	30	.28	$\pm .08$	3.6	$\pm .2$



The approximate computing time on a VAX-750 for one iteration is  $2.7NM^2 \times 10^{-6}$  minutes on a  $M \times M$  grid and given  $N$  projections. This time can be improved by performing reconstruction on newer hardware (e.g. 80386, 68030, etc.).

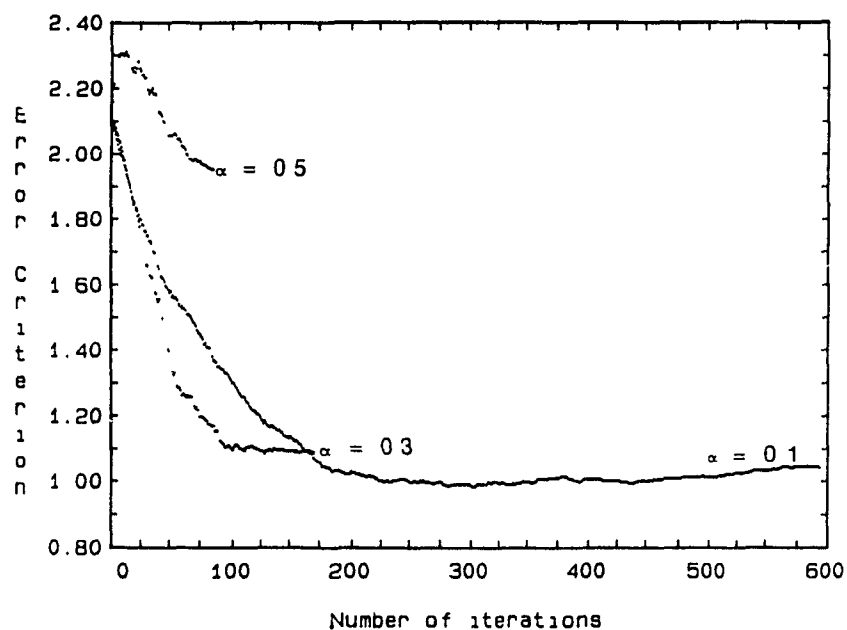
The convergence rates for method III using 5 given projections applied to phantom C is illustrated for no noise and  $\sigma_a=5$  in Figs. 5.22 and 5.23 respectively. The convergence criterion is set to  $c = 2.0$  which is below the average image background value. Plots in Fig. 5.22a) show that the rate of convergence increases with increasing gain, but that the final level of error in image extent is also higher. When gain is increased to  $\alpha = 0.5$ , the error increases then decreases. The initial rise in error is due to an over-estimation of peak values used to update the Mclean image. As more points in the image extent are found, this error decreases. The consequence of over-estimating reconstructed values is also seen in plots for  $\alpha = 0.1$  and 0.3 as spurious increases in the error curve. Generally, Mclean converges slowly since it operates on only one pixel per iteration.

The plots in Fig. 5.22a) show that after 300, 150, and 60 iterations, when convergence criteria is less than average background pixel values for  $\alpha = 0.1, 0.3$ , and 0.5 respectively, that there was no further improvements in image extent. In contrast, error in image background increases with further iteration as shown in Fig. 5.22b). The magnitude of these errors also increases with increasing gain. The rise in image background error begins when image pixel values corresponding to the true objects and background in the reduced layergram become comparable. If the iterative process in these examples were allowed to continue until the layergram was reduced to zero, the final recovered image would resemble the initial masked layergram.

Fig. 5.23 shows the convergence rates for reconstruction from projections with additive noise ( $\sigma_a=5$ ). The effect of noise is seen to increase the final level of error in pixel values of the image extent. The problem of over-estimating pixel values is also more common as seen by the increased occurrence and size of spurious fluctuations in the error plots shown in Fig. 5.23a).

Figure 5.22 Convergence rates for method III using 5 given projections with no noise and gains of  $\alpha = 0.1$ ,  $0.3$ , and  $0.5$  applied to phantom C. The error criterion is plotted for a) image extent  $\Omega_-$  and b) image background  $\Omega_+$ .

a) Image extent  $\Omega_-$



b) Image background  $\Omega_+$

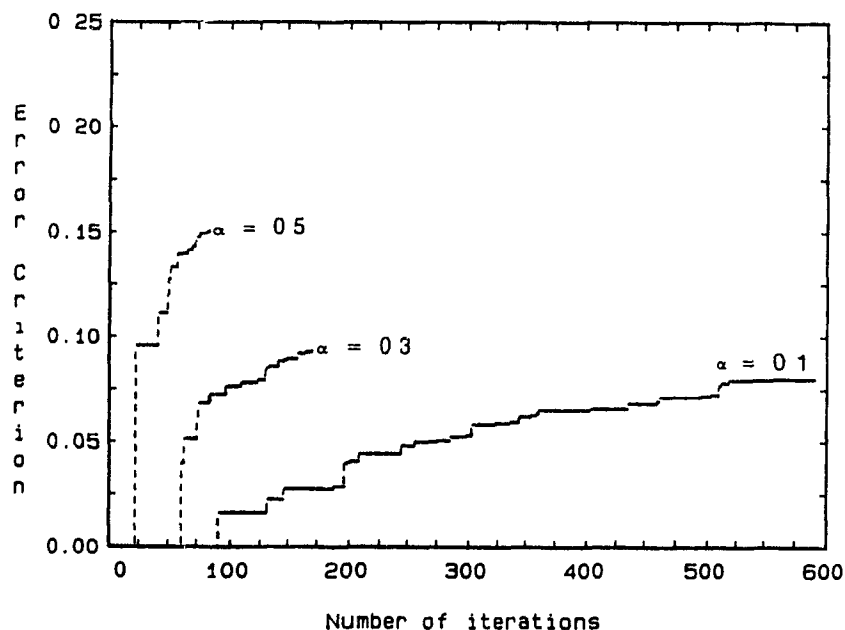
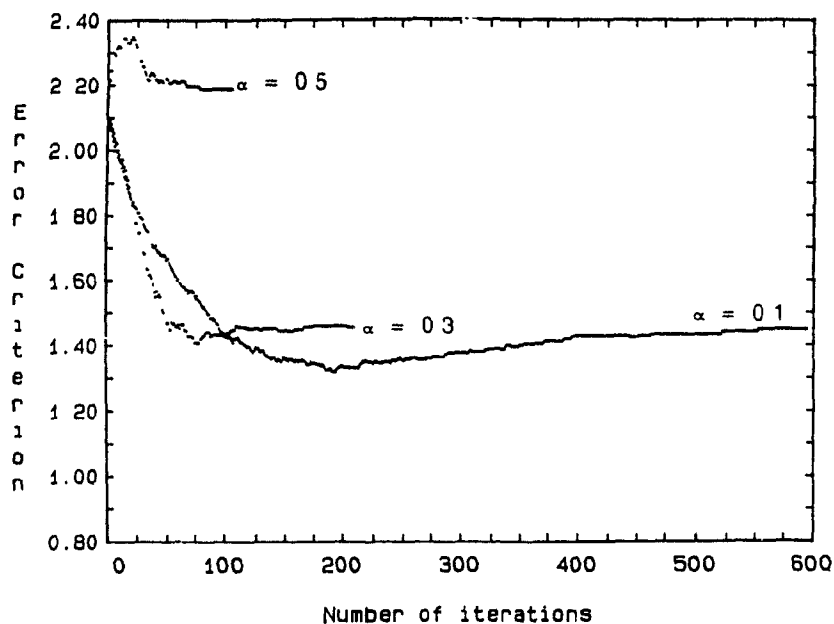
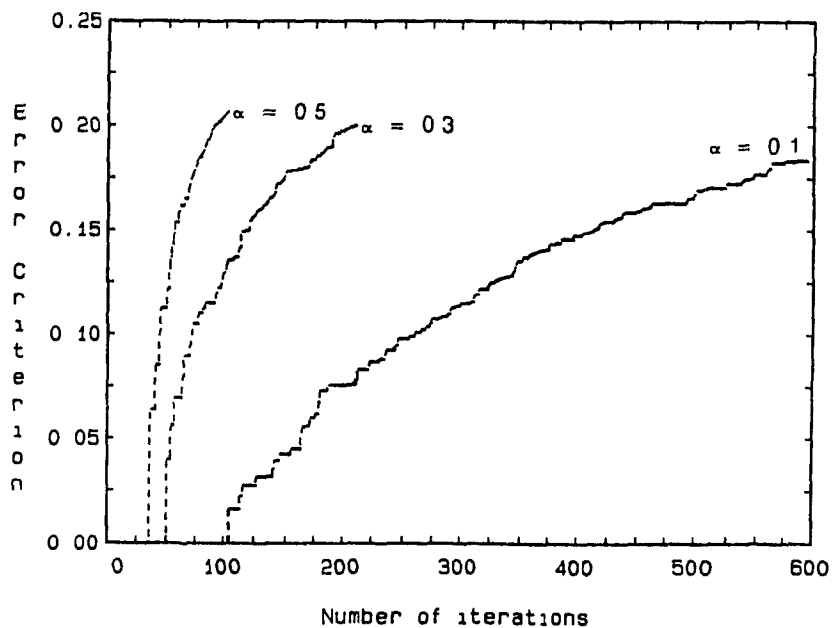


Figure 5.23 Convergence rates for method III using 5 given projections with noise ( $\sigma_a = 5$ ) and gains of  $\alpha = 0.1, 0.3$ , and  $0.5$  applied to phantom C. The error criterion is plotted for a) image extent  $\Omega_-$  and b) image background  $\Omega_+$ .

a) Image extent  $\Omega_-$



b) Image background  $\Omega_+$



## 5.7 Phantom experiments

The Mclean reconstruction algorithm was evaluated on a 3-d wire phantom resembling the cerebral blood vessels. The phantom consists of a network of soldered aluminum wires ranging from 0.5 to 1.0 mm in thickness embedded in a 6 cm diameter cylinder of wax. Referring to Fig. 5.24, the phantom was positioned 5 cm from the center of the image intensifier, where the distance between the image intensifier and x-ray source was 115 cm. Different projections were obtained by rotating the phantom by  $\phi$  degrees about its long axis. Fig. 5.25 shows a subtracted digital x-ray image of the 3-d wire object used as the test phantom. The image was recorded on a Technicare DR-960 DSA unit interfaced to a Philips 154mm/231mm image intensifier (operating in 154mm mode) and was digitized to 10 bits and sampled on a 512x512 matrix. For convenience and flexibility the subsequent reconstruction was performed on a separate computer system, a VAX 11/750.

Four, six, and eight projections equally spaced over  $\pi$  radians were used as input in the reconstruction process. A corresponding mask image for each projection was matched, and each image pair was then logarithmically processed and subtracted in such a manner as to give positive contrast. Projections consisting of 128 samples each, centered on the 512x512 image matrix, were used in reconstructing the phantom's cross sections on a grid of 64x64 pixels. The degree of pin-cushion distortion occurring in the region of the image matrix containing each projection was found to be negligible. The gain was set to  $\alpha = 0.2$ , and the convergence criterion was set equal to the average image background value in each section.

To illustrate the results of Mclean, the 27<sup>th</sup> and 66<sup>th</sup> sections (Fig. 5.25) of the reconstructed phantom were compared to the same sections reconstructed by method I (convolution back-projection). The reconstructed phantom was also re-projected and compared to the original projections of the phantom at 10 and 110 degrees. These projections were selected because they were different from the projections used in the reconstruction process. Peters' (1981) algorithm was used for the re-projection operation (§5.5.3.2).

Figure 5.24 Data collection geometry for 3-d wire phantom.

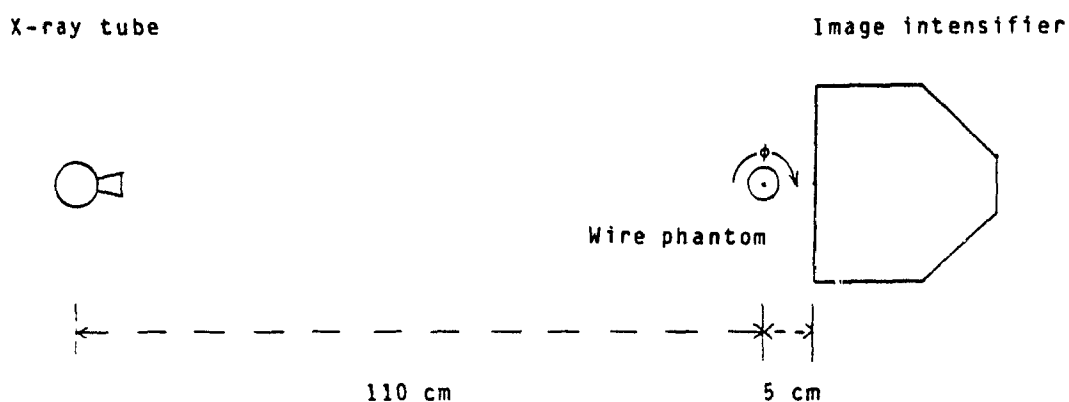
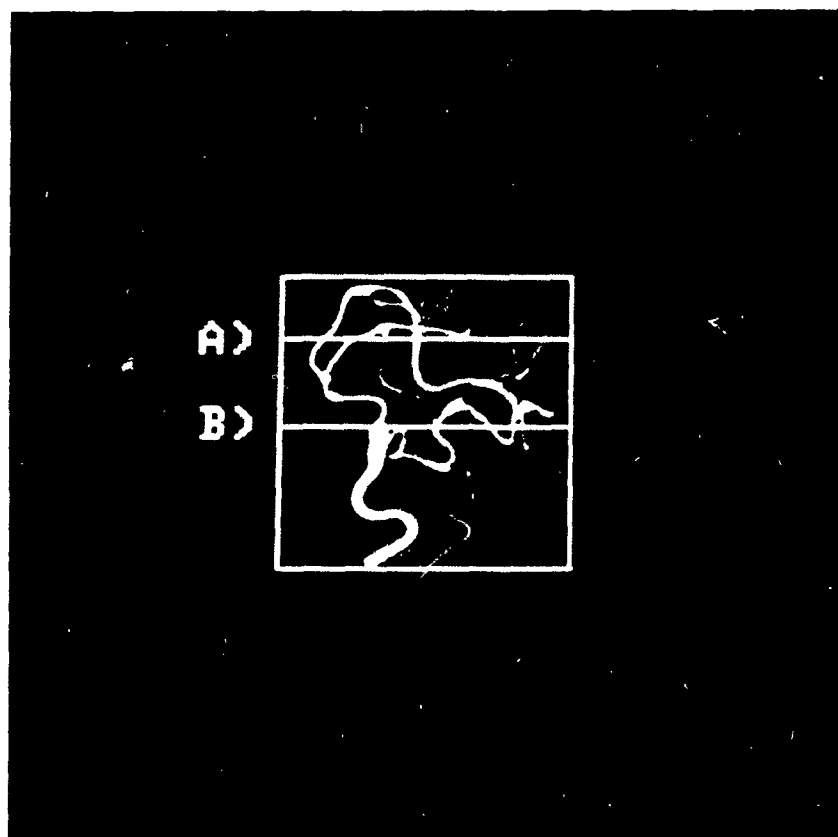


Figure 5.25 Digital subtracted x-ray image of the wire phantom indicating A) 27th and B) 66th of the 128 sections in the phantom. Images are windowed between 0 and 100.



### 5.7.1 Results

Figs. 5.26-29 show the results of applying method I to 4, 6, 8, and 32 projections of the test phantom. Comparing reconstructed images from 4, 6, and 8 projections to images from 36 projections, the degree of correspondence between the centers of the star-patterns and object structure is observed. Streaks extending from objects in the sections reconstructed from 36 projections are artifacts due to angular and translation errors associated with encoding the projection angles and computing the center of rotation in each projection respectively.

After an average of 150 iterations the images reconstructed by Mclean, Figs. 5.26-29, show good correspondence to the original sections. However, the accuracy of the reconstructed pixel values is limited as also demonstrated by simulation experiments (§5.6.3.3). In the presence of noise the reduced layergram or difference image  $d(x,y)$  (eq. 5.29) cannot be reduced to zero, and the reconstruction method arrives at the most probable image of the true section. As the number of projections is increased, object extent is better reconstructed.

Figs. 5.30-31 show the reconstructed phantom re-projected and compared with the original phantom projections at 10 and 110 degrees. In each projection the position of wires in the reconstructed phantom generally match the original. Again the extent of agreement depends on both the degree to which the difference image can be reduced and the number of projections used.

In spite of the error level in individual reconstructed sections, it is seen that when the 3-d object stack is re-projected to form a 'radiographic view,' the visual images are similar for the 4, 6, 8 and ideal projections (Figs. 5.30-31). Artifacts in reconstructed sections can be visually discounted in the re-projected images since they bear no resemblance to the actual vessel-like objects. Simple algorithms to do this computationally, such as finding vessel connectivity through an inter-slice comparison, were tried and later abandoned since similar artifacts in adjacent slices are often correlated. It remains undetermined how to best incorporate this 'a

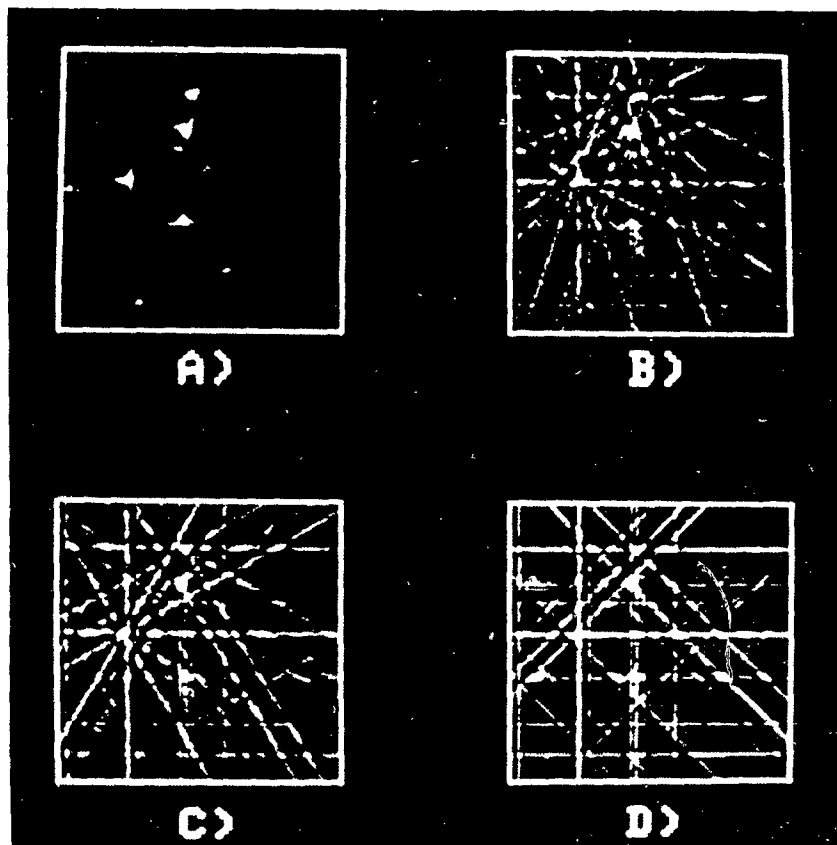


Figure 5.26 The 27th section of the phantom reconstructed by convolution back-projection from A) 36, B) 8, C) 6 and D) 4 projections. Images are windowed between 0 and 20.

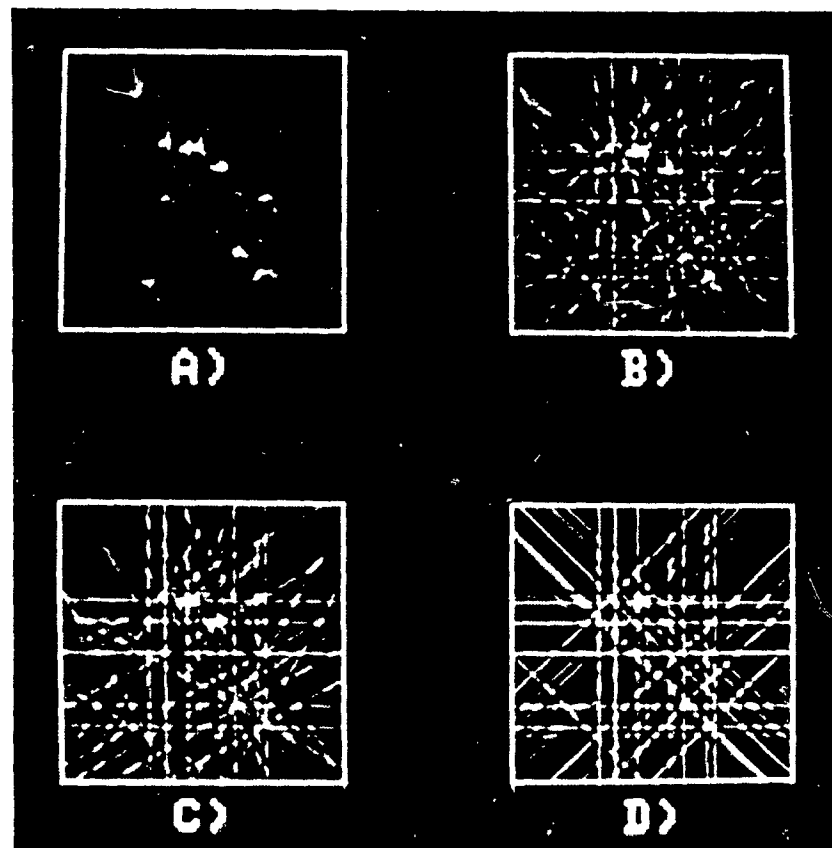


Figure 5.27 The 66th section of the phantom reconstructed by convolution back-projection from A) 36, B) 8, C) 6 & D) 4 projections. Images are windowed between 0 and 20.

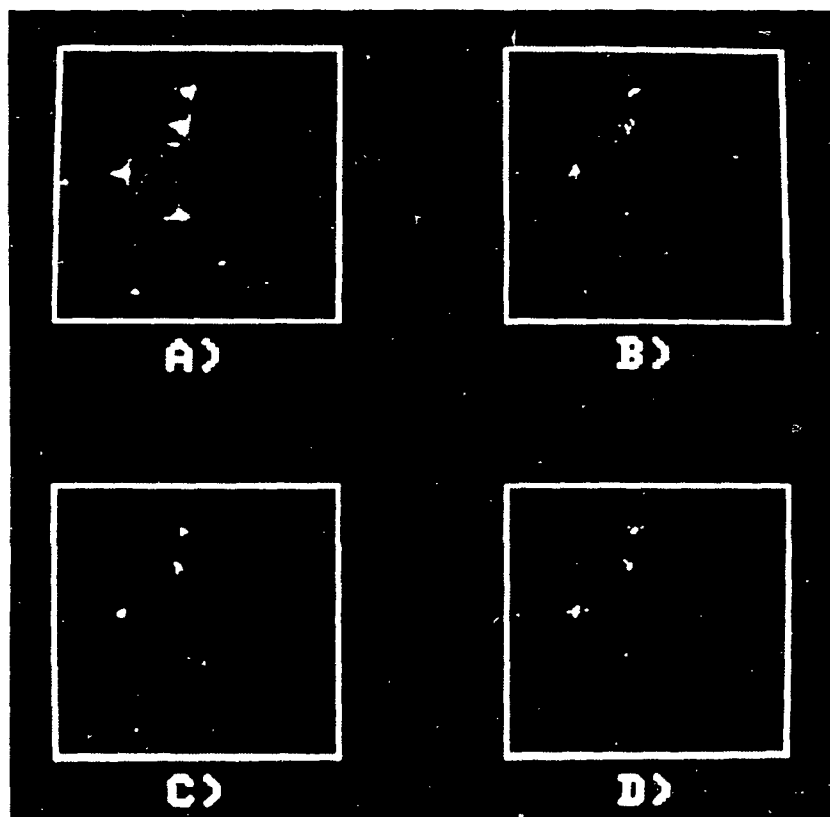


Figure 5.28 The 27th section of the phantom reconstructed by convolution back-projection from A) 36 projections and by Mclean from B) 8, C) 6 & D) 4 projection. Images are windowed between 0 and 20.

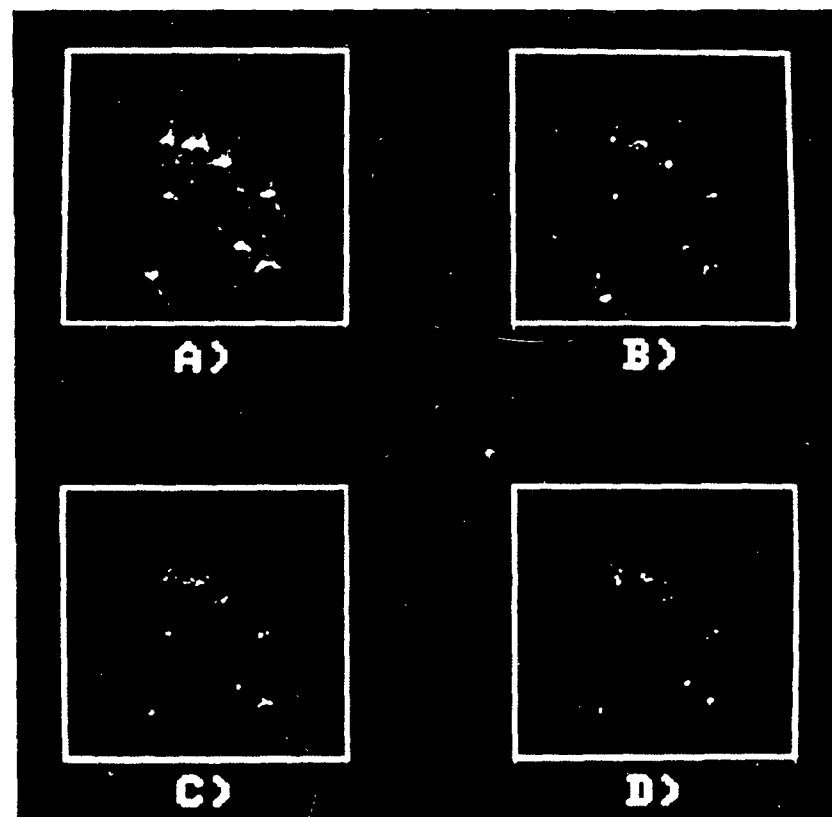


Figure 5.29 The 66th section of the phantom reconstruction by convolution back-projection from A) 36 projections and by Mclean from B) 8, C) 6 & D) 4 projections. Images are windowed between 0 and 20.



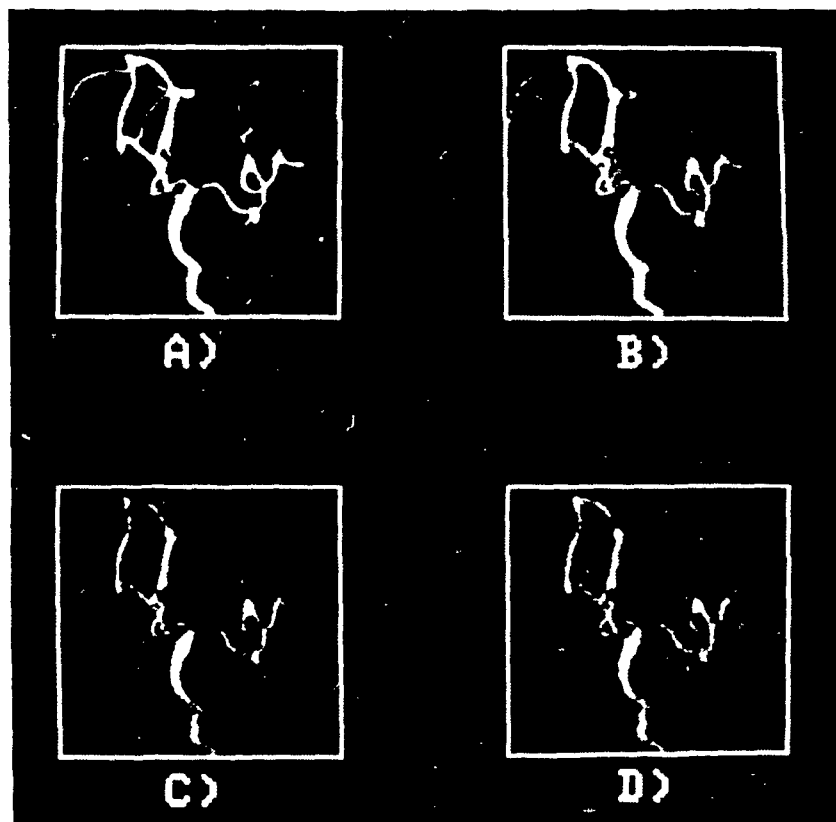


Figure 5.30 10 degree projection of the A) original phantom and the phantom reconstructed by Mclean from B) 8, C) 6, & D) 4 projections. Images are windowed between 0 and 100.

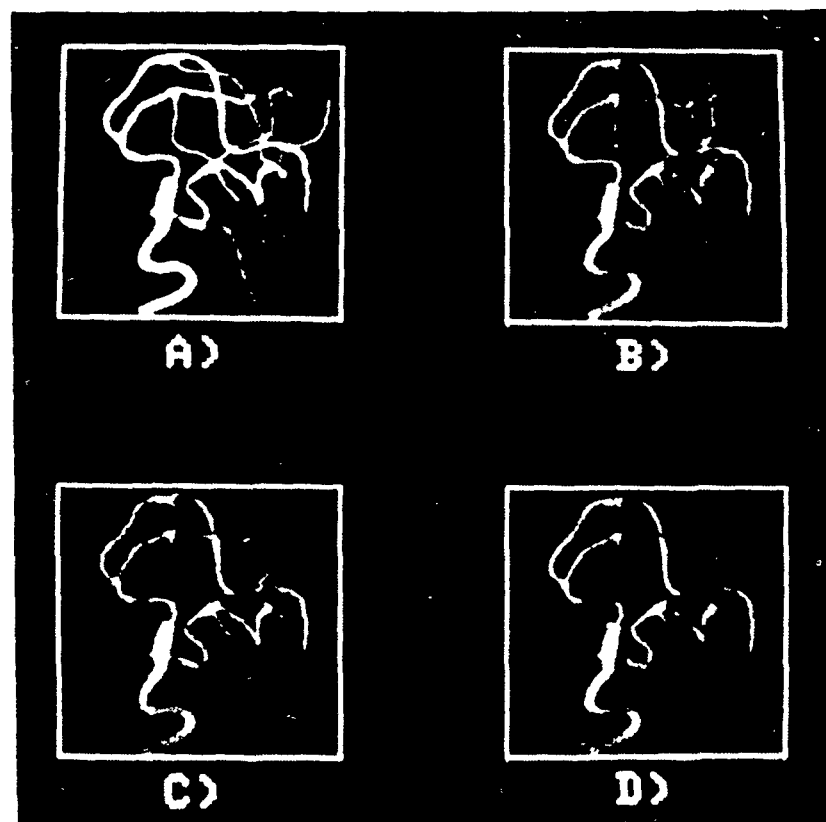


Figure 5.31 110 degree projection of the A) original phantom and the phantom reconstructed by Mclean from B) 8, C) 6, & D) 4 projections. Images are windowed between 0 and 100.

priori' knowledge in reconstruction.

Thus from a qualitative viewpoint, where the structure of the vessels rather than the density is important, such algorithms operating on a small number of views may well have a future.

## 5.8 Conclusions

The problem of few projections in image reconstruction may be formulated as a restoration task when the true image consists of point-approximated objects. The original image is estimated by selectively reducing star-pattern artifacts in the layergram image. Restoration is guided by the 'a priori' information that for sparse and point-like objects a general isometry exists between the original and its layergram image.

Results of the computer simulation experiments (§5.6) have shown that the accuracy of Mclean depends largely on the number of given projections and to a lesser degree on noise in measured projections. For the phantoms considered, Mclean requires at least the same number of projections as there are piece-wise constant objects in the section to be reconstructed. Furthermore, these objects should all have almost the same density values. Under such conditions there is sufficient isometry between the true image and its layergram that object location is faithfully reconstructed. By comparison to reconstruction by direct and masked convolution back-projection, the Mclean reconstructed image is not dominated by streak artifacts. In cases where 4 projections are sufficient for reconstruction, 4 equally spaced views render a more accurate reconstruction than that from biplane stereo views. Overall the accuracy of value of the reconstructed pixels is less impressive than the correspondence between true and reconstructed objects. It is possible that pixel accuracy can be further improved by adapting Mclean to deconvolve the layergram from all points in the computed image extent simultaneously rather than point by point. This would only be practical if the computed extent of the image was known exactly.

In the presence of both additive and multiplicative Gaussian noise, the

1 Mclean algorithm remains robust as reconstruction error increases slowly with increasing noise levels in the given projections. Mclean's performance does not change much when it is not possible to estimate the image extent. This is a clear advantage over computed image extent based methods. Gain and convergence criterion values selected by the operator determine the accuracy of Mclean. It was found that gain should be no larger than  $\alpha = 0.3$ . Results can be improved by making  $\alpha$  as small as computing time expense allows. Since the final reconstruction depends on gain and convergence parameters, the image reconstructed by Mclean is not unique. Instead Mclean reconstructs a good estimate of the true image that is consistent with projections and 'a priori' information.

For the class of objects typified by the phantoms considered here, the minimum number of projections needed by Mclean should be equal to the number of objects in the section. Although numbers less than this are possible since artifacts present in the reconstruction can usually be visually discounted. Given sections with other combinations of object sizes and shapes, the minimum number of projections would have to be determined empirically because Mclean is based on certain expectations about the object to be recovered. It is expected that for more extended or larger sized objects, Mclean would not be as efficient.

Mclean was also shown to successfully reconstruct all sections of a 3-d test phantom from projections collected on a DSA unit. This experiment (see §5.7) also highlighted two potential problems associated with the practical implementation of Mclean. The first problem is determining the correct angular encoding and measurement of center of rotation as most DSA units are not designed to provide this information. Misalignment of projections would result in an incorrectly formed layergram from which Mclean would proceed to deconvolve star-pattern artifacts from wrong locations. This problem may be remedied by the use of some sort of stereotactic marker set which allows the fiducials to be recorded in the desired projections. The other problem of implementation is the x-ray cone beam geometry of DSA systems. Mclean for purposes of study and ease of implementation was based on a parallel beam geometry. This problem was avoided in the experiment described in §5.7 by making the test phantom small in size and by keeping geometric magnification

near unity in order to approximate a parallel beam geometry. A possible solution to this problem would be to adapt Mclean to deconvolve a 3-d layergram formed from back-projecting the given 2-d projections. There are other problems associated with image-intensifier based computed tomography that need to be considered (Ning and Kruger 1988). These include the time-variant nature of vascular iodine concentration, image pin-cushion distortion, and the effects of detector noise, x-ray exposure levels, and levels of x-ray scatter.

As demonstrated both by the simulation and phantom experiments, details of vessel-like objects in the cleaned reconstructed cross section are much improved by comparison to the back-projected image and the computed image extent. Mclean is similar to iterative algorithms (see §5.2.4.3) in that difference projections are computed, but is different in that only those pixels that are deemed to be part of the actual objects are re-projected. Consequently, iterative techniques only partially remove streaking artifact and at the expense of blurring object details (Spears et al. 1988). The advantage offered by Mclean is that most if not all streak artifacts are removed. This makes the reconstructed data set suitable for re-projection. The cost associated with Mclean is that the extent of the object is not always entirely reconstructed, and reconstructed pixel values are inaccurate. If the structure of the vessels is the important factor, rather than the absolute vessel density values, then these drawbacks may be overlooked.

The main conclusion that can be drawn from these experiments is that the location and boundaries of the vascular structure in cross section can be reconstructed from a few views using Mclean, an iterative back-projection deconvolution method. The accuracy of Mclean is limited to the given projection set, or rather to within the limits set by the initial layergram.

## CHAPTER SIX

### CONCLUSIONS AND SUGGESTIONS FOR FUTURE RESEARCH

Two different methods of reconstructing vessels from DSA images have been presented. In chapters 3 and 4 a method of geometric reconstruction from stereo and biplane images was described and evaluated. Chapter 5 was concerned with vascular image reconstruction from a small number of given projections. This final chapter presents conclusions and suggestions for further research with respect to 3-d vessel reconstruction from cerebral angiograms.

#### 6.1 Geometric reconstruction from DSA image pairs

Chapter 3 describes a reconstruction method in which 3-d vessel center-lines are computed from its traces in different views. The aim there was to improve accuracy of stereo pair reconstruction by using biplane images. Because of the complexity of the vasculature in the anterior-posterior projection, an approach was taken to use re-projected vessels reconstructed from lateral stereo images to help the observer find the correct vessel in the anterior-posterior image. Chapter 4 investigated the propagation of several different types of measurement errors in this reconstruction method.

Simulation experiments demonstrated that reconstruction errors were proportional to measurement error magnitude in test point image coordinates and inversely proportional to the geometric magnification. This is in agreement with Sherlock and Aitken's results (1980). In addition these simulation experiments revealed a similar relationship for measurement error in the fiducial image coordinates, and that this source of error was important in stereo image pairs. For biplane images, test point image coordinate measurement error dominates reconstruction. Simulation results also indicate that for the given geometrical parameters of the image collection procedure described here, the error magnitude is position variant.

Reconstruction accuracy was determined physically to be  $\pm 0.5\text{mm}$  in each coordinate for biplane analysis and  $\pm 0.5\text{mm}$  in 'x', 'y' coordinates and  $\pm 2.0\text{mm}$  in 'z' for stereo analysis. This base-line level of accuracy can be improved if DSA units with finer sampling matrices are available. In the presence of observation and correspondence error, reconstruction accuracy is degraded. Stereo depth reconstruction error of  $\gg 2.0\text{mm}$  can be expected which is not tolerable in surgical planning.

Correspondence of a point-pair was measured on the basis of the distance between 3-d intersecting rays from the pair. This measure was improved by relaxation labeling given constraints of disparity and vessel connectivity. The correspondence algorithm was found to have a mean error in disparity that ranged from 1 to 3 pixels after relaxation labeling. Simulation experiments showed that this algorithm encountered difficulties with classifying match pairs between horizontal segments of vessels, and where one of the vessels being matched is greatly foreshortened. Although these problems can be remedied by interpolating across the segments where correspondence failed, algorithms which are not limited by such vessel geometries are needed. The correspondence measure was also found to be limited when there are large errors in the measured fiducial image coordinates. For the particular system of fiducial markers employed here, measurement error in the fiducial image coordinates is primarily due to sampling.

Application of the reconstruction procedure to actual DSA images showed that anterior-posterior re-projection of stereo reconstructed vessels helped the observer identify vessels in the angiogram. Because of the complexity of projected vessels in the anterior-posterior image, a skilled observer is still the only means of reliably tracing the desired vessels. Despite the advantages of this method there is a need for computer segmentation of vessels in cerebral angiograms. Reliable segmentation algorithms would minimize tracking error and provide additional information about the vessel that could be incorporated into the proposed correspondence algorithm. Additional modeling of vessel features and the imaging process would be necessary to completely automate detection of vessels in biplane cerebral

angiograms. This is an interesting area for future research.

## 6.2 Iterative 3-d reconstruction of vascular images from a few views

A method of reconstructing images from a small number of given projections is investigated in chapter 5. It was found that the use of 'a priori' knowledge about the object gives reconstructions which are superior to those obtained by either convolution or masked-convolution back-projection. The reconstruction algorithm Mclean is used to selectively reduce star-pattern artifacts in the layergram. This technique assumes that the section being reconstructed consists of point or piece-wise constant objects. Object sections containing vessels are sufficiently piece-wise in their extent to be reconstructed by Mclean. Deconvolution of star-pattern or streak artifacts in a layergram is guided primarily by the general isometry that exists between the true object section and its layergram.

Simulation results indicate Mclean requires that the amplitudes of the section's objects should all have nearly the same high values. The accuracy of reconstructed pixel values was shown to be less impressive than the correspondence between the true and reconstructed objects. A solution for this needs further study.

The number of required projections for reconstruction by Mclean depends on the number of objects in the section. For phantom objects considered, it was found that at least the same number of projections as objects are needed in order to reconstruct images where artifact levels are tolerable. Because the groups of object sections considered for reconstruction were not exhaustive, this observation requires further investigation.

In the presence of both multiplicative and additive noise in simulated projections, reconstruction error increased moderately with increasing noise levels. Mclean was also shown to successfully reconstruct sections of a 3-d vessel-like phantom from its projections recorded on a DSA unit. Before actual vessels can be reconstructed using Mclean, the practical problems associated with image-intensifier based computed tomography need to be considered. Simulation results indicate that the Mclean algorithm should be

sufficiently robust to handle non-linearities in projection data due to time-variant nature of vascular iodine concentration and noise. However, adapting the algorithm to a cone-beam geometry requires further investigation.

Simulation and phantom experiments have demonstrated that details of vessel-like objects can be reconstructed from a small number of projections by Mclean. This is achieved at the expense of pixel value accuracy as noted above and after many iterations. The slow rate of convergence may be too time consuming if many sections are to be reconstructed. The convergence rate can be improved by adapting Mclean to deconvolve the layergram from all points in the computed image extent simultaneously rather than sequentially. This may be possible providing an accurate estimate of the extent of the image is known. Means to compute the image extent are needed.

### 6.3 Summary

In summary, two new methods for reconstructing the cerebral blood vessels have been presented. Of the two, the stereo-biplane method would be preferred when the number of different available views is strictly limited (i.e. 3 or 4 projections). Furthermore, this method offers an advantage when only a few selected vessel branches need to be reconstructed in the planning of a neurosurgical procedure. The results of vessel reconstruction by this method are also in a more suitable form for merging with images from different modalities and for the purposes of an interactive stereoscopic display of the vessels (Appendices A and B). The other reconstruction method, Mclean, would be preferred when 6 to 10 different projections are available and would provide a more efficient reconstruction of all the cerebral blood vessel branches. In cases where planning is concerned with a region of interest that spans a few axial sections, Mclean is better suited. Finally, the results of Mclean may be a more appropriate starting point from which other techniques can be used to infer additional information regarding the vessel's lumen shape and density.

Another avenue for further research is the incorporation of measurements obtained from one reconstruction technique into another. For example,



results of stereo-biplane reconstruction may be merged into the Mclean algorithm to provide additional 'a priori' object information with which to tie down uncertainty in reconstruction. Alternately, Mclean may be used as a starting point for the other technique.

## APPENDIX A

### DISPLAY OF 3-D RECONSTRUCTION RESULTS

Information available from a reconstructed 3-d angiogram can be presented by many different techniques. The problem remains as to which technique best presents this information. This chapter briefly describes several of the common 3-d display strategies possible (§A.1) and suggests the use of a stereo re-projection technique (§A.2).

#### A.1 Display of 3-d data

There are several ways of displaying information about vessel structure and if later computed, the iodine density distribution of a reconstructed 3-d angiogram. Two approaches to the problem of displaying 3-d information in general have been identified by Udupa (1983). The first involves displaying the 3-d information, the structure and density distribution of the object, as a continuous image in 3-d space. The second approach involves extracting important information and displaying it effectively in two dimensions.

The first approach is implemented using optical means of creating 'space-filling' 3-d displays. Such displays attempt to construct the optical equivalent of a three-dimensional array of image points illuminated to form a model of the object. The observer's inter-ocular spacing provides the perspective difference which generates the binocular depth clues without the aid of special viewing devices. These methods include holograms (Lesem and Hirsh 1968; Huang 1971; Gabor 1972; Benton 1977; Greguss 1977; Perlmutter 1982), integral photography using arrays of lenses (i.e. autostereoscopy using multiple stereoscopic images) (Lippmann 1908; de Montebello 1977a), and vibrating or rotating mirror and lens devices (Withey 1958; Muirhead 1961; Traub 1967; de Montebello 1977b; Mark and Hull 1977; Simon and Walters 1977; Fajans 1979).

Holography and integral photography are at present considered impractical for image display because of long image production times which

preclude interactive manipulation. In any case, these methods afford only a limited range of viewing angles. Most vibrating or rotating mirror and lens devices have mechanical properties that prevent routine use, with exception of the 'vari-focal' or 'vibrating' mirror (Muirhead 1961; Traub 1967; Rawson 1969; Baxter 1978; Yamanaka et al. 1988). Vari-focal mirror displays may suffer from problems of ambiguity in 3-d synthesis which can be overcome by pre-processing techniques such as surface detection and voxel dimming (Mills, Fuchs, and Pizer 1984).

An alternative approach to the 3-d image display is to use 2-d renditions of the 3-d image space. This is the approach most commonly taken to display 3-d angiograms. Of the various 2-d CRT-based methods only those that would be useful for angiograms are discussed. A survey of 2-d CRT-based methodologies and applications can be found in Herman et al. (1982) and Udupa (1983).

The simplest method to display 3-d angiograms is to re-project the vessel center-lines at any arbitrary angle (Vignaud et al. 1979; Smith and Starmer 1976). This offers the advantage of generating projection images that are not available to the imaging device. The 'stick-figure' images of the vessels can also be re-projected in the form of stereo pairs and displayed using one of the methods described in §3.4.4. Taking advantage of the data source, the generation of multiple stereo pairs from various projection directions is possible. This allows a limited look-around capability similar to the optical space filling displays described above.

If vessel width is available at each sample or center-line point, images of the vessels can be rendered in solid form using 'shading' techniques (Parker et al. 1985; Legout et al. 1985; Mol et al. 1986). Solid images of vessels would be helpful in the diagnosis of vascular diseases, for example, involving vascular malformations. The computer techniques used to render a solid image of the vessels are described in a standard text on computer graphics (Newman and Sproull 1979).

The last method to display 3-d angiograms is to partition the 3-d information into a sequence of 2-d sections at any angle and present these

as a montage of image panels similar to CT images. This is particularly useful if the 2-d section can be merged with data from different imaging modalities in the same 3-d space (Rubin and Sayre 1978; Vignaud et al. 1979). A major advantage of these computer image/graphic techniques is that they can be implemented on existing digital hardware of most medical imaging facilities.

## A.2 Re-projection algorithm

Three-dimensional vessel structure can be represented on a CRT as a two-dimensional line image with an appreciation of depth by producing a stereo pair of the structure, separate line images to each eye. The perception of depth can be appreciably augmented by smoothly rotating the 3-d structure about an axis to allow continuous observation of the changing projections as they appear on the CRT display screen (i.e. motion parallax). The required image rotation and stereo projection of the vessel structure are achieved by coordinate transformation of the 3-d center-line points.

To permit observation of various projections of the 3-d structure, it is necessary to orient the structure to the desired viewing angles by rotation. Rotation about a fixed point in three dimensions can be represented by three successive 2-d rotations about a fixed set of orthogonal axes (Fig. A.1). Given an arbitrary data point  $P^{\rightarrow}$  with coordinates  $(x,y,z)$  and a rotation sequence first about 'x', then 'y', and finally 'z' the resulting location of  $P^{\rightarrow}$  in the reference system with rotated coordinates  $(x',y',z')$  is (Rogers and Adams 1976)

$$\left. \begin{aligned} x' &= x \cos(\theta) \cos(\phi) + y (\sin(\alpha) \sin(\theta) \cos(\phi) - \cos(\alpha) \sin(\phi)) \\ &\quad + z (\cos(\alpha) \sin(\theta) \cos(\phi) + \sin(\alpha) \sin(\phi)) \\ y' &= x \cos(\theta) \sin(\phi) + y (\sin(\alpha) \sin(\theta) \sin(\phi) + \cos(\alpha) \cos(\phi)) \\ &\quad + z (\cos(\alpha) \sin(\theta) \sin(\phi) - \sin(\alpha) \cos(\phi)) \\ z' &= -x \sin(\theta) + y \sin(\alpha) \cos(\theta) + z \cos(\alpha) \cos(\theta) \end{aligned} \right\} \quad (A.1)$$

Once the desired orientation of the 3-d structure has been obtained, separate projections are used to generate the stereo image pair. The 3-d coordinates of point  $P^{\rightarrow}$  are projected for the left and right eye views as

Figure A.1 Definition of rotation angles about coordinate axes  $x, y, z$ :

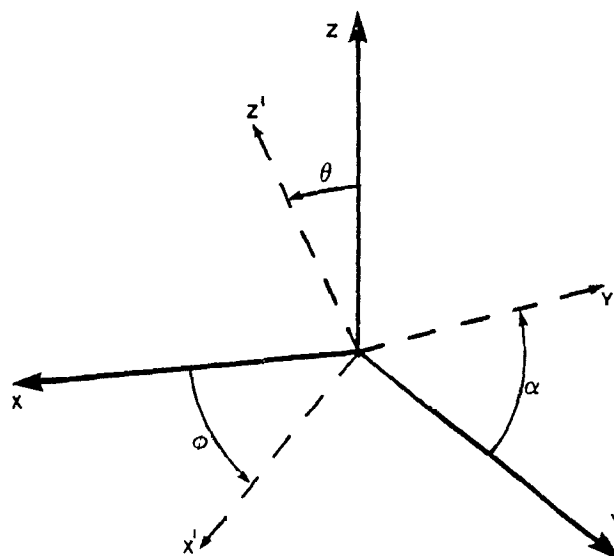
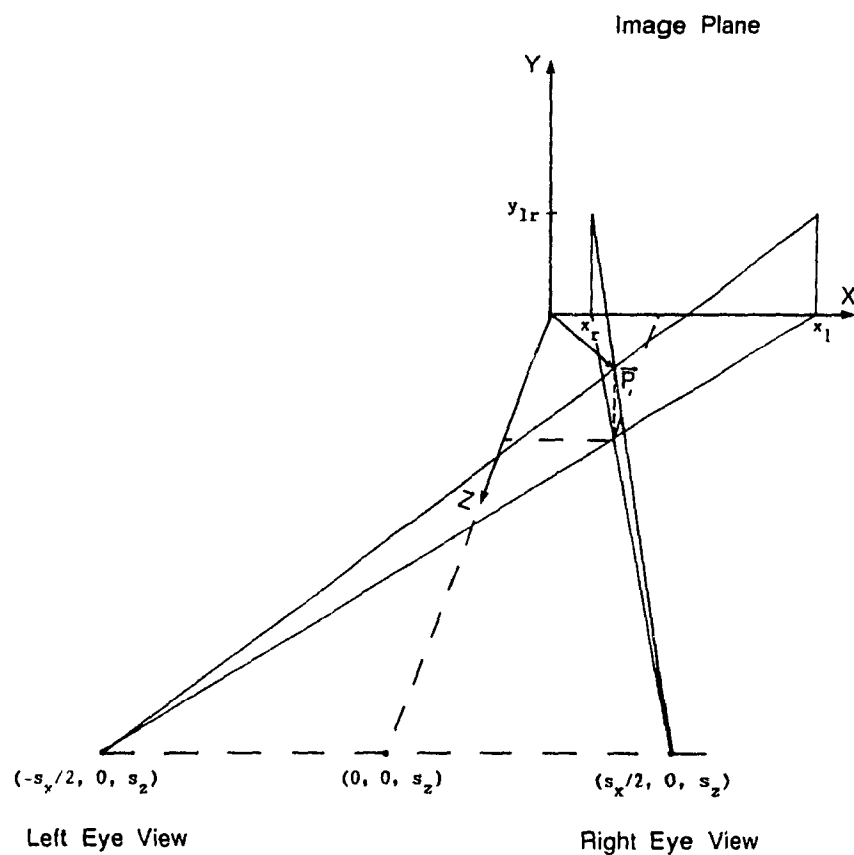


Figure A.2 Geometry of stereo projections.



shown in Fig. A.2. The projected coordinates of  $P^{\rightarrow}$  for each view is given by

$$\left. \begin{aligned} x_l &= (s_z x + (s_x z/2))/(s_z - z) \\ x_r &= (s_z x - (s_x z/2))/(s_z - z) \\ y_{lr} &= (s_z y)/(s_z - z) \end{aligned} \right\} \quad (A.2)$$

where  $x_l$  and  $x_r$  are the 'x' coordinates of the projected point in left and right eye views respectively. Both the viewing distance  $s_z$  and the inter-ocular separation  $s_x$  are inputted by the operator. The stereo image pair can then be displayed as anaglyphs (§3.4.4).

## APPENDIX B

### INTERACTION WITH STEREOSCOPIC IMAGES

It is necessary not only to view but to be able to interact with the 3-d space created by stereoscopic images. With either stereo DSA images or stereo re-projections of 3-d reconstructed vessels the capacity to determine the 3-d coordinates of points on vessels and 'clear' corridors of 3-d space for safe passage of probes is important. What is commonly used is a '3-d cursor' consisting of a point or cross shaped object at a 3-d location in space which is appropriately projected into each image of the stereo pair (Kim et al. 1987; Takemura et al. 1988; Suetens et al. 1988). The 3-d cursor works by having the operator adjust the position of the cursor so that it appears in the same 3-d position as the point of interest in the image. This type of cursor is often referred to as a 'floating-dot.'

The idea of a floating-dot has been extended to lines in the planning of probe trajectories in stereo angiograms (Ghosh and Boulianne 1984). They describe a mechanical system for use on stereo film angiograms to position a line in 3-d space of the angiogram such that no vessels are cut. Extension of this method of simulating probe trajectory in stereo DSA images is straightforward to implement using a stereo cursor. First, the location of the probe-end-point is determined using the stereo cursor and then marked in the stereo angiogram. Next, the entry-point of the probe is positioned using the cursor so as to stretch a 3-d line through space to the end-point of the probe. In this way a safe probe trajectory can be determined in either the stereo DSA images recorded or the stereo re-projections of the reconstructed angiogram.

The problem of implementing a 3-d cursor involves two aspects: the stereo projection of points or lines and finding a suitable physical device to move the 3-d cursor. Both aspects are considered.

The projected coordinates of the 3-d cursor in each image of the stereo

pairs are computed by coordinate transformation for a known set of view parameters. For stereo re-projection, the coordinates are transformed according to the viewing distance and inter-ocular separation of the 3-d display system (§A.2). In the case of stereo DSA images, the view transformation matrices computed at calibration (§3.4.3) are used to re-project the cursor into each image of the stereo pair (§3.4.6).

In the anaglyph presentation of stereo images (§3.4.4), the cursor object and line are written into the image with the appropriate intensity values. The values of the pixels at the location of the cursor or line are saved before the cursor or line is written into the image display. As the cursor or line is moved old values are restored from the saved copies. Fig. B.1 shows a pair of stereo DSA images with a possible probe trajectory constructed using a 3-d cursor.

Sometimes points of interest may lie in regions of the image that have poor stereo fusion for such reasons as large parallax values, parallax in 'y' direction, or local stereo misregistration due to pin-cushion distortion. In these instances the ray-projection technique (§3.3.1.3) may be used to find the corresponding projection of a 3-d point.

The other aspect in the problem of implementing a 3-d cursor is how to physically move the cursor in 3-d space created by the stereo images on the CRT display. Manual control of the 3-d cursor is usually done with some 2-d control, such as a joystick, or puck/trackball, plus a separate control for depth. The awkwardness of these devices has led to the development of ergonomic one-handed 3-d track control devices. Herman (1986) describes two commercially available devices. Unfortunately such devices can be often quite costly.

Instead, a one-handed 3-d track control using the numeric key-pad of a CRT terminal keyboard (VT-220, Digital Equipment Company) is proposed. Fig. B.2 shows the programmed cursor direction and function assignment of each key. Keys '1' to '9' except '5' move the cursor in the image plane in fixed pre-determined steps. Key '5' moves the cursor into or out of the image plane, where the actual direction may be toggled by stroking the '0' key.



Figure B.1 Simulated probe in DSA stereo anaglyph image.

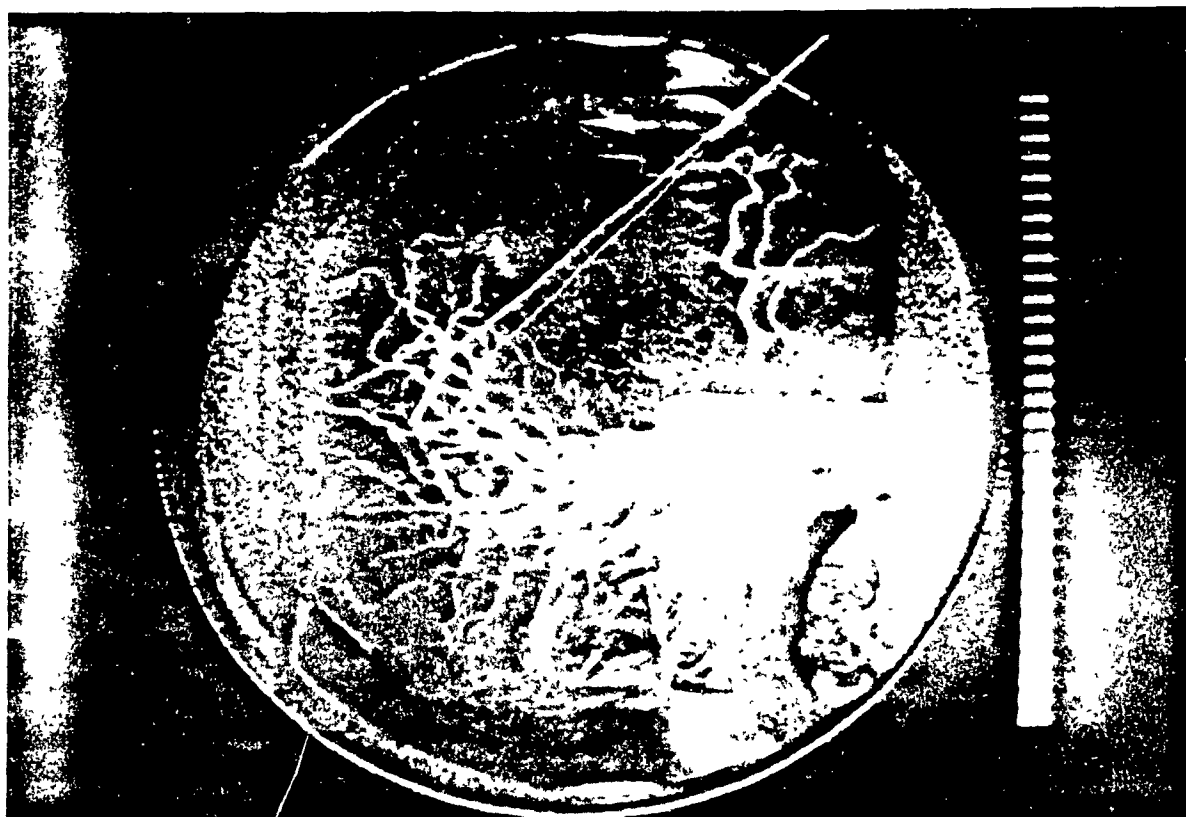


Figure B.2 3-d cursor control using terminal key-board numeric pad.

a) Original function assignments of numeric key-pad.

PF1	PF2	PF3	PF4
7	8	9	-
4	5	6	,
1	2	3	ENTER
0	.		

b) Programmed cursor direction and function assignment of each key.

↖	↑	↗	
←	Z•	→	
↙	↓	↘	Exit
Change Z direction			

The 'ENTER' key is used to exit the cursor mode of the program. The preset steps at which the cursor moves at can be temporarily increased by successively stroking the desired key. If the time lapsed between successive key strokes is smaller than a pre-determined period then the step size is incremented proportionately to the frequency of the key stroke.

It was found that after a minimum of training, observers were able to manipulate the cursor without any difficulties. However, this arrangement was found to be quite inconvenient for left-handed users since the numeric key-pad is located on the right hand side of the keyboard.

## REFERENCES

- Adams L.P., "X-ray stereo photogrammetry locating the precise, three-dimensional position of image points," **Med. & Biol. Eng. & Comput.**, vol.19, pp.569-578, 1981.
- Alderman E.L., Berte L.E., Harrison D.C., Sanders W., "Quantitation of coronary artery dimensions using digital image processing," **Proc. SPIE**, vol.314, pp.273-278, 1981.
- Alker G., Kelly P.J., "An overview of CT based stereotactic systems for the localization of intracranial lesions," **Comput. Radiol.**, vol.8, pp.193-196, 1984.
- Barba J., Fenster P., Suardiaz M., Wong K.K., Herrold E.M., Kenet R.O., Borer J.S., "3D arterial traces from biplane projections," **Proc. SPIE**, vol.767, pp.441-448, 1987.
- Barnard S.T., Thompson W.B., "Disparity analysis of images," **IEEE Trans. Pat. Anal. Mach. Intell.**, vol.2, pp.333-339, 1980.
- Barrett H.H., Swindell W., **Radiological Imaging: The theory of image formation, detection, and processing**, Academic Press, New York, 1981.
- Bates J.H.T., Fright W.R., Bates R.H.T., "Wiener filtering and cleaning in a general image processing context," **Mon. Not. R. Astr. Soc.**, vol.211, pp.1-14, 1984.
- Bates J.H.T., Fright W.R., Millane R.P., Seagar A.D., Bates G.T.H., Norton W.A., McKinnon A.E., Bates R.H.T., "Subtractive image restoration. III: Some practical applications," **Optik**, vol.62, pp.333-346, 1982.
- Bates J.H.T., McKinnon A.E., Bates R.H.T., "Subtractive image restoration. I: Basic theory," **Optik**, vol.61, pp.349-364, 1982.
- Bates J.H.T., McKinnon A.E., Bates R.H.T., "Subtractive image restoration. II: Comparison with multiplicative deconvolution," **Optik**, vol.62, pp.1-14, 1982.
- Bates R.H.T., McDonnell M.J., **Image Restoration and Reconstruction**, Clarendon Press, Oxford, 1986.
- Bates R.H.T., Peters T.M., "Towards improvements in tomography," **New Zealand J. Sci.**, vol.14, pp.883-896, 1971.
- Baxter B., "Three-dimensional display viewing device for examining internal structure," **Proc. SPIE**, vol.283, pp.111-115, 1981.
- Benton S.A., ed., **Three-dimensional Imaging**, **Proc. SPIE**, vol.120, 1977.
- Bergström M., Riding M., Greitz T., "The limitations of definition of blood vessels with computer intravenous angiography," **Neuroradiol.**, vol.11, pp.35-40, 1976.

- Bevington P.R., **Data Reduction and Error Analysis for Physical Sciences**, New York, McGraw-Hill, 1969.
- Block M., Bove A.A., Ritman E.L., "Coronary angiographic examination with the dynamic spatial reconstructor," *Circ.*, vol.70, pp.209-216, 1984.
- Blume W.M., **Reconstructing a Three-dimensional Network of Curved Lines from a Small Number of Projections**, M.S. thesis, Pattern Recognition Project, Department of Electrical Engineering, University of California, Irvine, California 92717, U.S.A., 1984.
- Boone J.M., "Scatter correction algorithm for digitally acquired radiographs: Theory and results," *Med. Phys.*, vol.13, pp.319-328, 1986.
- Bosh D.A., **Stereotactic Techniques in Clinical Neurosurgery**, Springer Verlag, New York, 1986.
- Bracewell R.N., "Correction for collimator width (restoration) in reconstructive x-ray tomography," *J. Comput. Assist. Tomogr.*, vol.1, pp.6-15, 1977.
- Bracewell R.N., "Strip integration in radioastronomy algorithms," *Austr. J. Phys.*, vol.9, pp.198-217, 1956.
- Bracewell R.N., **The Fourier Transform and Its Applications**, McGraw-Hill, New York, 1978.
- Bracewell R.N., Riddle A.C., "Inversion of fan-beam scans in radio astronomy" , *Astrophys. J.*, vol.150, pp.427-434, 1967.
- Brooks R.A., Di Chiro G., "Principles of computer assisted tomography (CAT) in radiographic and radioisotopic imaging," *Phys. Med. Biol.*, vol.21, pp.689-732, 1976.
- Brown B.G., Bolson E., Frimer M., Dodge H.T., "Quantitative coronary arteriography. Estimation of dimensions, hemodynamic resistance, and atheroma mass of coronary artery lesions using the arteriograms and digital computations," *Circ.*, vol.55, pp.329-337, 1977.
- Brown R.A., "A stereotactic head frame for use with CT body scanners," *Invest. Radiol.*, vol.14, pp.300-304, 1979.
- Bursch J., Johs R., Heintzen P.H., "Validity of Lambert-Beer's law in roentgendensitometry of contrast material (urografin) using continuous radiation," [In] **Roentgen-, Cine- and Video-densitometry. Fundamentals and applications for blood flow and heart volume determinations**, P.H. Heintzen, Ed., Thieme, Stuttgart, pp.81-84, 1971.
- Casperson L.W., Spiegler P., Grollman Jr J.H., "Characterization of aberrations in image-intensified fluoroscopy," *Med. Phys.*, vol.3, pp.103-106, 1976.

- Censor Y., "Finite series-expansion reconstruction methods," *Proc. IEEE*, vol.71, pp.409-419, 1983.
- Censor Y., "Row-action methods for huge and sparse systems and their applications," *SIAM Rev.*, vol.23, pp.444-464, 1981.
- Chakraborty D.P., "Image intensifier distortion correction," *Med. Phys.*, vol.14, pp.249-252, 1987.
- Christensen E.E., Curry T.S., Nunnally J.E., *An Introduction to the Physics of Diagnostic Radiology*, E.E. Christensen et al., Eds., Philadelphia, Lea and Febiger, 1972.
- Cloutier L., Nguyen D.N., Ghosh S.K., Boulianne M., Labissonniere P., Bouvier G., Beique R., "Simulator allowing spatial viewing of cerebral probes by using a floating line concept," *Proc. SPIE*, vol.602, pp.315-319, 1985.
- Collorec R., Coatrieux J.L., "Vectorial tracking and directed contour finder for vascular network in digital subtraction angiography," *Pat. Rec. Let.*, vol.8, pp.353-358, 1988.
- Colombo F., Benedetti A., Pozza F., Avanzo R.C., Marchetti C., Chierago G., Zanardo A., "External stereotaxic irradiation by linear accelerator," *Neurosurg.*, vol.16, pp.154-160, 1985.
- Crowther R.A., DeRosier D.J., Klug A., "The reconstruction of a three-dimensional structure from projections and its applications to electron microscopy," *Proc. Roy. Soc. Lond. A.*, vol.317, pp.319-340, 1970.
- Crowther R.A., Klug A., "Art and science or conditions for three-dimensional reconstruction from electron microscope images," *J. Theor. Biol.*, vol.32, pp.199-203, 1971.
- Crummy A.B., Stieghorst M.F., Turski P.A., Strother C.M., Lieberman R.P., Sackett J.F., Turnispeed W.D., Detmer D.E., Mistretta C.A., "Digital subtraction angiography: Current status and use of intra-arterial injection," *Radiol.*, vol.145, pp.303-307, 1982.
- Dallas W.J., Roehrig H., "A dynamically programmed computer algorithm for assisting the radiologist in locating vessels," *Proc. SPIE*, vol.767, pp.462-470, 1987.
- Davison M.E., "The ill-conditioned nature of the limited angle tomography problem," *SIAM J. Appl. Math.*, vol.43, pp.428-448, 1983.
- Davson H., *The Physiology of the Eye*, 2<sup>nd</sup> Ed. Boston: Little Brown Co., 1963.
- Dietz K., Kuhn H., "Stereo magnification angiography," *Electromedica*, vol.48, pp.124-129, 1980.

- Doi K., Duda E.E., "Detectability of depth information by use of magnification stereoscopic technique in cerebral angiography," *Radiol.*, vol.146, pp.91-95, 1983.
- Doi K., Patronas N.J., Duda E.E., Geldner E., Dietz K., "X-ray imaging of blood vessels to the brain by use of magnification stereoscopic technique," [In] *Advance in Neurology, Vol.30: Diagnosis and Treatment of Brain Ischemia*, Carney A.L. et al., Eds., Raven Press, New York, pp.175-189, 1981.
- Doi K., Rossmann K., Duda E.E., "Application of longitudinal magnification effect to magnification stereoscopic angiography: A new method of cerebral angiography," *Radiol.*, vol.124, pp.395-401, 1976.
- Duda R.O., Hart P.E., *Pattern Recognition and Scene Analysis*, Wiley, New York, 1973.
- Fahimi H., Macovski A., "Reducing the effects of scattered photons in x-ray projection imaging," *IEEE Trans. Med. Imag.*, vol.8, pp.56-63, 1989.
- Fajans J., "Three-dimensional display," *Proc. SPIE*, vol.199, pp.23-28, 1979.
- Feinberg D.A., Crooks L., Hoenninger J., Arakawa M., Watts J., "Pulsatile blood velocity in human arteries displayed by magnetic resonance imaging," *Radiol.*, vol.153, pp.177-180, 1984.
- Ferguson E.T., "Some notes on stereoscopic display, and an isochromic anaglyph C.R.T.," *J. SIDS*, vol.9, pp.201-207, 1968.
- Frei W., Shibata T., Chen C.C., "Fast matching of non-stationary images with false fix protection," *Proc. 5th Int. Conf. Pat. Recogn.*, pp.208-212, 1980.
- Frieden B.R., "Statistical models for the image restoration problem," *Comput. Graph. Image Proces.*, vol.12, pp.40-59, 1980.
- Fujii S., Kaneda Y., Mure H., Nomura K., Matsuo M., "Three dimensional reconstruction of cerebral arteries from biplane cerebral angiograms," [In] *Medinfo-83*, van Bommel et al., Eds., North-Holland, Amsterdam, pp.341-344, 1983.
- Fukui T., Yachida M., Tsuji S., "Detection and tracking of blood vessels in cine-angiograms," *Proc. 5th Int. Conf. Pat. Rec.*, pp.383-385, 1980.
- Gabor D., "Holography, 1948-1971," *Sci.*, vol.177, pp.299-313, 1972.
- Garden K.L., Bates R.H.T., "Image reconstruction from projections VII: Interactive reconstruction of piecewise constant images from few projections," *Optik*, vol. 68, pp.161-173, 1984.
- Garibotto G., Giorgi C., Cerchiari U., "Stereoscopic analysis of vascular and neuro-anatomic data with application in functional stereotactic neurosurgery," *Proc. CAR 85*, Springer Verlag, Berlin, pp.660-665, 1985.

- Gerbrands J.J., Rieber J.H.C., Scholts B., Langhout G., Kooijman C.J., "Structural analysis of the coronary arterial tree," *Proc. IEEE Comp. Soc. Intl. Symposium. on Med. Imag. & Imag. Interp.*, pp.54-58, 1982.
- Gerchberg R.W., "Super resolution through error energy reduction," *Optica Acta*, vol.21, pp.709-720, 1974.
- Ghosh S.K., Boulianne M., "X-ray photogrammetry and floating lines in support of neurosurgery," *Intl. Soc. Photogr. Rem. Sens., XVth Congress*, pp.335-343, 1984.
- Ghosh-Roy D.N., Kruger R.A., Yih B., Del Rio F., "Selective plane removal in limited angle tomographic imaging," *Med. Phys.*, vol.12, pp.65-70, 1985.
- Gilbert P.F.C., "Iterative methods for the reconstruction of three-dimensional objects from projections," *J. Theor. Biol.*, vol.36, pp.105-117, 1972a.
- Gilbert P.F.C., "The reconstruction of a three-dimensional structure from projections and its application to electron microscopy II, direct methods," *Proc. Roy. Soc. Lond. B.*, vol.182, pp.89-102, 1972b.
- Goitein M., "Three-dimensional density reconstruction from a series of two-dimensional projections," *Nucl. Instr. Methods*, vol.101, pp.509-518, 1971.
- Gordon R., Bender R., Herman G.T., "Algebraic reconstruction techniques (ART) for three-dimensional electron microscopy and x-ray photography," *J. Theor. Biol.*, vol.29, pp.471-481, 1970.
- Gordon R., Herman G.T., "Three-dimensional reconstruction from projections: A review of algorithms," in G.F. Bourne and J.F. Danielli, Eds., *International Review of Cytology* - vol.38, New York, Academic Press pp.111-151, 1974.
- Grant D.G., "Tomosynthesis: A three-dimensional radiographic imaging technique," *IEEE Trans. Biomed. Eng.*, vol.19, pp.20-28, 1972.
- Greguss P., "Holographic displays for computer assisted tomography," *J. Comput. Assist. Tomogr.*, vol.1, pp.184-186, 1977.
- Haaker P., Klotz E., Koppe R., Linde R., Moller H., "A new digital tomosynthesis method with less artifact for angiography," *Med. Phys.*, vol.12, pp.431-436, 1985.
- Hale J.D., Valk P.E., Watts J.C., Kaufman L., Crooks L.E., Higgins C.B., Deconinck F., "MR imaging of blood vessels using three-dimensional reconstruction: Methodology," *Radiol.*, vol.157, pp.727-733, 1985.
- Hanson K.M., "CT reconstruction from limited projection angles," *Proc. SPIE*, vol.347, pp.166-173, 1982a.

- Hanson K.M., "Limited angle CT reconstruction using a priori information," *Proc. IEEE Comp. Soc. Intl. Symp. on Med. Imag. & Imag. Interp.*, pp.527-533, 1982b.
- Hartmann G.H., Schlegel W., Sturm V., Kober B., Pastyr O., Lorenz W.J., "Cerebral radiation surgery using moving field irradiation at a linear accelerator facility," *Int. J. Rad. Oncol. Biol. Phys.*, vol.11, pp.1185-1192, 1985.
- Heffernan P.B., Bates R.H.T., "Image reconstruction from projections. VI: Comparison of interpolation methods," *Optik*, vol.60, pp.129-142, 1982.
- Heffernan P.B., Robb R.A., "Difference image reconstruction from a few projections for nondestructive materials inspection," *Appl. Optics*, vol.24, pp.4105-4110, 1985.
- Heifetz M.D., Wexler M., Thompson R., "Single-beam radiotherapy knife," *J. Neurosurg.*, vol.60, pp.814-818, 1984.
- Heintzen P.H., Moldenhauer M., "X-ray absorption by contrast material using pulsed radiation," [In] *Roentgen-, Cine- and Video- densitometry. Fundamentals and applications for blood flow and heart volume determinations*, P.H. Heintzen, Ed., Thieme, Stuttgart, pp.73-81, 1971.
- Herman G.T., "Dynamic stereo display and interaction with surfaces of medical objects," *Proc. SPIE*, vol.671, pp.124-131, 1986.
- Herman G.T., Lent A., "Iterative reconstruction algorithms," *Comput. Biol. Med.*, vol.6, pp.273-294, 1976b.
- Herman G.T., Lent A., "Quadratic optimization for image reconstruction, I," *Comput. Graph. Image Proces.*, vol.5, pp.319-332, 1976a.
- Herman G.T., Lent A., Rowland S., "ART: Mathematics and applications: A report on the mathematical foundations and on the applicability to real data of the algebraic reconstruction techniques," *J. Theor. Biol.*, vol.43, pp.1-32, 1973.
- Herman G.T., Reynolds R.A., Udupa J.K., "Computer techniques for the representation of three-dimensional data on a two-dimensional display," *Proc. SPIE*, vol.367, pp.3-14, 1982.
- Hodges L.F., McAllister D.F., "Stereo and alternating-pair techniques for display of computer-generated images," *IEEE CGA*, vol.38, pp.38-45, 1985.
- Hoffmann K.R., Doi D., Chan H.P., Chua K.G., "Computer reproduction of the vasculature using an automated tracking method," *Proc. SPIE*, vol.767, pp.449-453, 1987.



- Hoffmann K.R., Doi K., Chan H.P., Fencil L., Fujita H., Muraki A., "Automated tracking of the vascular tree in DSA images using a double-square-box region-of-search algorithm," **Proc. SPIE**, vol.626, pp.326-333, 1986.
- Högbom J.A., "Aperture synthesis with a non-regular distribution of interferometer baselines," **Astron. Astrophys. Suppl.**, vol.15, pp.417-426, 1974.
- Huang T.S., "Digital holography," **Proc. IEEE**, vol.59, pp.1335-1346, 1971.
- Inouye T., "Image reconstruction with limited angle projection data," **IEEE Trans. Nucl. Sci.**, vol.26, pp.2666-2669, 1979.
- Jarre H.A., Teschendorf O.E.W., "Roentgen-Stereoscopy: A review of its present status," **Radiol.**, vol.21, pp.139-155, 1933.
- Johns J.E., Cunningham J.R., **The Physics of Radiology**, Charles C. Thomas, Springfield IL., 1984.
- Julesz B., **Foundations of Cyclopean Perception**, University of Chicago Press, Chicago IL, 1971.
- Kaczmarz S., "Angenaherte aufloesung von systemen linearer gleichungen," **Bull. Acad. Polon. Sci. Lett. A.**, vol.35, pp.355-357, 1937.
- Kampp T.D., "The backprojection method applied to classical tomography," **Med. Phys.**, vol.13, pp.329-333, 1986.
- Kawata S., Sklansky J., "Elimination of nonpivotal plane images from x-ray motion tomograms," **IEEE Trans. Med. Imag.**, vol.4, pp.153-159, 1985.
- Kelly P.J., Alker G.J., Kall B.A., Goerss S., "Method of computed tomography-based stereotactic biopsy with arteriographic control," **Neurosurg.**, vol.14, pp.172-177, 1984.
- Kim H.C., Min B.G., Lee T.S., Lee S.J., Lee C.W., Park J.H., Han M.C., "Three-dimensional digital subtraction angiography," **IEEE Trans. Med. Imag.**, vol.1, pp.152-158, 1982.
- Kim W.S., Ellis S.R., Tyler M.E., Hannaford B., Stark L.W., "Quantitative evaluation of perspective and stereoscopic displays in three-axis manual tracking tasks," **IEEE Trans. Sys. Man Cyber.**, vol.17, pp.61-72, 1987.
- Kimura K., Kato H., Yamada H., Saito M., Ueda M., Kanno T., Yamaguchi M., Ouchi H., Ikuse J., Yamamura T., Nishio K., Oizumi M., "Experimental stereoradiographic x-ray tube -- Performance and effect on errors in stereoscopic measurements," **Toshiba Med. Rev.**, vol.10, pp.23-32, 1983.
- Kitamura K., Tobis J.M., Sklansky J., "Estimating the 3-<sup>1</sup> skeletons and transverse areas of coronary arteries from biplane angiograms," **IEEE Trans. Med. Imag.**, vol.7, pp.173-187, 1988.

- Kooijman C.J., Reiber J.H.C., Gerbrands J.J., Schuurbijs J.C.H., Slager C.J., Den Boer A., Serruys P.W., "Computer-aided quantitation of the severity of coronary obstructions from single view cineangiograms," *Proc. IEEE Comp. Soc. Intl. Symposium. on Med. Imag. & Imag. Interp.*, pp.59-64, 1982.
- Kruger R.A., Mistretta C.A., Riederer S.J., "Physical and technical considerations of computerized fluoroscopy difference imaging," *IEEE Trans. Nuc. Sci.*, vol.28, pp.205-212, 1981.
- Kruger R.A., Nelson J.A., Ghosh-Roy D., Miller F.J., Anderson R.E., Liu P., "Dynamic tomographic digital subtraction angiography using temporal filtration," *Radiol.*, vol.147, pp.863-867, 1983.
- Kruger R.A., Reinecke D.R., Smith S.W., Ning R., "Reconstruction of blood vessels from x-ray subtraction projections: Limited angle geometry," *Med. Phys.*, vol.14, pp.940-949, 1987.
- Kruger R.A., Riederer S.J., *Basic Concepts of Digital Subtraction Angiography*, G.K. Hall Medical Publishers, Boston, 1984.
- Kruger R.A., Sedaghati M., Roy D.G., Liu P., Nelson J.A., Kubal W., Del Rio P., "Tomosynthesis applied to digital subtraction angiography," *Radiol.*, vol.152, pp.805-808, 1984.
- Kruger R.A., Smith S.W., "Real time circular tomography system for cardiac imaging," *Proc. SPIE*, vol.914, pp.270-280, 1988.
- Lane B., "Stereoscopic displays," *Proc. SPIE*, vol.367, pp.20-32, 1982.
- Legault R., "The aliasing problem in two-dimensional sampled imagery," [In] *Perception of Displayed Information*, L.M. Biberman, Ed., Plenum Press, New York, pp.279-312, 1973.
- Legout A., Gibaud B., Barillot C., Moreau J.J., "3-D representation of cerebral blood vessels using photogrammetry and computer graphics," *Proc. SPIE*, vol.602, pp.295-300, 1985.
- Leksell L., "Stereotaxic apparatus for intracerebral surgery," *Acta Chir. Scand.*, vol.99, pp.229-233, 1949.
- Leksell L., "The stereotactic method and radiosurgery of the brain," *Acta Chir. Scand.*, vol.102, pp.315-319, 1951.
- Lent A., "Maximum entropy and multiplicative ART," [In] *Image Analysis and Evaluation*, Soc. Phot. Sci. Eng., pp.249-257, 1977.
- Lent A., Tuy H., "An iterative method for the extrapolation of band-limited functions," *J. Math. Anal. Applic.*, vol.83, pp.554-565, 1981.
- Lesem L.B., Hirsch P.M., "Computer synthesis of holograms for 3-d display," *Comm. ACM*, vol.11, pp.661-674, 1968.

- Levine M.D., O'Handley D.A., Yagi G.M., "Computer determination of depth maps," *Comput. Graph. Image Proces.*, vol.2, pp.131-150, 1973.
- Lewitt R.M., "Reconstruction algorithms: Transform methods," *Proc. IEEE*, vol.71, pp.390-408, 1983.
- Lewitt R.M., Bates R.H.T., Peters T.M., "Image reconstruction from projections. II: Modified back-projection methods." *Optik*, vol.50, pp.85-109, 1978.
- Lippmann G., *Comptes-Rendus*, vol.146, pp.446-451, 1908.
- Lipton L., Meyer L., "A flicker-free field-sequential stereoscopic video system," *SMPTE J.*, Nov., pp.1047-1051, 1984.
- Lirov Y., Vannier M.W., "System analysis of stereotactic neurosurgery based on CT scans," *Comp. & Maths. with Appls.*, vol.12A, pp.839-858, 1986.
- Liu J., Nishimura D., Macovski A., "Vessel imaging using dual-energy tomosynthesis," *Med. Phys.*, vol.14, pp.950-955, 1987.
- Louis A.K., Natterer F., "Mathematical problems of computerized tomography," *Proc. IEEE*, vol.71, pp.379-389, 1983.
- Love A.L., Kruger R.A., "Scatter estimation for a digital radiographic system using convolution filtering," *Med. Phys.*, vol.14, pp.178-185, 1987.
- MacKay S.A., Sayre R.E., Potel M.J., "3-D Galatea: Entry of three-dimensional moving points from multiple perspective views," *Comput. Graph.*, vol.16, pp.213-222, 1982.
- Macovski A., "Selective projection imaging: Applications to radiography and NMR," *IEEE Trans. Med. Imag.*, vol.1, pp.42-47, 1982.
- Macovski A., *Medical Imaging Systems*, Prentice-Hall, New Jersey, 1983.
- Maravilla K.R., Murry R.C., Diehl J., Suss R., Allen L., Chang K., Crawford J., McCoy R., "Digital tomosynthesis: Technique modifications and clinical applications for neurovascular anatomy," *Radiol.*, vol.152, pp.719-724, 1984.
- Mark H., Hull F., "Three-dimensional viewing of tomographic data - the Tomax system," *Proc. SPIE*, vol.120, pp.192-194, 1977.
- McNeil G.T., "X-ray stereo photogrammetry," *Photogr. Eng.*, pp.993-1004, 1966.
- Meacham G.B.K., "Autostereoscopic displays - past and future," *Proc. SPIE*, vol.624, pp.90-101, 1986.
- Mills P.H., Fuchs H., Pizer S.M., "High-speed interaction on a vibrating-mirror 3-d display," *Proc. SPIE*, vol.507, pp.93-101, 1984.

- Minerbo G., "MENT: A maximum entropy algorithm for reconstructing a source from projection data," *Comput. Graph. Image Proces.*, vol.10, pp.48-68, 1979.
- Mistretta C., "The use of a general description of the radiological transmission image for categorizing image enhancement," *Opt. Eng.*, vol.13, pp.134-138, 1974.
- Mol C.R., Burridge J.M., Morffew A.J., "Three-dimensional graphics display of x-ray angiography data," *Comput. Biomed. Res.*, vol.19, pp.47-55, 1986.
- Montebello de R.L., "The synthalyzer for three-dimensional synthesis and analysis by optical dissection," *Proc. SPIE*, vol.120, pp.184-189, 1977b.
- Montebello de R.L., "Wide-angle integral photography - the integral system," *Proc. SPIE*, vol.120, pp.73-79, 1977a.
- Mori K.I., Kidode M., Asada H., "An iterative prediction and correction method for automatic stereocomparison," *Comput. Graph. Image Proces.*, vol.2, pp.393-401, 1973.
- Muehllehner G., Wetzel R.A., "Section imaging by computer calculation," *J. Nuc. Med.*, vol.12, pp.76-84, 1971.
- Muirhead J.C., "Variable focal length mirrors," *Rev. Sci. Instr.*, vol.32, pp.210-211, 1961.
- Nadjmi M., Weiss H., Klotz E., Linde R., "Flashing tomosynthesis - a new tomographic method," *Neuroradiol.*, vol.19, pp.113-117, 1980.
- Naidich T.P., Pudlowski R.M., Leeds N.E., Naidich J.B., Chisolm A.J., Rifkin M.D., "The normal contrast-enhanced computed axial tomogram of the brain," *J. Comput. Assist. Tomogr.*, vol.1, pp.16-29, 1977.
- Naimuddin S., Hasegawa B., Mistretta C.A., "Scatter-glare correction using a convolution algorithm with variable weighting," *Med. Phys.*, vol.14, pp.330-334, 1987.
- Nalcioğlu O., Lou R.Y., "Post-reconstruction method for beam hardening in computerised tomography," *Phys. Biol. Med.*, vol.24, pp.330-340, 1979.
- Nalcioğlu O., Seibert J.A., Boone J.M., Wang Y., Roeck W.W., Henry W.L., Tobis J.M., Johnston W.D., "The effect of physical problems on the determination of ventricular ejection fraction by video densitometry," [In] *Digital Imaging in Cardiovascular Radiology*, P.H. Heintzen and R. Brennecke, Eds., Thieme, Stuttgart, pp.104-115, 1983.
- Nassi M., Brody W.R., Medoff B.P., Macovski A., "Iterative reconstruction - reprojection: an algorithm for limited data cardiac-computed tomography," *IEEE Trans. Biomed. Eng.*, vol.29, pp.333-340, 1982.

- Nauta H.J.W., Guinto F.C., Pisharodi M., "Arterial bolus contrast medium enhancement for computed tomographically guided stereotactic biopsy," *Surg. Neurol.*, vol.22, pp.559-564, 1984.
- Newman W.M., Sproull R.F., *Principles of Interactive Computer Graphics*, New York, McGraw-Hill, 1979.
- Nguyen T.V., Sklansky J., "Computing the skeleton of coronary arteries in cineangiograms," *Comput. Biomed. Res.*, vol.19, pp.428-444, 1986.
- Ning R., Hu H., Kruger R.A., "Image intensifier-based CT volume image for angiography," *Proc. SPIE.*, vol.914, pp.282-290, 1988.
- Ning R., Kruger R.A., "Computer simulation of image intensifier-based computed tomography detector: Vascular application," *Med. Phys.*, vol.15, pp.188-192, 1988.
- Nishimura D.G., Macovski A., Pauly J.M., "Magnetic resonance angiography," *IEEE Trans. Med. Imag.*, vol.5, pp.140-151, 1986.
- Nyquist H., "Certain topics in telegraph transmission theory," *A.I.E.E. Trans.*, p.617, 1928.
- Olivier A., Peters T.M., Bertrand G., "Stereotaxic systems and apparatus for use with MRI, CT, and DSA," *Appl. Neurophysiol.*, vol.48, p.94-96, 1985.
- Oppenheim B.E., "Reconstruction tomography from incomplete projections," [In] *Reconstruction Tomography in Diagnostic Radiology and Nuclear Medicine*, M.M. Ter-Pogossian et al., Eds., Baltimore, MD, University Park Press, pp.155-183, 1977.
- Ortony A., "A system for stereo viewing," *Comput. J.*, vol.14, pp.140-144, 1970.
- Parker D.L., Pope D.L., Van Bree R., Desai R., "Three dimensional reconstruction of vascular beds from digital angiographic projections," *Proc. SPIE*, vol.671, pp.50-59, 1986.
- Parker D.L., Pope D.L., Van Bree R., Marshall H.W., "Three-dimensional reconstruction of moving arterial beds from digital subtraction angiography," *Comput. Biomed. Res.*, vol.20, pp.166-185, 1987.
- Parker D.L., Pope D.L., White K.S., Tarbox L.R., Marshall H.W., "Three dimensional reconstruction of vascular beds," *Proceedings of the Conference on Information Processing in Medical Imaging*, Georgetown, June 10-14, 1985.
- Parker D.L., Pryor T.A., "Analysis of b-scan speckle reduction by resolution limited filtering," *Ultras. Imag.*, vol.4, pp.108-175, 1982.
- Perlmutter R.J., "Digital holography display of medical CT images," *Proc. SPIE*, vol.367, pp.109-114, 1982.

- Peters T.M., **Image Reconstruction from Projections**, Ph.D. thesis, University of Canterbury, New Zealand, 1973.
- Peters T.M., "Algorithms for fast back- and re-projection in computed tomography," **IEEE Trans. Nucl. Sci.**, vol.28, pp.3641-3647, 1981.
- Peters T.M., Clark J.A., Olivier A., Marchand E., Mawko G., Dieumegarde M., Muresan L.V., Ethier R., "Integrated stereotactic imaging with CT, MRI, and DSA," **Radiol.**, vol.161, pp.821-826, 1986.
- Peters T.M., Olivier A., "C.T. aided stereotaxy for depth electrode implantation and biopsy," **Can. J. Neurol. Sci.**, vol.10, pp.166-169, 1983.
- Pickens D.R., Price R.R., Erikson J.J., James Jr. A.E., "Digital image motion correction by spatial warp methods," **Med. Phys.**, vol.14, pp.56-61, 1987.
- Pike B., Podgorsak E.B., Peters T.M., Pla C., "Dose distributions in dynamic stereotactic radiosurgery," **Med. Phys.**, vol.14, pp.780-789, 1987.
- Pope D.L., Parker D.L., Clayton P.D., Gustafson D.E., "Dynamic search algorithms in left ventricular border recognition and analysis of coronary arteries," **Comput. in Cardiol.**, pp.71-75, 1984.
- Pope D.L., Parker D.L., Clayton P.D., Gustafson D.E., "Left ventricular border recognition using a dynamic search algorithm," **Radiol.**, vol.155, pp.513-518, 1985.
- Potel M.J., Rubin J.M., MacKay S.A., Aisen A.M., Al-Sadi J., Sayre R.E., "Methods for evaluating cardiac wall motion in three dimensions using bifurcation points of the coronary arterial tree," **Invest. Radiol.**, vol.18, pp.47-57, 1983.
- Potel M.J., Sayre R.E., Robertson A., "A system for interactive film analysis," **Comput. Biol. Med.**, vol.9, pp.237-256, 1979.
- Rabischong P., Vignaud J., Pardo P., Thurel R., Yver J.P., "Stereoradiogrammetry and angiography," [In] **Advances in Cerebral Angiography**, Salamon G., Ed., Springer-Verlag, pp.141-147, 1975.
- Ramachandran G.N., Lakshminarayanan A., "Three-dimensional reconstruction from radiographs and electron micrographs: Applications of convolutions instead of Fourier transforms," **Proc. Natl. Acad. Sci. U.S.**, vol.68, pp.2236-2240, 1971.
- Rawson E.G., "Vibrating varifocal mirrors for 3-d imaging," **IEEE Spect.**, vol.6, pp.37-43, 1969.
- Reiber J.H.C., Kooijman C.J., Slager C.J., Gerbrands J.J., Schuurbijs J.C.H., Den Boer A., Wijns W., Serruys P.W., "Computer assisted analysis of the severity of obstructions from coronary cineangiograms: A methodological review," **Automedica**, vol.5, pp.219-238, 1984.

- Riederer S.J., Pelc N.J., Georges J.P.L., Keyes G.S., Lehmann L.A., Hall A.L., "Beam hardening, noise, and contrast considerations in selective iodine digital radiography," *IEEE Trans. Nuc. Sci.*, vol.28, pp.213-218, 1981.
- Ritchings R.T., Colchester A.C.F., Wang H.Q., "Knowledge-based analysis of carotid angiograms," *Imag. Vis. Comp.*, vol.3, pp.217-222, 1985.
- Roehrig H., Nudelman S., Fisher H.D., Frost M.M., Capp M.P., "Photoelectric imaging for radiology," *IEEE Trans. Nucl. Sci.*, vol.28, pp.190-204, 1981.
- Roese J.A., Turner A.J., "Single monitor stereoradiological television system using PLZT electroptic shutters," *Radiol.*, vol.121, pp.743-744, 1976.
- Rogers D.F., Adams J.A., **Mathematical Elements for Computer Graphics**, McGraw-Hill, 1976.
- Rosenfeld A., Hummel R.A., Zucker S.W., "Scene labeling by relaxation operations," *IEEE Trans. Sys. Man Cyber.*, vol.6, pp.420-433, 1976.
- Rosenfeld A., Kak A.C., **Digital Picture Processing**, 2nd ed., Academic Press, New York, 1982.
- Rossi D.J., Willsky A.S., "Reconstruction from projections based on detection and estimation of objects - Parts I and II: Performance analysis and robustness analysis," *IEEE Trans. Acous. Speech Sig. Proces.*, vol.32, pp.886-906, 1984.
- Rougee A., Hanson K.M., Saint-Felix D., "Comparison of 3-d tomographic algorithms for vascular reconstruction," *Proc. SPIE.*, vol.914, pp.397-405, 1988.
- Rubin J.M., Patronas N.J., Duda E.E., Sayre R.E., Potel M.J., "Clinical applications of combined cerebral angiograms and brain CT scans," *A.J.N.R.*, vol.1, pp.83-87, 1980.
- Rubin J.M., Sayre R.E., "A computer-aided technique for overlaying cerebral angiograms onto computed tomograms," *Invest. Radiol.*, vol.13, pp.362-367, 1978.
- Rudell E.A., Sheiman D., "Dual fresnel lenses make 3-d image," *Mach. Des.*, vol.55, p.77, 1983.
- Ruttimann U.E., Groenhuis R.A.J., Webber R.L., "Restoration of digital multiplane tomosynthesis by a constrained iteration method," *IEEE Trans. Med. Imag.*, vol.3, pp.141-148, 1984.
- Sand R., "A system for stereo viewing," *Comput. J.*, vol.14, pp.140-144, 1970.

- Sato T., Norton S.J., Linzer M., Ikeda O., Hiram M., "Tomographic image reconstruction from limited projections using iterative revisions in image and transform spaces," *Appl. Optics*, vol.20, pp.359-399, 1981.
- Saunders B.G., "Stereoscopic drawing by computer - is it orthoscopic?," *Appl. Opt.*, vol.17, pp.1499-1504, 1968.
- Saw C.B., Ayyangar K., Suntharalingam N., "Coordinate transformations and calculation of the angular and depth parameters for a stereotactic system," *Med. Phys.*, vol.14, pp.1042-1044, 1987.
- Sayre R.E., Rubin J.M., Duda E.E., Patronas N.J., "Quantitative three-dimensional angiograms: Application, including augmentation of computed tomograms," *Proc. SPIE Conf. on Comput. Applic. in Radiol.*, pp.95-102, 1979.
- Scanlon J.G., Gustafson D.B., Chevalier P.A., Robb R.A., Ritman E.L., "Evaluation of ischemic heart disease with a prototype volume imaging computed tomographic (CT) scanner: Preliminary experiments," *Amer. J. Cardiol.*, vol.46, pp.1263-1268, 1980.
- Schwarz U.J., "Mathematical-statistical description of the iterative beam removing technique (method clean)," *Astron. Astrophys.*, vol.65, pp.345-356, 1978.
- Seibert J.A., Boone J.M., "X-ray scatter removal by deconvolution," *Med. Phys.*, vol.15, pp.567-575, 1988.
- Seibert J.A., Nalcioglu O., Roeck W.W., "Removal of image intensifier veiling glare by mathematical deconvolution techniques," *Med. Phys.*, vol.12, pp.281-288, 1985.
- Shaw C.G., Ergun D.L., Van Lysel M.S., Peppler W.W., Dobbins J.T., Zarnstorff W.C., Myerowitz P.D., Swanson D.K., Lasser T.A., Mistretta C.A., Strother C.M., Crummy A.B., "Quantitation techniques in digital subtraction videoangiography," *Proc. SPIE*, vol.314, pp.121-129, 1981.
- Shaw C.G., Ergun D.L., Myerowitz P.D., Van Lysel M.S., Mistretta C.A., Zarnstorff W.C., Crummy A.B., "A technique of scatter and glare correction for videodensitometric studies in digital subtraction videoangiography," *Radiol.*, vol.142, pp.209-213, 1982.
- Shaw C.G., Plewes D., "Quantitative digital subtraction angiography: Two scanning techniques for correction of scattered radiation and veiling glare," *Radiol.*, vol.157, pp.247-252, 1985.
- Shepp L.A., Logan B.F., "The Fourier reconstruction of a head section," *IEEE Trans. Nucl. Sci.*, vol.21, pp.21-43, 1974.
- Sherlock R.A., Aitken W.M., "A method of precision position determination using x-ray stereography," *Phys. Med. Biol.*, vol.25, pp.349-355, 1980.



- Simon W., Walter T., "A spinning mirror autostereoscopic display," *Proc. SPIE*, vol.120, pp.180-183, 1977.
- Singer J.R., Crooks L.E., "Nuclear magnetic resonance blood flow measurements in the human brain," *Sci.*, vol.221, pp.654-656, 1983.
- Smets C., Verbeeck G., Suetens P., Oosterlinck A., "A knowledge-based system for the delineation of blood vessels on subtraction angiograms," *Pat. Rec. Let.*, vol.8, pp.113-121, 1988.
- Smith C.R., Grandy Jr. W.T., Eds., **Maximum Entropy and Bayesian Methods in Inverse Problems**, D. Reidel Publishing Co., Dordrecht Holland, 1985.
- Smith P.R., Peters T.M., Bates R.H.T., "Image reconstruction from a finite no. of projections," *J. Phys. A.*, vol.6, pp.361-382, 1973.
- Smith W.M., Starmer C.F., "Computer representation of coronary arterial trees," *Comput. Biomed. Res.*, vol.9, pp.187-201, 1976.
- Smith W.S., Kruger R.A., "Fast circular tomography device for cardiac imaging: Image deflection mechanism and evaluation," *IEEE Trans. Med. Imag.*, vol.6, pp.169-173, 1987.
- Spears J.R., Sandor T., Hanlon W., Sinclair I.N., James L., Minerbo G., "Computerized axial tomographic reconstruction of coronary tree cross sections from a small number of cineradiographic views," *Comput. Biomed. Res.*, vol.21, pp.227-243, 1988.
- Stansfield S.A., "ANGY: A rule-based expert system for automatic segmentation of coronary vessels from digital subtracted angiograms," *IEEE Trans. Pat. Anal. Mac. Int.*, vol.8, pp.188-199, 1986.
- Stevenson D.J., Smith L.D.R., Robinson G., "Working towards the automatic detection of blood vessels in x-ray angiograms," *Pat. Rec. Let.*, vol.6, pp.107-112, 1987.
- Stearns S.D., **Digital Signal Analysis**, Hayden Book Company Inc, Rochelle Park, New Jersey, p.45, 1975.
- Strang G., **Linear Algebra and Its Applications**, 2nd ed., Academic Press, 1980.
- Suetens P., Baert A.L., Gybels J., Haegemans A., Jansen P., Oosterlinck A., Wilms G., "An integrated 3-d image of the cerebral blood vessels and CT view of tumor," [In] **Frontiers in European Radiology**, Vol.3, Baert A.L. et al., Eds., Springer-Verlag, pp.81-100, 1984.
- Suetens P., Gybels J., Oosterlinck A., Haegemans A., "Digital Radiography in stereotactic and functional neurosurgery," *Appl. Neurophysiol.*, vol.45, pp.365-373, 1982.

- Suetens P., Jansen P., Haegemans A., Oosterlinck A., Gybels J., "3D reconstruction of the blood vessels of the brain from a stereoscopic pair of subtraction angiograms," *Imag. Vis. Comput.*, vol.1, pp.43-51, 1983.
- Suetens P., Vandermeulen D., Oosterlinck A., Gybels J., Marchal G., "A 3-d display system with stereoscopic, movement parallax and real-time rotation capabilities," *Proc. SPIE*, vol.914, pp.885-859, 1988.
- Sun Y., "Automated identification of vessel contours in coronary arteriograms by an adaptive tracking algorithm," *IEEE Trans. Med. Imag.*, vol.8, pp.78-88, 1989.
- Sutherland I.E., "Three-dimensional data input by tablet," *Proc. IEEE*, vol.62, pp.453-461, 1974.
- Szikla G., Bouvier G., Hori T., "In vivo localization of brain sulci by arteriography: A stereotactic anatomoradiological study," *Brain Res.*, vol.95, pp.497-502, 1975.
- Tam K.C., Perez-Mendez V., "Limits to image reconstruction from restricted angular input," *IEEE Trans. Nucl. Sci.*, vol.28, pp.179-183, 1981.
- Takemura H., Tomono A., Kobayashi Y., "An evaluation of 3-d object pointing using a field sequential stereoscopic display," *Graphics Interface'88*, pp.112-118, 1988.
- Tektronix Inc., Beaverton, Oregon, USA, 1989.
- Tipal Instruments Inc., Montreal, Canada, 1989.
- Traub A.C., "Stereoscopic display using rapid varifocal mirror oscillations," *Appl. Opt.*, vol.6, pp.1085-1087, 1967.
- Udupa J.K., "Display of 3-d information in discrete 3-d scenes produced by computerized tomography," *Proc. IEEE*, vol.71, pp.420-431, 1983.
- Valk P.E., Hale J.D., Kaufman L., Crooks L.E., Higgins C.B., "MR imaging of the aorta with three-dimensional vessel reconstruction: Validation by angiography," *Radiol.*, vol.157, pp.721-725, 1985.
- Venot A., Leclerc V., "Automated correction of patient motion and grey values prior to subtraction in digitized angiography," *IEEE Trans. Med. Imag.*, vol.3, pp.179-186, 1984.
- Vignaud J., Korach G., "Stereoscopie et photogrammetrie," *J. Radiol. Electrol.*, vol.54, pp.572-575, 1973.
- Vignaud J., Rabischong P., Yver J.P., Pardo P., Thurel C., "Multidirectional reconstruction of angiograms by stereogrammetry and computer. Application to computed tomography," *Neuroradiol.*, vol.18, pp.1-7, 1979.

- Von Helmholtz H., **Helmholtz's Treatise on Physiological Optics**, Vol.III, 3<sup>rd</sup> ed., Optical Society of America, Menasha, Wisc., 1925.
- Wagner W., "Incomplete scan geometries in fast x-ray scanners," **Biomed. Tech.**, vol.24, pp.140-147, 1979.
- Wedeen V.J., Meuli R.A., Edelman R.R., Geller S.C., Frank L.R., Brady T.J., Rosen B.R., "Projective imaging of pulsatile flow with magnetic resonance," **Sci.**, vol.230, pp.946-948, 1985.
- Wedeen V.J., Rosen B.R., Buxton R., Brady T.J., "Projective MRI angiography and quantitative flow-volume densitometry," **Mag. Reson. in Med.**, vol.3, pp.226-241, 1986.
- Weinstein M.A., Duchesneau P.M., Weinstein C., "Computed angiotomography," **A.J.R.**, vol.129, pp.699-701, 1977.
- Withey E.L., "Cathode-ray tube adds third dimension," **Elect.**, vol.31, pp.81-83, 1958.
- Wolvin J., "Anaglyph stereoscopic crt display system," **J. SIDS.**, vol.8, pp.169-176, 1967.
- Yakimovski Y., Cunningham R., "A system for extracting three dimensional measurements from a stereo pair of tv cameras," **Comput. Graph. Image Proces.**, vol.7, pp.195-210, 1978.
- Yamanaka R., Yamamoto K., Handa N., Yoshikura H., "A 3-d display with a linearly moving mirror to reflect a series of 2-d cross sections and it application to noninvasive angiography," **IEEE Trans. Med. Imag.**, vol.7, pp.193-197, 1988.
- Ziedses des Plantes B.G., "Eine neue methods zur differenzierung in der roentgenographie," **Acta Radiol.**, vol.13, pp.182-192, 1932.
- Ziedses des Plantes B.G., **Plantinigraphie en subtractie: Roentgenographische differentiatiemethoden**. Thesis, University of Utrecht, 1934.
- Ziedses des Plantes B.G., **Subtraktion**. Stuttgart, Thieme, 1962.
- Zucker S.W., "Relaxation labeling and the reduction of local ambiguities," **IJCPR**, pp.852-861, 1976.

# GLOSSARY

## List of Important Symbols

<u>Symbol</u>	<u>Chapter</u>	<u>Meaning</u>	<u>Typical Units</u>
a	3	constants	various
	5	weighting factor	—
a()	5	general function	various
A	5	length of major axis	various
A()	3	2-d matrix	various
b	2	grey level	—
B	2	total number of grey levels	—
	5	length of minor axis	various
B()	3	2-d matrix	various
c	5	convergence criterion	—
C	2	object contrast	—
d	2	thickness	cm
	3,4,5	distance	cm
d()	5	2-d difference matrix	various
D	3	damping factor	—
	4	distance	cm
	5	diameter	cm
E	2	energy	erg, J, eV, keV
	5	difference measure	various
f	2,3	length	cm
f()	5	projection	various
F{}	throughout	Fourier operator	—
g()	5	projection	various
G	3,4	gain parameter	—
G()	5	2-d function	—
K	2,3,4	pure number	—
I	5	pure number	—
J	5	pure number	—
l	3	disparity vector	—
L	3	set of disparity vectors	—
M	2,4	geometric magnification	—
	3,5	pure number	—
M()	3	2-d matrix	various
N	throughout	pure number	—
P	3,4	probability	—
	5	constant	—
q, q()	5	filter coefficients, filter kernel	—
Q	3,4	damping parameter	—
r	2	resolution	lp cm <sup>-1</sup>
	3,4	sample index number	—
	5	radius	cm
R	throughout	real numbers	—
R{}	5	reconstruction operator	—
s	2,3,4	distance	cm
S()	5	2-d function	various
T()	3	2-d matrix	—

# GLOSSARY

## List of Important Symbols

<u>Symbol</u>	<u>Chapter</u>	<u>Meaning</u>	<u>Typical Units</u>
$u$	5	spatial frequency component conjugate to $x$	$\text{cm}^{-1}$
$U()$	3	2-d matrix	—
$v$	5	spatial frequency component conjugate to $y$	$\text{cm}^{-1}$
$v()$	3	general function	various
$w$	3	similarity measure	—
$W$	2	diameter	cm
	4	difference measure	various
	5	window function	—
$x$	2	cartesian coordinate, general variable	cm
$y$	2	cartesian coordinate	cm
$z$	2	cartesian coordinate	cm
$\alpha$	5	gain parameter	—
	A	angle	—
$\beta$	3,A	angle	—
$\delta()$	throughout	Dirac delta function	various
$\Delta$	throughout	change in something	—
$\epsilon$	5	difference measure	various
$\eta$	2	weighting factor	—
	5	rotated coordinate conjugate to $y$	cm
$\theta$	throughout	angle	—
$\lambda(x,y)$	throughout	2-d function	—
$\Lambda(\xi,\eta)$	throughout	Fourier transform of $\lambda()$	—
$\mu$	throughout	linear attenuation coefficient	$\text{cm}^{-1}$
$\xi$	5	rotated coordinate conjugate to $x$	cm
$\pi$	throughout	3.14159	—
$\rho$	5	spatial frequency component conjugate to $r$	$\text{cm}^{-1}$
$\sigma$	throughout	standard deviation (square root of variance)	various
$\sigma^2$	throughout	variance	various
$\phi$	5	angle	—
$\Phi$	throughout	particle fluence	$\text{cm}^{-2}$
$\psi$	3,4	constant	various
	5	angle	—
$\Omega$	5	region of image space	—

## GLOSSARY

### Named Functions

<u>Name</u>	<u>Meaning</u>
sinc(x)	$\sin(\pi x)/\pi x$
PSF	point spread function
RMS	root mean square value

### Abbreviations

<u>Name</u>	<u>Meaning</u>
ADC	analog-to-digital converter
AP	anterior-posterior
CRT	cathode ray tube
CsI	cesium iodide
CT	comput(eriz)ed tomography
DAC	digital-to-analog converter
DSA	digital subtraction angiography
Fortran	computer language
II	image intensifier
LAT	lateral
LEXIDATA	computer display/processor trademark
LUT	look-up-table
MR	magnetic resonance
PHILIPS	trademark
PLZT	lead lanthanum zirconate titanate
TECHNICARE	trademark
TV	television
VAX,VMS	trademarks labeling computer, operating systems
VT-220	key-board trademark
2-d	two dimensions, two-dimensional
3-d	three dimensions, three-dimensional